

**Tailored Design of Functional
Nanoporous Carbon Materials towards
Electrochemical Applications**

電気化学的な応用に向けた機能性ナノポーラス
カーボンのテーラード合成

July 2016

Jing TANG

汤 静

**Tailored Design of Functional
Nanoporous Carbon Materials towards
Electrochemical Applications**

電気化学的な応用に向けた機能性ナノポーラス
カーボンのテーラード合成

July 2016

Waseda University

Graduate School of Advanced Science and Engineering

Department of Nanoscience and Nanoengineering

Research on Synthetic Chemistry of Nanomaterials

Jing TANG

汤 静

Preface

Porous carbons have been considered as promising electrode materials due to their excellent virtues such as low cost, designable porous framework, and good electrical conductivity. Lots of synthetic methods have been developed for fabrication of functionalized nanoporous carbon materials with high specific surface areas, tunable and accessible nanopores, high degree of graphitization and heteroatoms doping, as introduced in **Chapter 1**.

Herein, I focus on synthesis of nanoporous carbon materials with tailored properties, including relatively high specific surface area, accessible nanopore, relatively high degree of graphitization, and nitrogen doping, by using the hard-templating, soft-templating and self-templating methods.

In **Chapter 2**, nitrogen-doped mesoporous carbon spheres with large pore sizes are successfully prepared through self-polymerization of dopamine and spontaneous co-assembly linked with diblock copolymer micelles (PS-*b*-PEO).

Chapter 3 introduces a facile and sustainable procedure for the synthesis of nitrogen-doped hierarchical porous carbons with three-dimensional interconnected framework. The strategy, based on a colloidal crystal templating method, utilizes nitrogenous dopamine as the precursor.

Chapter 4 combines the synthetic methods developed in **Chapter 2** and **3**, designs and successfully synthesizes nitrogen-doped hollow carbon spheres with engineered large tunable mesoporous (~20 nm) shells for the first time.

From **Chapter 5** and **7**, I use self-designed zeolite imidazole framework (ZIF) as both the self-template and carbon precursor. In **Chapter 5**, core-shell structured ZIF-8@ZIF-67 crystals are prepared through a seed-mediated growth method, and firstly used for preparation of selectively functionalized nanoporous carbon.

Chapter 6 explores a novel cage-type highly graphitic porous carbon-Co₃O₄ polyhedron (GPC-Co₃O₄) by executing a two-step annealing of core-shell ZIF-8@ZIF-67, inspired by the research in **Chapter 5**.

In **Chapter 7**, I oriented synthesize of nanoporous carbons with adjustable functionalities by using bimetallic ZIF as the precursor, which merges the advantages of zinc and cobalt ions in one ZIF crystal.

Chapter 8 summarizes my achievements in the tailored design and synthesis of functional nanoporous carbon materials, as well as the future prospects.

Contents

Chapter 1	1
Designed Fabrication of Nanoporous Carbon Materials towards Electrochemical Applications	1
1.1. Introduction	2
1.2. Control of Pore Size, Morphology, and Structure	4
1.2.1. Pore Size Control	4
1.2.2. Morphological and Structural Controls	11
1.2.3. Control of Graphitization Degree	12
1.2.4. Surface Modification of Porous Carbon	17
1.2.5. Heteroatom-Doped Nanoporous Carbon	20
1.2.6. Encapsulation of Nanoparticles in Porous Carbon	26
1.3. Conclusion and Objective	30
References	33
Chapter 2	43
Synthesis of Nitrogen-Doped Mesoporous Carbon Spheres with Extra-Large Pores through Assembly of Diblock Copolymer Micelles	43
2.1. Introduction	44
2.2. Experimental Sections	46
2.2.1. Chemicals	46
2.2.2. Preparation of Nitrogen-Doped Mesoporous Carbon Spheres (NMCS)	46
2.2.3. Characterization	47
2.2.4. Electrochemical Measurements	47
2.3. Results and Discussion	48
2.3.1. Synthesis and Characterization of NMCS	48
2.3.2. Formation Mechanism of NMCS	56

2.3.3. Electrocatalytic Activity of NMCS for Oxygen Reduction Reaction	64
2.4. Conclusion	75
References	75
Chapter 3	80
Three-Dimensional Nitrogen-Doped Hierarchical Porous Carbon as an Electrode for High-Performance Supercapacitors	80
3.1. Introduction	81
3.2. Experimental Sections	83
3.2.1. Chemicals.....	83
3.2.2. Preparation of Silica Spheres.....	83
3.2.3. Preparation of Three-Dimensional Nitrogen-Doped Hierarchical Porous Carbon (NHPC-3D)	83
3.2.4. Characterization	84
3.2.5. Electrochemical Measurements.....	84
3.3. Results and Discussion	85
3.3.1. Synthesis and Characterization of NHPC-3D	85
3.3.2. Electrochemical Supercapacitor with the NHPC-3D Electrode	92
3.4. Conclusion	95
References	95
Chapter 4	98
Nitrogen-Doped Hollow Carbon Spheres with Large Mesoporous Shells Engineered from Diblock Copolymer Micelles.....	98
4.1. Introduction	99
4.2. Experimental Sections	101
4.2.1. Chemicals.....	101
4.2.2. Preparation of Silica Spheres.....	101

4.2.3. Preparation of Nitrogen-Doped Hollow Mesoporous Carbon Spheres (NHCS-LM)	101
4.2.4. Characterization	102
4.2.5. Electrochemical Measurements	103
4.3. Results and Discussion	104
4.3.1. Synthesis and Characterization of NHCS-LM	104
4.3.2. The Potential Applications of NHCS-LM	111
4.4. Conclusion	113
References	113
Chapter 5	116
Thermal Conversion of Core–Shell Metal–Organic Frameworks: A New Method for Selectively Functionalized Nanoporous Hybrid Carbon	116
5.1. Introduction	117
5.2. Experimental Sections	120
5.2.1. Chemicals	120
5.2.2. Preparation of ZIF-8 Seeds with Different Particle Sizes	120
5.2.3. Preparation of ZIF-67	120
5.2.4. Preparation of Core–Shell ZIF-8@ZIF-67 Crystals	120
5.2.5. Carbonization of Core–Shell ZIF-8@ZIF-67 Crystals	121
5.2.6. Characterization	121
5.2.7. Electrochemical Measurements	122
5.3. Results and Discussion	124
5.3.1. Synthesis and Characterization of Core–Shell ZIF-8@ZIF-67 Crystals	124
5.3.2. Thermal Conversion of Core–Shell ZIF-8@ZIF-67 Crystals to Nanoporous NC@GC Materials	130
5.3.3. Electrochemical Supercapacitors with NC@GC Electrodes	138
5.4. Conclusion	145

References	145
Chapter 6	150
Cage-Type Highly Graphitic Porous Carbon–Co₃O₄ Polyhedron as the Cathode of Lithium–Oxygen Batteries	150
6.1. Introduction	151
6.2. Experimental Sections	154
6.2.1. Chemicals.....	154
6.2.2. Synthesis of ZIF-8 Seeds.....	154
6.2.3. Synthesis of Core–Shell ZIF-8@ZIF-67 Crystals	154
6.2.4. Preparation of the Cage-Type Highly Graphitic Porous Carbon-Co ₃ O ₄ (GPC-Co ₃ O ₄) Polyhedron Composite.....	154
6.2.5. Characterization	155
6.2.6. Battery Assembly	156
6.2.7. Electrochemical Measurements and Characterization	156
6.3. Results and Discussion	157
6.3.1. Thermal Conversion of Core–Shell ZIF-8@ZIF-67 Crystals to Cage-Type GPC-Co ₃ O ₄	157
6.3.2. Electrochemical Performance of the Li–O ₂ Battery with a GPC-Co ₃ O ₄ Electrode	164
6.4. Conclusion	169
References	169
Chapter 7	173
Bimetallic Metal–Organic Frameworks for Controlled Catalytic Graphitization of Nanoporous Carbons	173
7.1. Introduction	174
7.2. Experimental Sections	176

7.2.1. Chemicals.....	176
7.2.2. Preparation of Bimetallic ZIFs ($\text{Co}_x\text{Zn}_{1-x}(\text{MeIm})_2$)	176
7.2.3. Carbonization of Bimetallic ZIFs ($\text{Co}_x\text{Zn}_{1-x}(\text{MeIm})_2$)	176
7.2.4. Characterization	177
7.2.5. Electrochemical Measurements.....	178
7.3. Results and Discussion	179
7.3.1. Synthesis and Characterization of Bimetallic ZIFs ($\text{Co}_x\text{Zn}_{1-x}(\text{MeIm})_2$)	179
7.3.2. Thermal Conversion of Bimetallic ZIFs to Nanoporous Carbon Materials.....	183
7.3.3. Electrochemical Supercapacitors with Bimetallic-ZIF-Derived Carbon Electrodes	192
7.4. Conclusion.....	196
References	196
Chapter 8	199
General Conclusions and Future Perspective	199
8.1. Overview of the Achievements	200
<i>(I) Synthesis of N-Doped Porous Carbon based on a Templating Method and Using Nitrogenous Dopamine as the Precursor</i>	<i>200</i>
<i>(II) Synthesis of Selectively Functionalized Nanoporous Hybrid Carbon based on Self-Templating Method and Using designed MOFs as the Precursor</i>	<i>201</i>
8.2. Future Perspective.....	202
<i>(I) MOFs Functionalized with Nanoparticles via In Situ Encapsulation</i>	<i>203</i>
<i>(II) MOFs-Decorated Carbon Nanofiber Network as Flexible Freestanding Electrode Materials.....</i>	<i>203</i>
<i>(III) Extending the Morphology of MOF from Polyhedron into One or Two Dimensions</i>	<i>204</i>
References	207

List of Publications	208
Acknowledgements	213

Chapter 1

Designed Fabrication of Nanoporous Carbon Materials towards Electrochemical Applications

1.1. Introduction

Considering global warming and other environmental issues caused by the traditional fossil-based energy generation technologies as well as the increasing demand for portable electronic devices in modern society, the new-type energy devices, such as fuel cells,[1] lithium-ion batteries,[2] lithium-air batteries,[3] and electrochemical capacitors[4] have been the focus of research. Their low operation temperature, small dimension, and high efficiency make them as the ideal power supplies for portable electronic devices, automobiles, and distributed stationary power sources.[5,6]

Porous carbons have been considered as promising electrode materials for these energy devices due to its excellent virtues such as low cost, designable carbon framework and surface, high chemical and mechanical stability, high conductivity along with high specific surface area and abundant porosity.[7,8] Due to the well-developed synthetic methods, a number of nanoporous carbon materials with high surface areas and tunable and accessible pores have recently been utilized in the field of energy conversion and storage devices.[9,10] These nanoporous carbon materials with controllable morphologies are synthesized by using a wide variety of hard templates such as ordered mesoporous silica (e.g., MCM-41[11] and SBA-15[12]) and aluminosilicate, colloidal silica particles, colloidal crystals, and so on.[13-16] Pore size of the resultant nanoporous carbon materials has been tuned from micropore to macropore regions. Alternative to the nanocasting method, nanoporous carbon or carbon composites with high surface area, tuned pore size, designed porosity, multiple length scale, and different compositions have been obtained by the self-assembly of amphiphilic organic molecules as soft template with carbon precursors.[17,18] Mesoporous carbon fibers with hierarchical porous structures can also be obtained by integration of the hard and soft-templating methods.[19] Various kinds of nanoporous carbon materials with random pores have been prepared via self-templating method by directly carbonization of carbon precursors, such as polymer, biomaterials, sucrose, and metal–organic frameworks.[20,21] Considering the application in electrochemical fields, lots of highly graphitic carbon materials have been explored by adopting high annealing temperature or adding some specific metals as the

catalysts. Furthermore, heteroatoms doping has been demonstrated as an effective way to modify the electron donor/accepter characteristics of carbons, endowing carbon materials with new functionalities and broadening their applications.

Nanoporous carbon materials with designed properties are critical for application. This review article aims to systematically summarize works concentrated on optimizing properties of nanoporous carbon materials for illustrating demanded electrochemical performance as electrodes. In this review, researches on the design of functional porous carbon materials are categorized into several chapters, as illustrated in **Figure 1.1**.

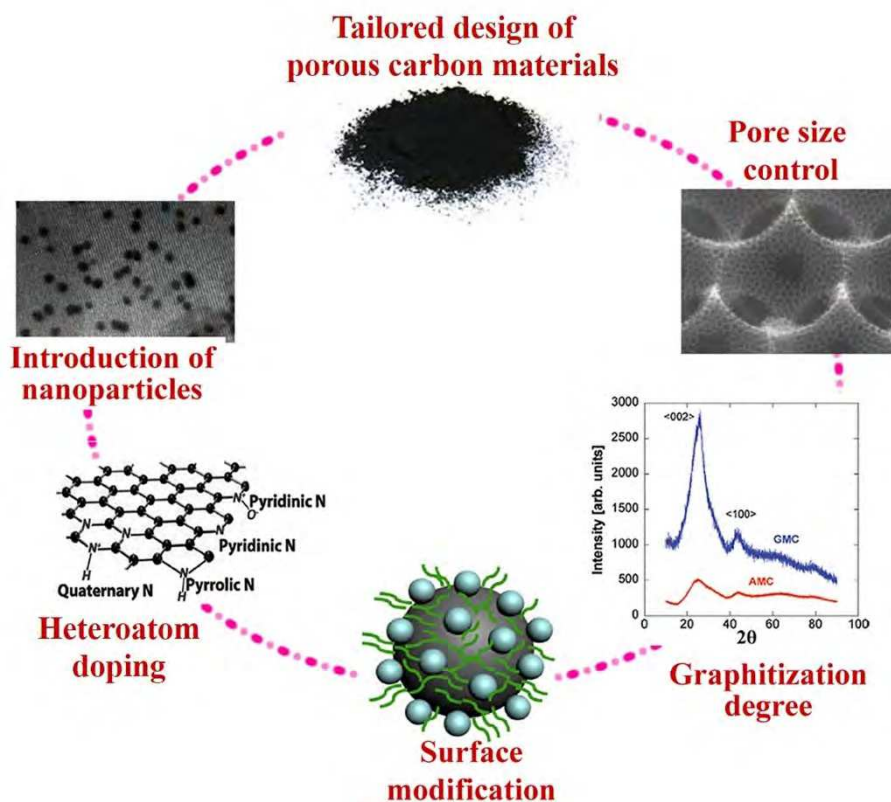


Figure 1.1 Tailored design of nanoporous carbon materials towards electrochemical applications. Reproduced with permission from ref. [123], Copyright 2013, Wiley-VCH. Reproduced with permission from ref. [63], Copyright 2009, ref. [89], Copyright 2010, ref. [111], Copyright 2012, ref. [166], Copyright 2013, American Chemical Society.

1.2. Control of Pore Size, Morphology, and Structure

1.2.1. Pore Size Control

Porous structure of carbon materials is a determining factor that is related to electrochemical performance.[22,23] Many parameters including connectivity, pore size distribution, and pore length influence ion transportation resistance and diffusion distance. Consequently, carbon materials with different pore sizes in the region from micropore to macropore have been synthesized by several methods such as direct carbonization of carbon precursor, nanocasting, and organic-organic self-assembly methods.[24-27] The electrolyte diffusion as well as catalytic performance can be tuned by tailoring pore size of carbon materials from micropore to macropore regions. Carbon materials with meso/macropores provide facile transfer and diffusion of reactants and products in the reactions over electrodes. Micropores in carbons can provide high specific surface area, confining ions, and accommodating charges, which are especially important for electrochemical double-layer capacitor. Preparation of hierarchical porous carbon materials with integrated properties would offer opportunity to commercial carbon electrodes for practical applications. In this section, I classify representative synthetic methods of nanoporous carbon based materials by pore size in **Table 1.1**, and focus on summarizing effects of the pore size on electrochemical performance.

Table 1.1 The representative methods of synthesis of nanoporous carbon powders.

Pore size	Method	Template	Carbon sources	Pore size, Morphology and Description	Ref	
Microporous	Direct carbonization	Self-template	MOFs	< 2 nm	25	
			Al-PCP	< 2 nm specific surface area (SSA) (5000 m ² g ⁻¹)	28	
			ZIF-8	~1.1 nm SSA > 1110 m ² g ⁻¹	29,30	
	Resorcinol/formaldehyde		Microporous carbon spheres, SSA of 504 m ² g ⁻¹	33		
	Extended Stöber method					
Nanocasting	FAU type zeolite	Poly(acrylonitrile) and poly(furfuryl alcohol)	< 2 nm SSA > 1300 m ² g ⁻¹	34,35, 36		
Mesoporous	Nanocasting	Ordered mesoporous silica	Sucrose	2.2-3.3 nm 2D hexagonally ordered mesoporous structures	37	
		Silica and add boric acid as pore expanding agent		3-10 nm	38	
		MWSBA-15		5-9 nm	39	
		SiO ₂ particles with diameter of 16.8-39 nm		12.4-34.5 nm	44	
	Organic-organic self-assembly	Soft-templating by using thermally decomposable surfactant and thermosetting polymer				
		Pluronic F127	Resorcinol/formaldehyde and triethyl orthoacetate	~6 nm SSA of ~1300 m ² g ⁻¹	45	
			Resol (phenol/formaldehyde)	6.8 nm, SSA of 652 m ² g ⁻¹	46	
		Pluronic P123	Resol (phenol/formaldehyde)	3.8 nm, SSA of 550 m ² g ⁻¹	47	
	Pluronic F127	Formaldehyde and resorcinol	~3 nm mesoporous CNSs	48		

			Phenolic resol	~3 nm, SSA of ~900 m ² g ⁻¹ OMC nanospheres	78
		Block copolymers with long hydrophobic chains	Resol	> 10 nm	54,55
		Polystyrene- <i>block</i> -poly(4-vinylpyridine) (PS- <i>b</i> -P4VP)	Resorcinol-formaldehyde	36 nm	56
		PEO- <i>b</i> -PS diblock copolymers with various PS chain lengths	Phenolic resol	12-33 nm	57
		Diblock copolymer PEO ₁₂₅ - <i>b</i> -PS ₂₃₀ homopolystyrene (h-PS ₄₉) as a pore expander	Resol	23-37 nm	58
Hierarchically nanoporous structure	Direct carbonization	Self-template	Carbide	Hierarchical pore architectures	24
			MOFs	Micro- and mesopores SSA of 990-1820 m ² g ⁻¹	64
	Hard-templating	Silica or zirconia with bimodal mesoporous-macroporous structure	Furfuryl alcohol	Interconnected macroporous and mesoporous	26,27, 59,60
		Submicrometer-size solid core/mesoporous shell silica spheres	Phenol and paraformaldehyde	Spherical carbon capsules	74
		Ordered hierarchical nanostructured silica	Furfuryl alcohol	Ordered hierarchical nanostructured carbons	63
		Colloidal silica	Monodisperse polystyrene latex	OMC with mesoporous walls	67

		MgO	Thermoplastic (e.g., poly(vinyl alcohol), hydroxyl propyl cellulose, poly(ethylene terephthalate))	Aperiodic hierarchical porous structures	65
		Ni(OH) ₂ /NiO	phenolic resin	3D aperiodic hierarchical porous structures	66
	Dual-templating approach by combining hard- and soft-templating method	Monodispersed silica colloidal crystals and amphiphilic triblock copolymer PEO-PPO-PEO	Soluble phenolic formaldehyde	Macropore sizes 230–430 nm, mesopore sizes ~11 nm	61
		Poly(methyl methacrylate) colloidal crystals and amphiphilic triblock copolymer surfactants		Ordered macropores (~342 nm) and mesopores (~3 nm)	62
Macroporous	Hard-templating method	Monodisperse silica nanoparticles with size of 150-800 nm	Phenol and formaldehyde	200 nm	68
		Monodisperse silica particles of a diameter in the range of 40–90 nm		62 nm	69
		12 nm colloidal silica spheres	Sucrose and cyanamide	Ordered macroporous carbon 150 nm	70
	Direct carbonization	Self-template	Poly(divinylbenzene)	Macropore SSA of 2360 m ² g ⁻¹	71
			Resorcinol-formaldehyde aerogels	70-80 nm	72

As shown in **Table 1.1**, microporous carbon can be synthesized by direct carbonization of porous solid precursors containing abundant micropores and large carbon content like porous coordination polymer (PCP)[28] and metal–organic frameworks (MOFs).[29,30] Since the first report by Xu et al.,[31,32] several groups have reported unique conversion pathways of MOFs to nanoporous carbons. Recently, a simple Stöber method was extended for preparation of monodispersed microporous carbon spheres.[33] By utilizing a nanocasting method, the pore size of nanoporous carbon has been adjusted in the range from micropore to macropore regions by choosing suitable hard template with various pore sizes. Kyotani et al. reported a kind of microporous carbon by using FAU type zeolite, which is a pioneering study of carbon materials prepared with hard template.[34-36] Mesoporous templates such as silica and aluminosilicate have been studied for preparation of mesoporous carbon materials with designed internal (ordered or disordered porous structure, large-sized mesopores, and hierarchical nanostructures) and external morphologies (powders, fibers, spheres, rods, and monoliths).[37-44] Alternative to the hard-templating method, mesoporous carbon materials can be synthesized according to the organic-organic self-assembly approach of thermosetting polymer and thermally decomposable surfactant, which is called as the “soft-templating” method, is convenient and efficient.[45-48] According to the development of the soft-templating approach, mesoporous polymer and carbon films have also been developed by several groups.[45,49-53] Mesoporous carbon materials with pore size larger than 10 nm were obtained using non-Pluronic surfactants showing strong hydrophobic/hydrophilic contrast.[54-58] Bimodal mesoporous-macroporous carbon and silica-carbon composite were thus designed by combination of the hard- and soft-templating methods; the silica-carbon composite can be converted to hierarchical porous carbon based materials.[59-63] Hierarchical porous carbon materials with disordered structure were obtained by direct carbonization of carbide and MOFs, or using metal oxides as sacrificial templates.[24,64-66] Macroporous carbon materials with pore size larger than 50 nm were also synthesized through replication of large solid templates and carbonization of polymeric precursor gels.[67-72] Although the soft-templating method appears appealing in comparison of the hard-templating method, it remains difficulty to have

fully reproducible syntheses in different batch scale, in terms of porosity parameters (pore size, structure, and surface area) and materials texture and morphology.

In recent years, many efforts have been made to consider influence of pore sizes of nanoporous carbon materials on electrochemical performance. Du et al. deposited platinum (Pt) nanoparticles on a series of carbon aerogel samples with different pore sizes and investigated their electrocatalytic activity for oxygen reduction reaction (ORR). Then the Pt nanoparticles deposited on carbon aerogel with the mean mesopore size of 18.5 nm exhibited the best electrochemical performance for ORR.[73] According to Joo's study, Pt nanoparticles over ordered mesoporous carbon (OMC) showed an improved electrocatalytic activity for oxygen reduction, compared to that over common microporous carbon materials such as carbon black, charcoal, and activated carbon fibers.[74] They mainly attributed the improved activity due to the expanded pore size. OMC materials (pore sizes between 2 nm and 50 nm) exhibit diffusion limitation for large reagent molecules and then larger pores opening are demanded after loading of catalyst particles. Therefore, design of nanoporous carbon with large and much accessible porous structure is highly desired.

Hierarchical nanostructured carbon materials obtained by replication of hierarchical nanostructured silica template were explored for the first time to support high loading of Pt nanoparticles (60 mass%) as cathode catalyst in proton exchange membrane fuel cell (PEMFC). The resulted catalyst with uniform dispersity, small particle size of Pt nanoparticles, and open network exhibited extremely improved catalytic activity in ORR by ca. 53-88%, compared to that of carbon black Vulcan XC-72 (VC)-supported Pt (60 mass%). The commercial carbon supports are dominantly composed of micropores which are easily blocked during loading Pt catalysts. Thus, the hierarchical porous carbon materials with high surface area, large pore volume, and well-interconnected bimodal porosity are more ideal candidates for porous catalyst support in fuel cells compared to commercial microporous carbon materials.[63,75] Two micrometer-sized carbon spheres named as PC-I and PC-II, which respectively consist of abundant mesopores and macropores, were synthesized from simple organic salt precursors by using an ultrasonic spray pyrolysis method. The SEM and TEM images are shown in **Figure**

1.2a-c. The porous carbon spheres were tested as pore-forming additives in Vulcan XC-72. According to the evaluation on unit cell performance, the anode catalyst mixture of PtRu/Vulcan and PtRu/PC-I showed the highest performance improvement (**Figure 1.2d**). For the reduction of O_2 over the cathode, the addition of PC-II in E-TEK commercial Pt/C catalyst significantly improved the performance of the reduction of O_2 over the cathode (**Figure 1.2e**).[76] These results demonstrate that inclusion of carbon materials with outsized pores is an effective way to facilitate smooth mass transport of air and methanol, emphasizing importance of porous structure for processing highly efficient self-breathing fuel cells.

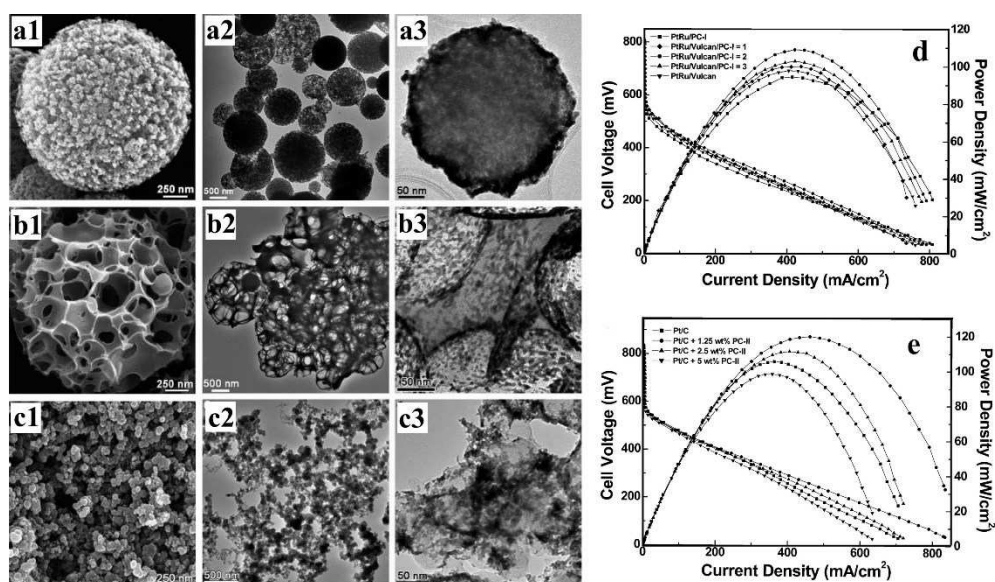


Figure 1.2 SEM micrographs of (a1) PC-I, (b1) PC-II, and (c1) Vulcan XC-72, TEM micrographs of carbons and PtRu catalysts supported on each carbon: (a2) PC-I, (a3) PtRu/PC-I, (b2) PC-II, (b3) PtRu/PC-II, (c2) Vulcan XC-72, and (c3) PtRu/Vulcan XC-72. (d) Voltage and power density responses of anode PtRu catalyst mixtures supported on PC-I and Vulcan XC-72, respectively and (e) cathode catalysts made from Pt/C (60 mass% Pt, E-TEK) mixed with various amounts of PC-II. Unit cell conditions: cell temperature, 70 °C; PtRu anode catalyst loading, 5 mg·cm⁻³; Pt cathode catalyst loading, 3 mg·cm⁻³; methanol flow rate, 2 cm³·min⁻¹; and airflow rate, 1000 cm³·min⁻¹. Reproduced with permission [76]. Copyright 2007, American Chemical Society.

1.2.2. Morphological and Structural Controls

In addition to pore size, other factors such as architecture, length and orientation of pores and external morphology have great potentials to design electrochemical activity of materials. For example, open and interconnected pores permit fluid to flow through whole materials. It is well known that morphology and porous structure of carbon materials affect electrochemical corrosion (often named as “oxidation resistance”). Mesoporous carbon materials have been synthesized with morphological controls to polyhedrons, rods, fibers, monoliths, and spheres.[77,78] By integration of porous anodic alumina membrane utilized as a hard template, together with the soft template of Pluronic F127 triblock copolymer, OMC nanofibers with highly ordered parallel channels and regularly circulated pores have been developed.[19] The transport of ions, reactants, and products is demonstrated to be much easier in three-dimensional (3-D) ordered macroporous carbon materials with highly interconnected pores, leading to small resistance, short diffusion pathway, and high electrochemical performance.[68,79,80] Two different mesoporous carbon materials with similar physicochemical property, but different mesoporous structures, namely, CMK-3 with ordered mesospaces and wormhole-like mesoporous carbon have been used for loading Pt nanoparticles.[81] Hexagonally arrayed carbon nanorods of CMK-3 provide Pt nanoparticles with a number of electrochemically active sites at the surfaces. Consequently, Pt/CMK-3 exhibited a good activity in both ethanol electrooxidation and ORR, with the mass activity increased by a factor of 6 and 3.6 times, respectively. It suggested that the desirable pore morphology of mesoporous carbon would be very prominent in the case of liquid reaction in terms of the role of easy mass transportation. As to channel length of nanoporous carbon, it has been demonstrated that carbon materials with short channel length have better electrochemical performance compared to those with longer channels,[82,83] since the decrease in the channel length will lower the resistance of mass transportation during electrochemical process.

1.2.3. Control of Graphitization Degree

It is well known that the conductivity of porous carbon materials is proportional to its graphitization degree that will affect internal Ohmic resistance, Ohmic polarization, concentration polarization, and electrochemical performance while using such porous carbon electrodes. Improvement of graphitization degree is helpful to alleviate corrosion of the carbon and thus improve the durability. Therefore, porous carbon with graphitic structure on the atomic scale is highly desirable. Recently, a multitude of mesoporous carbon materials with designed pore structure and graphitic and/or semigraphitic walls have been synthesized by employing several methods and using different carbon sources.[84-86] As summarized in **Table 1.2**, the synthetic methods are classified into four major groups: (1) inverse replication technique, based on impregnating fluid of easily graphitized carbon precursor into hard templates of mesoporous silica and alumina; (2) catalytic graphitization, as an effective way to obtain graphitic porous carbon under relatively low temperature without sacrificing porosity; (3) chemical vapor deposition (CVD) method, based on depositing gaseous carbon precursor into silica template; and (4) bridging method, by combining nanoporous carbon with other highly conductive carbon materials.

Table 1.2 The synthetic methods of nanoporous graphitic carbons.

Method		Template	Carbon sources	Carbonization temperature	Ref
Impregnation method		KIT-6	Mesophase pitch	900 °C	89
		MCM-48 and KIT-6	Furfuryl alcohol, sucrose, acenaphthene and mesophase pitch	900-2400 °C	90
		Self-template	Ion-exchange resin	800-1400 °C	91
Catalytic graphitization by adding metal species	Fe, Ni, Mn	Silica xerogel	Phenolic resin	900 °C.	98
	FeCl ₂	Self-template	Ionic liquid monomers or poly (ionic liquid) polymers	900 °C and 1000 °C	94
	Fe		Iron-based coordination polymer nanodisks	900 °C	99
	Ni		Ni ₃ C	450 °C	96
	Ni	SBA-15	Nickel phthalocyanine	900 °C	95
CVD		SBA-15	benzene	900 °C	100
			ferrocene	> 850 °C	101
Hybridization		SBA-15	OMC and CNT prepared from benzene vapor	900 °C	104
		F127	Phenolic resin-based mesoporous carbons and carbon blacks and carbon onions	850 °C	103
		P123 /F127	OMCs and reduced graphene oxide	850/900 °C	105 106

Graphitization degree of the resultant porous carbon is controlled by careful selection of carbon precursors that are easily graphitized at appropriate temperature. For example, when double gyroid mesoporous silica (KIT-6[87,88]) was used as a hard template, a carbon material obtained from the mesophase pitch was much more graphitic than that obtained from furfuryl alcohol, as demonstrated by XRD (**Figure 1.3a**).[89] In addition, high temperature annealing can largely improve the degree of graphitization at expense of sacrificing porosity of the resultant carbon materials. Ryoo and co-workers infiltrated different carbon precursors into ordered mesoporous silica followed by heating in the range from 900 °C to 2400 °C. The thermal treatment led to a gradual deterioration of the carbon structure, and meanwhile led to a significant improvement in the degree of graphitization.[90] In order to maintain the original porous structure, amorphous carbon should be graphitized at low temperature with the aid of catalysts by means of heterogeneous graphitization. Many transition metals such as Fe, Co, and Ni have been demonstrated to be effective catalysts for preparation of graphitic carbon with high crystallinity.[91-97] Fuertes and co-workers reported the preparation of graphitic porous carbon materials by using silica xerogel as a hard template, phenolic resin as a carbon precursor, and metallic salt (e.g., Fe, Ni, Mn) as a catalyst. After heating at relatively low temperature (e.g., 900 °C), these graphitized carbon materials exhibited high electrical conductivity up to two orders larger than the corresponding non-graphitized samples.[98] Recently, graphitic mesoporous carbon (GMC) nanodisks were directly fabricated through catalytic carbonization of coordination polymers containing Fe catalyst at 900 °C.[99] A CVD method is a simple route to afford GMC with desired nanostructure by using gaseous carbon precursor (e.g., benzene, ferrocene) and hard template.[100,101] Pyrolysis temperature below 850 °C leads to gradual improvement of the graphitization degree and that above 850 °C results in appearance of the considerable amount of entangled graphitic ribbons with partial collapse. Carbon nanotubes (CNTs) and graphenes exhibit higher conductivity than general porous carbon materials.[102] Therefore, hybridize nanoporous carbon with other highly graphitic carbons paves the way to obtain highly conductive porous carbon materials. After bridging nanoporous carbon with highly conductive carbon materials like carbon black, carbon onion, CNT, and

graphene, the formed interconnected network facilitates electron transport between the nanoporous carbon particles.[103-106]

As mentioned before, GMC and amorphous mesoporous carbon (AMC) were prepared by using KIT-6 silica as a template, mesophase pitch and furfuryl alcohol as carbon sources, respectively. TEM images of Pt supported on GMC and AMC after calcination at low temperature (≤ 500 °C) are shown in **Figure 1.3b and c**. **Figure 1.3d and e** illustrated that Pt catalyst supported on the graphitic carbon showed negligible loss in mass activity and active surface area after an accelerated durability test (1000 cycles, 0.5-1.2 V), whereas the commercial Pt on amorphous carbon lost $\sim 70\%$ in activity and area. The high stability could be attributed to oxidation resistance of the graphitized carbon and strong interaction between Pt nanoparticles and graphitic carbon framework, resulting from metal/support orbital overlap (π -backbonding) coupled with partial charge transfer.[89]

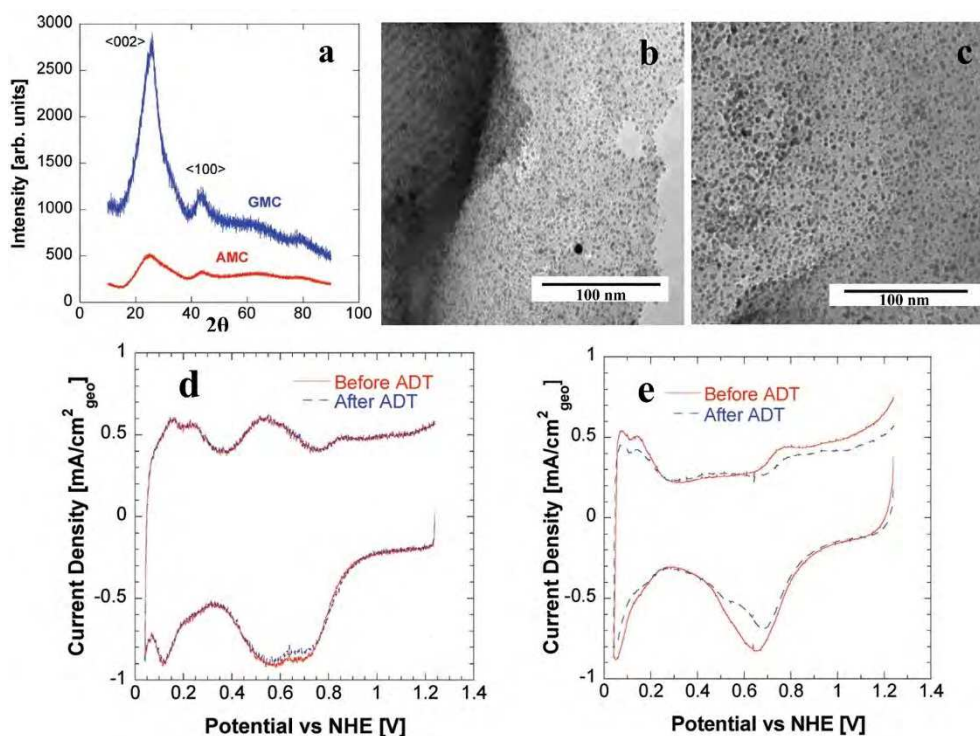


Figure 1.3 (a) XRD of GMC and AMC, TEM images of 20% Pt on (b) GMC and (c) AMC after calcination at low temperature ≤ 500 °C, CV curves of (d) Pt/GMC and (e) Pt/AMC before and after accelerated durability tests cycling at $20 \text{ mV} \cdot \text{s}^{-1}$. Reproduced with permission [89]. Copyright 2010, American Chemical Society.

As shown in the **Figure 1.4a and b**, Chen and co-workers fabricated a porous carbon-nanotube/carbon-nanofiber (CNT-CNF) composites by a novel in situ CVD method.[107] After being assembled as an anode in a lithium-ion battery, CNT-CNF composites displayed a high reversible capacity of 1150 mAh g⁻¹ at 0.1 A g⁻¹ even after 70 cycles, an excellent rate capability, and a long cycling life of over 3500 times while fading less than 20% at 8 A g⁻¹ (**Figure 1.4c**). The outstanding electrochemical performance can be attributed to the novel structure of CNT-CNF. The porous structure reduces the diffusion length of lithium ions. The growth of graphitic carbon nanotube greatly increases the electrical conductivity, provides more contact between electrode materials with electrolyte for transferring lithium ions, and promotes the rapid charge-transfer reaction.

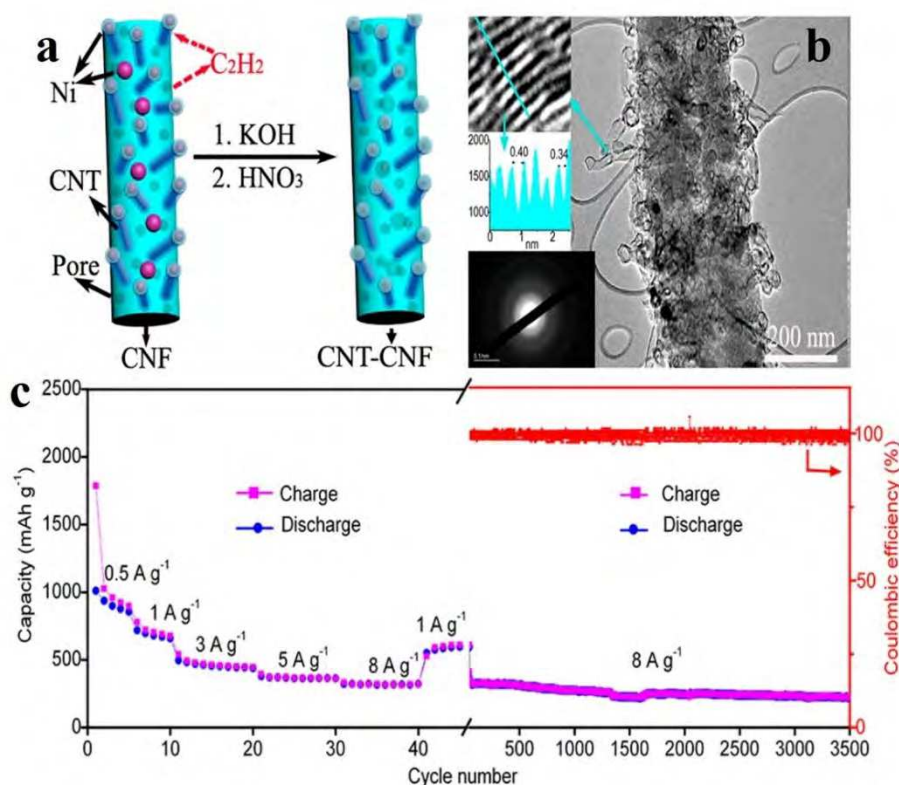


Figure 1.4 (a) Schematic of CNT-CNF hybrid material. (b) TEM image and SAED pattern of the CNT-CNF hybrid material, line profiles of the *d*-spacing of graphene sheets of the wall of CNT. (c) Capacities at various rates and cycling performances of the CNT-CNF hybrid electrodes tested between 3 and 0 V versus Li⁺/Li. Reproduced with permission [107]. Copyright 2013, American Chemical Society.

1.2.4. Surface Modification of Porous Carbon

The surface chemistry of porous carbon materials is important for employing them as electrode materials and improving their functions. For example, in order to deposit additional functional metal catalysts over porous carbon surfaces uniformly and efficiently, surface modification is generally adopted as an effective way to modify the interfacial properties and boost the interactions with guest molecules. Surface functional groups will act as anchoring sites for metal catalysts and aid adsorption of metallic species over the carbon surfaces by several mechanisms such as adsorption, coordination reaction, and ion-exchange. Kinetics of the electrochemical processes involving carbon are highly relied on surface characteristics of the carbon materials used. Then, surface modification can be applied to enhance electrochemical reactivity and durability of the carbon materials. Among a number of existing methods for surface modifications, oxidation, polymer decoration, and grafting with functional groups have frequently been utilized for synthesis of designed electrode materials.

Wettability of porous carbon materials is improved by introducing oxygen-containing functional groups such as carboxylic, anhydride, and carbonyl ones to the carbon surfaces through oxidation by gaseous (e.g., ozone) and liquid oxidant (e.g., concentrated mineral acids and aqueous solutions of hydrogen peroxide and potassium permanganate). Specific surface area and porosity also increase to some extent by generation of micropores. Metal catalysts on porous carbon materials after surface modification usually exhibit improved electrochemical performance in PEMFC and direct methanol fuel cell (DMFC) because of the high dispersion of the metal nanoparticles. For example, carboxyl groups are created on the surfaces of nanoporous carbon materials by oxidizing with concentrated nitric acid, being helpful for making the bonding between Pt colloids and the carbon surfaces strong, and thereby leading to enhancement of electrocatalytic activity in the methanol oxidation.[108,109] However, the oxidation conditions such as oxidant, temperature, and treatment duration need to be chosen carefully because excessive oxidation leads to structural collapse and dissolution of carbon. Oxidation also decreases the electrical conductivity of the porous carbon materials, which is unfavorable for application as electrodes.

Some porous carbon materials are modified by surface grafting with functional groups. Lee et al. synthesized pitch-based porous carbon materials with surface $-\text{SO}_3\text{H}$ groups.[110] The as-synthesized materials are carbonized from the mesophase pitch followed by sulfonation. Chen et al. decorated Pt/C with polyaniline (PANI) to obtain a core-shell catalyst.[111] The greatest enhancement in the catalytic property was observed at a thickness of 5 nm of the PANI shell. The Pt/C@PANI core-shell type catalyst also illustrated more outstanding stability than non-decorated Pt/C catalyst. The enhanced activity and stability of the novel PANI-decorated core-shell structure are induced by both the electron delocalization between Pt *d*-orbitals and PANI π -conjugated ligand and the electron transfer from Pt nanoparticles to the thin PANI layers that also protect the carbon support from direct exposure to the corrosive environment. Porous carbon is the fundamental electrode material for electrochemical capacitors. After decorating porous carbon materials with electrically conducting polymers, the energy density of carbon-based electrochemical capacitor will be greatly increased.[112,113] As shown in **Figure 1.5**, polyaniline (PANI) shells were decorated on the surface of hollow carbon spheres (HCS) via chemical oxidative polymerization.[114] The HCS-PANI composites exhibit a much higher gravimetric capacitance (525 F g^{-1}) and significantly enhanced energy density (17.2 Wh kg^{-1}) compared to the pure HCS (268 F g^{-1} and 9.1 Wh kg^{-1}), due to the pseudo-capacitance produced by PANI.

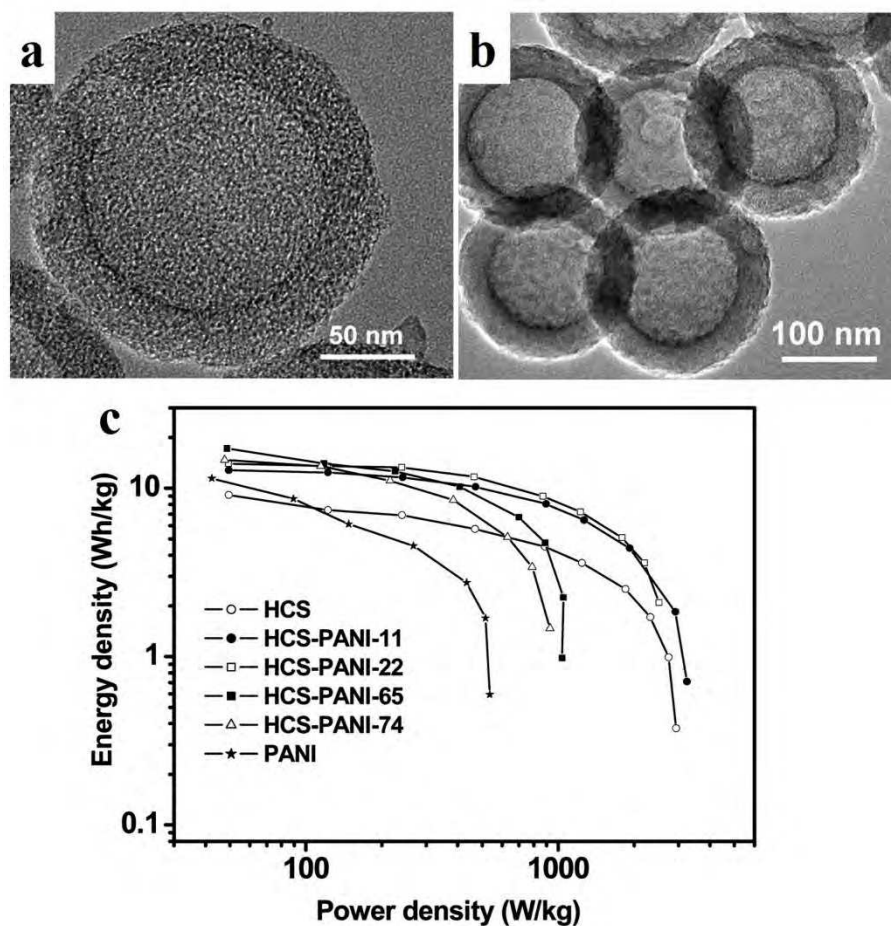


Figure 1.5 TEM images of (a) HCS and (b) HCS-PANI-65. (c) Ragone plots of symmetric supercapacitor measured in aqueous solution of $2.0 \text{ mol L}^{-1} \text{ H}_2\text{SO}_4$. Data obtained from the galvanostatic discharge process at current densities varying from 0.1 to 10 A g^{-1} . HCS-PANI- x samples, x represents the mass percentage of PANI in the composites. Reproduced with permission [114]. Copyright 2010, American Chemical Society.

1.2.5. Heteroatom-Doped Nanoporous Carbon

In order to endow nanoporous carbon-based materials with novel physical and electrochemical properties, heteroatoms such as boron (B), nitrogen (N), sulfur (S), fluorine (F), and phosphorus (P) have been doped as secondary phases into carbon frameworks. N-doped carbon-based materials have been developed in recent years such as N-doped porous carbon nanospheres (CNSs), mesoporous carbon materials, CNTs, and graphenes.[115-119] In this section, the synthetic methods to prepare heteroatom-doped porous carbon materials and their electrochemical performances as electrodes in energy conversion and storage devices are summarized and discussed.[120,121]

The synthesis of N-containing porous carbon materials can be categorized according to the following strategies. The first approach is direct carbonization of N-containing carbon precursors; resultant carbon materials usually possess disordered nanopores.[25,122] A kind of porous N-rich carbon was achieved by carbonization of furfuryl alcohol filled in N-rich porous organic framework (POF).[123] A scheme of the synthesis is illustrated in **Figure 1.6**, with the form of nitrogen in the carbon frameworks. Other N-containing polymers such as polypyrrole are also promising; N-doped porous CNSs have been synthesized via carbonization of polypyrrole nanospheres.[118] The second one is post-treatment of carbon materials in N-containing atmosphere and polymer (e.g., NH_3 , polyaniline) at high temperatures.[124] The third one is filling N-containing liquid and vapor phase carbon precursors into the pores of mesoporous silica and aluminosilicate templates via liquid impregnation or CVD, respectively. This approach not only ensures the uniform distributions of nitrogen species but also avoids pore breakdown. A variety of N-containing organic molecules like acetonitrile, pyrrole, aniline, cyanamide, dicyandiamide, gelatin biomolecule, ethylenediamine, transition metal macrocyclic compounds, and N-containing aromatic dyestuff have been adopted.[125-133] Polyacrylonitrile (PAN) is a common source to generate N-containing carbon materials.[134] Schüth and co-workers reported the synthesis of OMC containing nitrogen groups using SBA-15 type silica as a hard template and PAN as a carbon source.[135,136] The nitrogen content of N-doped carbon materials decreases along with the increase of temperatures for

carbonization. The above three methods to prepare N-doped nanoporous carbon are extended to doping of other non-metallic heteroatoms (e.g., B, P, F, S).[83,120,137-139] In addition, a direct co-assembly method has also been utilized for doping of B, N, F, and P atoms.[140,141] The previous works on heteroatom-doped nanoporous carbon are selectively summarized and listed in **Table 1.3**.

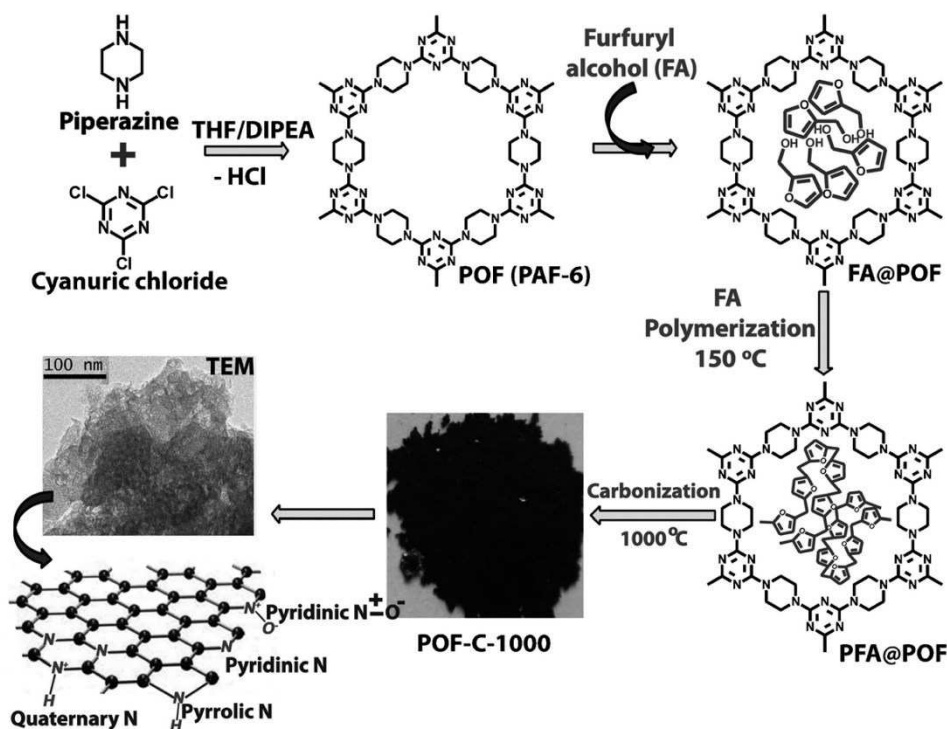


Figure 1.6 Synthesis of N-rich porous carbon by carbonization of furfuryl alcohol filled in N-rich POF at 1000 °C. Reproduced with permission [123]. Copyright 2013, Wiley-VCH.

Table 1.3 The preparation of heteroatom-doped nanoporous carbon materials.

Doped atoms	Method	Precursors	Structures	Ref
N	Directly carbonization of N-containing carbon precursors	ZIF or polypyrrole	Disordered nanoporous	117,122
	Post-treatment of carbon in N-containing atmosphere or polymer	Nanoporous carbon treated with NH ₃ or polyaniline	Disordered or ordered nanoporous carbon	124
	Filling N-containing carbon precursors into porous templates	Acetonitrile, pyrrole, aniline, cyanamide, gelatin, transition metal macrocyclic compounds, ethylenediamine, and N-containing aromatic dyestuff	Disordered or ordered nanoporous carbon	125-129, 131,133
F	Organic-organic self-assembly	Phenol, formaldehyde, monomer of <i>p</i> -fluorophenol, and Pluronic F127	Ordered mesoporous	120
B	Organic-organic self-assembly	Resol, boric acid, and F127	Ordered mesoporous	138
	Nanocasting	Sucrose, boric acid, and SBA-15	Ordered mesoporous	137
P	Nanocasting	SBA-15, triphenylphosphine, and phenol	Ordered mesoporous	83
Binary doping of S and N	Nanocasting	SBA-15, sucrose, and thiourea	3D hierarchical pore structures	139
Ternary doping of N, B, P	Pyrolysis	Dicyandiamide, boric acid, phosphoric acid, and metal chlorides	Mesoporous	121

Latest advances discover that N-doped carbon materials are capable of providing high electron mobility, creating beneficial interaction of catalyst support, and improving activity and stability of catalysts.[142-144] It has been proven that N-doped carbon materials lead to homogeneous and efficient deposition of Pt nanoparticles.[145,146] Although Pt-based catalysts are the best for the ORR catalysis, they suffer from slow reduction kinetics, time-dependent drift, and high cost that are drawbacks for large-scale commercialization of low-temperature fuel cells. Hence, great efforts have been devoted to exploring substitution of Pt catalysts into Pt-alloys, non-precious metals, and metal-free species. For most of the non-precious metal catalysts (Mn, Fe, Co, etc.), nitrogen species, especially pyridinic type nitrogen, plays an important role in improving the catalytic activity for ORR.[147,148] The pristine MnO hardly showed electrocatalytic activity and mesoporous N-doped carbon itself exhibited a dominant two-electron process for ORR. However, the as-prepared MnO-containing mesoporous N-doped carbon nanocomposite catalyst exhibited high electrocatalytic activity for ORR and dominant four-electron oxygen reduction pathway in $0.1 \text{ mol}\cdot\text{L}^{-1}$ KOH aqueous solution, due to the synergetic effect between MnO and mesoporous N-doped carbon.[149] More importantly, researchers found out that N-containing carbon materials act as metal-free electrodes showing good electrocatalytic activity in ORR.[117,150] They attributed the catalytic performance to the electron accepting ability of the nitrogen atoms, which creates a net positive charge on adjacent carbon atoms and readily attracts electrons from the anode for facilitating ORR.[151] A novel N-doped ordered mesoporous graphitic arrays based on a metal-free nanocasting technology exhibited superior electrocatalytic activity, excellent long-term stability, and resistance to crossover effects for ORR compared to a commercial catalyst Pt-C.[133] The schematic illustration of the preparation and the catalytic activity for ORR is shown in **Figure 1.7**. The results reveal that pyridinic and pyrrolic derivative nitrogen atoms in the carbon networks and highly graphitized carbon structure are mainly responsible for the enhanced activity of the metal-free N-C species.[152-154] Not only N-doped but also P- and B-doped nanoporous carbon materials are further exploited as potentially efficient and

inexpensive metal-free ORR catalysts with long-term stability and excellent tolerance to crossover effects of methanol in alkaline medium.[155,156]

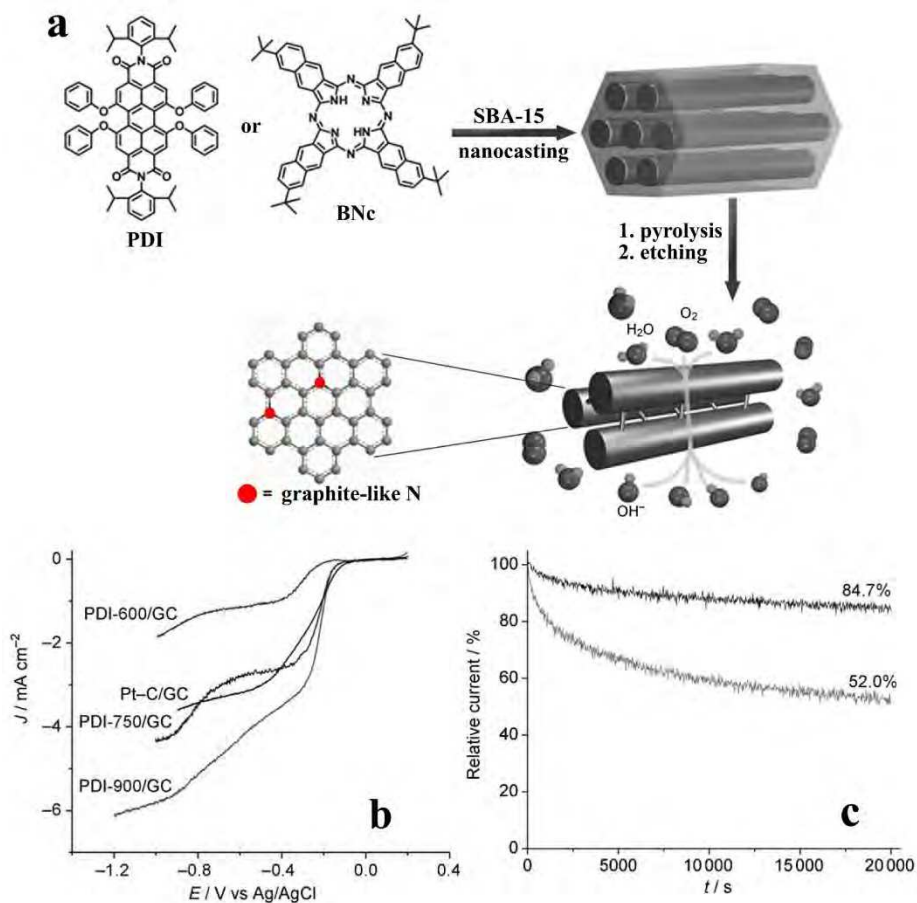


Figure 1.7 (a) Illustration during the preparation of N-doped graphitic nanorod arrays with ordered mesostructure, (b) rotating-disk voltammograms of the mesoporous graphitic arrays calcined at 600 °C, 750 °C, and 900 °C and Pt-C supported on GC electrodes in an O_2 -saturated $0.1 \text{ mol}\cdot\text{L}^{-1}$ solution of KOH at a scan rate of $10 \text{ mV}\cdot\text{s}^{-1}$ at a rotation rate of 1600 rpm, (c) current-time chronoamperometric response of the mesoporous graphitic arrays calcined at 900 °C and Pt-C-modified GC electrodes at -0.26 V in O_2 -saturated $0.1 \text{ mol}\cdot\text{L}^{-1}$ KOH at a rotation rate of 1600 rpm. Reproduced with permission [133]. Copyright 2010, Wiley-VCH.

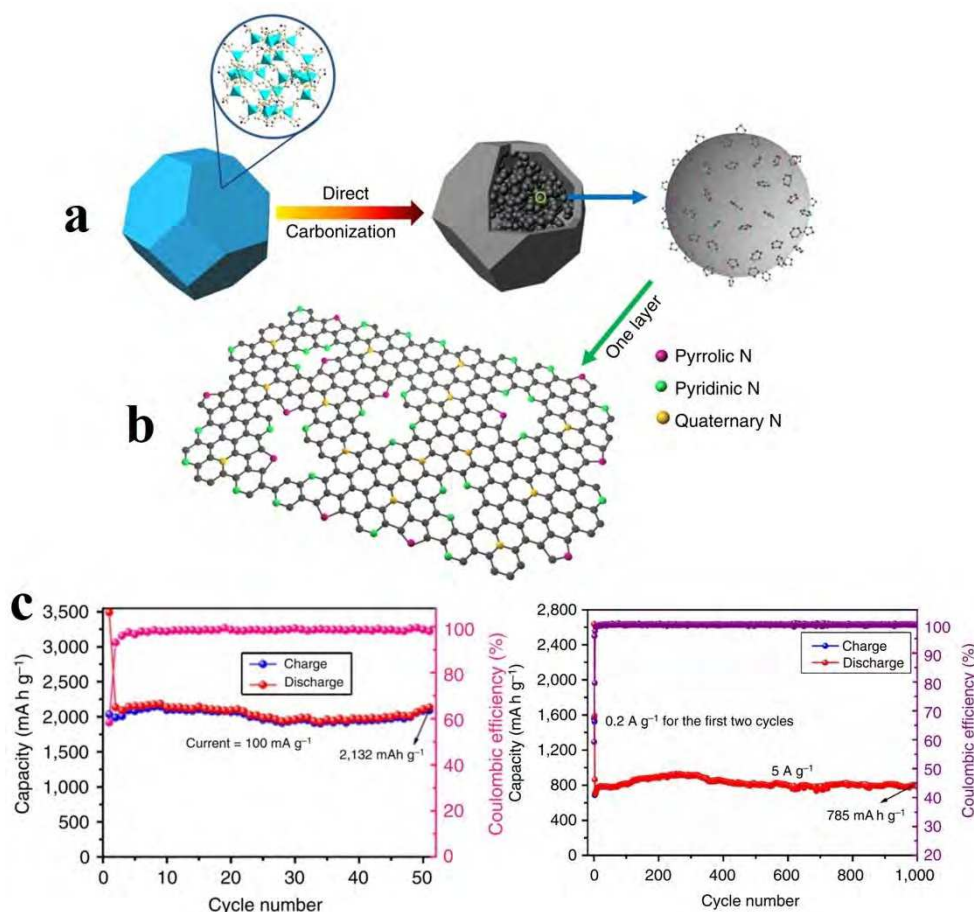


Figure 1.8 (a) Schematic illustration of the synthetic procedure for N-doped graphene analogous particles. (b) The schematic of three types of bonding configurations of N atoms within the hexagonal lattice and edges of a graphene layer. (c) Cycling performance at a current density of 100 mA g^{-1} (left) and 5 A g^{-1} (right). Reproduced with permission [158]. Copyright 2014, Nature Publishing Group.

In addition, N-doped carbons are promising electrode materials for lithium-ion batteries. The strong interactions between N-doped carbon and lithium ions are favourable for lithium insertion, leading to an increased lithium storage capacity.[157] Very recently, Chen et al prepared N-doped graphene particle analogues composed of a high nitrogen content of 17.7 wt% by calcination a nitrogen-containing MOFs,[158] shown in the **Figure 1.8a**. The product showed an outstanding lithium storage performance as an anode for lithium-ion batteries, displaying a remarkable and stable capacity of $2,132 \text{ mAh g}^{-1}$ after 50 cycles at a current density of 100 mA g^{-1} , and 785 mAh g^{-1} after 1,000 cycles at 5 A g^{-1} (**Figure 1.8c**). The exceptional

electrochemical performance can be ascribed to the high nitrogen doping within the hexagonal lattice and edges of graphene analogous particles (**Figure 1.8b**). Although high specific surface area is the predominant factor for a carbon-based electrochemical capacitor, lately, heteroatoms doping (e.g., B, N, P) has been proved to be an effective method to increase the electrochemical capacitance of a carbon-based electrode by modifying the wettability and providing extra reversible pseudocapacitance.[159,161] For example, Kowalewski and co-workers fabricated a novel nanoporous nitrogen-enriched carbon materials through carbonization of a self-assembled block copolymer consist of polyacrylonitrile and poly(n-butyl acrylate).[162] Supercapacitors fabricated from the nitrogen-enriched carbons with hierarchical pore structures showed extraordinarily high capacitance per unit surface area ($> 30 \mu\text{F cm}^{-2}$) because of the pseudocapacitance obtained from the high nitrogen content (16.5 wt%).

1.2.6. Encapsulation of Nanoparticles in Porous Carbon

Incorporation of the secondary metallic phases will provide carbon with new functions and additional electrochemical activity, thus broaden the application fields of porous carbon systems. This section contains several methods of direct incorporation of metallic nanoparticles in carbon frameworks with the prospects as electrode materials for electrochemical applications.

In order to disperse metal species uniformly over carbon frameworks with retention of the porous structure, the metal species are generally introduced into carbon precursor during the synthesis. Porous carbon-based composites with metals (e.g., Fe, Ni, Co, Nb) have been prepared by nanocasting method. The detailed process is as follows: (1) metal precursors are infiltrated into the channels of hard templates together with carbon precursors, (2) metal salts or metal oxides are spontaneously reduced to metal nanoparticles by carbon-thermic reduction and embedded in the carbon frameworks during carbonization in an inert atmosphere, and (3) the template is removed by chemical etching without solution of the metal particles. Fulvio et al. reported the preparation of mesoporous carbon materials with ultra-thin pore walls and highly dispersed Ni nanoparticles by using nickel nitrate hexahydrate as a metal source, 2,3-dihydroxynaphthalene as a carbon precursor and two SBA-15 type silica-based materials as

hard templates.[163] The metallic Ni nanoparticles with uniform size of ca. 3 nm were homogeneously dispersed on the tubular carbon walls. Su et al. incorporated Ni and Co nanoparticles into the mesopore walls by sucrose-impregnation and benzene CVD routes, respectively.[164] It was found that the introduction of metal nanoparticles via both synthesis routes hardly had influence on pore structure.

Another approach to introduce nanoparticles is a direct multi-component co-assembly between carbon precursor, block copolymer, and metal salts.[165,166] OMCs with uniform Fe/Co-containing nanoparticles were synthesized from chelate-assisted multi-component co-assembly by using acetylacetonate as a chelating agent, phenolic resin as a carbon source, ferric nitrates/cobalt nitrates as metal sources, and triblock copolymer Pluronic F127 as a template.[167] After carbonization, the nanocomposites have 2-D hexagonally arranged structures with uniform mesopores (~ 4.0 nm) and high specific surface area (~ 500 m²·g⁻¹). Ferric and cobalt oxide nanoparticles with uniform size tunable from 8 nm to 22 nm by simply adjusting the amount of acetylacetonate, highly dispersed throughout the carbon matrix. Cobalt/vanadium oxide-containing mesoporous carbon composite thin films were synthesized by tri-constituent self-assembly of Pluronic F127, phenol-formaldehyde oligomer, and cobalt (and vanadyl) acetylacetonate (acac).[168] During pyrolysis at 800 °C, the *d*-spacing usually decreases significantly due to the uniaxial contraction. The Co/V content mechanically strengthens the framework and leads to a decrease in the contraction from about 68% to 50%. In addition, the electrical conductivity of the mesoporous carbon film increases from 22 S/cm to 40 S/cm by adding 10 mass% of either Co(acac)₂ and VO(acac)₂ in the precursor solutions.

The third approach is called self-templating method by directly carbonization of metal-containing carbon precursors. During the past five years, metal-organic frameworks (MOFs) (or porous coordination polymers, PCPs) have become a rapidly rising star as a convenient self-templated precursor for preparing metal-containing carbon-based materials. Liu and co-workers reported a simple strategy of preparing a non-platinum group metal electrocatalyst for oxygen reduction reaction through thermal activation of cobalt imidazolate framework.[169] The cobalt imidazolate framework has clearly-defined porous three-dimensional structures and

the initial entities of CoN_4 moieties throughout the regular cell structure. After thermal activation, the imidazolate is converted to carbon frameworks, a fraction of nitrogen is retained in the form of pyridinic or pyrrolic moieties and coordinates with cobalt to form catalytic sites of CoN_4 . A wide range of MOF-derived carbon composites, such as core-shell-structured porous $\text{Fe}/\text{Fe}_3\text{C}@C$ nanoboxes supported on graphene[170] and Co_3O_4 -carbon porous nanowire arrays,[171] have been synthesized in the very recent years.

Metal-containing porous carbon composites have been demonstrated to be effective electrode materials in fuel cell and battery systems. Recently, researchers reported that some non-precious metals (e.g., Fe and Co) connected with N-doped carbons have outstanding catalytic activities for ORR in PEMFC even in acidic electrolyte.[172,173] Kramm et al synthesized an iron-based catalyst reached the highest density of FeN_4 sites ever reported, and revealed that catalysts with desired homogeneous composition of MeN_4 (Me = metal) sites in the carbon would possess a significant enhancement in ORR activity.[174] Transition metal oxides have high theoretical capacities as anode materials for lithium-ion batteries. However, they have low electrical conductivities and suffer a large volume expansion/contraction during the Li^+ insertion/extraction process, resulting in electrode pulverization and poor cycling. Fabrication of metal oxide/carbon composites have been explored as an effective approach to alleviate the shortcoming of metal oxide. As shown in the **Figure 1.9**, Gu and co-workers prepared mesoporous peapod-like $\text{Co}_3\text{O}_4@\text{CNT}$ arrays through nanocasting process.[175] The Co_3O_4 nanoparticles confined exclusively in the intratubular pores of the carbon nanotubes have controllable particle sizes between 3-7 nm and adjustable loading amount from 45 to 70 wt%. The carbon nanotubes work as conductive networks and provide open pores for electrolyte diffusion to the Co_3O_4 nanoparticles. As a result, the $\text{Co}_3\text{O}_4@\text{CNT}$ electrode showed a high specific capacity, an excellent rate capacity, and good cycling performance in lithium-ion batteries.

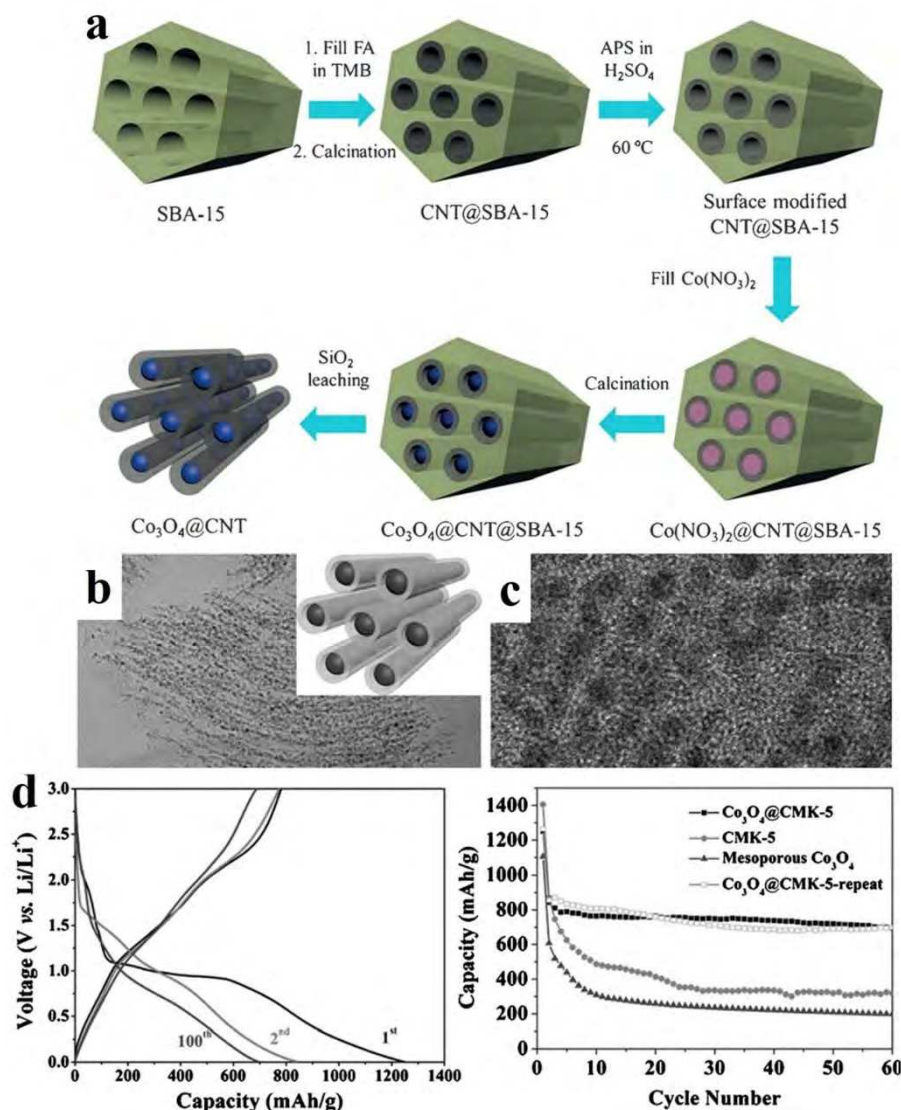


Figure 1.9 (a) Schematic illustration of the formation process of the mesoporous peapod-like $\text{Co}_3\text{O}_4@\text{CNT}$. (b,c) TEM images of thin microtome sections of $\text{Co}_3\text{O}_4@\text{CNT}$. The insets is the corresponding schematic image. (d) Charge/discharge curves of the $\text{Co}_3\text{O}_4@\text{CNT}$ electrode (left), cycling performance of the $\text{Co}_3\text{O}_4@\text{CNT}$, ordered mesoporous carbon (CMK-5), and mesoporous Co_3O_4 electrodes (right). Current density is 0.1 Ag^{-1} . Reproduced with permission [175]. Copyright 2015, Wiley-VCH.

1.3. Conclusion and Objective

The recent progress to functionalize various nanoporous carbon materials was reviewed in this article. At the first part, the tremendous progresses in the controls of pore size, porous structure and morphology were summarized because properties of nanomaterials highly depend on structure and morphology. Compared to traditional carbon materials, porous carbon materials with high specific surface area, accessible pore (pore size from 2 to 50 nm, 3-D interconnected pore), and highly graphitic structure are desirable for loading catalysts and accelerating mass and electron transportation. A multitude of nanoporous carbon materials with designed porous structure, graphitic and/or semi-graphitic walls are useful for applications in electrochemical devices. Surface functionalization of porous carbon is essential towards the application as electrode materials. The surface functional groups will act as anchoring sites for the metal catalysts and aid the adsorption of metallic species on the carbon surfaces.

In terms of the introduction of the secondary phases into carbon frameworks, selecting N-doped nanoporous carbon as a typical example, metal-free catalysts for fuel cell applications have been reviewed as the most outstanding electrochemical application. Recent advances in carbon materials discover that heteroatom-doped carbon materials are capable of providing high electron mobility, creating beneficial interaction between catalyst and carbon support, and then improving the activity and stability of the catalysts. Heteroatom-containing nanoporous carbon materials can act as metal-free electrodes with good electrocatalytic activity for ORR which paves the new way to substitute Pt in the cathode electrode. Metal incorporation is an excellent method to endow porous carbon materials with novel electrochemical activities and expand their application in fuel cells and rechargeable batteries.

Through the overview on the modified nanoporous carbon materials, the correlation among pore size, morphology and structure, surface property of porous carbon materials need to be identified for the designed applications. In my thesis, I focus on exploring new synthetic procedures for fabricating functionalized porous carbon materials with engineered nanoarchitecture towards application in energy storage and conversion devices, especially paying attention to the pore size distribution, N-doping, and degree of graphitization.

Templating method is popular to precisely control the pore size of nanomaterials. Thus, I conduct soft-templating (diblock copolymer micelles), hard-templating (silica nanospheres), and dual-templating methods, to synthesize carbon materials with designed porous structure and morphology. For in situ preparing N-doped carbon materials, nontoxic nitrogenous dopamine is selected as both the carbon and nitrogen sources because of its excellent properties, including (1) the self-polymerization under mild alkaline conditions at room temperature and pressure, (2) conformal deposition nature on solid surfaces, and (3) a high yield after carbonization (close to 50 wt% at 1000 °C) and well-preservation of nitrogen in the final carbons. As shown in the **Figure 1.10**, N-doped mesoporous carbon spheres (NMCS) with extra-large pores are prepared through assembly of diblock copolymer micelles, three-dimensional N-doped hierarchical porous carbons (NHPC-3D) are fabricated by using silica nanospheres as the hard template. N-doped hollow carbon spheres with large mesoporous shells (NHCS-LM) are engineered from diblock copolymer micelles and silica spheres. Without adding metal as the catalyst, the degree of graphitization in the carbon product is increased slightly by using a higher calcination temperature.

Functionalized nanoporous carbon materials can be fabricated by using designed metal–organic framework (MOF) as the self-templated precursor. As shown in the **Figure 1.11**, core–shell MOF and bimetallic MOF are designed elaborately and have been prepared successfully, for integrating the individual advantages of two kinds of single MOFs ($\text{Zn}(\text{MeIm})_2$ and $\text{Co}(\text{MeIm})_2$). The ratio of Co/Zn in MOF precursor is able to determine the properties of the derived carbon materials, including the ratio of micropore/mesopores, content of nitrogen, and degree of graphitization. As a result, selectively functionalized nanoporous hybrid carbon and self-adjusted nanoporous carbon with adjustable properties have been obtained.

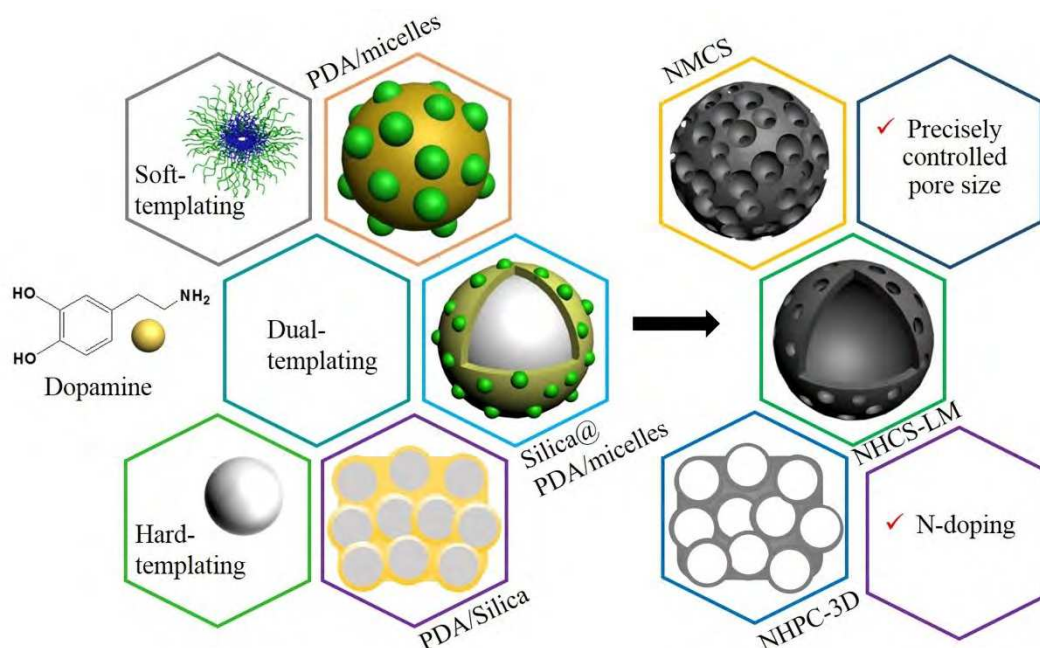


Figure 1.10. Synthesis of N-doped porous carbon materials by using templating methods.

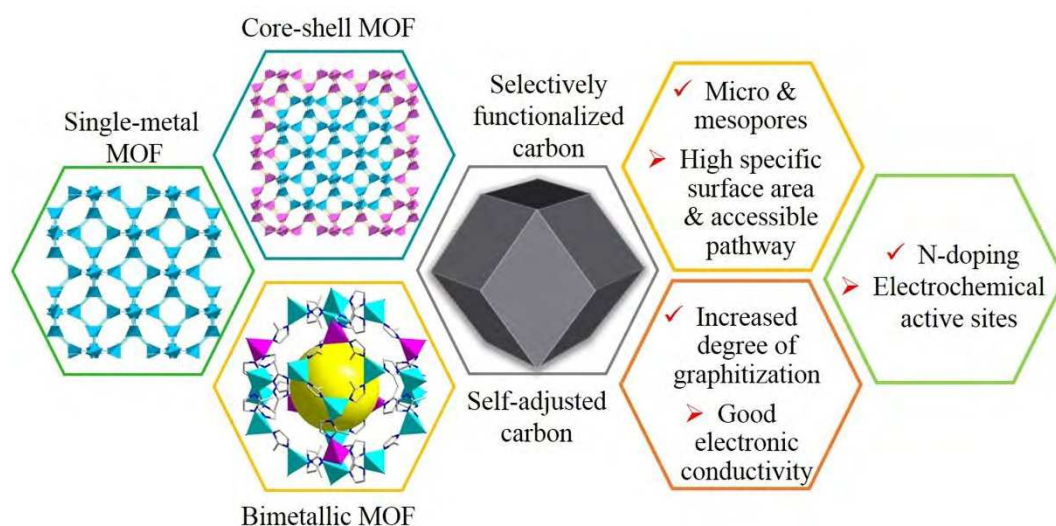


Figure 1.11. Synthesis of functionalized nanoporous carbon materials by using designed novel MOFs as the self-templated precursors.

The target of my thesis is to prepare functional porous carbon materials towards electrochemical applications. The pore size distribution, N-doping, and degree of graphitization can be controlled by the following approaches: (1) templating method will produce carbon materials with precisely controlled pore size, whereas self-templating approach will produce random pore size but adjustable ratio of micropores/mesopores; (2) nitrogenous organic compounds (e.g., dopamine and methylimidazole) are effective precursors for preparing N-doped carbon materials; (3) incorporated metal catalyst (cobalt) is able to greatly

increase the degree of graphitization of carbon materials at relatively low calcination temperatures (<1000 °C). Considering the comprehensive properties of each prepared porous carbon, the carbon products can be used as the electrode materials in oxygen reduction reaction, electric double-layer capacitor, or rechargeable batteries.

References

- [1] S. J. C. Cleghorn, X. Ren, T. E. Springer, M. S. Wilson, C. Zawodzinski, T. A. Zawodzinski, S. Gottesfeld, *Int. J. Hydrogen Energy*, 1997, **22**, 1137.
- [2] J.-M. Tarascon, M. Armand, *Nature*, 2001, **414**, 359.
- [3] K. M. Abraham, Z. Jiang, *J. Electrochem. Soc.*, 1996, **143**, 1.
- [4] P. Simon, Y. Gogotsi, *Nat. Mater.*, 2008, **7**, 845.
- [5] R. F. Service, *Science*, 2002, **296**, 1222.
- [6] A. S. Aricò, P. Bruce, B. Scrosati, J.-M. Tarascon, W. V. Schalkwijk, *Nat. Mater.*, 2005, **4**, 366.
- [7] H. Chang, S. H. Joo, C. Pak, *J. Mater. Chem.*, 2007, **17**, 3078.
- [8] J. Wang, H. L. Xin, D. Wang, *Part. Part. Syst. Charact.*, 2014, **31**, 515.
- [9] C. D. Liang, Z. J. Li, S. Dai, *Angew. Chem. Int. Ed.*, 2008, **47**, 3696.
- [10] A.-H. Lu, S. Dai, *J. Mater. Chem. A*, 2013, **1**, 9326.
- [11] J. S. Beck, J. C. Vartuli, W. J. Roth, M. E. Leonowicz, C. T. Kresge, K. D. Schmitt, C. T. W. Chu, D. H. Olson, E. W. Sheppard, S. B. McCullen, J. B. Higgins, J. L. Schlenker, *J. Am. Chem. Soc.*, 1992, **114**, 10834.
- [12] D. Zhao, J. Feng, Q. Huo, N. Melosh, G. H. Fredrickson, B. F. Chmelka, G. D. Stucky, *Science*, 1998, **279**, 548.
- [13] R. Ryoo, S. H. Joo, S. Jun, *J. Phys. Chem. B*, 1999, **103**, 7743.
- [14] H. Yang, D. Zhao, *J. Mater. Chem.*, 2005, **15**, 1217.
- [15] Z. Li, M. Jaroniec, *J. Am. Chem. Soc.*, 2001, **123**, 9208.
- [16] A. A. Zakhidov, R. H. Baughman, Z. Iqbal, C. Cui, I. Khayrullin, O. Dantas, J. Marti, V. G. Ralchenko, *Science*, 1998, **282**, 897.

- [17] Z. X. Wu, W. D. Wu, W. J. Liu, C. Selomulya, X. D. Chen, D. Y. Zhao, *Angew. Chem. Int. Ed.*, 2013, **52**, 13764.
- [18] Y. Wan, Y. F. Shi, D. Y. Zhao, *Chem. Commun.*, 2007, **9**, 897.
- [19] G. W. Zhao, J. P. He, C. X. Zhang, J. H. Zhou, X. Chen, T. Wang, *J. Phys. Chem. C*, 2008, **112**, 1028.
- [20] W. Qian, F. Sun, Y. Xu, L. Qiu, C. Liu, S. Wang, F. Yan, *Energy Environ. Sci.*, 2014, **7**, 379.
- [21] S. Ma, G. A. Goenaga, A. V. Call, D.-J. Liu, *Chem. Eur. J.*, 2011, **17**, 2063.
- [22] J. Jin, S. Tanaka, Y. Egashira, N. Nishiyama, *Carbon*, 2010, **48**, 1985.
- [23] A. D. Moore, S. M. Holmesa, E. P. L. Roberts, *RSC Adv.*, 2012, **2**, 1669.
- [24] M. Oschatz, L. Borchardt, M. Thommes, K. A. Cychosz, I. Senkowska, N. Klein, R. Frind, M. Leistner, V. Presser, Y. Gogotsi, S. Kaskel, *Angew. Chem. Int. Ed.*, 2012, **51**, 7577.
- [25] W. Chaikittisilp, K. Ariga, Y. Yamauchi, *J. Mater. Chem. A*, 2013, **1**, 14.
- [26] A. Taguchi, J. H. Smått, M. Lindén, *Adv. Mater.*, 2003, **15**, 1209.
- [27] B. L. Su, A. Vantomme, L. Surahy, R. Pirard, J. P. Pirard, *Chem. Mater.*, 2007, **19**, 3325.
- [28] M. Hu, J. Reboul, S. Furukawa, N. L. Torad, Q. Ji, P. Srinivasu, K. Ariga, S. Kitagawa, Y. Yamauchi, *J. Am. Chem. Soc.*, 2012, **134**, 2864.
- [29] W. Chaikittisilp, M. Hu, H. Wang, H. S. Huang, T. Fujita, K. C. W. Wu, L. C. Chen, Y. Yamauchi, K. Ariga, *Chem. Commun.*, 2012, **48**, 7259.
- [30] N. L. Torad, M. Hu, Y. Kamachi, K. Takai, M. Imura, M. Naitoa, Y. Yamauchi, *Chem. Commun.*, 2013, **49**, 2521.
- [31] H. L. Jiang, B. Liu, Y. Q. Lan, K. Kuratani, T. Akita, H. Shioyama, F. Q. Zong, Q. Xu, *J. Am. Chem. Soc.*, 2011, **133**, 11854.
- [32] B. Liu, H. Shioyama, T. Akita, Q. Xu, *J. Am. Chem. Soc.*, 2008, **130**, 5390.
- [33] J. Liu, S. Z. Qiao, H. Liu, J. Chen, A. Orpe, D. Y. Zhao, G. Q. Lu, *Angew. Chem. Int. Ed.*, 2011, **50**, 5947.
- [34] T. Kyotani, T. Nagai, S. Inoue, A. Tomita, *Chem. Mater.*, 1997, **9**, 609.
- [35] K. Matsuoka, Y. Yamagishi, T. Yamazaki, N. Setoyama, A. Tomita, T. Kyotani, *Carbon*, 2005, **43**, 876.

- [36] Z. X. Ma, T. Kyotani, A. Tomita, *Chem. Commun.*, 2000, **23**, 2365.
- [37] J. Lee, S. H. Joo, R. Ryoo, *J. Am. Chem. Soc.*, 2002, **124**, 1156.
- [38] H. I. Lee, J. H. Kim, D. J. You, J. E. Lee, J. M. Kim, W. S. Ahn, C. Pak, S. H. Joo, H. Chang, D. Seung, *Adv. Mater.*, 2008, **20**, 757.
- [39] L. C. Sang, A. Vinu, M. O. Coppens, *J. Mater. Chem.*, 2011, **21**, 7410.
- [40] A. H. Lu, F. Schüth, *Adv. Mater.*, 2006, **18**, 1793.
- [41] S. Shrestha, W. E. Mustain, *J. Electrochem. Soc.*, 2010, **157**, B1665.
- [42] H. J. Liu, X. M. Wang, W. J. Cui, Y. Q. Dou, D. Y. Zhao, Y. Y. Xia, *J. Mater. Chem.*, 2010, **20**, 4223.
- [43] Y. S. Li, Y. Q. Yang, J. L. Shi, M. L. Ruan, *Microporous Mesoporous Mater.*, 2008, **112**, 597.
- [44] Z. B. Lei, Y. Xiao, L. Q. Dang, M. Lu, W. S. You, *Microporous Mesoporous Mater.*, 2006, **96**, 127.
- [45] S. Tanaka, N. Nishiyama, Y. Egashira, K. Ueyama, *Chem. Commun.*, 2005, **16**, 2125.
- [46] Y. Meng, D. Gu, F. Q. Zhang, Y. F. Shi, H. F. Yang, Z. Li, C. Z. Yu, B. Tu, D. Y. Zhao, *Angew. Chem. Int. Ed.*, 2005, **44**, 7053.
- [47] F. Q. Zhang, Y. Meng, D. Gu, Y. Yan, C. Z. Yu, B. Tu, D. Y. Zhao, *J. Am. Chem. Soc.*, 2005, **127**, 13508.
- [48] J. Liu, T. Y. Yang, D. W. Wang, G. Q. Lu, D. Y. Zhao, S. Z. Qiao, *Nat. Commun.*, 2013, **4**, 2798.
- [49] S. Tanaka, Y. Katayama, M. P. Tate, H. W. Hillhouse, Y. Miyake, *J. Mater. Chem.*, 2007, **17**, 3639.
- [50] C. Liang, S. Dai, *J. Am. Chem. Soc.*, 2006, **128**, 5316.
- [51] J. Schuster, R. Köhn, A. Keilbach, M. Döblinger, H. Amenitsch, T. Bein, *Chem. Mater.*, 2009, **21**, 5754.
- [52] T. Kimura, A. M. Emre, K. Kato, Y. Hayashi, *J. Mater. Chem. A.*, 2013, **1**, 15135.
- [53] M. Si, D. Feng, L. B. Qiu, D. S. Jia, A. A. Elzatahry, G. F. Zheng, D. Y. Zhao, *J. Mater. Chem. A.*, 2013, **1**, 13490.
- [54] Y. H. Deng, J. Wei, Z. K. Sun, D. Y. Zhao, *Chem. Soc. Rev.*, 2013, **42**, 4054.

- [55] J. Y. Zhang, Y. H. Deng, J. Wei, Z. K. Sun, D. Gu, H. Bongard, C. Liu, H. H. Wu, B. Tu, F. Schüth, D. Y. Zhao, *Chem. Mater.*, 2009, **21**, 3996.
- [56] C. D. Liang, K. L. Hong, G. A. Guiochon, J. W. Mays, S. Dai, *Angew. Chem. Int. Ed.*, 2004, **43**, 5785.
- [57] Y. H. Deng, Y. Cai, Z. K. Sun, D. Gu, J. Wei, W. Li, X. H. Guo, J. P. Yang, D. Y. Zhao, *Adv. Funct. Mater.*, 2010, **20**, 3658.
- [58] Y. H. Deng, J. Liu, C. Liu, D. Gu, Z. K. Sun, J. Wei, J. Y. Zhang, L. J. Zhang, B. Tu, D. Y. Zhao, *Chem. Mater.*, 2008, **20**, 7281.
- [59] Z. Wang, F. Li, N. S. Ergang, A. Stein, *Chem. Mater.*, 2006, **18**, 5543.
- [60] Z. Y. Yuan, B. L. Su, *J. Mater. Chem.*, 2006, **16**, 663.
- [61] Y. H. Deng, C. Liu, T. Yu, F. Liu, F. Q. Zhang, Y. Wan, L. J. Zhang, C. C. Wang, B. Tu, P. A. Webley, H. T. Wang, D. Y. Zhao, *Chem. Mater.*, 2007, **19**, 3271.
- [62] Z. Wang, E. R. Kiesel, A. Stein, *J. Mater. Chem.*, 2008, **18**, 2194.
- [63] B. Z. Fang, J. H. Kim, M. Kim, J. S. Yu, *Chem. Mater.*, 2009, **21**, 789.
- [64] S. Lim, K. Suh, Y. Kim, M. Yoon, H. Park, D. N. Dybtsev, K. Kim, *Chem. Commun.*, 2012, **48**, 7447.
- [65] T. Morishita, Y. Soneda, T. Tsumura, M. Inagaki, *Carbon*, 2006, **44**, 2360.
- [66] D. W. Wang, F. Li, M. Liu, G. Q. Lu, H. M. Cheng, *Angew. Chem. Int. Ed.*, 2008, **47**, 373.
- [67] S. W. Woo, K. Dokko, H. Nakano, K. Kanamura, *J. Mater. Chem.*, 2008, **18**, 1674.
- [68] J. S. Yu, S. Kang, S. B. Yoon, G. Chai, *J. Am. Chem. Soc.*, 2002, **124**, 9382.
- [69] S. Kang, J. S. Yu, M. Kruk, M. Jaroniec, *Chem. Commun.*, 2002, **16**, 1670.
- [70] J. Liang, Y. Zheng, J. Chen, J. Liu, D. Hulicova-Jurcakova, M. Jaroniec, S. Z. Qiao, *Angew. Chem. Int. Ed.*, 2012, **51**, 3892.
- [71] G. Hasegawa, K. Kanamori, K. Nakanishi, T. Hanada, *Carbon*, 2010, **48**, 1757.
- [72] S. Mulik, C. Sotiriou-Leventis, N. Leventis, *Chem. Mater.*, 2008, **20**, 6985.
- [73] H. D. Du, L. Gan, B. H. Li, P. Wu, Y. L. Qiu, F. Y. Kang, R. W. Fu, Y. Q. Zeng, *J. Phys. Chem. C*, 2007, **111**, 2040.
- [74] S. H. Joo, S. J. Choi, I. Oh, J. Kwak, Z. Lin, O. Terasaki, R. Ryoo, *Nature*, 2001, **412**, 169.
- [75] B. Z. Fang, J. H. Kim, C. Lee, J. S. Yu, *J. Phys. Chem. C*, 2008, **112**, 639.

- [76] J. H. Bang, K. Han, S. E. Skrabalak, H. Kim, K. S. Suslick, *J. Phys. Chem. C*, 2007, **111**, 10959.
- [77] X. J. Bo, L. D. Zhu, G. Wang, L. P. Guo, *J. Mater. Chem.*, 2012, **22**, 5758.
- [78] Y. Fang, D. Gu, Y. Zou, Z. X. Wu, F. Y. Li, R. C. Che, Y. H. Deng, B. Tu, D. Y. Zhao, *Angew. Chem. Int. Ed.*, 2010, **49**, 7987.
- [79] F. B. Su, X. S. Zhao, Y. Wang, J. H. Zeng, Z. C. Zhou, J. Y. Lee, *J. Phys. Chem. B*, 2005, **109**, 20200.
- [80] Z.-S. Wu, Y. Sun, Y.-Z. Tan, S. Yang, X. Feng, K. Müllen, *J. Am. Chem. Soc.*, 2012, **134**, 19532.
- [81] S. Q. Song, Y. R. Liang, Z. H. Li, Y. Wang, R. W. Fu, D. C. Wu, P. Tsiakaras, *Appl. Catal. B: Environ.*, 2010, **98**, 132.
- [82] M. L. Lin, C. C. Huang, M. Y. Lo, C. Y. Mou, *J. Phys. Chem. C*, 2008, **112**, 867.
- [83] D. S. Yang, D. Bhattacharjya, S. Inamdar, J. Park, J. S. Yu, *J. Am. Chem. Soc.*, 2012, **134**, 16127.
- [84] T. W. Kim, I. S. Park, R. Ryoo, *Angew. Chem. Int. Ed.*, 2003, **42**, 4375.
- [85] Y. Xia, Z. Yang, R. Mokaya, *Chem. Mater.*, 2006, **18**, 140.
- [86] D. S. Yuan, F. L. Zeng, J. Yan, X. L. Yuan, X. J. Huang, W. J. Zou, *RSC Adv.*, 2013, **3**, 5570.
- [87] N. Suzuki, S. Kiba, Y. Yamauchi, *Mater. Lett.*, 2011, **65**, 544.
- [88] H. J. Wang, H. Y. Jeong, M. Imura, L. Wang, L. Radhakrishnan, N. Fujita, C. Toen, O. Terasaki, Y. Yamauchi, *J. Am. Chem. Soc.*, 2011, **133**, 14526.
- [89] G. Gupta, D. A. Slanac, P. Kumar, J. D. Wiggins-Camacho, J. Kim, R. Ryoo, K. J. Stevenson, K. P. Johnston, *J. Phys. Chem. C*, 2010, **114**, 10796.
- [90] K. P. Gierszal, M. Jaroniec, T. W. Kim, J. Kim, R. Ryoo, *New J. Chem.*, 2008, **32**, 981.
- [91] Z. X. Yan, M. Cai, P. K. Shen, *J. Mater. Chem.*, 2012, **22**, 2133.
- [92] W. J. Gao, Y. Wan, Y. Q. Dou, D. Y. Zhao, *Adv. Energy Mater.*, 2011, **1**, 115.
- [93] D. S. Yuan, X. L. Yuan, W. J. Zou, F. L. Zeng, X. J. Huang, S. L. Zhou, *J. Mater. Chem.*, 2012, **22**, 17820.
- [94] J. Y. Yuan, C. Giordano, M. Antonietti, *Chem. Mater.*, 2010, **22**, 5003.

- [95] K. T. Lee, X. L. Ji, M. Rault, L. F. Nazar, *Angew. Chem. Int. Ed.*, 2009, **48**, 5661.
- [96] Z. L. Schaefer, M. L. Gross, M. A. Hickner, R. E. Schaak, *Angew. Chem.*, 2010, **122**, 7199.
- [97] J. Tang, J. P. He, T. Wang, Y. X. Guo, H. R. Xue, *Acta Chim. Sin.*, 2011, **69**, 1751.
- [98] M. Sevilla, A. B. Fuertes, *Carbon*, 2006, **44**, 468.
- [99] P. P. Su, L. Jiang, J. Zhao, J. W. Yan, C. Li, Q. H. Yang, *Chem. Commun.*, 2012, **48**, 8769.
- [100] F. B. Su, J. H. Zeng, X. Y. Bao, Y. S. Yu, J. Y. Lee, X. S. Zhao, *Chem. Mater.*, 2005, **17**, 3960.
- [101] Z. B. Lei, S. Y. Bai, Y. Xiao, L. Q. Dang, L. Z. An, G. N. Zhang, Q. Xu, *J. Phys. Chem. C*, 2008, **112**, 722.
- [102] M. Terrones, A. R. Botello-Méndez, J. Campos-Delgado, F. López-Urías, Y. I. Vega-Cantú, F. J. Rodríguez-Macías, A. L. Elías, E. Muñoz-Sandoval, A. G. Cano-Márquez, J.-C. Charlier, H. Terrones, *Nano Today*, 2010, **5**, 351.
- [103] P. F. Fulvio, R. T. Mayes, X. Q. Wang, S. M. Mahurin, J. C. Bauer, V. Presser, J. McDonough, Y. Gogotsi, S. Dai, *Adv. Funct. Mater.*, 2011, **21**, 2208.
- [104] F. B. Su, X. S. Zhao, Y. Wang, J. Y. Lee, *Microporous Mesoporous Mater.*, 2007, **98**, 323.
- [105] J. Tang, T. Wang, X. Sun, Y. Y. Hu, Q. Q. Xie, Y. X. Guo, H. R. Xue, J. P. He, *Electrochim. Acta.*, 2013, **90**, 53.
- [106] X. Sun, J. P. He, J. Tang, T. Wang, Y. X. Guo, H. R. Xue, G. X. Li, Y. Ma, *J. Mater. Chem.*, 2012, **21**, 10900.
- [107] Y. Chen, X. Li, K. Park, J. Song, J. Hong, L. Zhou, Y.-W. Mai, H. Huang, J. B. Goodenough, *J. Am. Chem. Soc.*, 2013, **135**, 16280.
- [108] A. Guha, W. J. Lu, T. A. Zawodzinski Jr., D. A. Schiraldi, *Carbon*, 2007, **45**, 1506.
- [109] J. R. C. Salgado, J. J. Quintana, L. Calvillo, M. J. Lázaro, P. L. Cabot, I. Esparbé, E. Pastor, *Phys. Chem. Chem. Phys.*, 2008, **10**, 6796.
- [110] J. Lee, Y. Park, O. Yang, Y. Kang, K. Jun, Y. Lee, H.Y. Kim, K. Lee, W. C. Choi, *J. Power Sources*, 2006, **158**, 1251.
- [111] S. Chen, Z. D. Wei, X. Q. Qi, L. C. Dong, Y. G. Guo, L. J. Wan, Z. G. Shao, L. Li, *J. Am. Chem. Soc.*, 2012, **134**, 13252.

- [112] Y. Yan, Q. Cheng, Z. Zhu, V. Pavlinek, P. Saha, C. Li, *J. Power Sources*, 2013, **240**, 544.
- [113] L. L. Zhang, S. Li, J. Zhang, P. Guo, J. Zheng, X. S. Zhao, *Chem. Mater.*, 2010, **22**, 1195.
- [114] Z. Lei, Z. Chen, X. S. Zhao, *J. Phys. Chem. C*, 2010, **114**, 19867.
- [115] Y. G. Chen, J. J. Wang, H. Liu, M. N. Banis, R. Y. Li, X. L. Sun, T. K. Sham, S. Y. Ye, S. Knights, *J. Phys. Chem. C*, 2011, **115**, 3769.
- [116] G. Imamura, K. Saiki, *J. Phys. Chem. C*, 2011, **115**, 10000.
- [117] K. P. Gong, F. Du, Z. H. Xia, M. Durstock, L. M. Dai, *Science*, 2009, **323**, 760.
- [118] F. B. Su, Z. Q. Tian, C. K. Poh, Z. Wang, S. H. Lim, Z. L. Liu, J. Y. Lin, *Chem. Mater.*, 2010, **22**, 832.
- [119] T. Wang, J. P. He, D. Sun, Y. X. Guo, Y. O. Ma, Y. Hu, G. X. Li, H. R. Xue, J. Tang, X. Sun, *J. Power Sources*, 2011, **196**, 9552.
- [120] Y. Wan, X. F. Qian, N. Q. Jia, Z. Y. Wang, H. X. Li, D. Y. Zhao, *Chem. Mater.*, 2008, **20**, 1012.
- [121] C. H. Choi, S. H. Park, S. I. Woo, *ACS Nano*, 2012, **6**, 7084.
- [122] D. B. Kim, D. H. Lim, H. J. Chun, H. H. Kwon, H. I. Lee, *Carbon*, 2010, **48**, 673.
- [123] P. Pachfule, V. M. Dhavale, S. Kandambeth, S. Kurungot, R. Banerjee, *Chem. Eur. J.*, 2013, **19**, 974.
- [124] Y. X. Guo, J. P. He, T. Wang, H. R. Xue, Y. Y. Hu, G. X. Li, J. Tang, X. Sun, *J. Power Sources*, 2011, **196**, 9299.
- [125] Y. Xia, R. Mokaya, *Adv. Mater.*, 2004, **16**, 1553.
- [126] Y. Xia, R. Mokaya, *Chem. Mater.*, 2005, **17**, 1553.
- [127] C. M. Yang, C. Weidenthaler, B. Spliethoff, M. Mayanna, F. Schueth, *Chem. Mater.*, 2005, **17**, 355.
- [128] Z. Lei, L. An, L. Dang, M. Zhao, J. Shi, S. Bai, Y. Cao, *Microporous Mesoporous Mater.*, 2009, **119**, 30.
- [129] S. S. Park, S. W. Chu, C. F. Xue, D. Y. Zhao, C. S. Ha, *J. Mater. Chem.*, 2011, **21**, 10801.
- [130] M. Hu, J. Reboul, S. Furukawa, L. Radhakrishnan, Y. Zhang, P. Srinivasu, H. Iwai, H. Wang, Y. Nemoto, N. Suzuki, S. Kitagawa, Y. Yamauchi, *Chem. Commun.*, 2011, **47**, 8124.

- [131] G. P. Mane, S. N. Talapaneni, C. Anand, S. Varghese, H. Iwai, Q. Ji, K. Ariga, T. Mori, A. Vinu, *Adv. Funct. Mater.*, 2012, **22**, 3596.
- [132] K. K. R. Datta, V. V. Balasubramanian, K. Ariga, T. Mori, A. Vinu, *Chem. Eur. J.*, 2011, **17**, 3390.
- [133] R. L. Liu, D. Q. Wu, X. L. Feng, K. Müllen, *Angew. Chem. Int. Ed.*, 2010, **49**, 2565.
- [134] A. Lu, A. Kiefer, W. Schmidt, F. Schüth, *Chem. Mater.*, 2004, **16**, 100.
- [135] C. Weidenthaler, A. H. Lu, W. Schmidt, F. Schüth, *Microporous Mesoporous Mater.*, 2006, **88**, 238.
- [136] M. Kruk, B. Dufour, E. B. Celer, T. Kowalewski, M. Jaroniec, K. Matyjaszewski, *J. Phys. Chem. B*, 2005, **109**, 9216.
- [137] D. W. Wang, F. Li, Z. G. Chen, G. Q. Lu, H. M. Cheng, *Chem. Mater.*, 2008, **20**, 7195.
- [138] T. Wang, C. X. Zhang, X. Sun, Y. X. Guo, H. Guo, J. Tang, H. R. Xue, M. Z. Liu, X. X. Zhang, L. Zhu, Q. Q. Xie, J. P. He, *J. Power Sources*, 2012, **212**, 1.
- [139] Z. Liu, H. G. Nie, Z. Yang, J. Zhang, Z. P. Jin, Y. Q. Lu, Z. B. Xiao, S. M. Huang, *Nanoscale*, 2013, **5**, 3283.
- [140] J. Wei, D. D. Zhou, Z. K. Sun, Y. H. Deng, Y. Y. Xia, D. Y. Zhao, *Adv. Funct. Mater.*, 2013, **23**, 2322.
- [141] X. C. Zhao, A. Q. Wang, J. W. Yan, G. Q. Sun, L. X. Sun, T. Zhang, *Chem. Mater.*, 2010, **22**, 5463.
- [142] R. Czerw, M. Terrones, J. C. Charlier, X. Blase, B. Foley, R. Kamalakaran, N. Grobert, H. Terrones, D. Tekleab, P. M. Ajayan, W. Blau, M. Rühle, D. L. Carroll, *Nano Lett.*, 2001, **1**, 457.
- [143] L. T. Qu, Y. Liu, J. Baek, L. M. Dai, *ACS Nano*, 2010, **4**, 1321.
- [144] J. P. Paraknowitsch, J. Zhang, D. S. Su, A. Thomas, M. Antonietti, *Adv. Mater.*, 2010, **22**, 87.
- [145] Y. Y. Shao, J. H. Sui, G. P. Yin, Y. Z. Gao, *Appl. Catal. B: Environ.*, 2008, **79**, 89.
- [146] B. Yue, Y. W. Ma, H. S. Tao, L. S. Yu, G. Q. Jian, X. Z. Wang, X. S. Wang, Y. N. Lu, Z. J. Hu, *Mater. Chem.*, 2008, **18**, 1747.
- [147] J. Y. Choi, R. S. Hsu, Z. W. Chen, *J. Phys. Chem. C*, 2010, **114**, 8048.

- [148] X. X. Yuan, X. Zeng, H. J. Zhang, Z. F. Ma, C. Y. Wang, *J. Am. Chem. Soc.*, 2010, **132**, 1754.
- [149] Y. M. Tan, C. F. Xu, G. X. Chen, X. L. Fang, N. F. Zheng, Q. J. Xie, *Adv. Funct. Mater.*, 2012, **22**, 4584.
- [150] V. Nallathambi, J. W. Lee, S. P. Kumaraguru, G. Wu, B. N. Popov, *J. Power Sources*, 2008, **183**, 34.
- [151] L. S. Panchalkarla, A. Govindaraj, C. N. R. Rao, *ACS Nano*, 2007, **1**, 450.
- [152] D. Shin, B. Jeong, B. S. Mun, H. Jeon, H. J. Shin, J. Baik, J. Lee, *J. Phys. Chem. C*, 2013, **117**, 11619.
- [153] C. Jeyabharathia, P. Venkateshkumarb, M. S. Raoa, J. Mathiyarasua, K. L. N. Phania, *Electrochim. Acta*, 2012, **74**, 171.
- [154] S. Chen, J. Y. Bi, Y. Zhao, L. J. Yang, C. Zhang, Y. W. Ma, Q. Wu, X. Z. Wang, Z. Hu, *Adv. Mater.*, 2012, **24**, 5593.
- [155] Z. W. Liu, F. Peng, H. J. Wang, H. Yu, W. X. Zheng, J. Yang, *Angew. Chem. Int. Ed.*, 2011, **50**, 3257.
- [156] X. J. Bo, L. P. Guo, *Phys. Chem. Chem. Phys.*, 2013, **15**, 2459.
- [157] X. Wang, Q. Weng, X. Liu, X. Wang, D.-M. Tang, W. Tian, C. Zhang, W. Yi, D. Liu, Y. Bando, D. Golberg, *Nano Lett.*, 2014, **14**, 1164.
- [158] F. Zheng, Y. Yang, Q. Chen, *Nat. Commun.*, 2014, **5**, 5261.
- [159] D. Hulicova-Jurcakova, A. M. Puziy, O. I. Poddubnaya, F. Suárez-García, J. M. D. Tascón, G. Q. Lu, *J. Am. Chem. Soc.*, 2009, **131**, 5026.
- [160] Z. S. Wu, A. Winter, L. Chen, Y. Sun, A. Turchanin, X. L. Feng, K. Müllen, *Adv. Mater.*, 2012, **24**, 5130.
- [161] C. O. Ania, V. Khomenko, E. Raymundo-Pinero, J. B. Parra, F. Beguin, *Adv. Funct. Mater.*, 2007, **17**, 1828.
- [162] M. Zhong, E. K. Kim, J. P. McGann, S.-E. Chun, J. F. Whitacre, M. Jaroniec, K. Matyjaszewski, T. Kowalewski, *J. Am. Chem. Soc.*, 2012, **134**, 14846.
- [163] P. F. Fulvio, C. D. Liang, S. Dai, M. Jaroniec, *Eur. J. Inorg. Chem.*, 2009, **5**, 605.

- [164] F. B. Su, C. K. Poh, J. H. Zeng, Z. Y. Zhong, Z. L. Liu, J. Y. Lin, *J. Power Sources*, 2012, **205**, 136.
- [165] J. H. Zhou, J. P. He, T. Wang, D. Sun, G. W. Zhao, X. Chen, D. J. Wang, Z. Y. Di, *J. Mater. Chem.*, 2008, **18**, 5776.
- [166] J. Tang, T. Wang, X. C. Pan, X. Sun, X. L. Fan, Y. X. Guo, H. R. Xue, J. P. He, *J. Phys. Chem. C*, 2013, **117**, 16896.
- [167] Z. K. Sun, B. Sun, M. H. Qiao, J. Wei, Q. Yue, C. Wang, Y. H. Deng, S. Kaliaguine, D. Y. Zhao, *J. Am. Chem. Soc.*, 2012, **134**, 17653.
- [168] M. Z. Dai, L. Y. Song, J. T. LaBelle, B. D. Vogt, *Chem. Mater.*, 2011, **23**, 2869.
- [169] S. Q. Ma, G. A. Goenaga, A. V. Call, D. J. Liu, *Chem. Eur. J.*, 2011, **17**, 2063.
- [170] Y. Hou, T. Huang, Z. Wen, S. Mao, S. Cui, J. Chen, *Adv. Energy Mater.*, 2014, **4**, 1400337
- [171] T. Y. Ma, S. Dai, M. Jaroniec, S. Z. Qiao, *J. Am. Chem. Soc.*, 2014, **136**, 13925.
- [172] J. Shui, C. Chen, L. Grabstanowicz, D. Zhao, D.-J. Liu, *Proc. Natl. Acad. Sci. U. S. A.*, 2015, **112**, 10629.
- [173] G. Wu, K. L. More, C. M. Johnston, P. Zelenay, *Science*, 2011, **332**, 443.
- [174] U. I. Kramm, I. Herrmann-Geppert, J. Behrends, K. Lips, S. Fiechter, P. Bogdanoff, *J. Am. Chem. Soc.*, 2016, **138**, 635.
- [175] D. Gu, W. Li, F. Wang, H. Bongard, B. Spliethoff, W. Schmidt, C. Weidenthaler, Y. Xia, D. Zhao, F. Schüth, *Angew. Chem. Int. Ed.*, 2015, **54**, 7060.

Chapter 2

Synthesis of Nitrogen-Doped Mesoporous Carbon Spheres with Extra-Large Pores through Assembly of Diblock Copolymer Micelles

2.1. Introduction

Porous carbon materials have unique characteristics, such as a good electrical conductivity, chemical inertness, high surface area, large porosity, and good biocompatibility, thereby showing many potential applications in a wide range of research fields (e.g., adsorption, energy conversion and storage, catalysis, and sensor technology).[1-6] As demonstrated in many studies, mesoporous materials show an excellent performance compared to microporous materials, because of the less limited diffusion. Using mesopores, especially large-sized mesopores, smooth mass transport can be realized for large reagent molecules.[7-10] The morphological control is also a critical factor. The spherical morphology attracts sustained research interests especially when the particle size is smaller than 200 nm, because it provides short pathways for mass transport and minimizes the viscous effects.[11-14] Several successful applications in drug delivery, gene therapy, supercapacitors, Li-S batteries, and CO₂ capture have been reported by using spherical carbon materials, due to their inherent short diffusion pathway and the effective intracellular endocytosis.[15-17]

So far, various porous carbon spheres have been prepared using different methods, including a Stöber-based method, hard- and soft-templating methods, and a direct polymerization method.[18-20] For example, microporous carbon spheres with particle sizes from 120 to 800 nm have been synthesized through direct self-polymerization and subsequent carbonization by Lu and co-workers.[21] Although the resultant carbon spheres have a high specific surface area after treatment with KOH, the pores in the spheres are still micropores with a pore size smaller than 2 nm. Zhao et al. developed a hydrothermal method for the synthesis of ordered mesoporous carbon spheres derived from co-assembly of resol and F127.[22] However, their pore sizes are still limited to 3 nm. Therefore, such a limitation on the pore size in carbon spheres significantly devalues their practical applications.

Until now, mesoporous materials with pore size larger than 10 nm have been successfully prepared by using various high-molecular-weight block polymers, such as polystyrene-*block*-poly(ethylene oxide) (PS-*b*-PEO), polyisobutylene-*block*-PEO (PIB-*b*-PEO), PS-*block*-poly(4-vinylpyridine) (PS-*b*-P4VP), and PEO-*block*-poly(methyl

methacrylate) (PEO-*b*-PMMA) as soft templates. However, they are mostly used in the form of films or irregularly shaped particles with micrometer sizes.[23-26] These systems are based on solvent evaporation processes which are not applicable to prepare mesoporous carbon spheres. Mesoporous carbon spheres with large-sized pores will lead to many applications which are not attainable by films and irregular particles, as mentioned above.

By using the micelles of a high-molecular-weight block polymer PS-*b*-PEO as a template, I propose a facile micelle route for the preparation of N-doped mesoporous carbon spheres (NMCS) with large mesopore sizes (up to 16 nm), as shown in **Figure 2.1**. The resultant mesoporous carbon spheres are promising catalysts for the oxygen reduction reaction (ORR) and also would show promising applications in large biomolecule adsorption and gene therapy. The key of my synthesis is the use of DA/PS-*b*-PEO composite micelles which are stably pre-formed in the reaction solution. Polymerization of the DA molecules and further co-assembly with the PS-*b*-PEO micelles result in the formation of PDA/PS-*b*-PEO composite spheres (where polymerized dopamine is abbreviated as PDA). The PS-*b*-PEO micelles acting as a sacrificial pore-forming agent are removed during the carbonization process, leaving the mesopores in the carbon spheres.

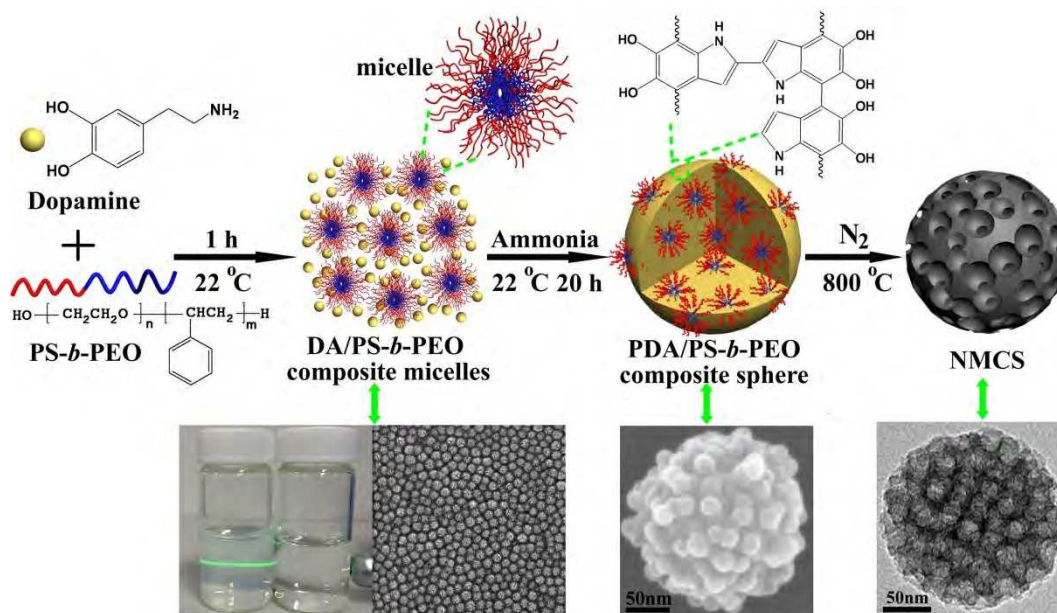


Figure 2.1 Formation process of the N-doped mesoporous carbon nanospheres (NMCS).

2.2. Experimental Sections

2.2.1. Chemicals

Dopamine hydrochloride (DA) was purchased from Aldrich. Amphiphilic block copolymer, polystyrene-*b*-poly(ethylene oxide) (PS-*b*-PEO) was purchased from Polymer Source Inc. All of chemicals were of analytical grade and used without further purification.

2.2.2. Preparation of Nitrogen-Doped Mesoporous Carbon Spheres (NMCS)

In a typical synthesis of NMCS with diameter of ~180 nm and pore size of 16 nm (NMCS-3), 200 mg of DA was dissolved in the mixed solution of ethanol and deionized water (with volume ratio of 1:2, 12 mL), and then the above solution poured into 4 mL THF containing 30 mg of diblock copolymer PS₁₇₃-*b*-PEO₁₇₀ under mild stirring. After 1 hour, 0.5 mL of ammonia aqueous solution (NH₄OH, 28-30 wt%) was injected to induce the self-polymerization of dopamine and the colour of the solution became brown. After continuous reaction for 20 hours, PDA/PS₁₇₃-*b*-PEO₁₇₀ composite spheres were obtained by centrifugation and washed with mixed solution of ethanol and deionized water for several times. For carbonization, the PDA/PS₁₇₃-*b*-PEO₁₇₀ composite spheres were pre-heated at 350 °C for 3 hours and finally heated at 800 °C for 2 hours under N₂ atmospheres with a heating rate of 1 °C min⁻¹. Finally, NMCS with the average particle size of ca. 200 nm and uniformly sized mesopores of 16 nm were obtained. All synthetic experiments were carried out at room temperature (ca. 22 °C). Through the above synthetic approach, DA shows several advantages for preparation of NMCS; (i) easy self-polymerization under mild condition, (ii) formation of strong interaction with common block polymer template, and (iii) preservation of stable N element after suffering heat treatment.

The pore sizes of NMCS were varied by changing the diblock copolymers (PS-*b*-PEO) with different chain lengths of the PS blocks. In this work, I also used other block copolymers, such as PS₃₁-*b*-PEO₂₈₄, PS₃₇-*b*-PEO₁₁₄, PS₈₇-*b*-PEO₂₂₇, and PS₁₇₈-*b*-PEO₈₈₆. For comparison, I synthesized N-doped carbon spheres (labelled as NCS) through carbonization PDA at 800 °C under N₂ atmosphere according to previous report.[21] The obtained NCS possess only

microporous structure. The specific surface area is $318 \text{ m}^2 \cdot \text{g}^{-1}$, the average particle size is 192 nm, and the N content is 7.7 wt% in NCS. These values are similar to the previous report.[21]

2.2.3. Characterization

The morphology of the samples was characterized by using a Hitachi SU-8000 field-emission scanning electron microscope (SEM) at an accelerating voltage of 5 kV. The interior structure of samples was characterized by using SEM that is equipped with a focused ion beam (FIB). Transmission electron microscopy (TEM) and elemental mapping analysis were measured by JEM-2100 operated at 200 kV. N_2 adsorption–desorption isotherms were obtained by using a BELSORP-mini (BEL, Japan) at 77 K. The surface areas were estimated by the Multipoint Brunauer–Emmett–Teller (BET) method at a P/P_0 range of 0.05-0.5 based on the adsorption data. The total pore volumes and pore size distributions were calculated from the adsorption branches of isotherms based on the Barrett–Joyner–Halenda (BJH) model. Raman spectra were measured by Horiba-Jovin Yvon T64000 with the excitation Laser of 364 nm. Thermogravimetric (TG) analysis was carried out by using a Hitachi HT-Seiko Instrument Exter 6300 TG/DTA in N_2 heating from room temperature to 1000 °C at $5 \text{ }^\circ\text{C} \cdot \text{min}^{-1}$, and keeping at 350 °C for 2 hours. X-ray photoelectronic spectroscopy (XPS) spectra were carried out at room temperature by using a JPS-9010TR (JEOL) instrument with an Mg $K\alpha$ X-ray source. All the binding energies were calibrated via referencing to C 1s binding energy (284.6 eV). The peaks of the N 1s spectrum were fitted with a Gaussian-Lorentzian sum function and a Shirley background. When the value of %G/L is fixed to be 50%, the N 1s spectra reach the optimized fitting.

2.2.4. Electrochemical Measurements

Polarization curve and current-time ($i-t$) amperometry for ORR were measured on a CHI 842B electrochemical workstation with a conventional three-electrode cell. Platinum and a Ag/AgCl (3M) electrode were selected as the counter electrode and reference electrode, respectively. The working electrode was prepared as follows. 1 mg of NCS, NMCS, or 20 wt% Pt/C (the mass fraction of Pt in commercial Pt/C catalyst is 20%) was dispersed in the mixture of ethanol (0.2 mL) and Nafion (5 wt%, 10 μL) under ultrasonication for 30 mins. Then, 10 μL

of the above suspension was dropped on the polished glassy carbon (GC) electrode with 3 mm diameter and dried under infrared lamp. The electrochemical measurements were performed in basic media (0.1 M KOH) saturated with O₂ at between -0.8 and 0.0 V (*vs.* Ag/AgCl) with a scan rate of 10 mV·s⁻¹ and rotating speed of 1600 rpm. The polarization curves for ORR were carried out by the rotating disk electrode (RDE) or a rotating ring-disk electrode (RRDE) technique. In this work, electrochemical tests for different electrocatalysts were repeated for three times.

2.3. Results and Discussion

2.3.1. Synthesis and Characterization of NMCS

DA is used as both the carbon and nitrogen sources in this study, which is critically important for high doping of N heteroatoms in the carbon matrix. Although DA has been often used for the preparation of N-doped carbon materials, microporous and/or non-porous carbon compounds have been always obtained through these methods.[21,27-30] It is difficult to control the pore sizes by using surfactants, probably because of the weak interaction between DA molecules and low-molecular-weight block copolymer or ionic surfactants. Carbon nanomaterials doped with heteroatoms, such as nitrogen, boron, and sulfur, have attracted much attention, because of their modification of electron donor/acceptor characteristics and the resulting enhancement of electrochemical properties.[31-34] N-doped carbon nanomaterials, such as N-doped nanotubes, graphene, and mesoporous carbon, have shown superior electrocatalytic performance and good stability for ORR. Therefore, the large pore-sized NMCS reported here would surely contribute to mass transportation by reducing and smoothing the diffusion pathways, which are expected to lead to high electrocatalytic activity for the ORR. These studies will provide not only a new synthesis method, but also important insight into designing mesoporous carbon spheres for various applications.

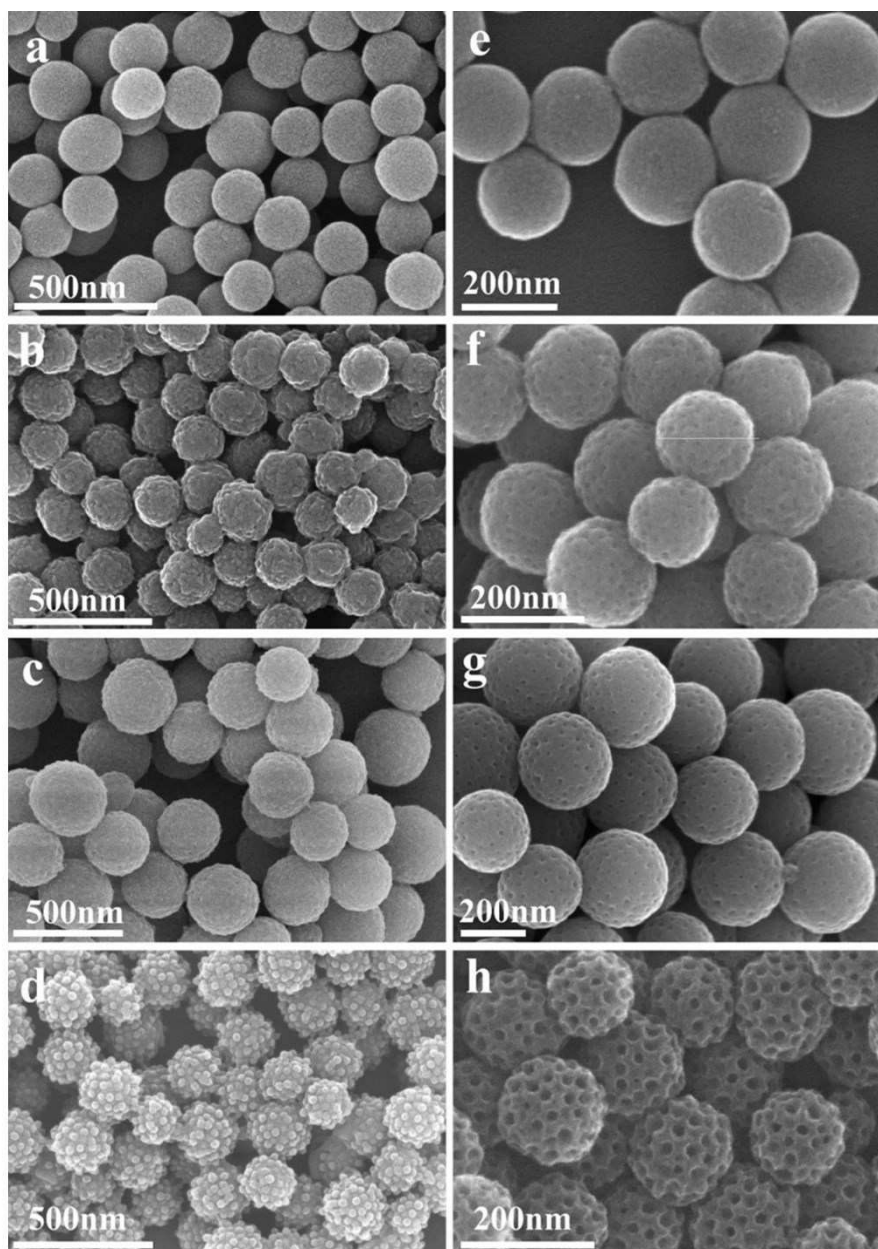


Figure 2.2 SEM images of (a) PDA spheres, (b) PDA/PS₃₇-*b*-PEO₁₁₄ composite spheres, (c) PDA/PS₁₇₈-*b*-PEO₈₈₆ composite spheres, and (d) PDA/PS₁₇₃-*b*-PEO₁₇₀ composite spheres. SEM images of the corresponding N-doped carbon spheres (NCS) and N-doped mesoporous carbon spheres (NMCS) carbonized at 800 °C for (e) NCS, (f) NMCS-1, (g) NMCS-2, and (h) NMCS-3.

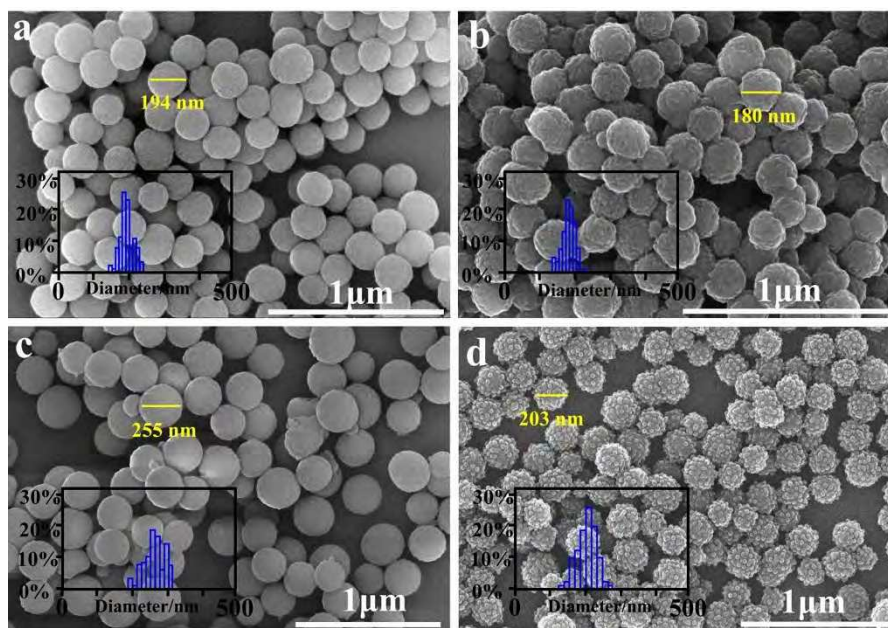


Figure 2.3 SEM images of (a) PDA spheres, (b) PDA/PS₃₇-*b*-PEO₁₁₄ composite spheres, (c) PDA/PS₁₇₈-*b*-PEO₈₈₆ composite spheres, and (d) PDA/PS₁₇₃-*b*-PEO₁₇₀ composite spheres, respectively. The inset images are the particle size distribution histograms that calculated from over 50 particles. The average particle sizes are (a) 194 nm, (b) 180 nm, (c) 255 nm, and (d) 203 nm, respectively.

Figure 2.2a-d show scanning electron microscope (SEM) images for PDA spheres prepared without using PS-*b*-PEO micelles and PDA/PS-*b*-PEO composite spheres prepared by employing three PS-*b*-PEO diblock copolymers with different polymerization degree of PS and PEO chains, namely, PS₃₇-*b*-PEO₁₁₄, PS₁₇₈-*b*-PEO₈₈₆, and PS₁₇₃-*b*-PEO₁₇₀. All the composite spheres show uniform particle sizes and shapes, and their average particle sizes are 194 nm, 180 nm, 255 nm, and 203 nm for PDA spheres, PDA/PS₃₇-*b*-PEO₁₁₄, PDA/PS₁₇₈-*b*-PEO₈₈₆, and PDA/PS₁₇₃-*b*-PEO₁₇₀ composite spheres, respectively, as shown in low-magnified SEM images (**Figure 2.3**). The PDA spheres prepared without PS-*b*-PEO micelles have a very smooth surface (**Figure 2.2a**), while clear round bumps are observed on the surface of PDA/PS-*b*-PEO composite spheres (**Figure 2.2b-d** and **Figure 2.4**). The bumpiness on the particle surface is obviously increased by using the diblock copolymer with longer PS chains. When using PS₁₇₃-*b*-PEO₁₇₀ as a template, the micelles as a template are more clearly confirmed (**Figure 2.2d**).

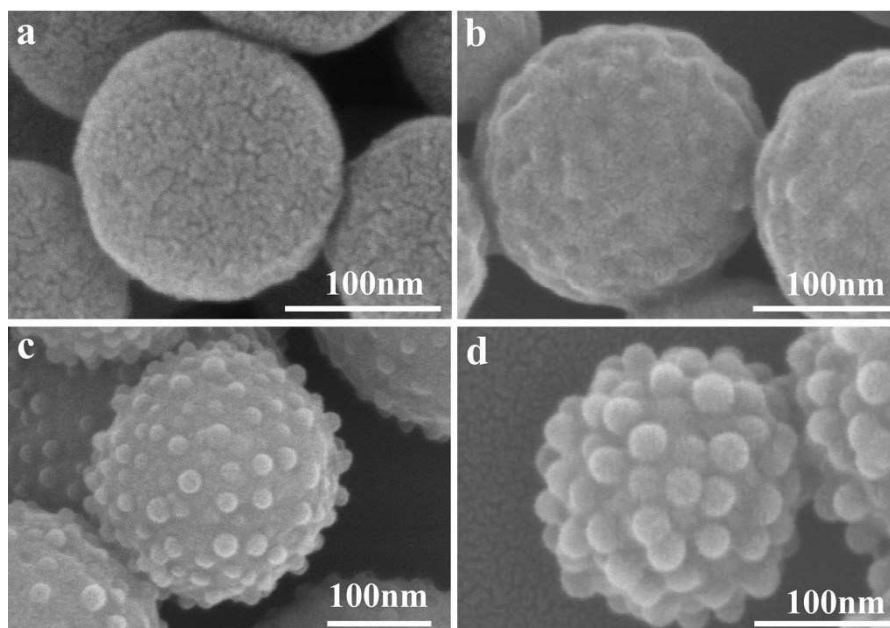


Figure 2.4 High resolution SEM images of (a) PDA spheres, (b) PDA/PS₃₇-*b*-PEO₁₁₄ composite spheres, (c) PDA/PS₁₇₈-*b*-PEO₈₈₆ composite spheres, and (d) PDA/PS₁₇₃-*b*-PEO₁₇₀ composite spheres, respectively.

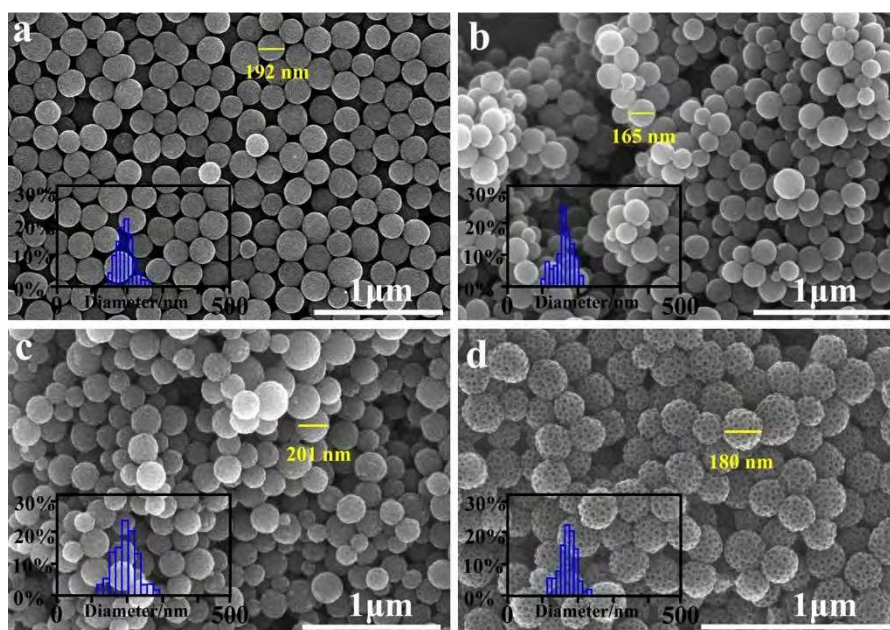


Figure 2.5 SEM images of (a) NCS, (b) NMCS-1, (c) NMCS-2, and (d) NMCS-3 prepared from PDA spheres, PDA/PS₃₇-*b*-PEO₁₁₄ composite spheres, PDA/PS₁₇₈-*b*-PEO₈₈₆ composite spheres, and PDA/PS₁₇₃-*b*-PEO₁₇₀ composite spheres, respectively. The insets are the particle size distribution histograms that calculated from over 100 particles. The average particle sizes are (a) 192 nm, (b) 165 nm, (c) 201 nm, and (d) 180 nm, respectively.

After heat treatment at 800 °C in N₂ atmosphere (i.e., carbonization), the PDA/PS-*b*-PEO composite spheres were converted to NMCS. Three types of NMCS were prepared from PDA/PS₃₇-*b*-PEO₁₁₄, PDA/PS₁₇₈-*b*-PEO₈₈₆, and PDA/PS₁₇₃-*b*-PEO₁₇₀ composite spheres. These samples are denoted as NMCS-1, NMCS-2, and NMCS-3, respectively. For comparison, PDA spheres prepared without using PS-*b*-PEO micelles were also thermally converted to N-doped carbon spheres (NCS) without mesopores. The original spherical morphology is completely retained without formation of cracks and holes. The sizes of NMCS are decreased compared with the PDA/PS-*b*-PEO composite spheres before the carbonization (**Figure 2.5**). Uniformly sized mesopores are well distributed on the sphere surface and their mesopore sizes roughly estimated from SEM images distinctly expand from 5 to 16 nm by increasing the PS chain lengths (**Figure 2.2f-h**). The lengths (i.e., molecular weights) of the PS chains strongly influence the pore sizes in the final NMCS, which will be discussed later. Focused ion-beam scanning electron microscope (FIB-SEM) shows that mesopores existed in both the exterior and interior of the carbon spheres (**Figure 2.6**). The spherical morphology and large-sized mesoporous structure in the NMCS still remain intact even extending the carbonization temperature to 1000 °C, showing good structural stability (**Figure 2.7**).

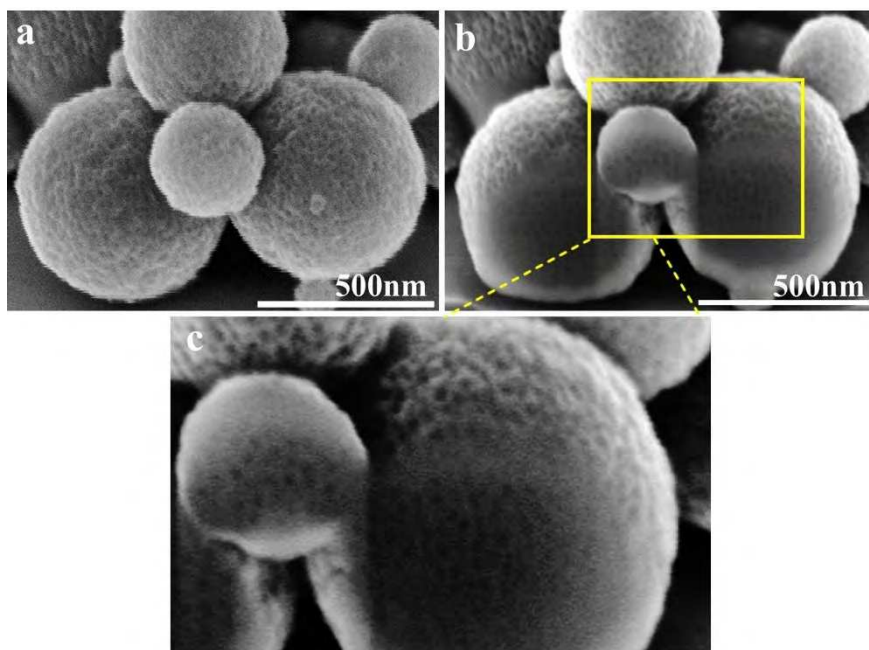


Figure 2.6 FIB-SEM images of NMCS-3 prepared from PDA/PS₁₇₃-*b*-PEO₁₇₀ composite spheres.

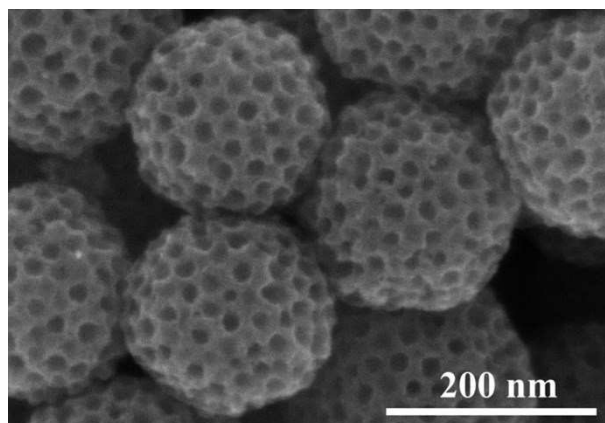


Figure 2.7 SEM image of NMCS-3 prepared from PDA/PS₁₇₃-*b*-PEO₁₇₀ composite spheres after carbonization at 1000 °C under N₂ atmosphere.

As revealed by TEM images (**Figure 2.8**), the PDA/PS-*b*-PEO composite spheres (**Figure 2.8b-d**) have rough surfaces compared with PDA spheres (**Figure 2.8a**), which corresponds with the SEM results (**Figure 2.2a-d**). NMCS carbonized from PDA/PS-*b*-PEO composite spheres show distinct mesopores throughout the whole spheres (**Figure 2.8f-h**). N₂ adsorption–desorption isotherms were measured to investigate the porosities of both NCS and NMCS. The isotherms of the NCS are type I isotherms (**Figure 2.9A**). The high N₂ adsorption shown in the adsorption branch at a relative low pressure is typically associated with micropores. Thus, without the templates, the carbonization in the polymeric matrix causes the formation of micropores because of the generation of gas in the spheres, which has been reported previously.[21] In contrast, NMCS-1, NMCS-2, and NMCS-3 show type IV isotherms with hysteresis loops. This behavior is typically associated with the capillary condensation of N₂ into the mesopores. The mesopores in NMCS are not cylindrical type with uniform size and smooth surface. These mesopores in NMCS are distributed randomly and are not uniform strictly. During the adsorption process along with the increased relative pressure, the nitrogen was condensed first within the smallest mesopores. The pressure increased until all pores were filled with nitrogen. Then, the pressure decreased and induced desorption of nitrogen. Because the last filled large mesopores were connected with a few small mesopores, the nitrogen desorption in the same large mesopores happened at a lower relative pressure compared with adsorption process, leading to the formation of a hysteresis loop.

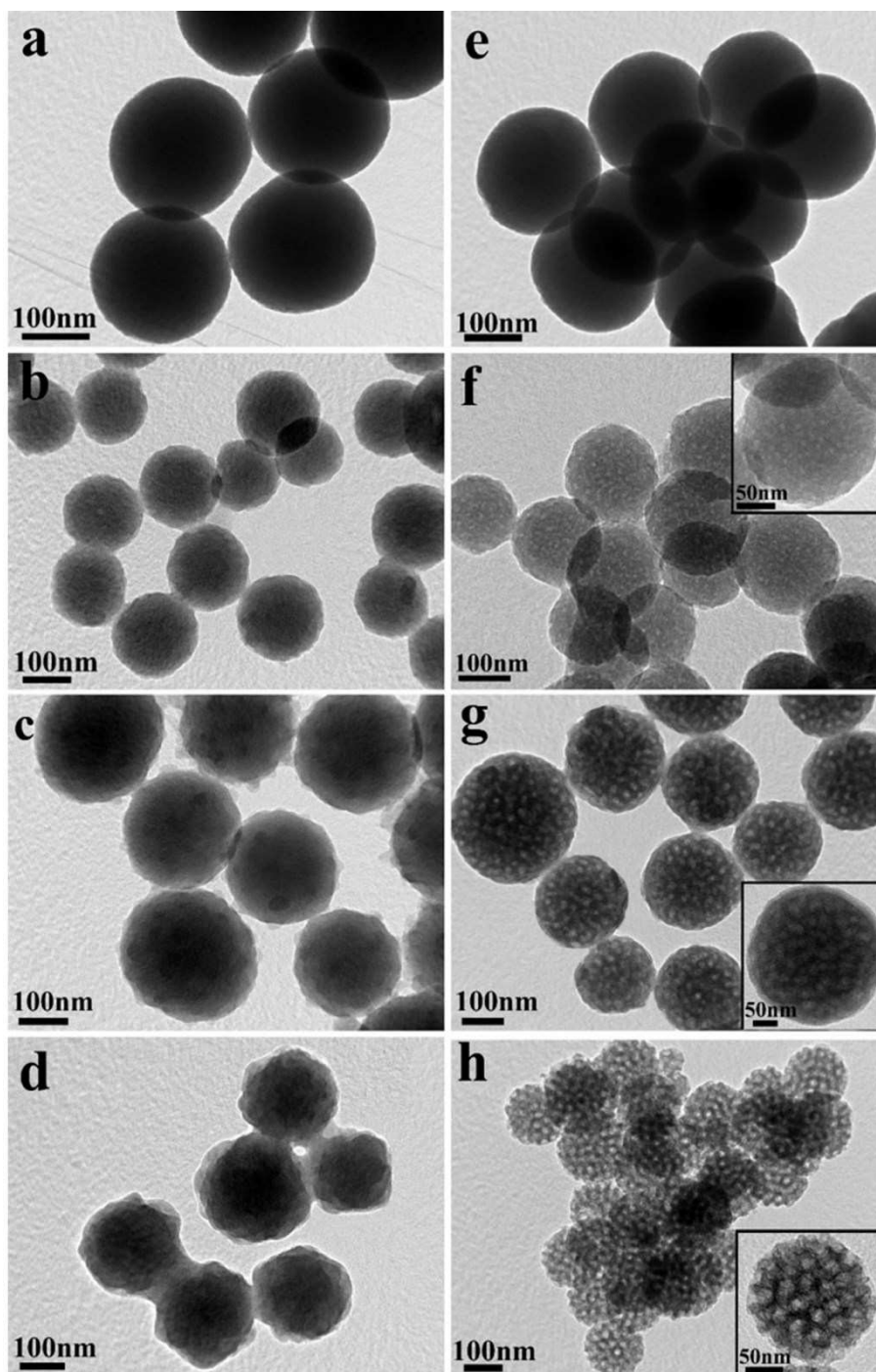


Figure 2.8 TEM images of (a) PDA spheres, (b) PDA/PS₃₇-*b*-PEO₁₁₄ composite spheres, (c) PDA/PS₁₇₈-*b*-PEO₈₈₆ composite spheres, and (d) PDA/PS₁₇₃-*b*-PEO₁₇₀ composite spheres, respectively. TEM images of the corresponding NCS and NMCS after carbonization ((e) NCS, (f) NMCS-1, (g) NMCS-2, and (h) NMCS-3). The samples before carbonization show weak contrast, because there is no large difference in the chemical compositions between the micelles and the polydopamine (PDA).

The Brunauer–Emmett–Teller (BET) surface areas, total pore volumes, and average pore sizes are summarized in **Table 2.1**. From the pore size distribution curves (**Figure 2.9B**), it is demonstrated that NMCS possess uniformly sized mesopores. The average pore size of NMCS-1 is 5.4 nm, while those of NMCS-2 and NMCS-3 are as large as 16.0 nm. These values are almost the same as those observed by SEM (**Figure 2.2f-h**).

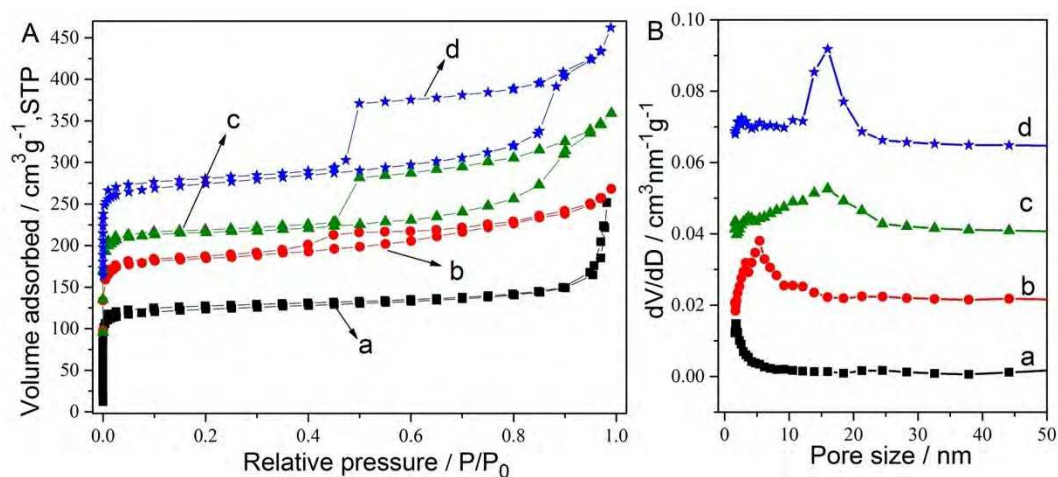


Figure 2.9 (A) N₂ adsorption–desorption isotherms and (B) pore size distribution curves of (a) NCS, (b) NMCS-1, (c) NMCS-2, and (d) NMCS-3, respectively. For clarity, the isotherms for (b), (c), and (d) are offset by 50, 50, and 150 cm³ g⁻¹, respectively. The pore size distribution curves for (b), (c), and (d) are offset vertically by 0.02, 0.04, and 0.06 cm³ nm⁻¹ g⁻¹, respectively.

Table 2.1 Physicochemical properties and average particle sizes of NMCS-1, NMCS-2 and NMCS-3 samples.

Sample	Surface area (m ² g ⁻¹)	Pore volume (cm ³ g ⁻¹)	Pore size (nm)	Particle size (nm)
NMCS-1	363	0.48	5.4	165
NMCS-2	356	0.45	16.0	201
NMCS-3	343	0.48	16.0	180

2.3.2. Formation Mechanism of NMCS

Based on the above observation, I propose the formation mechanism, as described in **Figure 2.1**. In the experimental process, PS-*b*-PEO was firstly mixed in THF solution, in which it was completely dissolved and existed as a unimer. After adding water and ethanol, the micellization process occurred, in which the Tyndall effect was clearly observed (**Figure 2.10a**). As a typical example, the SEM image of the PS₁₇₃-*b*-PEO₁₇₀ micelle solution shows the presence of the diblock polymer micelles with a diameter of ~25 nm (**Figure 2.10b**), which is corresponding to the micelles size observed in **Figure 2.4d**. After addition of DA, the DA species surrounded the micelle surface by hydrogen bonding between the catechol and the N-H groups in DA and -OH group in the PEO block.[35-37] According to a zeta-potential measurement, the DA/PS-*b*-PEO composite micelles were slightly positive charged, thereby further inducing a good dispersion of micelles (**Figure 2.10c**). The SEM image in **Figure 2.10c** also indicates the existence of well-dispersed DA/PS-*b*-PEO composite micelles. After adding ammonia solution, the polymerization reaction of DA molecules proceeds under alkaline condition.[35,36,38] During this stage, the DA/PS-*b*-PEO composite micelles are self-assembled and polymerized to form PDA/PS-*b*-PEO composite spheres, as shown in **Figure 2.1**. The PDA still strongly interacts with the PS-*b*-PEO template because of the catechols/quinone groups present in the PDA.[35,36] After 2 hours of reaction, small-sized PDA/PS-*b*-PEO composite spheres (with an average size of 185 nm) are formed (**Figure 2.11a**). With increase of the reaction time, the average particle sizes gradually grow to 378 nm (**Figure 2.11b-d**). In my approach, the PS-*b*-PEO micelles act as a sacrificial pore-forming agent during carbonization. The mesopore sizes observed on the surface of the NMCS are slightly smaller than the micelle sizes observed on the original PDA/PS-*b*-PEO composite spheres (**Figure 2.4**), due to thermal shrinkage of the pore walls.

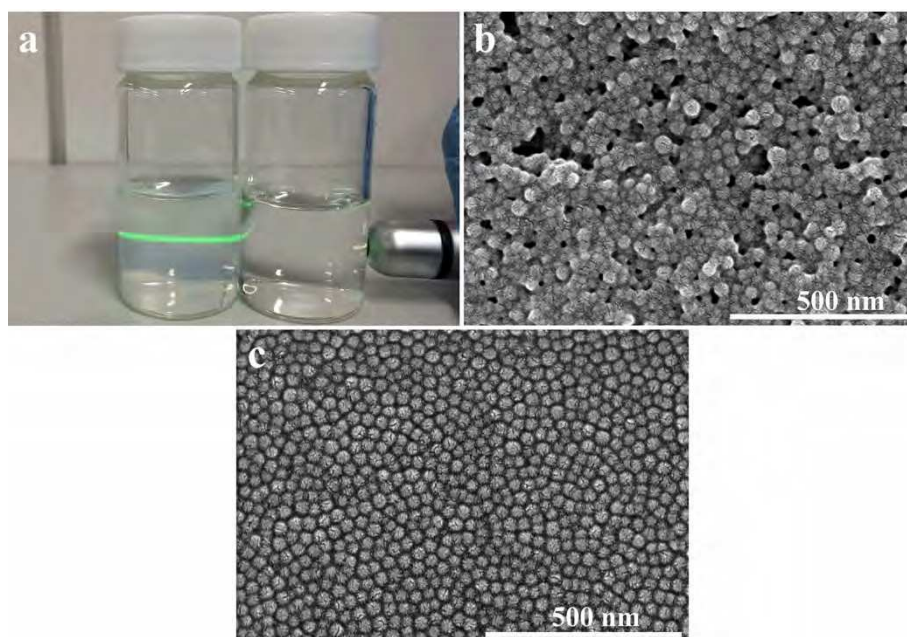


Figure 2.10 (a) Photograph of (right) transparent PS₁₇₃-*b*-PEO₁₇₀ solution dissolved in THF and (left) PS₁₇₃-*b*-PEO₁₇₀ micelle solution after adding water and ethanol. (b) SEM image of PS₁₇₃-*b*-PEO₁₇₀ micelles before adding DA and (c) SEM image of PS₁₇₃-*b*-PEO₁₇₀ micelles after adding DA.

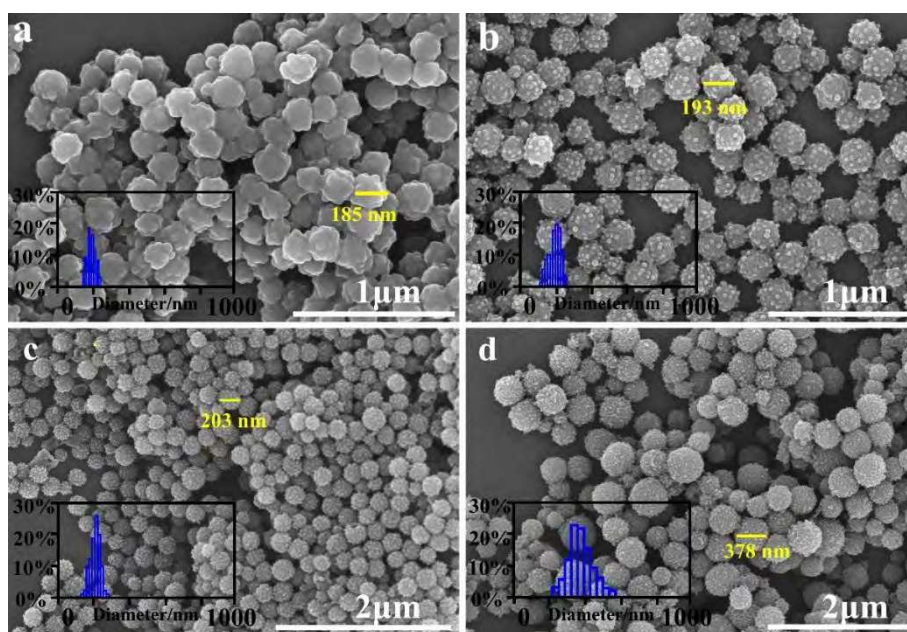


Figure 2.11 SEM images of PDA/PS₁₇₃-*b*-PEO₁₇₀ composite spheres obtained after reacting for (a) 2 hours, (b) 5 hours, (c) 20 hours, and (d) 40 hours. The inset images are the particle size distribution histograms that calculated from over 100 particles. The average particle sizes are (a) 185 nm, (b) 193 nm, (c) 203 nm, and (d) 378 nm, respectively.

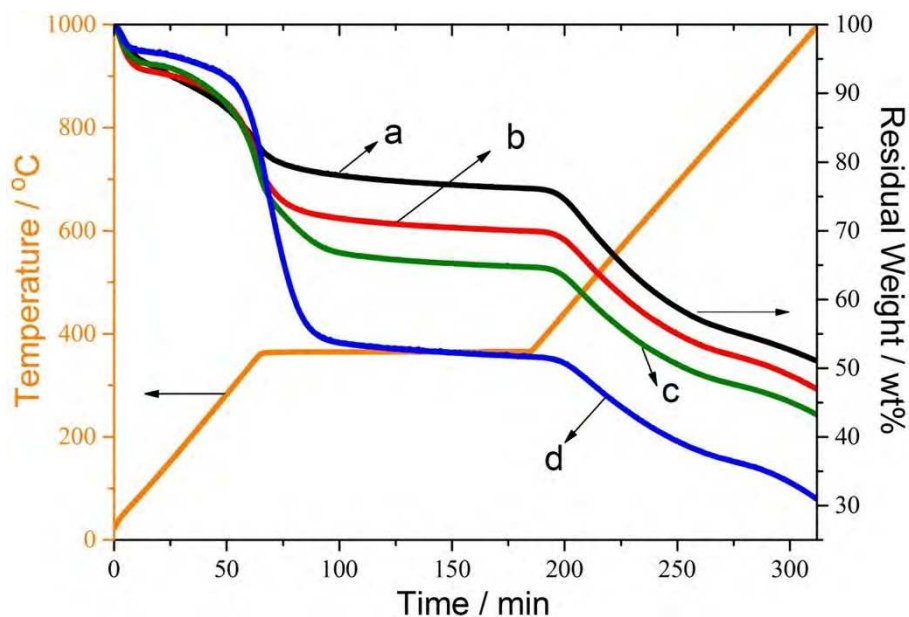


Figure 2.12 TG curves of (a) PDA spheres, (b) PDA/PS₃₇-*b*-PEO₁₁₄ composite spheres, (c) PDA/PS₁₇₈-*b*-PEO₈₈₆ composite spheres, and (d) PDA/PS₁₇₃-*b*-PEO₁₇₀ composite spheres measured under N₂ atmosphere.

Table 2.2 The remaining weight percentages of PDA spheres and PDA/PS-*b*-PEO composite spheres after keeping at 350 °C for 2 hours and at 1000 °C during thermogravimetric analysis, which are noted as W_{350%} and W_{1000%}, respectively.

Sample	W _{350%}	W _{1000%}	Δ (W _{350%} –W _{1000%})
PDA	76.2	50.9	25.3
PDA/PS ₃₇ - <i>b</i> -PEO ₁₁₄	69.8	46.9	22.9
PDA/PS ₁₇₈ - <i>b</i> -PEO ₈₈₆	64.7	43.1	21.6
PDA/PS ₁₇₃ - <i>b</i> -PEO ₁₇₀	51.5	30.8	20.7

The detailed carbonization process along with the weight loss of PDA spheres and PDA/PS-*b*-PEO composite spheres were investigated by thermogravimetric (TG) analysis (**Figure 2.12** and **Table 2.2**). The PDA spheres show a good thermal stability, in which the residues remain 76.2 % at 350 °C because of the loss of functional groups, and then illustrate a satisfied carbonization yield of 50.9 % at 1000 °C. On the other hand, the carbonization yields for PDA/PS₃₇-*b*-PEO₁₁₄, PDA/PS₁₇₈-*b*-PEO₈₈₆, and PDA/PS₁₇₃-*b*-PEO₁₇₀ composite spheres are 46.9, 43.1, and 30.8 wt%, respectively. PDA/PS-*b*-PEO composite spheres display

a larger mass decrease and less residues at 350 °C. Compared with PDA spheres, the extra weight loss of PDA/PS₃₇-*b*-PEO₁₁₄, PDA/PS₁₇₈-*b*-PEO₈₈₆, and PDA/PS₁₇₃-*b*-PEO₁₇₀ at 350 °C are 6.40, 11.5, and 24.7 wt%, respectively. Nevertheless, they illustrate similar weight loss (ca. 21 wt%) from 350 to 1000 °C (**Table 2.2**). These results suggest that the extra weight loss of PDA/PS-*b*-PEO composite spheres at 350 °C is probably due to the removal of PS-*b*-PEO micelles with different molecular weights of the PS and PEO blocks. As revealed by SEM images of PDA/PS₁₇₃-*b*-PEO₁₇₀ composite spheres carbonized from 300 to 350 °C, the micelles on the surface gradually disappear and finally they are completely removed at 350 °C (**Figure 2.13**).

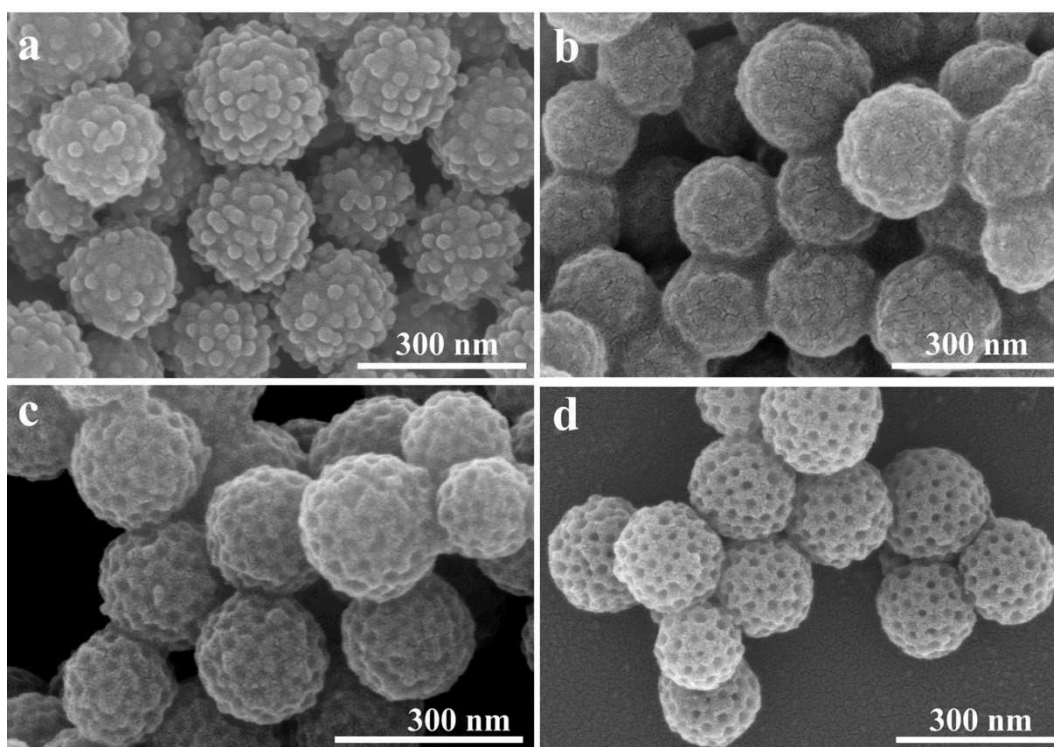


Figure 2.13 SEM images of (a) PDA/PS₁₇₃-*b*-PEO₁₇₀ composite spheres and their heated samples under N₂ atmospheres for 2 hours at different temperatures ((b) 300 °C, (c) 320 °C, and (d) 350 °C).

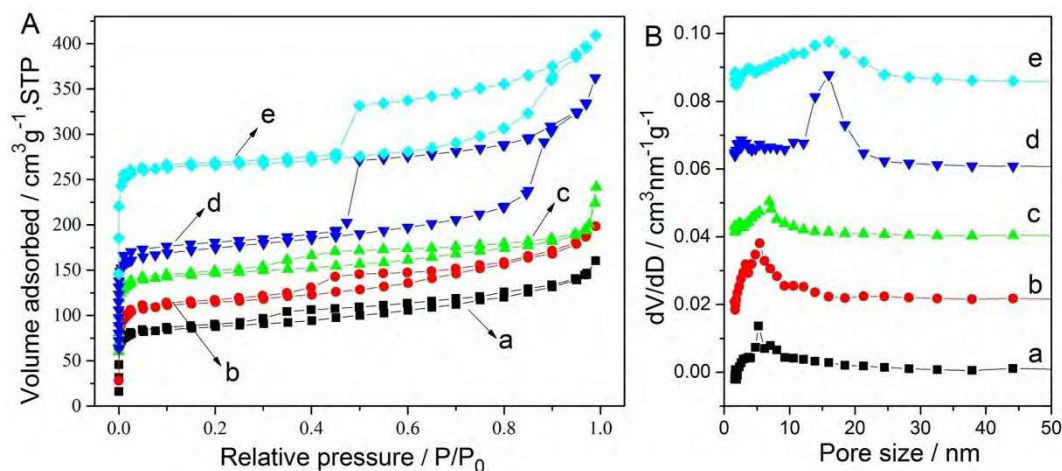


Figure 2.14 (A) N₂ adsorption–desorption isotherms, (B) pore size distribution curves of NMCS prepared from (a) PDA/PS₃₁-*b*-PEO₂₈₄ composite spheres, (b) PDA/PS₃₇-*b*-PEO₁₁₄ composite spheres, (c) PDA/PS₈₇-*b*-PEO₂₂₇ composite spheres, (d) PDA/PS₁₇₃-*b*-PEO₁₇₀ composite spheres, and (e) PDA/PS₁₇₈-*b*-PEO₈₈₆ composite spheres, respectively. For clarity, the isotherms for (c), (d), and (e) are offset by 50, 50, and 100 cm³ g⁻¹, respectively, and the pore size distribution curves for (b), (c), (d), and (e) are offset vertically by 0.02, 0.04, 0.06, and 0.08 cm³ nm⁻¹ g⁻¹, respectively.

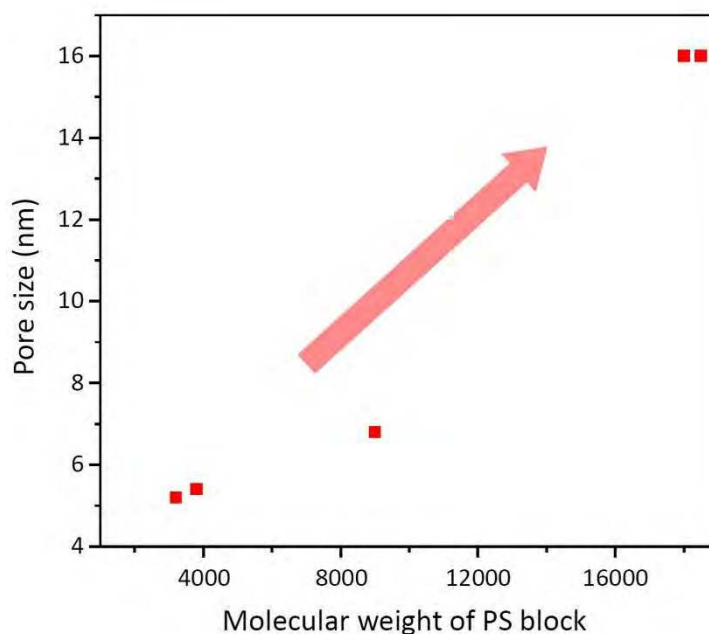


Figure 2.15 Relationship between the mesopore sizes and the molecular weights of PS block. The mesopore sizes are measured by N₂ adsorption–desorption isotherms (as shown in **Figure 2.14**).

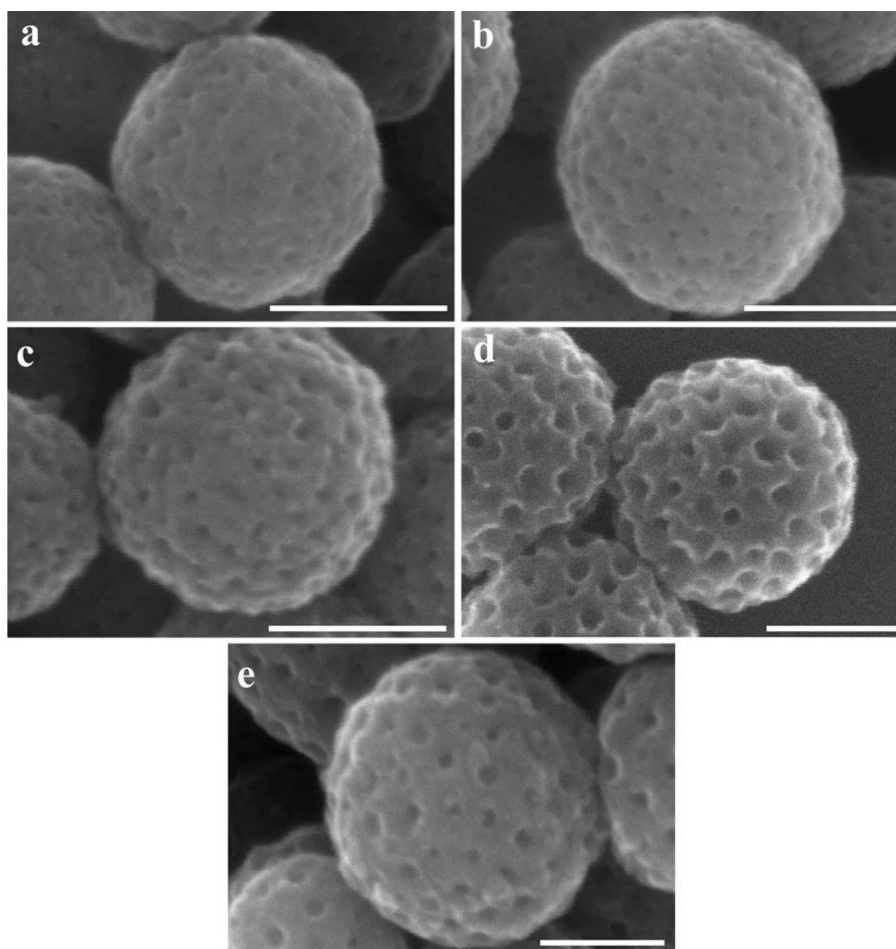


Figure 2.16 SEM images of NMCS prepared from (a) PDA/PS₃₁-*b*-PEO₂₈₄ composite spheres, (b) PDA/PS₃₇-*b*-PEO₁₁₄ composite spheres, (c) PDA/PS₈₇-*b*-PEO₂₂₇ composite spheres, (d) PDA/PS₁₇₃-*b*-PEO₁₇₀ composite spheres, and (e) PDA/PS₁₇₈-*b*-PEO₈₈₆ composite spheres, respectively. The scale bar is 100 nm.

As mentioned in **Figure 2.2**, the PS core sizes in the micelles determine the pore sizes in the obtained NMCS. In addition to NMCS-1, NMCS-2, and NMCS-3, I prepared another two kinds of NMCS using PS₃₁-*b*-PEO₂₈₄ and PS₈₇-*b*-PEO₂₂₇ as the templates. The pore sizes were determined by N₂ adsorption–desorption measurement (**Figure 2.14**). Notably, the increase of the molecular weight of the PS blocks leads to a gradual expansion of the pore sizes (**Figure 2.15 and 2.16**). In addition, the PEO blocks (i.e., shell region of micelles) are interacting with the DA and PDA, in which the PEO shell thickness basically influences the wall thickness in the NMCS. Among the used five block copolymers, PS₁₇₃-*b*-PEO₁₇₀ shows the highest weight ratio of PS/PEO. Therefore, the resulting NMCS-3 possess a relatively thin

wall thickness and the mesopores are more closely packed inside the spheres, compared to the others (**Figure 2.16**).

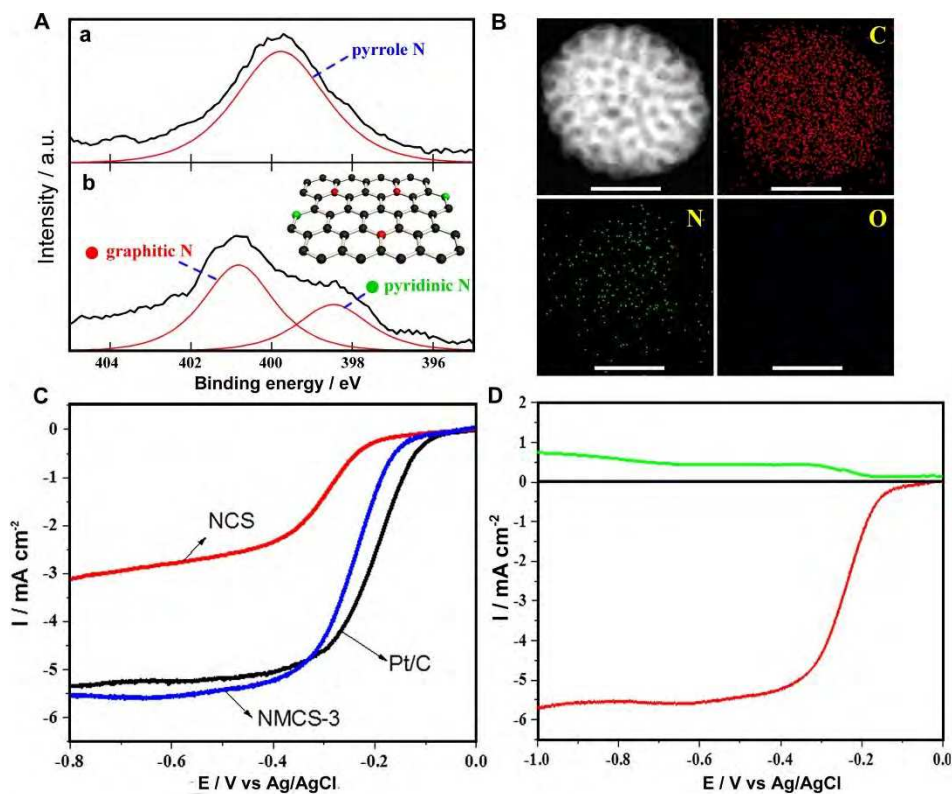


Figure 2.17 (A) The high-resolution N 1s XPS spectrum of (a) PDA/PS₁₇₃-b-PEO₁₇₀ composite spheres and (b) NMCS-3. The inset shows a schematic illustration of nitrogen atoms in NMCS-3. (B) high-angle annular dark-field scanning TEM (HAADF-STEM) image and elemental mapping of NMCS-3. The scale bar is 100 nm. (C) Polarization curves of NCS, NMCS-3, and Pt/C catalysts in O₂-saturated 0.1 M KOH solutions with a scan rate of 10 mV s⁻¹ and a rotating rate of 1600 rpm. (D) Rotating ring-disk electrode (RRDE) test of the ORR on NMCS-3 in an O₂-saturated 0.1 M KOH electrolyte at a scan rate of 10 mV s⁻¹. The rotation rate is 1600 rpm and the Pt ring electrode is poised at 1.0 V for oxidizing HO₂⁻ intermediate.

X-ray photoelectron spectroscopy (XPS) analysis was performed to determine the electric state of the N element. Both PDA/PS₁₇₃-b-PEO₁₇₀ composite spheres (before carbonization) and corresponding NMCS-3 (after carbonization) were measured, as shown in **Figure 2.17A**. The N 1s spectrum of the PDA/PS₁₇₃-b-PEO₁₇₀ composite sphere shows one

peak centered at 399.8 eV which is attributed to the pyrrole N.[39] After carbonization, the N 1s spectrum of NMCS-3 is deconvoluted into two binding energies centered at 398.4[39,40] and 400.8 eV,[41] which can be assigned to pyridinic-N and graphitic-N, respectively. Pyridinic-N, referring to the sp^2 -hybridized N atom bonded with two sp^2 -hybridized C neighbours via σ -bonds, possesses one lone-pair of electrons in the graphene plane and contributes one electron to the conjugated π system.[42] In the graphitic-N configuration, three sp^2 -hybridized N valence electrons form three σ -bonds with three sp^2 -hybridized C neighbours, one electron fills the π -orbitals, and the fifth electron enters the π^* -states of conduction band.[43] According to another report, the fifth electron is distributed in the local network of the carbon π -system, but a part of charge localizes on the graphitic-N dopant and electronically couples to its nearest C neighbours.[44] The presence of N atoms in NMCS-3 was further confirmed by the elemental mapping analysis (**Figure 2.17B**). The content of C and N in NMCS-3 detected by elemental analysis is 92.3 wt% and 7.6 wt%, respectively, which matches with the XPS data. The N content in the other NCS, NMCS-1, and NMCS-2 samples measured by elemental analysis are 7.7, 7.3, and 7.5 wt%, respectively (**Figure 2.18**). There is no large difference of the N content among the samples.

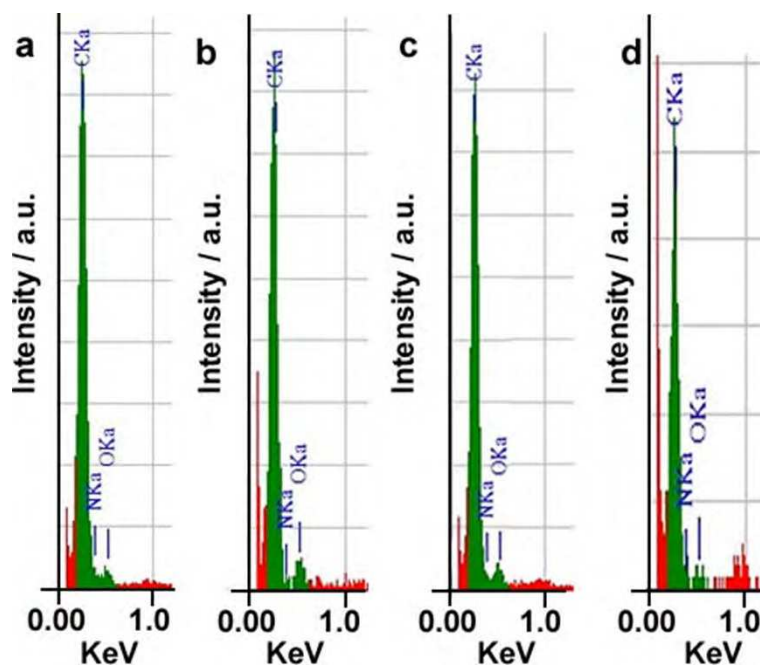


Figure 2.18 Energy dispersive X-ray (EDX) spectra of C, N, and O in (a) NCS, (b) NMCS-1, (c) NMCS-2, and (d) NMCS-3.

2.3.3. Electrocatalytic Activity of NMCS for Oxygen Reduction Reaction

Toward development of new energy system, researcher are searching for efficient nonprecious metal catalysts or metal-free catalysts as substitution of Pt for the oxygen reduction reaction which is intrinsically sluggish but important in the cathodic reaction. Doping of electron-accepting N atoms in the carbon plane, especially graphitic-N and pyridinic-N species, is critical for the ORR by imparting higher positive charge density on adjacent carbon atoms and weakening the O–O bond.[45-49] During the ORR, oxygen can be activated by direct bonding with the lone pair electrons of pyridinic-N atoms.[48] And, the graphitic-N atoms promote the ORR by electron transfer from the carbon electronic bands to the antibonding orbitals of O₂ and facilitating O₂ dissociation on the adjacent C atoms.[49] Here I evaluated the ORR activity of the NCS and NMCS samples by measuring linear-sweep voltammograms (LSVs) in O₂-saturated 0.1 M KOH solution using a rotating disk electrode (RDE). To emphasize the importance of my materials, the commercially available Pt catalyst (20 wt%) was also measured as a reference.

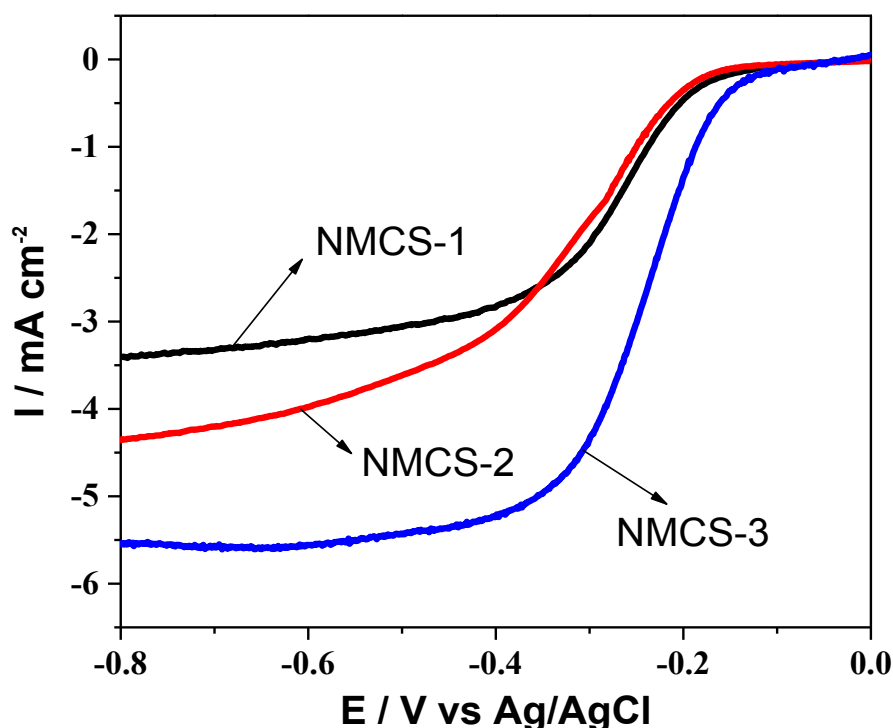


Figure 2.19 Polarization curves of NMCS-1, NMCS-2, and NMCS-3, in O₂-saturated 0.1 M KOH solutions with a scan rate of 10 mV s⁻¹ and a rotating rate of 1600 rpm.

The electrochemical activities are strongly relied on the porous structure of carbon materials. The presence of interconnected large-sized pores can accelerate the reactant diffusion in comparison with microporous carbon.[9,50-52] As shown in **Figure 2.17C and Figure 2.19**, the large-sized mesoporous NMCS-3 and NMCS-2 present higher diffusion-limited current compared with NCS with micropores and small-sized mesoporous NMCS-1. Besides, although NMCS-2 consist of large-sized mesopores, it exhibit worse ORR activity than NMCS-3 due to their lower porous density relative to NMCS-3 (**Figure 2.2g,h**). The results verify that the diffusion of oxygen, products, and electrolyte during ORR is more favourable in large-sized mesoporous structure with thin wall, leading to a higher activity in the diffusion controlled region.[9,50-53] The onset potentials of NCS, NMCS-1, NMCS-2, NMCS-3, and Pt/C are -0.15 , -0.13 , -0.12 , -0.11 , and -0.07 V, respectively, and the limiting currents are 3.14, 3.40, 4.35, 5.56, and 5.37 mA cm⁻², respectively (**Figure 2.17 C and Figure 2.19**). Clearly, NMCS with large mesopores show a more positive onset potential and a higher diffusion-limited current, compared to NCS with micropores, indicating their better electrocatalytic activity for the ORR. The improved electrochemical performance of NMCS is a result of their sufficient accessible porous architecture, which can reduce the diffusion resistance and enhance the three-phase boundary of gas, electrolyte, and solid catalyst.[50-52,54,55] Interestingly, NMCS-3 exhibit a similar diffusion-limited current for the ORR compared with Pt/C, although the onset potential is slightly negative.

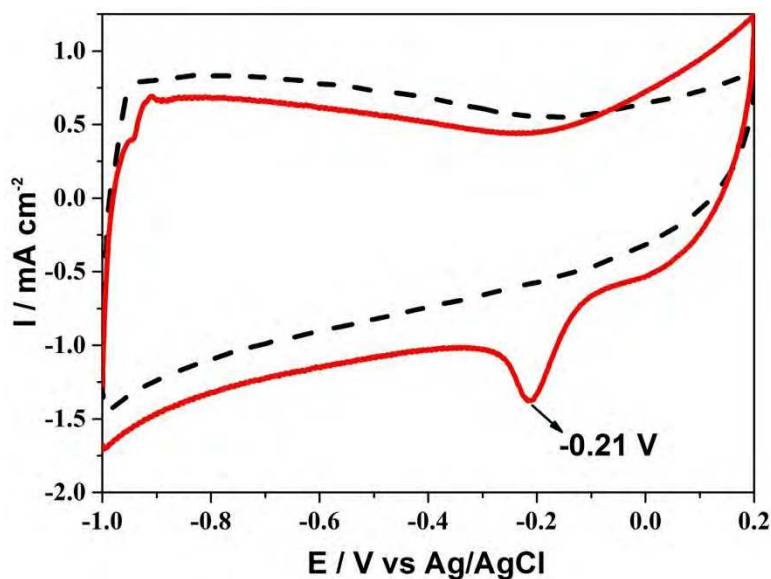


Figure 2.20 Cyclic voltammogram curves performed for NMCS-3 in N_2 - (dot line) and O_2 -saturated (solid line) 0.1 M KOH solution.

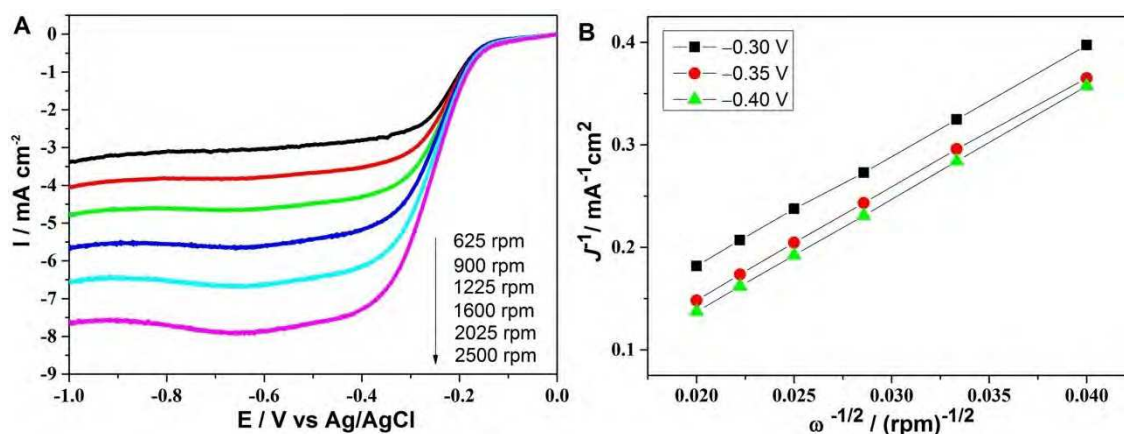


Figure 2.21 (A) Polarization curves of NMCS-3 at different rotation rates in O_2 -saturated 0.1 M KOH solutions with a scan rate of 10 mV s^{-1} . (B) The corresponding Koutecky-Levich plot of J^{-1} vs. $\omega^{-1/2}$ at different potentials.

Cyclic voltammogram curves of NMCS-3, performed in N_2 - and O_2 -saturated 0.1 M KOH solution (**Figure 2.20**), present a distinct cathodic ORR peak at -0.21 V after introducing O_2 , further demonstrating the pronounced electrocatalytic activity of NMCS-3 towards the ORR. In order to gain insight to the kinetics of ORR on NMCS-3, I conducted the RDE measurements under different rotation rates from 625 to 2500 rpm with a scan rate of 10 mV

s^{-1} . The polarization curves are shown in **Figure 2.21A**. The corresponding Koutecky-Levich plots (J^{-1} vs. $\omega^{-1/2}$) for NMCS-3 show good linearity and the slopes are almost the same at potential ranging from -0.30 to -0.40 V (**Figure 2.21B**), indicating the first-order reaction kinetics with respect to the oxygen concentration and constant electron transfer numbers for oxygen reduction at different potentials. The kinetic parameters can be analyzed on the basis of the following Koutecky-Levich equations.[52]

$$J^{-1} = J_L^{-1} + J_K^{-1} = B^{-1} \omega^{-1/2} + J_K^{-1}; B = 0.2nFC_0(D_0)^{2/3}\nu^{-1/6}$$

J is the measured current density, J_K and J_L are the kinetic- and diffusion-limiting current densities, ω is the angular velocity of the disk, n represent the overall number of electrons transferred in oxygen reduction, F is the Faraday constant ($F = 96485 \text{ C mol}^{-1}$), C_0 is the bulk concentration of O_2 , ν is the kinematic viscosity of the electrolyte, and k is the electrontransfer rate constant. The number of electrons transferred (n) can be obtained from the slope of the Koutecky-Levich plots. The constant is 0.2, when the rotating speed is in rpm. The electron transfer number involved in NMCS-3 for the ORR was estimated to be 3.4 from the slope of the Koutecky–Levich plots (**Figure 2.21B**)

To obtain in-depth understanding on the ORR process, a rotating ring-disk electrode (RRDE) test was also measured (**Figure 2.17D**). The corresponding amperometric current (upper curve) for the oxidation of hydrogen peroxide ions (HO_2^-) was recorded at the Pt ring electrode, which is effective to monitor the formation of intermediate peroxide species. The electron transfer number (n) per oxygen molecule involved in the ORR was calculated from RRDE voltammograms according to the following equation.[56]

$$n=4 \times I_D/(I_D+I_R/N)$$

where I_D is the disk current, I_R is the ring current, and $N = 0.37$ is the collection efficiency of Pt ring. The transferred electron number (n) was estimated to be 3.26 for the NMCS-3 electrode (at the potential of -0.40 V vs. Ag/AgCl). It corresponds to a mixed two-step two-electron reactions (37 %) via formation of HO_2^- intermediate and a fast direct four-electron reaction (63 %). The results indicate that the ORR using NMCS-3 involves both two-electron and four-electron reactions, which is common in N-doped metal-free carbon materials.[45, 52, 56] The

durability of the catalyst is another major concern in fuel-cell technology. I further investigated the stability of NMCS-3 and Pt/C by using the $i-t$ chronoamperometric measurement at a constant voltage of -0.6 V in O_2 -saturated 0.1 M KOH with rotation rate of 1600 rpm. Both the catalysts display a high transient current which fast degrades within the first 10 s. Then, NMCS-3 present less current loss (84%) at steady state than Pt/C (76%). Thus, it is proved that the durability of NMCS-3 is superior to that of the Pt/C catalyst.

In addition, I investigated the effect of the carbonization temperature on ORR activity. For this purpose, I carbonized the representative NMCS-3 at various temperatures from 700 to 1000 °C and investigated their physicochemical properties by N_2 adsorption–desorption isotherms (**Figure 2.22**), Raman spectra (**Figure 2.23**), EDX spectra (**Figure 2.24**), and XPS spectra (**Figure 2.25**). The physicochemical properties and element composition changes in NMCS-3 are concluded in **Table 2.3** and **Figure 2.26**. After increasing the carbonization temperature from 700 to 1000 °C, the specific surface areas and the pore volumes of NMCS-3 are gradually increased, due to the generation of microporous structures (**Table 2.3**). As seen in **Figure 2.22A**, initial N_2 uptakes at low pressure region (< 0.1) become clear with increase of the temperature. Even after 1000 °C, NMCS well preserve the large-sized mesopores without any distortion/collapse of mesopores, as also confirmed by **Figure 2.7**. Raman spectra of NMCS-3 carbonized at various temperatures (from 700 to 1000 °C) show two broad bands located at 1350 and 1593 cm^{-1} (**Figure 2.23**). The ratios of peak intensity (I_G/I_D) are gradually increased at a higher temperature, indicating the improvement in graphitic degree of the pore walls. The N content in the NMCS-3 roughly estimated by EDX measurement gradually decreases from 8.9 wt% to 3.4 wt% (**Figure 2.24**). As detected by XPS measurement (**Figure 2.25**), the N $1s$ spectra of NMCS-3 can be fitted into two binding energies centered at 398.4 and 400.8 eV, which are assignable to pyridinic-N and graphitic-N, respectively. The ratio of graphitic-N to pyridinic-N in NMCS-3 distinctly increases from 60.0% to 93.6% after increasing the carbonization temperature from 700 to 1000 °C.

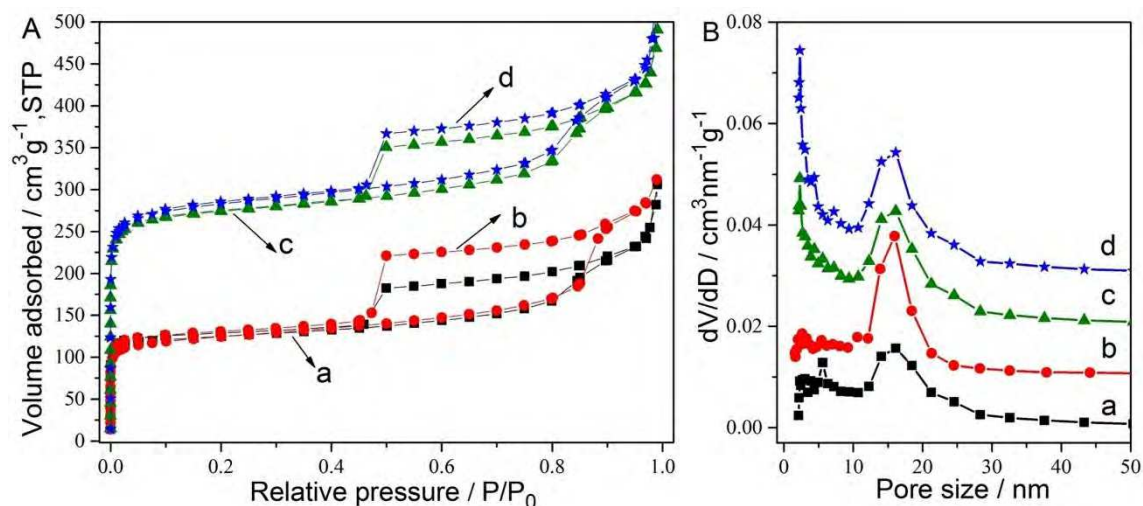


Figure 2.22 (A) N_2 adsorption–desorption isotherms and (B) pore size distribution curves of NMCS-3 after carbonization at various temperatures of (a) 700 °C, (b) 800 °C, (c) 900 °C, and (d) 1000 °C. For clarity, the pore size distribution curves for 800 °C, 900 °C, and 1000 °C are offset vertically by 0.01, 0.02, and 0.03 $\text{cm}^3 \text{nm}^{-1} \text{g}^{-1}$, respectively.

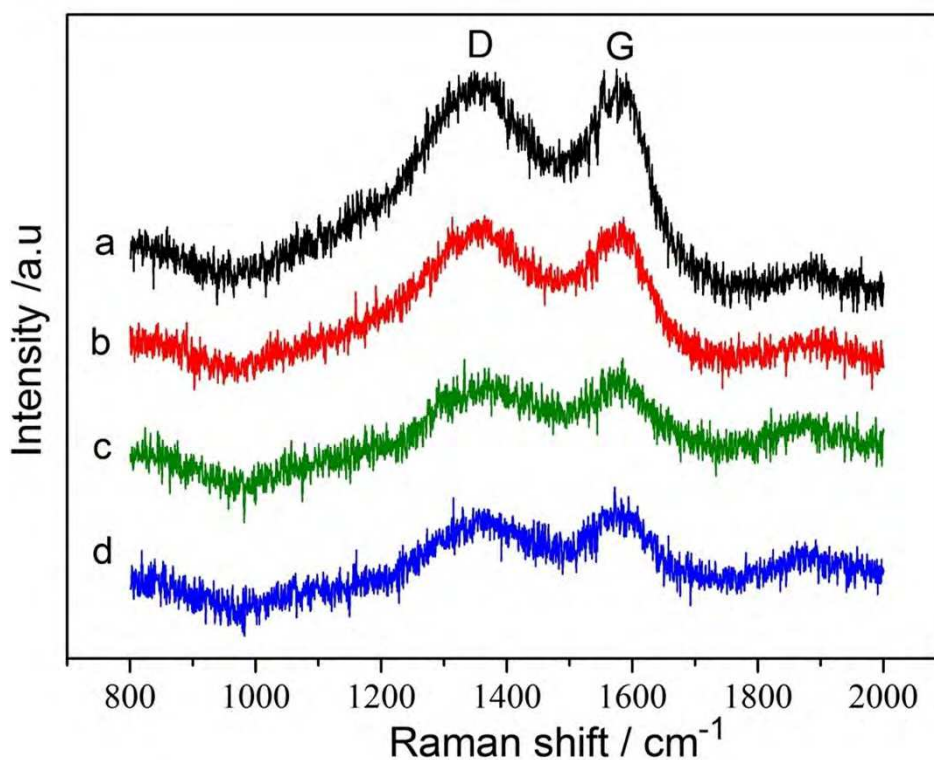


Figure 2.23 Raman spectra of NMCS-3 after carbonization at different temperatures of (a) 700 °C, (b) 800 °C, (c) 900 °C, and (d) 1000 °C under N_2 atmospheres.

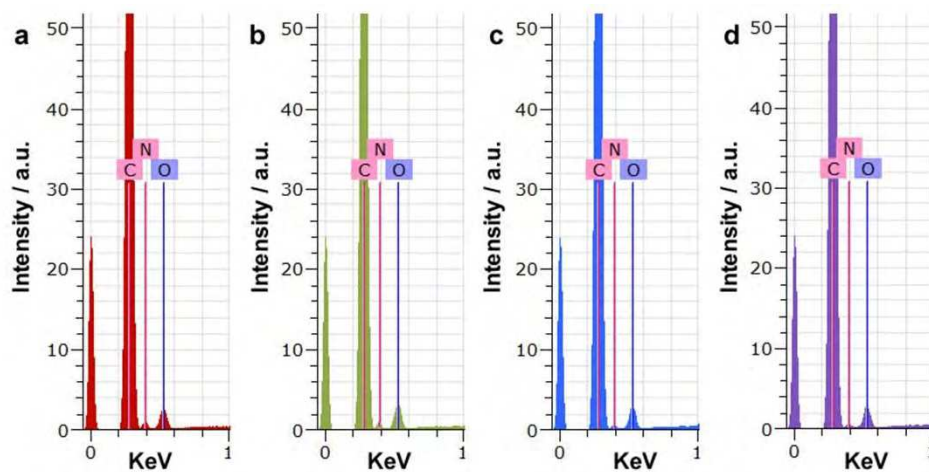


Figure 2.24 Energy dispersive X-ray (EDX) spectra of C, N, and O of NMCS-3 after carbonized under N_2 atmospheres at different temperatures of (a) 700 °C, (b) 800 °C, (c) 900 °C, and (d) 1000 °C.

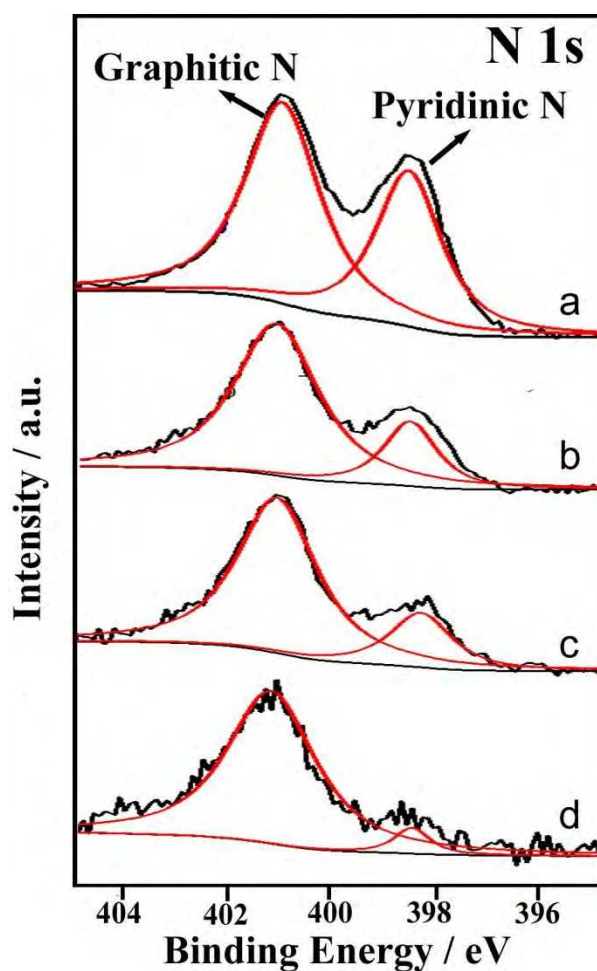


Figure 2.25 N 1s XPS spectra of NMCS-3 after carbonization at different temperatures of (a) 700 °C, (b) 800 °C, (c) 900 °C, and (d) 1000 °C.

Table 2.3 Physicochemical properties and element compositions of NMCS-3 after carbonization at various temperatures (700, 800, 900, and 1000 °C).

Carbonization temperature (°C)	Surface area (m ² g ⁻¹)	Pore volume (cm ³ g ⁻¹)	Pore size (nm)	I_G/I_D	N content (wt%)	Relative ratios of graphitic-N : pyridinic-N
700	336	0.46	16.0	0.98	8.9	60.0 : 40.0
800	343	0.48	16.0	1.00	7.6	77.6 : 22.4
900	724	0.75	16.0	1.02	5.3	78.9 : 21.1
1000	759	0.80	16.0	1.03	3.4	93.6 : 6.40

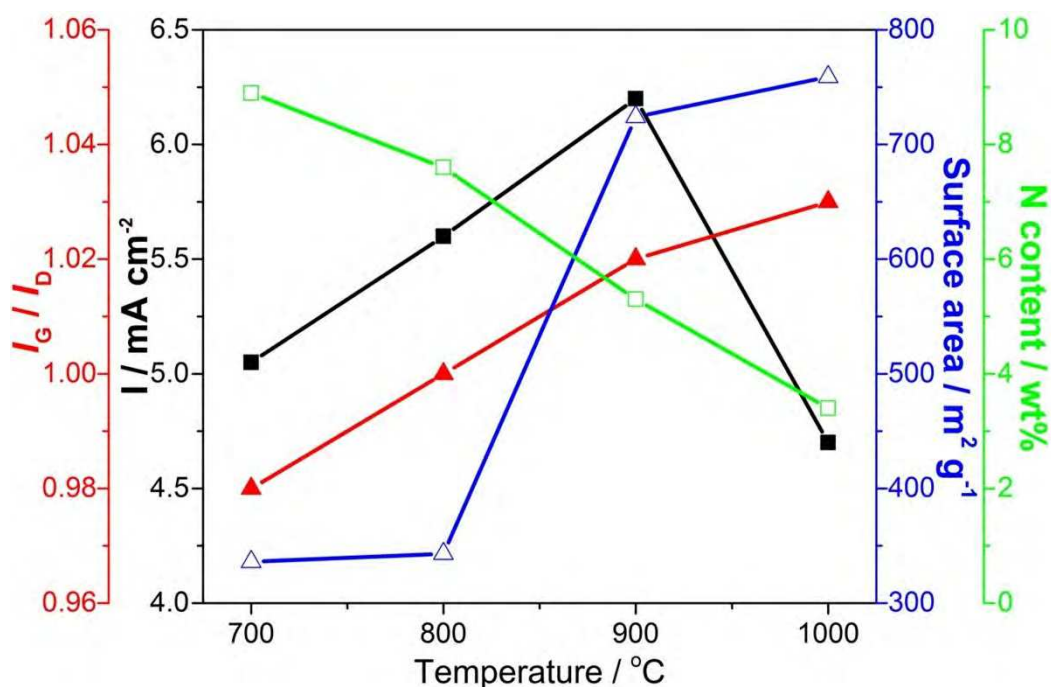


Figure 2.26 Current density (I), graphitization degree (I_G/I_D), surface area, and N content of NMCS-3 after carbonization at various temperatures (700, 800, 900, and 1000 °C).

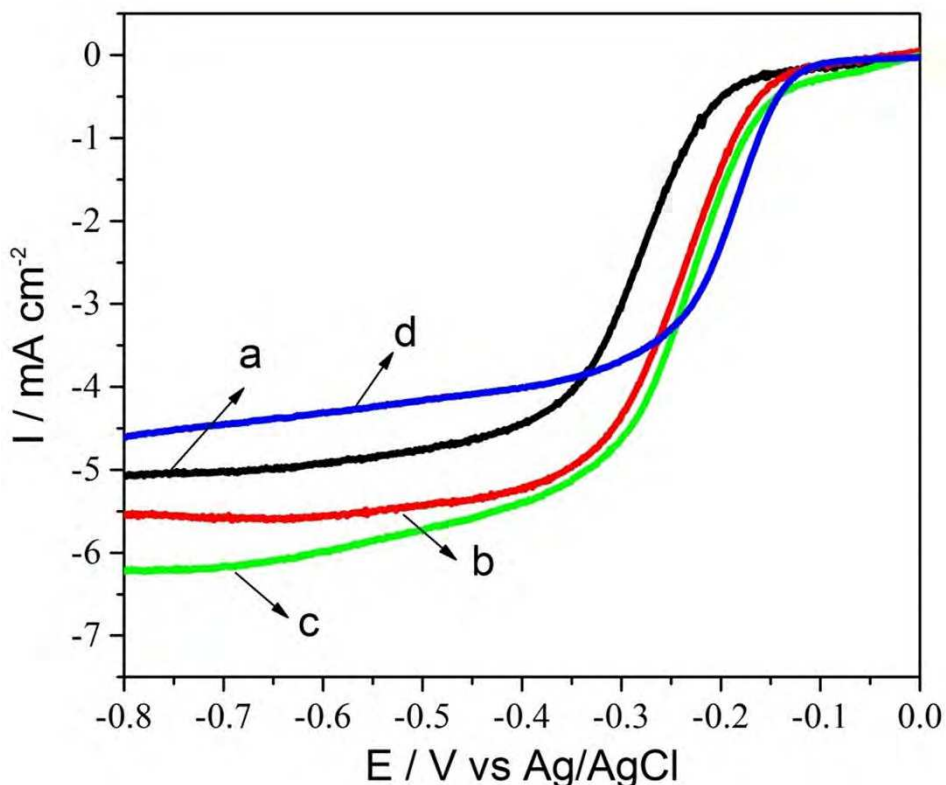


Figure 2.27 Polarization curves of NMCS-3 after carbonization at different temperatures of (a) 700 °C, (b) 800 °C, (c) 900 °C, and (d) 1000 °C under N_2 atmospheres in O_2 -saturated 0.1 M KOH solutions with a scan rate of 10 mV s^{-1} and a rotating rate of 1600 rpm.

The ORR activities of NMCS-3 carbonized at different temperatures (700 °C, 800 °C, 900 °C, and 1000 °C) were investigated. The linear-sweep voltammograms (LSVs) were performed in O_2 -saturated 0.1 M KOH solution by using rotating disk electrode (RDE). It has been generally known that the ORR activity is closely related to comprehensive physical and chemical properties of N-doped carbon materials. Thus, several factors, including graphitization degree, specific surface area, and N species as electrochemical active sites, should be taken into consideration.[46,57,58]

As seen in **Figure 2.27**, it is clear that NMCS-3 carbonized at 700 °C show the most negative onset potential among all the samples and exhibit lower diffusion-limited current compared with NMCS-3 carbonized at 800 and 900 °C. The relative poor ORR activity of NMCS-3 carbonized at 700 °C is probably due to its low graphitization degree, which largely

limits the electron conductivity and weakens the interaction between carbon and electrochemical active N sites in despite of the high N content (**Figure 2.26**).

When the carbonization temperature is higher than 700 °C, the onset potentials are similar. Especially, NMCS-3 carbonized at 900 °C exhibit the highest electrocatalytic activity for ORR, realizing the maximum current density. The current densities of NMCS-3 carbonized at 800, 900, and 1000 °C present the order of 900 °C (6.2 mA cm⁻²) > 800 °C (5.6 mA cm⁻²) > 1000 °C (4.6 mA cm⁻²). Considering the overall physicochemical properties and element compositions in NMCS-3 (as shown in **Table 2.3 and Figure 2.26**), my results highlight the balance among graphitization degree, specific surface area, and electrochemically active N species is critically important for realizing the best ORR activity.

As shown in **Table 2.3 and Figure 2.26**, although the N content in NMCS-3 carbonized at 900 °C decrease in comparison with NMCS-3 carbonized at 800 °C, the ratios of different active N species (graphitic-N to pyridinic-N, which have different functions during ORR[45-49]) are almost the same. More importantly, NMCS-3 carbonized at 900 °C possess a higher graphitization degree and also around twice higher specific surface area in comparison with NMCS-3 carbonized at 800 °C, which greatly contribute to facile electron and mass transportation during ORR, leading to an enhanced current density.[46,57,58] When the temperature further increases up to 1000 °C, the graphitization degree and the specific surface area of NMCS-3 are slightly increased, but the amount of N species, especially ORR-active pyridinic-N, are seriously decreased. This is the reason for the decrease of current density from 900 to 1000 °C. As a result, I can conclude that NMCS-3 carbonized at 900 °C exhibit the best catalytic activity for ORR with more positive onset potential and highest current density, due to its balance between the graphitization degree, specific surface area, and electrochemically active N species,[46,47] as shown in **Table 2.3 and Figure 2.26**. Compared with other metal-free carbon-based materials (**Table 2.4**), NMCS-3 have become one of the most active metal-free N-doped carbon catalysts towards ORR.[21,52,53,59-61]

Table 2.4 Comparison of catalytic activity of NMCS-3 towards ORR with other metal-free carbon-based materials.

Reference	Material	Onset potential (V vs. Ag/AgCl)	Cathodic ORR peak (V vs. Ag/AgCl)	Max. current density (mA cm ⁻²)	Scan rate (mV s ⁻¹)	Rotation rate (rpm)
This study	N-doped mesoporous carbon sphere (NMCS)	-0.11	-0.21	6.2	10	1600
Angew. Chem. Int. Ed. 2010, 49, 2565.	N-doped ordered mesoporous graphitic array	-0.13	-0.26	5.9	10	1600
Angew. Chem. Int. Ed. 2012, 51, 3892.	Ordered macroporous graphitic C ₃ N ₄ /carbon composite	-0.14	-0.30	4.8	5	1500
J. Am. Chem. Soc. 2012, 134, 16127.	P-doped ordered mesoporous carbon	-0.11	-0.23	5.1	10	1600
Adv. Mater. 2013, 25, 998.	N-doped carbon sub-micrometer sphere	-0.10	-0.22	5.8	10	1600
Adv. Mater. 2013, 25, 3192.	N-doped graphene/CNT nanocomposite	-0.10	----	3.3	20	1600
ACS Appl. Mater. Interfaces 2014, 6, 4214.	N-doped graphene nanoribbon	-0.10	-0.21	3.6	10	1600
Electrochimica Acta 2014, 129, 196.	N-doped graphitic carbon cage	-0.05	-0.25	4.1	10	1600

2.4. Conclusion

In conclusion, my present synthesis is based on co-assembly of diblock polymer PS-*b*-PEO micelles and nontoxic DA as the carbon and nitrogen sources. The use of DA offers a simple route for in situ introducing heteroatoms with high content into carbon materials. To the best of my knowledge, there have been no reports on highly N-doped mesoporous carbon spheres with extra-large mesopores (up to 16 nm). Both large-sized mesopores and high N-doping are very effective for acceleration of the ORR. My NMCS realize high electrocatalytic activity and excellent long-term stability towards the ORR, even comparable to the Pt/C catalyst. These results shed light on the synthesis of mesoporous carbon spheres for various applications in the emerging field. By further optimization of porous architectures and compositions, I can expect to realize promising materials as cathode electrode.[62] Moreover, by selecting other carbon sources which effectively interact with the micelle surface, various large-sized mesoporous carbons with different heteroatoms are expected for improving the capacitance,[28] surface polarity, and basic sites.[63]

References

- [1] C. D. Liang, Z. J. Li, S. Dai, *Angew. Chem. Int. Ed.*, 2008, **47**, 3696; *Angew. Chem.*, 2008, **120**, 3754.
- [2] Z. X. Wu, W. D. Wu, W. J. Liu, C. Selomulya, X. D. Chen, D. Y. Zhao, *Angew. Chem. Int. Ed.*, 2013, **52**, 13764; *Angew. Chem.*, 2013, **125**, 14009.
- [3] W. Luo, B. Wang, C. G. Heron, M. J. Allen, J. Morre, C. S. Maier, W. F. Stickle, X. L. Ji, *Nano Lett.*, 2014, **14**, 2225.
- [4] T. Y. Ma, J. R. Ran, S. Dai, M. Jaroniec, S. Z. Qiao, *Angew. Chem. Int. Ed.*, 2014, **53**, 7281; *Angew. Chem.*, 2014, **126**, 7409.
- [5] Y. Zheng, Y. Jiao, L. H. Li, X. Tan, Y. Chen, M. Jaroniec, S. Z. Qiao, *ACS Nano*, 2014, **8**, 5290.
- [6] Z. Y. Jin, A. H. Lu, Y. Y. Xu, J. T. Zhang, W. C. Li, *Adv. Mater.*, 2014, **26**, 3700.
- [7] S. H. Joo, S. J. Choi, I. Oh, J. Kwak, Z. Lin, O. Terasaki, R. Ryoo, *Nature*, 2001, **412**, 169.

- [8] J. H. Bang, K. Han, S. E. Skrabalak, H. Kim, K. S. Suslick, *J. Phys. Chem. C*, 2007, **111**, 10959.
- [9] H. D. Du, L. Gan, B. H. Li, P. Wu, Y. L. Qiu, F. Y. Kang, R. W. Fu, Y. Q. Zeng, *J. Phys. Chem. C*, 2007, **111**, 2040.
- [10] J. Tang, J. Liu, N. L. Torad, T. Kimura, Y. Yamauchi, *Nano Today*, 2014, **9**, 305.
- [11] J. Liu, T. Y. Yang, D. W. Wang, G. Q. Lu, D. Y. Zhao, S. Z. Qiao, *Nat. Commun.*, 2013, **4**, 2798.
- [12] X. Sun, Y. D. Li, *Angew. Chem. Int. Ed.*, 2004, **43**, 597; *Angew. Chem.*, 2004, **116**, 607.
- [13] A. H. Lu, G. P. Hao, Q. Sun, *Angew. Chem. Int. Ed.*, 2011, **50**, 9023; *Angew. Chem.*, 2011, **123**, 9187.
- [14] A. H. Lu, T. Sun, W. C. Li, Q. Sun, F. Han, D. H. Liu, Y. Guo, *Angew. Chem. Int. Ed.*, 2011, **50**, 11765; *Angew. Chem.*, 2011, **123**, 11969.
- [15] Z. A. Qiao, B. K. Guo, A. J. Binder, J. H. Chen, G. M. Veith, S. Dai, *Nano Lett.*, 2013, **13**, 207.
- [16] N. P. Wickramaratne, J. T. Xu, M. Wang, L. Zhu, L. M. Dai, M. Jaroniec, *Chem. Mater.*, 2014, **26**, 2820.
- [17] Y. Fang, G. F. Zheng, J. P. Yang, H. S. Tang, Y. F. Zhang, B. Kong, Y. Y. Lv, C. J. Xu, A. M. Asiri, J. Zi, F. Zhang, D. Y. Zhao, *Angew. Chem. Int. Ed.*, 2014, **53**, 5366; *Angew. Chem.*, 2014, **126**, 5470.
- [18] S. Wang, W. C. Li, G. P. Hao, Y. Hao, Q. Sun, X. Q. Zhang, A. H. Lu, *J. Am. Chem. Soc.*, 2011, **133**, 15304.
- [19] J. Liu, S. Z. Qiao, H. Liu, J. Chen, A. Orpe, D. Y. Zhao, G. Q. Lu, *Angew. Chem. Int. Ed.*, 2011, **50**, 5947; *Angew. Chem.*, 2011, **123**, 6069.
- [20] J. Choma, D. Jamiola, K. Augustynek, M. Marszewski, M. Gao, M. Jaroniec, *J. Mater. Chem.*, 2012, **22**, 12636.
- [21] K. Ai, Y. L. Liu, C. P. Ruan, L. H. Lu, G. Q. Lu, *Adv. Mater.*, 2013, **25**, 998.
- [22] Y. Fang, D. Gu, Y. Zou, Z. X. Wu, F. Y. Li, R. C. Che, Y. H. Deng, B. Tu, D. Y. Zhao, *Angew. Chem. Int. Ed.*, 2010, **49**, 7987; *Angew. Chem.*, 2010, **122**, 8159.

- [23] C. Liang, K. Hong, G. A. Guiochon, J. M. Mays, S. Dai, *Angew. Chem. Int. Ed.*, 2004, **43**, 5785; *Angew. Chem.*, 2004, **116**, 5909.
- [24] Y. H. Deng, J. Wei, Z. K. Sun, D. Y. Zhao, *Chem. Soc. Rev.*, 2013, **42**, 4054.
- [25] Y. H. Deng, C. Liu, D. Gu, T. Yu, B. Tu, D. Y. Zhao, *J. Mater. Chem.*, 2008, **18**, 91.
- [26] H. I. Lee, J. H. Kim, D. J. You, J. E. Lee, J. M. Kim, W. S. Ahn, C. Pak, S. H. Joo, H. Chang, D. Seung, *Adv. Mater.*, 2008, **20**, 757.
- [27] R. Liu, S. M. Mahurin, C. Li, R. R. Unocic, J. C. Idrobo, H. Gao, S. J. Pennycook, S. Dai, *Angew. Chem. Int. Ed.*, 2011, **50**, 6799; *Angew. Chem.*, 2011, **123**, 6931.
- [28] F. W. Ma, H. Zhao, L. P. Sun, Q. Li, L. H. Huo, T. Xia, S. Gao, G. S. Pang, Z. Shi, S. H. Feng, *J. Mater. Chem.*, 2012, **22**, 13464.
- [29] J. Sun, J. Zhang, M. Zhang, M. Antonietti, X. Fu, X. Wang, *Nat. Commun.*, 2012, **3**, 1139.
- [30] J. Yan, L. Yang, M. F. Lin, J. Ma, X. Lu, P. S. Lee, *Small*, 2013, **9**, 596.
- [31] X. H. Li, M. Antonietti, *Angew. Chem. Int. Ed.*, 2013, **52**, 4572; *Angew. Chem.*, 2013, **125**, 4670.
- [32] T. Wang, C. X. Zhang, X. Sun, Y. X. Guo, H. Guo, J. Tang, H. R. Xue, M. Z. Liu, X. X. Zhang, L. Zhu, Q. Q. Xie, J. P. He, *J. Power Sources*, 2012, **212**, 1.
- [33] Z. W. Liu, F. Peng, H. J. Wang, H. Yu, W. X. Zheng, J. Yang, *Angew. Chem. Int. Ed.*, 2011, **50**, 3257; *Angew. Chem.*, 2011, **123**, 3315.
- [34] Y. Q. Chang, F. Hong, C. X. He, Q. L. Zhang, J. H. Liu, *Adv. Mater.*, 2013, **25**, 4794.
- [35] H. Lee, S. M. Dellatore, W. M. Miller, P. B. Messersmith, *Science*, 2007, **318**, 426.
- [36] S. Hong, Y. S. Na, S. Choi, I. T. Song, W. Y. Kim, H. Lee, *Adv. Funct. Mater.*, 2012, **22**, 4711.
- [37] F. Q. Zhang, Y. Meng, D. Gu, Y. Yan, C. Z. Yu, B. Tu, D. Y. Zhao, *J. Am. Chem. Soc.*, 2005, **127**, 13508.
- [38] R. J. Li, K. Parvez, F. Hinkel, X. L. Feng, K. Müllen, *Angew. Chem. Int. Ed.*, 2013, **52**, 5535; *Angew. Chem.*, 2013, **125**, 5645.
- [39] E. Raymundo-Piñero, D. Cazorla-Amorós, A. Linares-Solano, J. Find, U. Wild, R. Schlögl, *Carbon*, 2002, **40**, 597.

- [40] M. C. Huang, H. S. Teng, *Carbon*, 2003, **41**, 951.
- [41] C. Weidenthaler, A. H. Lu, W. Schmidt, F. Schüth, *Microporous Mesoporous Mater.*, 2006, **88**, 238.
- [42] L. Lai, J. R. Potts, D. Zhan, L. Wang, C. K. Poh, C. Tang, H. Gong, Z. Shen, J. Lin, R. S. Ruoff, *Energy Environ. Sci.*, 2012, **5**, 7936.
- [43] D. Usachov, O. Vilkov, A. Grüneis, D. Haberer, A. Fedorov, V. K. Adamchuk, A. B. Preobrajenski, P. Dudin, A. Barinov, M. Oehzelt, C. Laubschat, D. V. Vyalikh, *Nano Lett.*, 2011, **11**, 5401.
- [44] T. Schiros, D. Nordlund, L. Pálová, D. Prezzi, L. Zhao, K. S. Kim, U. Wurstbauer, C. Gutiérrez, D. Delongchamp, C. Jaye, D. Fischer, H. Ogasawara, L. G. M. Pettersson, D. R. Reichman, P. Kim, M. S. Hybertsen, A. N. Pasupathy, *Nano Lett.*, 2012, **12**, 4025.
- [45] K. P. Gong, F. Du, Z. H. Xia, M. Durstock, L. M. Dai, *Science*, 2009, **323**, 760.
- [46] R. L. Liu, D. Q. Wu, X. L. Feng, K. Müllen, *Angew. Chem. Int. Ed.*, 2010, **49**, 2565; *Angew. Chem.*, 2010, **122**, 2619.
- [47] D. Guo, R. Shibuya, C. Akiba, S. Saji, T. Kondo, J. Nakamura, *Science*, 2016, **351**, 361.
- [48] D. H. Deng, X. L. Pan, L. A. Yu, Y. Cui, Y. P. Jiang, J. Qi, W. X. Li, Q. A. Fu, X. C. Ma, Q. K. Xue, G. Q. Sun, X. H. Bao, *Chem. Mater.*, 2011, **23**, 1188.
- [49] P. Wang, Z. K. Wang, L. X. Jia, Z. L. Xiao, *Phys. Chem. Chem. Phys.*, 2009, **11**, 2730.
- [50] G. S. Chai, I. S. Shin, J. S. Yu, *Adv. Mater.*, 2004, **16**, 2057.
- [51] B. Z. Fang, J. H. Kim, C. Lee, J. S. Yu, *J. Phys. Chem. C*, 2008, **112**, 639.
- [52] J. Liang, Y. Zheng, J. Chen, J. Liu, D. Hulicova-Jurcakova, M. Jaroniec, S. Z. Qiao, *Angew. Chem. Int. Ed.*, 2012, **51**, 3892; *Angew. Chem.*, 2012, **124**, 3958.
- [53] D. S. Yang, D. Bhattacharjya, S. Inamdar, J. Park, J. S. Yu, *J. Am. Chem. Soc.*, 2012, **134**, 16127.
- [54] S. An, J. H. Park, C. H. Shin, J. Joo, E. Ramasamy, J. Hwang, J. Lee, *Carbon*, 2011, **49**, 1108.
- [55] B. Z. Fang, J. H. Kim, M. Kim, J. S. Yu, *Chem. Mater.*, 2009, **21**, 789.
- [56] Y. Jiao, Y. Zheng, M. Jaroniec, S. Z. Qiao, *J. Am. Chem. Soc.*, 2014, **136**, 4394.

- [57] P. Pachfule, V. M. Dhavale, S. Kandambeth, S. Kurungot, R. Banerjee, *Chem. Eur. J.*, 2013, **19**, 974.
- [58] J. Tang, T. Wang, X. C. Pan, X. Sun, X. L. Fan, Y. X. Guo, H. R. Xue, J. P. He, *J. Phys. Chem. C*, 2013, **117**, 16896.
- [59] P. Chen, T. Y. Xiao, Y. H. Qian, S. S. Li, S. H. Yu, *Adv. Mater.*, 2013, **25**, 3192.
- [60] M. K. Liu, Y. F. Song, S. X. He, W. W. Tjiu, J. S. Pan, Y. Y. Xia, T. X. Liu, *ACS Appl. Mater. Interfaces*, 2014, **6**, 4214.
- [61] J. Yan, H. Meng, W. D. Yu, X. L. Yuan, W. R. Lin, W. P. Ouyang, D. S. Yuan, *Electrochim. Acta*, 2014, **129**, 196.
- [62] S. Wang, L. Zhang, Z. Xia, A. Roy, D. W. Chang, J. B. Baek, L. Dai, *Angew. Chem. Int. Ed.*, 2012, **51**, 4209; *Angew. Chem.*, 2012, **124**, 4285.
- [63] S. S. Feng, W. Li, Q. Shi, Y. H. Li, J. C. Chen, Y. Ling, A. M. Asiri, D. Y. Zhao, *Chem. Commun.*, 2014, **50**, 329.

Chapter 3

Three-Dimensional Nitrogen-Doped Hierarchical Porous Carbon as an Electrode for High-Performance Supercapacitors

3.1. Introduction

Porous carbon materials are widely used in dozens of fields due to their stable physicochemical properties, good electrical conductivity, and large storage capability.[1-3] It is well known that electric double-layer capacitors (EDLCs), which are based on electrical charge accommodation at the electric double-layer of a polarized electrode, are critical components applied in high-rate electric devices (hybrid vehicles) because of their high power density, high-speed recharging, and long working lifespan.[4] Porous carbons have been considered as the most promising electrode materials for EDLCs.[5,6] To obtain a high capacitance, high specific surface area and porosity are usually required.[7] In addition, the transportation resistance of the inner ions and the diffusion distance inside the carbon-based electrode must be minimized to increase the formation kinetics of the electric double-layer.[8] Although commercial activated carbons have a high specific surface area ($>1000 \text{ m}^2 \text{ g}^{-1}$), they are mostly composed of micropores and long diffusion pathways that are not favorable for ion transport and limit their effective capacitance.[9] Thus, porous carbon materials with a high surface area, short channels (less subject to tortuosity), as well as interconnected and hierarchical pore architectures are expected to be preferable for applications in supercapacitors.

Carbon materials with three-dimensional hierarchical porous textures (i.e., macropores integrated with meso- and micropores) have attracted much attention during the past decade because they are desirable electrode materials for EDLCs thanks to their small transport resistance, short pathways, and high surface area.[8,10-12] As demonstrated by many studies, macropores are essential for the electrolyte to achieve free permeation and for creating an ion-buffering reservoir.[8,10,11] On the other hand, mesopores facilitate ion mobility[12] and micropores contribute to increasing the surface area, confining ions, and accommodating charges.[13] The nanocasting method is the most popular approach to precisely control the porosity of the carbon materials by using colloidal silica as a template with suitable flexibility, controllability, and reproducibility.[14] First, colloidal silica with tunable particle sizes (from dozens of nanometers to several micrometers) is prepared by a modified Stöber method. Then, several carbon precursors, such as sucrose,[15] resol,[16] or pitch,[17] are introduced into the

void between the silica particles. After heat treatment under an inert atmosphere and sequential removal of the silica template with hydrofluoric acid, porous carbon materials with a multimodal pore distribution can be obtained. In some cases, the thermal decomposition of amphiphilic molecules as a secondary template can be employed to form mesopores.[18,19] In recent years, other simplified syntheses by direct carbonization of carbide,[20] biomass,[21,22] or metal–organic frameworks (MOFs)[23-26] have also been developed to fabricate various kinds of porous carbon materials.

Lately, heteroatom doping (e.g., B, N, P) has proved to be an effective approach to further enhance the electrochemical performance of carbon materials because of the increased electrical conductivity, surface polarity, and reversible pseudocapacitance derived from the doped functional groups.[27,28] To simplify the synthetic procedures and circumvent the use of hazardous carbon precursors, nontoxic nitrogenous dopamine can be employed as an excellent candidate for preparing nitrogen-doped carbon (NC) materials.[29] First, dopamine can self-polymerize under mild alkaline conditions at room temperature and pressure. Second, dopamine tends to deposit onto any kind of surface; thus, various sacrificial templates can be used to generate the pores.[30,31] Third, polymerized dopamine has a high carbonization yield (close to 50 wt%, even at 1000 °C) and nitrogen can be preserved in the final carbons.[32]

The aforementioned aspects constitute a satisfactory motivation to elaborate new three-dimensional hierarchical porous carbons with functional heteroatoms as the electrode materials for EDLCs based on a nanocasting method. Nitrogenous dopamine is selected as the organic precursor and colloidal silica nanoparticles about 80 nm in size are used as the template for the formation of macropores. The resulting N-doped hierarchical porous carbon framework (NHPC-3D) is composed of macropores as well as meso- and microporous textures, which provide a high specific surface area for electrical charge storage, free diffusion pathways for ion and mass transport, and nitrogen functional groups for pseudocapacitance when implemented in high-rate EDLCs.

3.2. Experimental Sections

3.2.1. Chemicals

Tetraethyl orthosilicate (TEOS), aqueous solution of ammonia (NH_4OH , 28 wt%), and dopamine hydrochloride were purchased from Aldrich. All chemicals were of analytical grade and were used without further purification.

3.2.2. Preparation of Silica Spheres

Silica spheres (≈ 80 nm) were prepared through a modified classic Stöber method. First, $\text{NH}_3 \cdot \text{H}_2\text{O}$ (0.68 mL, 28 wt%) was added to a mixture of water (15.00 mL) and ethanol (9.33 mL). At the same time, a solution of TEOS (2.25 mL) in ethanol (22.75 mL) was prepared. After stirring for 15 mins, the solution of TEOS in ethanol was added to the first alkaline solution in ethanol/water and reacted for another 3 hours under continuous stirring at 400 rpm. Then, the silica spheres could be collected through centrifugation and washed several times with deionized water and ethanol.

3.2.3. Preparation of Three-Dimensional Nitrogen-Doped Hierarchical Porous Carbon (NHPC-3D)

The detailed synthetic steps are described as follows. Solution A was prepared by dispersing 200 mg of silica spheres in 8 mL of ethanol under sonication for more than 1 hour. Meanwhile, solution B was prepared by dissolving 150 mg of dopamine hydrochloride in 8 mL of deionized water. Then, solution B was poured into solution A under mild stirring. Finally, 0.5 mL of ammonia aqueous solution was injected and the colour of the solution turned from oyster white to dark brown. After continuous reaction for 20 hours, the polydopamine/silica composite material (labelled as PDA/silica) was collected by centrifugation and was washed several times with deionized water and ethanol. The N-doped carbon/silica composite material (labelled as NC/silica) was obtained by carbonizing the PDA/silica at 800 °C (2 hours) under N_2 atmosphere with a heating rate of 2 °C min^{-1} . Finally, the N-doped hierarchical porous carbons with three-dimensional interconnected framework (labelled as NHPC-3D) was

obtained by removing the silica template using hydrofluoric acid aqueous solution (HF, 10 wt%).

3.2.4. Characterization

The morphology of the final products was observed on a Hitachi SU-8000 field-emission scanning electron microscope at an accelerating voltage of 5 kV. TEM and elemental mapping analysis was conducted by using a JEM-2100 microscope at a voltage of 200 kV. The N₂ adsorption–desorption isotherm was acquired with a Quantachrome Autosorb-iQ automated gas sorption system at 77 K. The specific surface area was calculated according to the BET model by using the adsorption branch data in the relative pressure (P/P_0) range of 0.05–0.35. The total pore volume and pore size distribution were estimated from the adsorption branches from the isotherm on the basis of a NLDFT method. Wide-angle powder XRD patterns were acquired on a Rigaku Rint 2000 X-ray diffractometer by using monochromated CuK α radiation (40 kV, 40 mA) at a scanning rate of 2° min⁻¹. Raman spectra were collected on a Horiba-Jovin Yvon T64000 instrument with an excitation laser wavelength of $\lambda = 514.5$ nm. XPS spectra were acquired on a PHI Quantera SXM (ULVAC-PHI) instrument with an AlK α X-ray source. All binding energies were calibrated with reference to the C 1s binding energy (285.0 eV). The peaks of the N 1s spectrum were fitted with a Gaussian-Lorentzian sum function and a Shirley background. Thermogravimetric (TG) analysis was carried out by using a Hitachi HT-Seiko Instrument Exter 6300 TG/DTA analyzer in air with heating from room temperature to 800 °C at 5 °C min⁻¹.

3.2.5. Electrochemical Measurements

The electrochemical measurements were carried out in a traditional three-electrode system. A platinum filament and Ag/AgCl (3 M KCl) electrode were utilized as counter and reference electrodes, respectively. The thin-film working electrode was prepared as follows: NHPC-3D (1 mg) was mixed with poly(vinylidene fluoride) (0.1 mg) and then well dispersed in N-methyl-2-pyrrolidone (0.4 mL) through ultrasonication. The black slurry was dropped onto a graphite substrate (1 cm²) and dried under an IR lamp to form a thin layer. The electrochemical measurements were conducted by using an electrochemical workstation (CHI

660E CH Instruments) in acid electrolyte (1.0 M H₂SO₄) at room temperature (22 °C). The electrochemical properties of the supercapacitor were studied by cyclic voltammogram (CV) and galvanostatic charge-discharge (GC-DC) measurements. The potential sweep rate ranged from 20 to 200 mV s⁻¹ and the GC-DC current density varied from 2 to 20 A g⁻¹. The specific capacitance was calculated from the GC-DC curves by using Equation (1):

$$C = \frac{I \times \Delta t}{m \times \Delta V} \quad (1)$$

in which I is the charge-discharge current at a discharge time Δt (s), ΔV is the potential range, and m is the mass of active electrode material.

3.3. Results and Discussion

3.3.1. Synthesis and Characterization of NHPC-3D

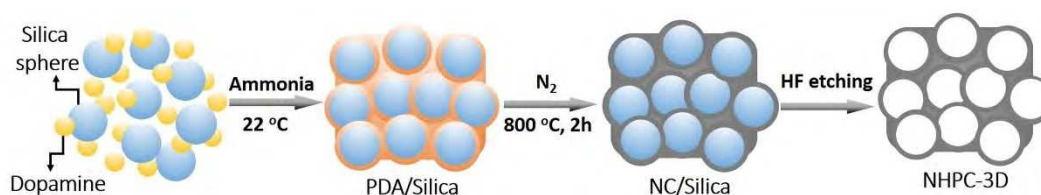


Figure 3.1 Schematic illustration of the synthetic procedure for NHPC-3D.

A schematic illustration of the synthetic procedure is shown in **Figure 3.1**. One solution was prepared by dispersing silica spheres (200 mg) in ethanol (8 mL) under sonication for more than 1 h. Meanwhile, another solution was prepared by dissolving dopamine hydrochloride (150 mg) in deionized water (8 mL). Then, the two solutions were mixed. Finally, an aqueous solution of ammonia (0.5 mL) was injected to induce the self-polymerization of dopamine and the color of the solution turned from oyster white to dark brown. After continuous reaction for 20 h, the PDA/silica composite material was collected by centrifugation and washed several times with deionized water and ethanol. The NC/silica composite material was obtained by carbonizing PDA/silica at 800 °C (2 hours) under a N₂ atmosphere with a heating rate of 2 °C min⁻¹. Finally, the N-doped hierarchical porous carbon with a three-dimensional

interconnected framework (labeled as NHPC-3D) was obtained by removing the silica template with an aqueous solution of hydrofluoric acid (HF, 10 wt%).

Changes in the morphology of the material in each step can be observed in the SEM image. First, dopamine and silica nanoparticles with a diameter of about 80 nm shown in **Figure 3.2** were homogeneously dispersed in a mixture of ethanol and water. Then, the solution was adjusted to be alkaline by adding ammonia to trigger the polymerization of dopamine molecules. During this stage, dopamine starts to polymerize and simultaneously deposits on the silica spheres. As shown in **Figure 3.3a**, PDA is well coated on the silica spheres; thus forming PDA/silica. After being treated at 800 °C under an inert atmosphere, the outer PDA layer is converted into N-doped carbon and the product of NC/silica retains the morphology of the initial PDA/silica sample (**Figure 3.3b**). Finally, the silica template is removed by HF etching, leaving self-standing NHPC-3D (**Figure 3.3c**). A multitude of macropores of similar dimensions to the original silica template can be observed on the final NHPC-3D (**Figure 3.3d**). To determine residual silica in NHPC-3D, thermogravimetric (TG) analysis was conducted in air with heating from room temperature to 800 °C at a heating rate of 5 °C min⁻¹. As shown in **Figure 3.4**, the NHPC-3D sample was stable up to 430 °C, then the weight decreased rapidly as the temperature increased from 430 to 590 °C due to the pyrolysis of N-doped carbon materials. Finally, 97.4 wt% weight loss was detected by TG analysis at 800 °C compared with the initial sample weight, which indicated that the silica template was almost removed by HF. The cross-linked carbon networks consist mainly of bowl-like thin-film (<10 nm) structures (**Figure 3.3d**), which suggests a relatively small ion-transport distance through the walls during the electrochemical process.

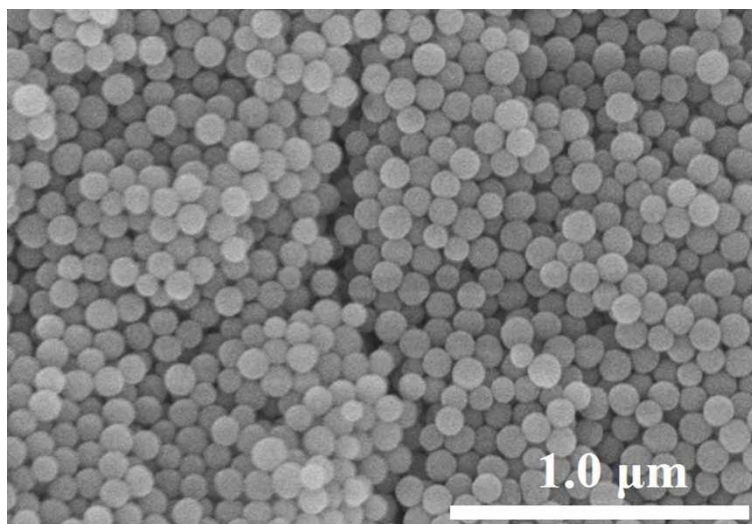


Figure 3.2 SEM image of silica template with a diameter of ~80 nm.

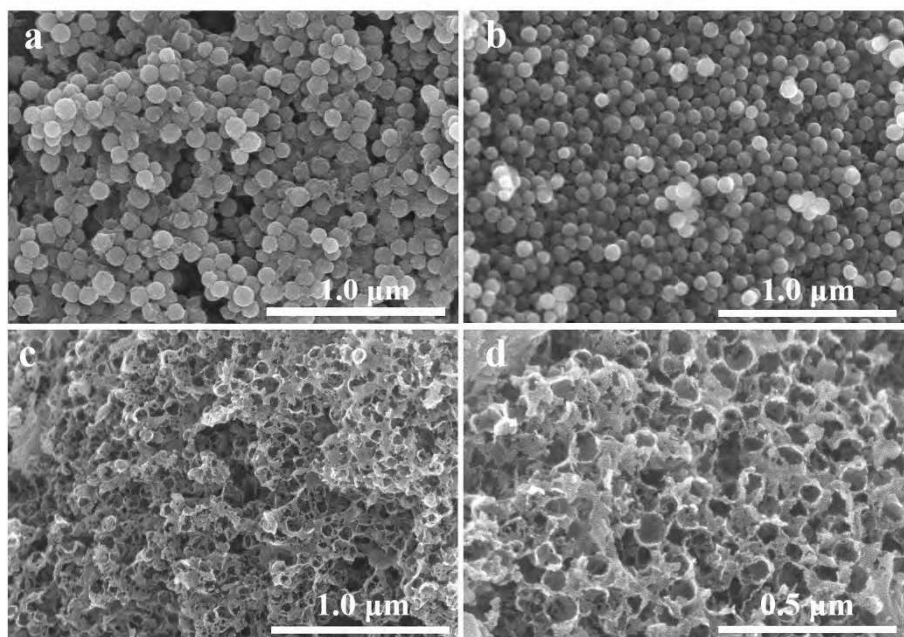


Figure 3.3 SEM images of as-synthesized (a) PDA/silica, (b) NC/silica, and (c,d) NHPC-3D.

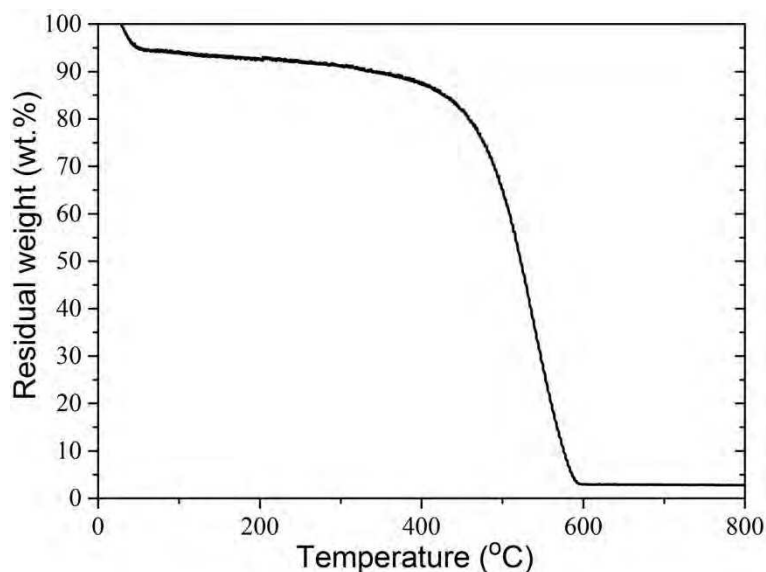


Figure 3.4 TG curve of NHPC-3D measured under an air atmosphere heating from room temperature to 800 °C with a heating rate of 5 °C min⁻¹.

As shown in the TEM image of **Figure 3.5a**, the NC/silica consists of silica nanoparticles coated with a thin carbon layer. After HF etching, the silica spheres are removed, leaving the templated macropores in the NHPC-3D frameworks (**Figure 3.5b**); this is consistent with the structural changes previously observed in the SEM images. Furthermore, the mesoporous structure also contains interconnected and overlapping carbon layers. The graphitic degree was investigated by HRTEM, which revealed that NHPC-3D was composed of disordered carbons (**Figure 3.5c**). The elemental spatial distribution of carbon, nitrogen, and oxygen in NHPC-3D is shown in **Figure 3.5d and e**, and confirms the good distribution of nitrogen atoms. Moreover, the nitrogen content was roughly estimated by energy-dispersive X-ray analysis to be about 8.2 wt% (**Figure 3.6**).

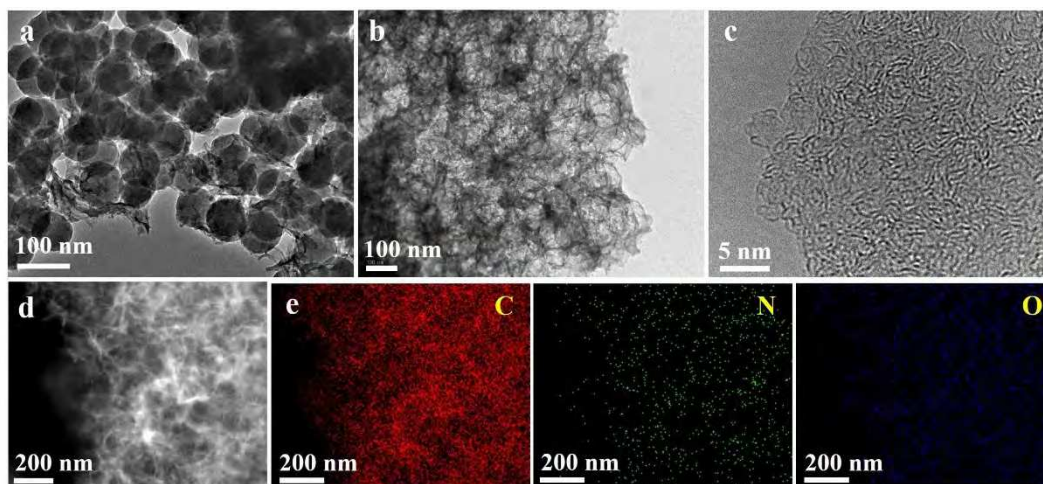


Figure 3.5 (a) TEM image of the NC/silica. (b) TEM, (c) high-resolution (HR) TEM, (d) scanning transmission electron microscopy (STEM) images, and (e) elemental mapping of NHPC-3D.

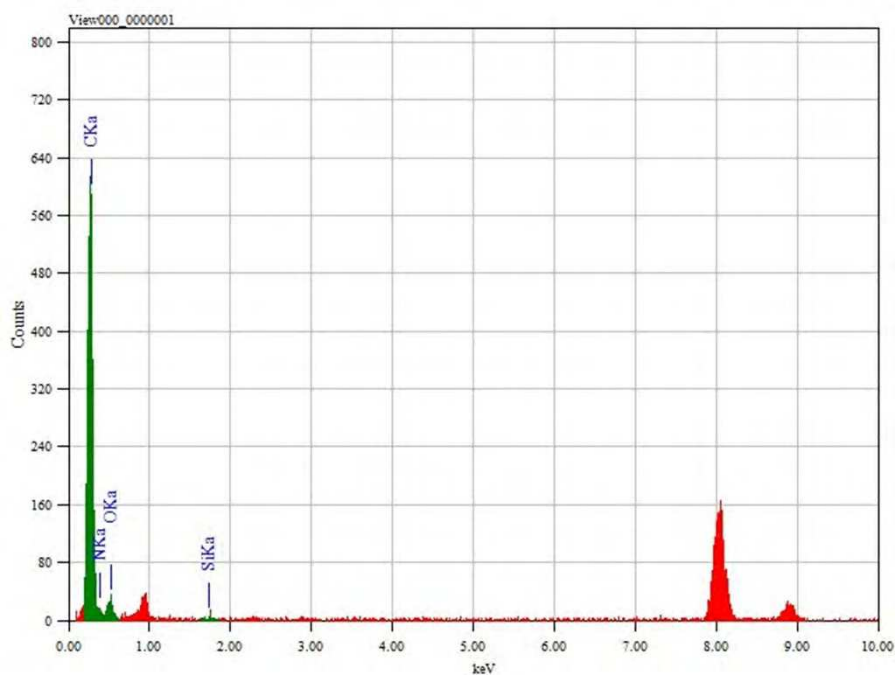


Figure 3.6 Energy-dispersive X-ray analysis of NHPC-3D.

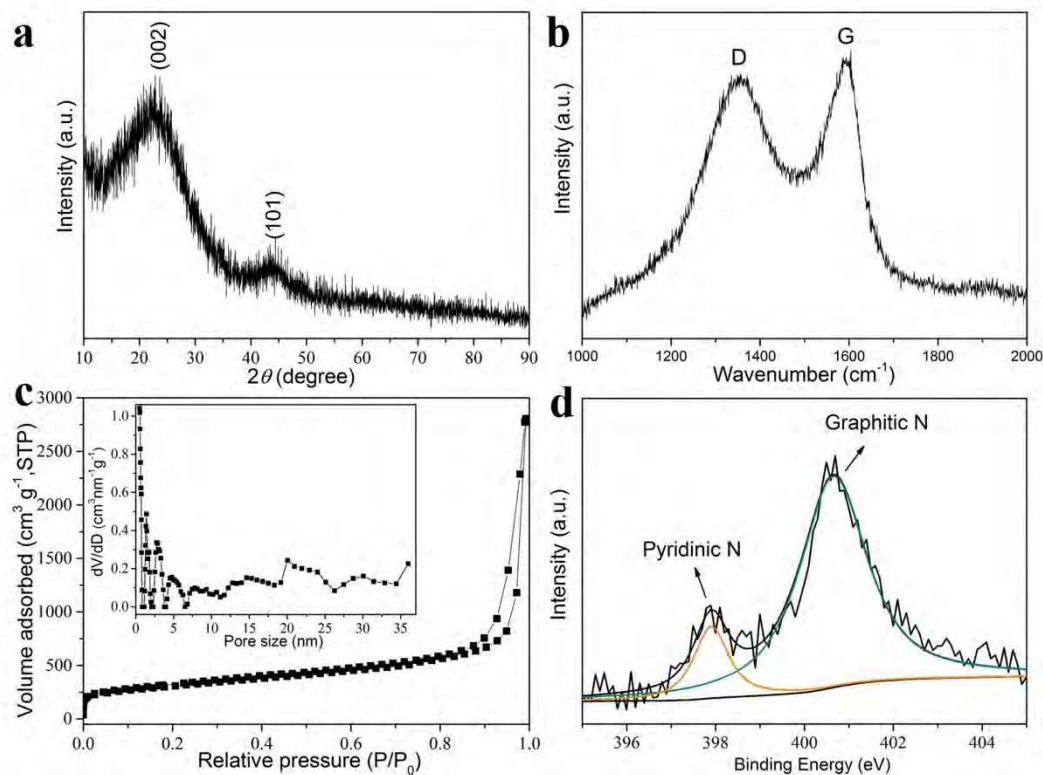


Figure 3.7 (a) Wide-angle XRD pattern, (b) Raman spectrum, (c) N₂ adsorption–desorption isotherm (inset shows the pore size distribution), and (d) high-resolution X-ray photoelectron spectroscopy (XPS) result centered on N 1s of the NHPC-3D.

The carbon state in NHPC-3D was investigated by XRD and Raman spectroscopy. As observed in **Figure 3.7a**, NHPC-3D exhibits two broad diffraction peaks located at 23.0° and 44.0°, which could be indexed to the (002) and (101) diffraction planes of amorphous carbon (disordered carbon layers), respectively.[33,34] The Raman spectrum (**Figure 3.7b**) displays two vibration bands at 1360 (D band) and 1590 cm⁻¹ (G band), which implies the coexistence of disordered carbon/defect and graphitic carbon sheets, respectively.[35,36] The porosity of the structure was estimated from the N₂ adsorption–desorption isotherm (**Figure 3.7c**). NHPC-3D exhibits a type IV isotherm with a hysteresis loop.[37] Nitrogen uptake at low relative pressure (<0.05) is caused by the presence of micropores that originate from the pyrolysis of PDA. A type IV isotherm can be associated with the capillary condensation of nitrogen taking place in large mesopores derived from the overlapping carbon frameworks. Moreover, there is no saturation in the adsorption at high relative pressure ($P/P_0 > 0.9$), which suggests the

existence of macropores inherited from the removed silica templates; this is consistent with the SEM and TEM images (**Figure 3.3d and 3.5b**). The multimodal pore size distributions from micro- to mesopore were analyzed through nonlocal density functional theory (NLDFT) and display in the inset of **Figure 3.7c**, which confirms the presence of hierarchical pores. From the adsorption branches in NHPC-3D, the calculations result in a large specific surface area of $1056 \text{ m}^2 \text{ g}^{-1}$ and a high pore volume of $2.56 \text{ cm}^3 \text{ g}^{-1}$. Furthermore, XPS was conducted to detect the electric state of nitrogen in NHPC-3D. The high-resolution N 1s spectrum can be deconvoluted into two binding energies located at 397.9 and 400.6 eV (shown in **Figure 3.7d**), which can be assigned to pyridinic-N and graphitic-N, respectively.[38] The percentage of nitrogen in the NHPC-3D samples estimated from the XPS spectrum by using the high-resolution N 1s spectrum is around 7.4 wt%, which is slightly lower than the result determined by energy-dispersive X-ray analysis (8.2 wt%); this is reasonable when considering the difference between the two facilities. The XPS result verifies the successful doping of nitrogen into the NHPC-3D.

3.3.2. Electrochemical Supercapacitor with the NHPC-3D Electrode

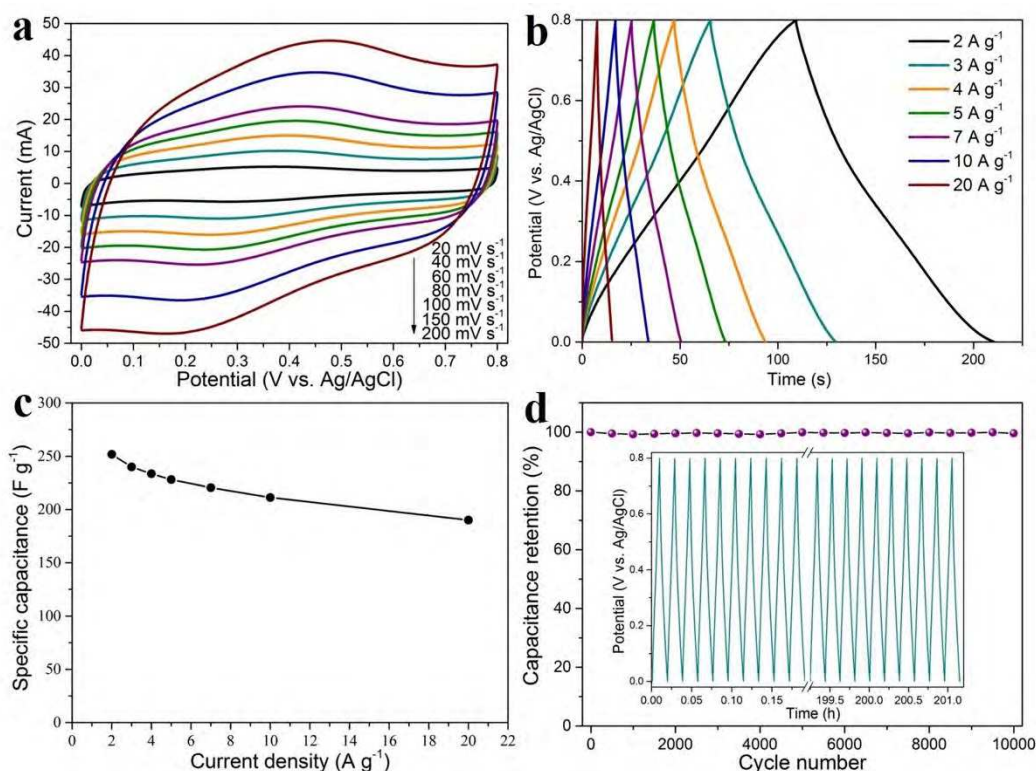


Figure 3.8 (a) Cyclic voltammograms with a potential sweep rate ranging from 20 to 200 mV s⁻¹. (b) GC-DC curves with a current density ranging from 2 to 20 A g⁻¹. (c) Specific capacitance values calculated from the GC-DC curves at different current densities. (d) Cyclic stability at a charge-discharge current density of 5 A g⁻¹ for 10000 cycles (inset shows the GC-DC curves) of the NHPC-3D electrode. All measurements were carried out in 1.0 M H₂SO₄ by using a three-electrode system.

The unique structural properties of NHPC-3D suggest a promising performance as an electrode material for high-performance EDLCs. To characterize the electrochemical properties of the NHPC-3D electrode implemented in a supercapacitor architecture, cyclic voltammetry (CV) and galvanostatic charge-discharge (GC-DC) measurements were conducted by using a three-electrode system in 1 M aqueous H₂SO₄ electrolyte. The CV curves were recorded at sweep rates ranging from 20 to 200 mV s⁻¹ (**Figure 3.8a**). It can be observed that NHPC-3D presents rectangular-like CV curves with a distinct hump, which implies that the capacitive response originates from both the electric double-layer capacitance and the

pseudocapacitance related to the doped nitrogen atoms.[39,40] It is well-known that heteroatom (e.g., nitrogen) doping could not only enhance the electric double-layer capacitance by increasing the wettability between electrolyte and carbon electrode,[39] but also give rise to pseudocapacitance effects by participating in pseudofaradaic charge-transfer reactions.[41] It is noteworthy that the quasi-rectangular CV shape is only slightly distorted, even at higher potential sweep rates, which implies efficient ion transfer and a rapid ion response inside the NHPC-3D electrode. The GC-DC measurements, which were performed to evaluate the specific capacitance of the NHPC-3D electrode (**Figure 3.8b**), were obtained at various current densities ranging from 2 to 20 A g⁻¹ in a three-electrode system. The NHPC-3D electrode presents a quasi-linear appearance accompanied by a slight bend due to the impact of pseudocapacitance originating from nitrogen doping.[42,43] The specific capacitance values were calculated from the GC-DC curves at different current densities and are plotted in **Figure 3.8c**. The NHPC-3D electrode shows an excellent specific capacitance of 252 F g⁻¹ at a current density of 2 A g⁻¹ in aqueous electrolyte, which is higher than or comparable to those of previously fabricated hierarchical porous carbons (**Table 3.1**). The specific capacitance of the NHPC-3D electrode at a higher current density of 20 A g⁻¹ remains 190 F g⁻¹, which results in a capacitance retention ratio as high as 75.7% during high-rate operations.

The exact mechanisms responsible for ion transport in the electrode material are complex, but the abundance of macropores and the thin porous walls effectively shorten the diffusion pathways and minimize the transport resistance of the electrolyte and ions from the bulk electrolyte to the inner surface, leading to excellent high-rate performances. More precisely, the macropores not only provide free pathways for the electrolyte but also bring out a buffer space for the electrolyte and ions, which helps to reduce the diffusion distance of the inner surface.[8,10,11] The meso- and micropores in the carbon walls lead to a high specific surface area and contribute to a high electrochemical double-layer capacitance.[12,13] Thus, the distinguished specific capacitance and high capacitive retention can be greatly attributed to advantageous structural properties of NHPC-3D, including the high specific surface area (1056 m² g⁻¹), interconnected hierarchical porous texture, and nitrogen functionalization.

Furthermore, the NHPC-3D electrode exhibits long-term cycling stability, as shown in **Figure 3.8d**. The specific capacitance is almost constant over 10000 cycles, which showcases that NHPC-3D is a promising candidate for practical applications.

Table 3.1 Comparison of the specific capacitances of hierarchical porous carbons in the previous literatures using three-electrode systems.

Materials	Electrolyte	Current density (A g ⁻¹)	Capacitance (F g ⁻¹)	Reference
N-doped hierarchical porous carbons	1.0 M H ₂ SO ₄	2	252	This study
Heteroatom-doped carbon	1.0 M H ₂ SO ₄	2	245	<i>Adv. Funct. Mater.</i> 23 (2013) 1305-1312
Hierarchical porous carbon hollow-spheres	6.0 M KOH	2	248	<i>J. Power Sources</i> 211 (2012) 92-96
Hierarchical porous carbon foams	6.0 M KOH	1	206	<i>J. Power Sources</i> 209 (2012) 152–157
N-doped porous nanofibers	6.0 M KOH	1	202	<i>ACS Nano</i> 6 (2012) 7092-7102
Hierarchical porous carbons	6.0 M KOH	1	190	<i>Carbon</i> 55 (2013) 221-232
Porous carbon through dual templates	6.0 M KOH	1	153	<i>J. Mater. Chem. A</i> 1 (2013) 7379-7383
N-containing hydrothermal carbons	1.0 M H ₂ SO ₄	2	240	<i>Adv. Mater.</i> 22 (2010) 5202-5206

3.4. Conclusion

I developed a facile procedure for the large-scale preparation of NHPC-3D by taking advantage of the self-polymerization and coating nature of nitrogenous dopamine. The three-dimensional interconnected hierarchical porous texture, as well as the high surface area, large pore volume, and heteroatom doping, in NHPC-3D make it an excellent candidate electrode material for high-rate supercapacitor applications by providing a sufficient surface for charge accommodation, and supplying reversible pseudocapacitance from the doped nitrogen atoms, which reduces the primary ion-transport resistance and pathways, and overcomes the kinetic limits in porous carbons during electrochemical processes.

References

- [1] Y. Xia, G. S. Walker, D. M. Grant, R. Mokaya, *J. Am. Chem. Soc.*, 2009, **131**, 16493.
- [2] W. D. Zhou, X. C. Xiao, M. Cai, L. Yang, *Nano Lett.*, 2014, **14**, 5250.
- [3] C. L. Long, X. Chen, L. L. Jiang, L. J. Zhi, Z. J. Fan, *Nano Energy*, 2015, **12**, 141.
- [4] P. Simon, Y. Gogotsi, *Nat. Mater.*, 2008, **7**, 845.
- [5] S. Y. Wang, B. Pei, X. S. Zhao, R. A. W. Dryfe, *Nano Energy*, 2013, **2**, 530.
- [6] Y. Zhou, S. L. Candelari, Q. Liu, E. Uchaker, G. Z. Cao, *Nano Energy*, 2015, **12**, 567.
- [7] A. S. Aricò, P. Bruce, B. Scrosati, J. M. Tarascon, W. V. Schalkwijk, *Nat. Mater.*, 2005, **4**, 366.
- [8] D. W. Wang, F. Li, M. Liu, G. Q. Lu, H. M. Cheng, *Angew. Chem. Int. Ed.*, 2008, **47**, 373; *Angew. Chem.*, 2008, **120**, 379.
- [9] E. Frackowiak, F. Beguin, *Carbon*, 2001, **39**, 937.
- [10] S. Shiraishi, H. Kurihara, L. Shi, T. Nakayama, A. Oya, *J. Electrochem. Soc.*, 2002, **149**, A855.
- [11] G. Salitra, A. Soffer, L. Eliad, Y. Cohen, D. Aurbach, *J. Electrochem. Soc.*, 2000, **147**, 2486.
- [12] K. S. Xia, Q. M. Gao, J. H. Jiang, J. Hu, *Carbon*, 2008, **46**, 1718.

- [13] Y. Lv, L. Gan, M. Liu, W. Xiong, Z. Xu, D. Zhu, D. S. Wright, *J. Power Sources*, 2012, **209**, 152.
- [14] Z. Wang, F. Li, N. S. Ergang, A. Stein, *Chem. Mater.*, 2006, **18**, 5543.
- [15] X.-Y. Zhou, J.-J. Tang, J. Yang, J. Xie, L.-L. Ma, *Electrochim. Acta*, 2013, **87**, 663.
- [16] N. Li, Q. Zhang, J. Liu, J. Joo, A. Lee, Y. Gan, Y. Yin, *Chem. Commun.*, 2013, **49**, 5135.
- [17] N. Jayaprakash, J. Shen, S. S. Moganty, A. Corona, L. A. Archer, *Angew. Chem. Int. Ed.*, 2011, **50**, 5904; *Angew. Chem.*, 2011, **123**, 6026.
- [18] Z. Y. Wang, E. R. Kiesel, A. Stein, *J. Mater. Chem.*, 2008, **18**, 2194.
- [19] Y. Deng, C. Liu, T. Yu, F. Liu, F. Zhang, Y. Wan, L. Zhang, C. Wang, B. Tu, P. A. Webley, H. Wang, D. Zhao, *Chem. Mater.*, 2007, **19**, 3271.
- [20] M. Oschatz, L. Borchardt, M. Thommes, K. A. Cychosz, I. Senkowska, N. Klein, R. Frind, M. Leistner, V. Presser, Y. Gogotsi, S. Kaskel, *Angew. Chem. Int. Ed.*, 2012, **51**, 7577; *Angew. Chem.*, 2012, **124**, 7695.
- [21] S. Dutta, A. Bhaumik, K. C.-W. Wu, *Energy Environ. Sci.*, 2014, **7**, 3574.
- [22] S. Joshi, L. K. Shrestha, Y. Kamachi, V. Malgras, M. A. Pradhananga, B. P. Pokhrel, T. Nakato, R. R. Pradhananga, K. Ariga, Y. Yamauchi, *Adv. Powder Technol.*, 2015, **26**, 894.
- [23] J. Tang, R. R. Salunkhe, J. Liu, N. L. Torad, M. Imura, S. Furukawa, Y. Yamauchi, *J. Am. Chem. Soc.*, 2015, **137**, 1572.
- [24] A. J. Amali, J.-K. Sun, Q. Xu, *Chem. Commun.*, 2014, **50**, 1519.
- [25] N. L. Torad, Y. Li, S. Ishihara, K. Ariga, Y. Kamachi, H.-Y. Lian, H. Hamoudi, Y. Sakka, W. Chaikittisilp, K. C.-W. Wu, Y. Yamauchi, *Chem. Lett.*, 2014, **43**, 717.
- [26] W. Chaikittisilp, M. Hu, H. Wang, H.-S. Huang, T. Fujita, K. C.-W. Wu, L.-C. Chen, Y. Yamauchi, K. Ariga, *Chem. Commun.*, 2012, **48**, 7259.
- [27] D. Hulicova-Jurcakova, A. M. Puziy, O. I. Poddubnaya, F. Suárez-García, J. M. D. Tascón, G. Q. Lu, *J. Am. Chem. Soc.*, 2009, **131**, 5026.
- [28] Z. S. Wu, A. Winter, L. Chen, Y. Sun, A. Turchanin, X. L. Feng, K. Müllen, *Adv. Mater.*, 2012, **24**, 5130.

- [29] R. Liu, S. M. Mahurin, C. Li, R. R. Unocic, J. C. Idrobo, H. Gao, S. J. Pennycook, S. Dai, *Angew. Chem. Int. Ed.*, 2011, **50**, 6799; *Angew. Chem.*, 2011, **123**, 6931.
- [30] H. Lee, S. M. Dellatore, W. M. Miller, P. B. Messersmith, *Science*, 2007, **318**, 426.
- [31] R. J. Li, K. Parvez, F. Hinkel, X. L. Feng, K. Müllen, *Angew. Chem. Int. Ed.*, 2013, **52**, 5535; *Angew. Chem.*, 2013, **125**, 5645.
- [32] K. Ai, Y. L. Liu, C. P. Ruan, L. H. Lu, G. Q. Lu, *Adv. Mater.*, 2013, **25**, 998.
- [33] J. Tang, T. Wang, X. C. Pan, X. Sun, X. L. Fan, Y. X. Guo, H. R. Xue, J. P. He, *J. Phys. Chem. C*, 2013, **117**, 16896.
- [34] J. Tang, N. L. Torad, R. R. Salunkhe, J.-H. Yoon, M. S. A. Hossain, S. X. Dou, J. H. Kim, T. Kimura, Y. Yamauchi. *Chem. Asian J.*, 2014, **9**, 3238.
- [35] T. Wang, J. Tang, X. L. Fan, J. H. Zhou, H. R. Xue, H. Guo, J. P. He, *Nanoscale*, 2014, **6**, 5359.
- [36] J. Tang, T. Wang, X. Sun, Y. X. Guo, H. R. Xue, H. Guo, M. Z. Liu, X. X. Zhang, J. P. He, *Microporous Mesoporous Mater.*, 2013, **177**, 105.
- [37] K. S. W. Sing, D. H. Everett, R. A. W. Haul, L. Moscou, R. A. Pierotti, J. Rouquérol, T. Siemieniowska, *Pure Appl. Chem.*, 1985, **57**, 603.
- [38] J. Tang, J. Liu, C. L. Li, Y. Q. Li, M. O. Tade, S. Dai, Y. Yamauchi, *Angew. Chem. Int. Ed.*, 2015, **54**, 588; *Angew. Chem.*, 2015, **127**, 598.
- [39] E. Iyyamperumal, S. Y. Wang, L. M. Dai, *ACS Nano*, 2012, **6**, 5259.
- [40] F. W. Ma, H. Zhao, L. P. Sun, Q. Li, L. H. Huo, T. Xia, S. Gao, G. S. Pang, Z. Shi, S. H. Feng, *J. Mater. Chem.*, 2012, **22**, 13464.
- [41] C. O. Ania, V. Khomenko, E. Raymundo-Piñero, J. B. Parra, F. Béguin, *Adv. Funct. Mater.*, 2007, **17**, 1828.
- [42] L. Zhao, L. Z. Fan, M. Q. Zhou, H. Guan, S. Qiao, M. Antonietti, M.-M. Titirici, *Adv. Mater.*, 2010, **22**, 5202.
- [43] L. F. Chen, X. D. Zhang, H. W. Liang, M. G. Kong, Q. F. Guan, P. Chen, Z. Y. Wu, S. H. Yu, *ACS Nano*, 2012, **6**, 7092.

Chapter 4

Nitrogen-Doped Hollow Carbon Spheres with Large Mesoporous Shells Engineered from Diblock Copolymer Micelles

4.1. Introduction

Future fabrication of advanced nano-devices will rely largely on the ability to control the synthesis of nanomaterials possessing unique structural features and multifunctional properties.[1] Porous carbon materials have been universally applied in dozens of fields due to their stable physicochemical properties, good electrical conductivity, low cost, and abundant storage.[2] Compared with other morphologies, the hollow spherical structure has many fascinating properties, including a high surface-to-volume ratio, low density, and large interior void fraction.[3-5] Hollow carbon spheres have consequently attracted a great deal of interest, generating abundant research efforts. Up to now, hollow carbon spheres have been fabricated by means of various synthetic approaches, including the hard-templating and soft-templating methods.[6,7] The hard-templating method has been commonly adopted to synthesize uniform hollow carbon spheres by coating the surface of the spherical template core with a carbon precursor (e.g., resol,[8] pitch,[9] glucose,[10] pyrrole[11]), followed by carbonization and subsequent template etching. The retained carbon shells and hollow cores originate from the sacrificial colloid hard templates, including monodispersed silica nanoparticles,[12] spherical polymers (e.g., polystyrene spheres[13]), and metal oxides.[14] The soft-templating method, which is based on the organic–organic self-assembly of thermosetting carbon precursors and thermally decomposable amphiphilic molecules, requires less synthetic steps.[15,16] Only a few hollow carbon spheres are obtained by using the soft-templating method.[6] These uniform hollow carbon spheres exhibit excellent potential for applications in adsorption,[4] catalysis,[17] and energy storage,[18] due to their stable physicochemical properties, good electrical conductivity and unique structural properties, including high specific surface area, accessible porous shell and high internal volume. In addition, the internal void provides a confined space which is especially attractive for drug delivery, gas storage, nanoreactors, and active material encapsulation.[1,19,20]

Research designed to promote applications of carbon materials has shown functionalized carbon materials with heteroatoms (e.g., N, B, P) to offer an effective approach to modifying intrinsic physicochemical properties of carbons.[21-23] Nitrogen-enriched

carbons with hierarchical pore structures present extraordinarily high capacitance per unit surface area ($> 30 \mu\text{F cm}^{-2}$), due to the pseudocapacitance obtained from the high nitrogen content.[23] The success of N-doped carbon materials in these applications depends on the increases in active surface sites, electrical conductivity, and the electron-donor effect between nitrogen and carbon in the N-doped carbons. In this context, N-doped hollow carbon spheres have recently been the subject of extensive research efforts. Since the first report in 2011 by Dai and coworkers, dopamine has been demonstrated to be a suitable precursor for the synthesis of N-doped carbon materials.[24] Compared with other carbon precursors, dopamine has many unique features. First, dopamine is a nontoxic biomolecule that can self-polymerize under alkaline conditions at just room temperature and, at the same time, coat almost any surface.[25,26] Secondly, polymerized dopamine (polydopamine) has a high carbonization yield of 50 wt%, even at a temperature of 1000 °C, and nitrogen can be preserved in the final carbons in the form of graphitic-N and pyridinic-N.[27] In **Chapter 2**, I have demonstrated a strong interaction between dopamine and the high-molecular-weight diblock copolymer PS-*b*-PEO, and have successfully obtained solid N-doped carbon spheres consisting of abundant large mesopores (up to 16 nm) for the first time.[28]

Although N-doped hollow carbon nanospheres have been developed by different synthetic strategies, including the use of dopamine as the precursor and silica spheres as the hard template,[29,30] most have only random micropores or small mesopores (3-5 nm) in the shell.[4,11,19] To the best of my knowledge, there are few reports that focus on precision engineering of the porous architecture of the shell in the hollow carbon spheres. Recently, monodispersed asymmetrical carbon nanohemispheres filled with ordered mesopores have been realized by Zhao's group, but the size of the pores in the shell is still less than 6 nm.[31] Hence, it remains a challenge to fabricate N-doped hollow carbon spheres with large mesopores in the shell, which could be more interesting for their ability to act as accessible pathways for mass transport, especially of large molecules. Inspired by the conformal deposition nature of polydopamine on solid surfaces, and the strong interaction between polydopamine and diblock copolymer PS-*b*-PEO, I report herein the synthesis through a dual-templating method of N-

doped hollow carbon spheres with large tunable mesopores (~20 nm) in the shell (NHCS-LM). Dispersed silica nanoparticles with sizes of ~350 nm were used as the hard template, and the diblock copolymer PS₁₇₃-*b*-PEO₁₇₀ was selected as the micelle soft template for the generation of mesopores in the shell.

4.2. Experimental Sections

4.2.1. Chemicals

Tetraethyl orthosilicate (TEOS), ammonia aqueous solution (NH₄OH, 28 wt%), and dopamine hydrochloride (DA) were purchased from Aldrich. Amphiphilic block copolymer, polystyrene-*b*-poly(ethylene oxide) (PS₁₇₃-*b*-PEO₁₇₀) was purchased from Polymer Source Inc. All the chemicals were of analytical grade and were used without further purification.

4.2.2. Preparation of Silica Spheres

Silica spheres about 350 nm in size were prepared using the modified classic Stöber method. First, 9 mL of 28 wt% NH₃·H₂O was added to a mixed solution of water (16.25 mL) and ethanol (24.75 mL). An ethanolic solution of TEOS was prepared simultaneously by dissolving TEOS (2.25 mL) in ethanol (22.75 mL). After stirring for 15 mins, the ethanolic solution of TEOS was added to the original alkaline ethanol-water solution and the solution was reacted for another 3 hours. Silica spheres about 350 nm in size were then collected through centrifugation and washed several times with deionized water and ethanol.

4.2.3. Preparation of Nitrogen-Doped Hollow Mesoporous Carbon Spheres (NHCS-LM)

In a typical synthesis of N-doped hollow mesoporous carbon spheres, 200 mg of DA was dissolved in deionized water (8 mL), and the above solution was then poured into a mixed solution of ethanol and THF (volume ratio 1:1, 8 mL) containing 30 mg of diblock copolymer (PS₁₇₃-*b*-PEO₁₇₀) and 50 mg of silica spheres about 350 nm in size under sonication. After 30 mins, 0.5 mL of ammonia aqueous solution (NH₄OH, 28 wt%) was injected to induce self-polymerization of the dopamine, and the colour of the solution turned from oyster white to dark

brown. After continuous reaction for 20 hours, silica@polydopamine/diblock copolymer micelles spherical composite materials consisting silica as the core and polydopamine/diblock copolymer micelles as the shell (assigned as silica@PDA/micelles) were collected by centrifugation and washed several times with deionized water and ethanol. The wall thickness of polydopamine in silica@PDA/micelles can be adjusted by repeating the coating process. During recoating, the pre-prepared silica@PDA/micelles were used as the core instead of silica spheres, and the products were assigned as silica@PDA/micelles-2). Carbonization was performed by heating the silica@PDA/micelles under a N₂ atmosphere at 350 °C for 3 hours and finally at 800 °C for 2 hours with a heating rate of 1 °C min⁻¹. The product is assigned as silica@NMCS (NMCS refers to the N-doped mesoporous carbon shell). Finally, N-doped hollow mesoporous carbon spheres (assigned as NHCS-LM) were obtained by removing the silica template using a hydrofluoric acid aqueous solution (HF, 10 wt%). N-doped hollow mesoporous carbon spheres with thicker walls were also prepared by carbonization of silica@PDA/micelles-2 and removal of the silica template by HF.

4.2.4. Characterization

The morphology of the products was determined with a Hitachi SU-8000 field-emission scanning electron microscope (SEM) at an accelerating voltage of 5 kV. Transmission electron microscopy (TEM) and energy-dispersive X-ray analysis (EDXA) were conducted with a JEM-2100 at a voltage of 200 kV. The N₂ adsorption–desorption isotherms were measured using a Quantachrome Autosorb-iQ Automated Gas Sorption System at 77 K. The specific surface area was calculated according to the Brunauer–Emmett–Teller (BET) model using adsorption branch data in the relative pressure (P/P_0) range of 0.05-0.35. The total pore volumes and pore-size distributions were estimated from the adsorption branches of isotherms according to the nonlocal density functional theory. Wide-angle X-ray diffraction (XRD) patterns were acquired with a Rigaku Rint 2000 X-ray diffractometer using monochromated Cu K α radiation (40 kV, 40 mA) at a scanning rate of 2° min⁻¹. Raman spectra were collected using a Horiba-Jovin Yvon T64000 instrument with an excitation laser wavelength of $\lambda=514.5$ nm. X-ray photoelectron spectroscopy (XPS) was conducted with a PHI Quantera SXM (ULVAC-PHI)

instrument with an Al K α X-ray source. All the binding energies were calibrated via referencing to the C 1s binding energy (285.0 eV). The peaks of the N 1s spectrum were fitted with a Gaussian-Lorentzian sum function and a Shirley background.

4.2.5. Electrochemical Measurements

The electrochemical measurements were conducted using a traditional three-electrode system. A platinum filament and a Ag/AgCl (3 M KCl) electrode acted as counter and reference electrodes, respectively. The thin-film working electrode was prepared as follows. NHCS-LM (0.4 mg) was mixed with poly(vinylidene fluoride) (0.1 mg) and then well-dispersed in N-methyl-2-pyrrolidone (0.2 mL) through ultrasonication. The resulting black slurry was dropped onto a graphite substrate (1 cm²) and dried under an infrared lamp to form a thin layer. Electrochemical measurements were conducted using an electrochemical workstation (CHI 660E CH Instruments) in acid electrolytes (1.0 M H₂SO₄) at room temperature (22 °C). The electrochemical properties of the supercapacitor were studied by cyclic voltammetry (CV) and galvanostatic charge-discharge (GC-DC) measurements. The potential sweep rate ranged from 20 to 200 mV s⁻¹, and the GC-DC current density varied from 1 to 10 A g⁻¹. The specific capacitance value was calculated from the CV curves by the following equation: $C = \frac{1}{ms(V_f - V_i)} \int_{V_i}^{V_f} I(V) dv$, where m is the mass of active electrode material, s is the potential scan rate, V_f and V_i are the integration limits of the voltammetric curve, and $I(V)$ denotes the current density. The specific capacitance was calculated from the GC-DC curves by the following equation, $C = \frac{I \times \Delta t}{m \times \Delta V}$, where I is the charge-discharge current at a discharge time of Δt (s), ΔV is the potential range, and m is the mass of active electrode material.

4.3. Results and Discussion

4.3.1. Synthesis and Characterization of NHCS-LM

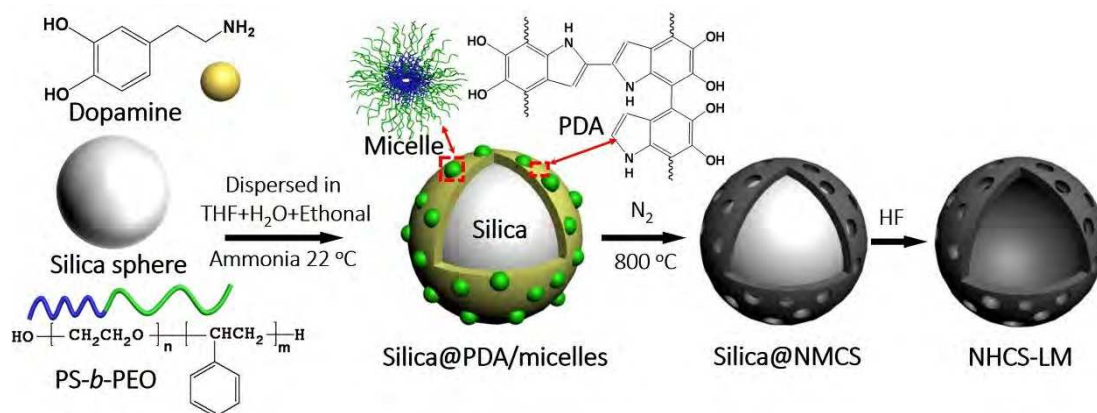


Figure 4.1 Schematic illustration of the preparation of NHCS-LM.

A schematic illustration of the preparation of NHCS-LM is displayed and the formation mechanism is proposed in **Figure 4.1**. In the experimental process, the diblock copolymer PS₁₇₃-*b*-PEO₁₇₀ dissolved in tetrahydrofuran (THF) solution, silica nanospheres well-dispersed in ethanol solution and dopamine (DA) dissolved in water were consecutively mixed together under continuous stirring. Under these conditions, the diblock copolymer PS₁₇₃-*b*-PEO₁₇₀ existed as micelles in the hybrid solution. The PS₁₇₃-*b*-PEO₁₇₀ micelles were surrounded by DA molecules because of the hydrogen bond interaction between the –OH group in the PEO block outside the micelles and the inherit catechol and N–H groups in the DA molecules.[25,32,33] The solution was then adjusted to become alkaline by adding a certain amount of ammonia solution. The pH value of the alkaline reaction solution was measured to be 11.35. The DA molecules proceeded to self-polymerize and continued to coat the surface of the silica spheres at this stage.[25,32] In the meantime, the micelles interacted strongly with the polymerized dopamine (abbreviated as PDA) due to the catechols/quinone groups present in the PDA,[25,32] and were thus forcibly co-deposited onto the surface of the silica spheres together with PDA to obtain core-shell silica@PDA/micelles composite spheres. Carbonization was conducted at 800 °C under an inert atmosphere. This involved converting the PDA into N-doped carbon, simultaneously removing the PS₁₇₃-*b*-PEO₁₇₀ micelles and creating large mesopores in the shell. The obtained sample is denoted as silica@NMCS at this

stage, where NMCS refers to the N-doped mesoporous carbon shell that is inherited from the PDA/micelles shell. Finally, the silica template was etched with hydrofluoric acid to obtain the macroporous core, leading to the formation of the target product, N-doped hollow carbon spheres with macroporous cores (~ 350 nm) and large mesoporous (~ 20 nm) shells (NHCS-LM).

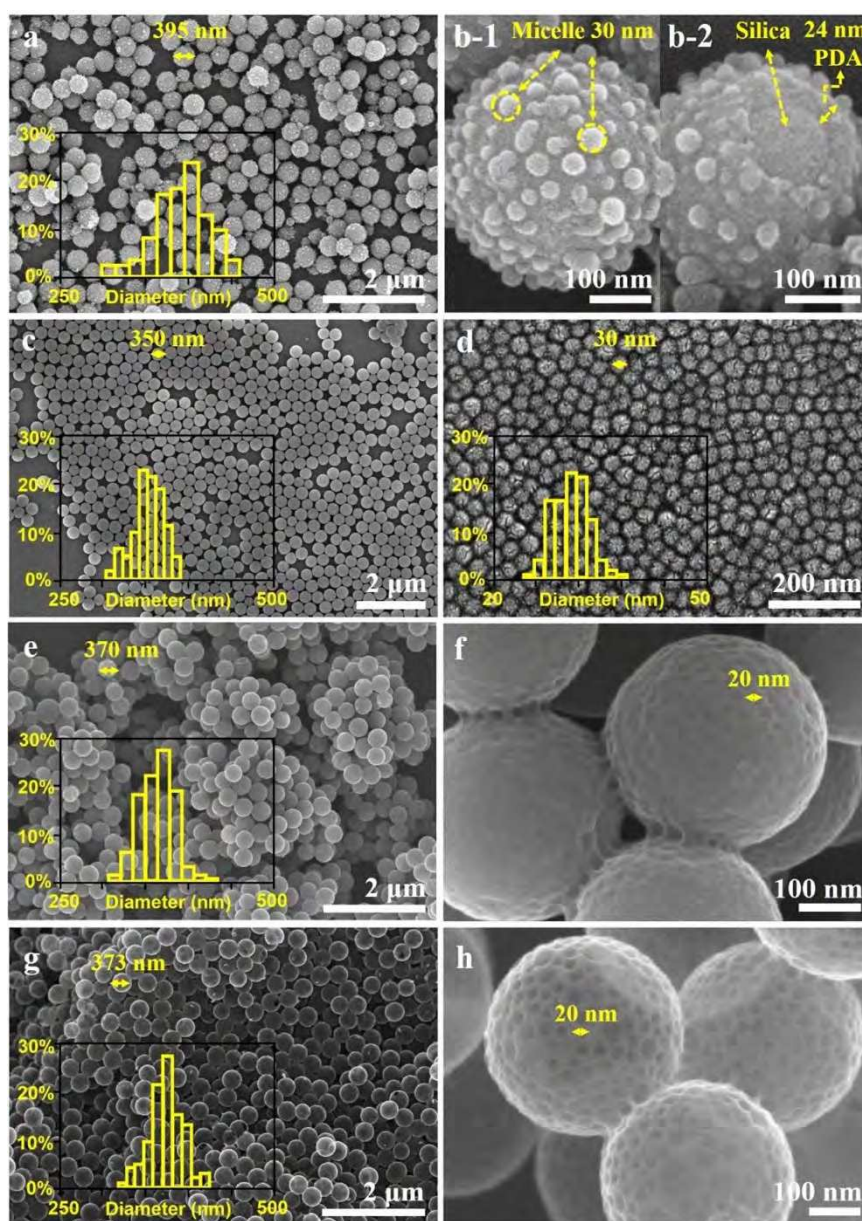


Figure 4.2 SEM images of (a and b) silica@PDA/micelles, (c) silica template, (d) micelles of diblock copolymer PS₁₇₃-b-PEO₁₇₀, (e and f) silica@NMCS, and (g and h) NHCS-LM. The insets in Figure 4.2a,c,d,e,g are the particle size distribution histograms that calculated from over 50 particles. The average particle sizes are (a) 395 nm, (c) 350 nm, (d) 30 nm, (e) 370 nm, and (g) 373 nm, respectively.

The practical morphology of the samples in each stage was revealed by scanning electron microscope (SEM) images. As shown in **Figure 4.2a**, the prepared core-shell silica@PDA/micelles preserve the spherical morphology of their parent silica templates, but they exhibit a larger average diameter of 395 nm (inset in **Figure 4.2a**) compared with the silica core templates with an average diameter of 350 nm (**Figure 4.2c**). A high resolution SEM image of the individual particle of silica@PDA/micelles is shown in **Figure 4.2b-1**. Many round bumps with sizes of ~30 nm, a configuration matching the morphology of PS₁₇₃-*b*-PEO₁₇₀ micelles (**Figure 4.2d**), can be clearly seen from the exposed hemispheres. The appearance of the silica@PDA/micelles is similar to my previously reported PDA/micelles spheres, demonstrating successful formation of a shell composed of PDA and PS₁₇₃-*b*-PEO₁₇₀ micelles.[28] Most of the spheres retain their integrity. When a random cracked shell is observed (**Figure 4.2b-2**), it reveals that the PDA/micelles layer coats the surface of the silica core uniformly and displays a shell thickness of 24 nm, which explains the increased diameter of the silica@PDA/micelles compared with the parent silica spheres. After carbonization at 800 °C under a N₂ atmosphere, the PDA could be converted to N-doped carbon shell and those thermal pyrolysis PS₁₇₃-*b*-PEO₁₇₀ micelles were simultaneously removed to leave mesopores (**Figure 4.2e and f**). Finally, the silica template was etched by hydrogen fluoride aqueous solution (HF) to produce the N-doped hollow carbon spheres with large-sized mesoporous shells (NHCS-LM, **Figure 4.2g**). As definitely observed from the high-magnification SEM image (**Figure 4.2h**), the shells of NHCS-LM possess large mesopores (~20 nm). This result has never been realized by other studies. In addition to the large mesopores that are replicated from the removal of the micelles, abundant micropores and small mesopores that originated from the pyrolysis of PDA co-exist in the shells, which are not clear in the SEM image and can be estimated by N₂ adsorption-desorption isotherms in the following section. Moreover, as verified in my previous study, the large mesopore size in the shell inherited from the diblock copolymer micelles can be easily adjusted by regulating the different molecular weights of the PS blocks in PS-*b*-PEO, which provides flexibility for tailored applications.[28]

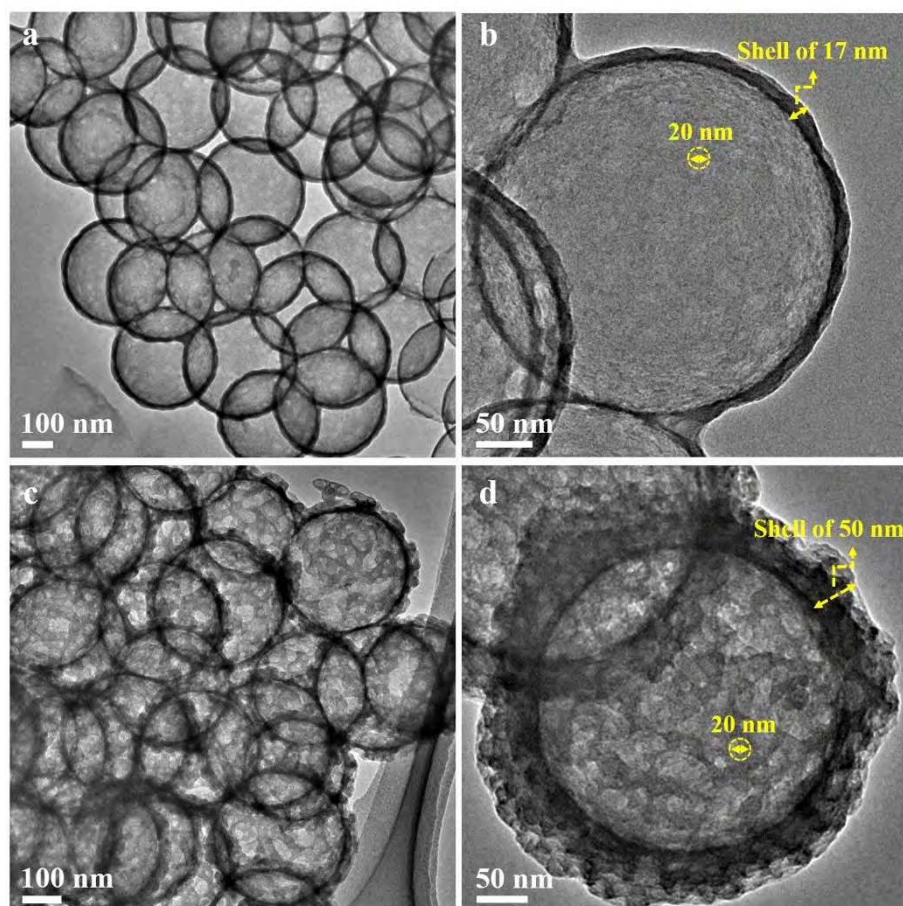


Figure 4.3 TEM images of NHCS-LM with an identical average macroporous core diameter of 350 nm but varied shell thickness: (a and b) 17 nm and (c and d) 50 nm.

The hollow structure and mesoporous shell of NHCS-LM were confirmed by transmission electron microscopy (TEM) images. As clearly shown in **Figure 4.3a**, NHCS-LM have a central hollow core with a diameter of around 350 nm, which matches the size of the silica template. The average porous shell thickness in NHCS-LM is about 17 nm, however, which is thinner than the PDA/micelles layer (24 nm), due to shrinkage of the PDA polymer during carbonization. The large mesopores that inherited from the diblock copolymer micelles in the shell also seem to appear in the TEM images (**Figure 4.3a and b**). The nitrogen content in NHCS-LM roughly estimated by energy-dispersive X-ray analysis (EDXA) is ~8 wt% (**Figure 4.4**). I further demonstrate that the thickness of the mesoporous shell is adjustable by controlling the coating times. After silica@PDA/micelles composite spheres were obtained, for example, these composite spheres have been redispersed into the ethanol solution and added

to the primary solution composed of PS₁₇₃-*b*-PEO₁₇₀ and dopamine, after which the process of coating the PDA/micelles layer has been repeated. The following carbonization and template etching steps are similar. As presented in **Figure 4.3c and d**, NHCS-LM after twice-repeated coating have an increased shell thickness of ~50 nm.

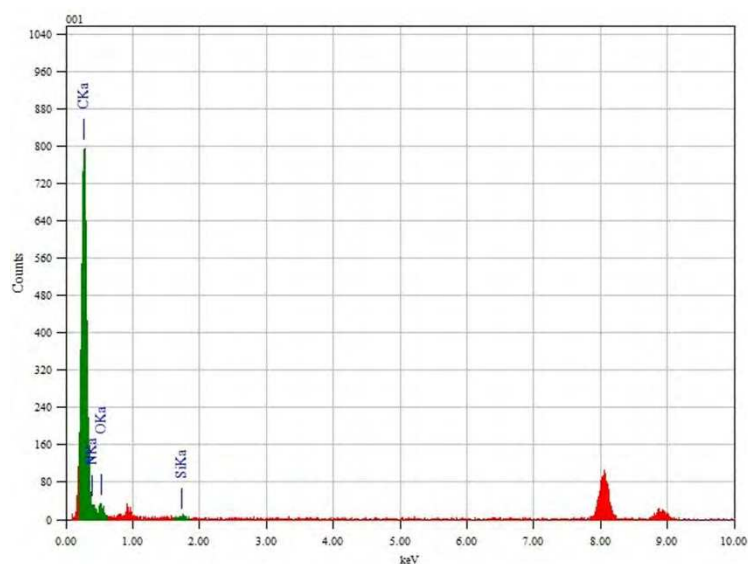


Figure 4.4 Energy-dispersive X-ray analysis (EDXA) of NHCS-LM.

The carbon state in NHCS-LM was identified by XRD and Raman spectroscopy. As shown in **Figure 4.5a**, NHCS-LM present two broad diffraction peaks at 2θ of 24° and 44° , which can be indexed to the (002) and (101) diffraction planes of the carbon and which suggest a predominantly amorphous nature of NHCS-LM.[34,35] As shown in **Figure 4.5b**, the Raman spectra of NHCS-LM show two distinct bands located at 1360 (D band) and 1590 (G band) cm^{-1} , respectively. The D band is generally related to the vibrations of disordered carbon and defects in the plane terminations, and the G band is associated with vibrations of sp^2 -bonded ordered graphitic carbon sheets.[36,37] Thus, graphitic and disordered carbons co-exist in NHCS-LM, which corresponds with the XRD result.

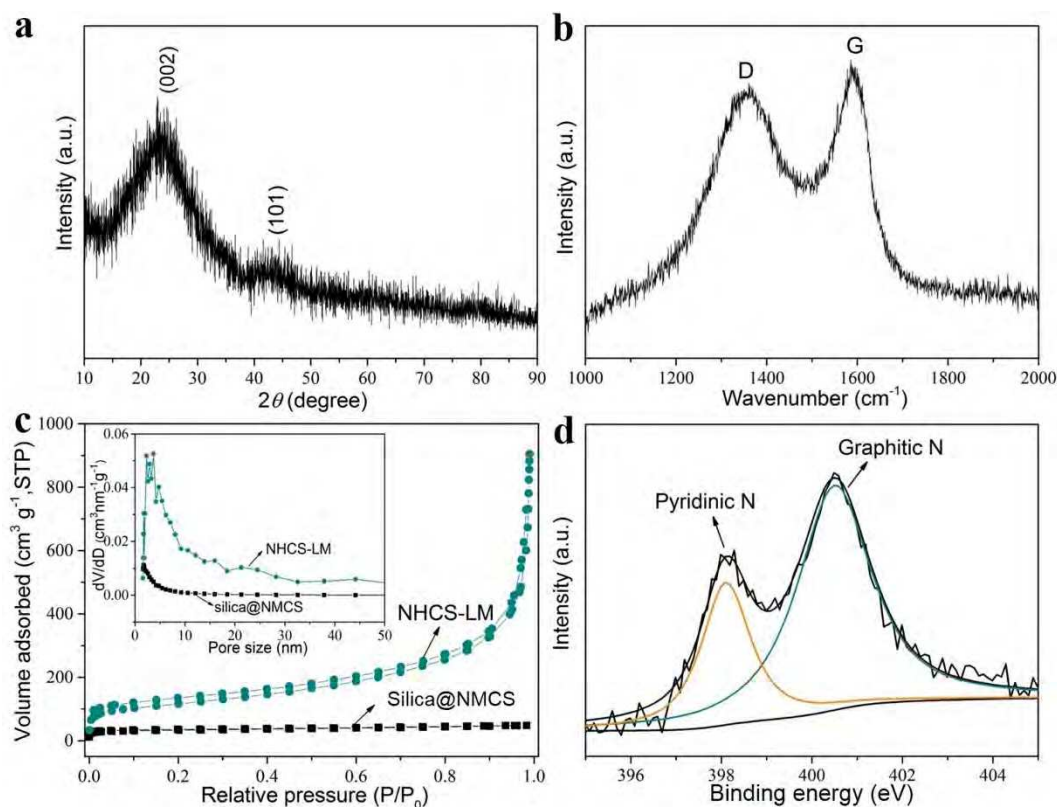


Figure 4.5 (a) Wide-angle XRD patterns, (b) Raman spectra, (c) N_2 adsorption–desorption isotherms and pore-size distributions, (d) high-resolution N 1s spectrum of an NHCS-LM sample.

The porosity and electric state of nitrogen were also determined by nitrogen sorption analysis (**Figure 4.5c**) and X-ray photoelectron spectroscopy (XPS) (**Figure 4.5d**). The N_2 adsorption–desorption isotherms of the prepared silica@NMCS and NHCS-LM before and after removal of the silica template are shown in **Figure 4.5c**, and the inset shows the pore size distribution curves. It is clear that before removal of the silica template, the nitrogen adsorption is very low in silica@NMCS. The main nitrogen adsorption in the silica@NMCS is concentrated below a relative pressure of 0.05, due to the microporosity distribution in the shell. Silica@NMCS have a poor porosity with a BET specific surface area of $94 \text{ m}^2 \cdot \text{g}^{-1}$ and a total pore volume of $0.07 \text{ cm}^3 \cdot \text{g}^{-1}$. After removal of the silica core from silica@NMCS, NHCS-LM exhibit a type II isotherm which is closely associated with the macroporous texture (**Figure 4.5c**). Aside from the obvious existence of macropores revealed by the unsaturated nitrogen adsorption at high relative pressure ($P/P_0 > 0.9$), the nitrogen uptakes at low relative pressure

($P/P_0 < 0.05$) is caused by the presence of micropores, and the gradual nitrogen uptake in the relative pressure range of $0.05 < P/P_0 < 0.9$ is associated with nitrogen adsorption in the mesopores. The absence of hysteresis loop is probably due to the very thin shell thickness (~17 nm) and the independent mesopores (~20 nm) in the shell, thus the nitrogen adsorption and desorption happened in the same relative pressure. The detailed micro- and meso-pore size distributions are analyzed based on nonlocal density functional theory using the adsorption branches of the isotherms, and the hierarchical pore size distributions are illustrated in the inset in **Figure 4.5c**. The micropores and small mesopores are mainly originated from the pyrolysis of PDA during carbonization, and the large mesopores with size around 20 nm are mostly due to the removal of the micelles as observed in SEM image (**Figure 4.2h**). The hierarchical porous structure of NHCS-LM leads to an increased BET specific surface area of $427 \text{ m}^2 \cdot \text{g}^{-1}$ and a total pore volume of $1.39 \text{ cm}^3 \cdot \text{g}^{-1}$. X-ray photoelectron spectroscopy (XPS) was also carried out, moreover, to investigate the electric state of nitrogen in the NHCS-LM. As illustrated in **Figure 4.5d**, the high-resolution N 1s spectrum of NHCS-LM can be fitted into two binding energies located at 398.1 and 400.5 eV, which are indexed to pyridinic-N and graphitic-N, respectively, demonstrating the successful doping of nitrogen into the carbon matrix of NHCS-LM.

4.3.2. The Potential Applications of NHCS-LM

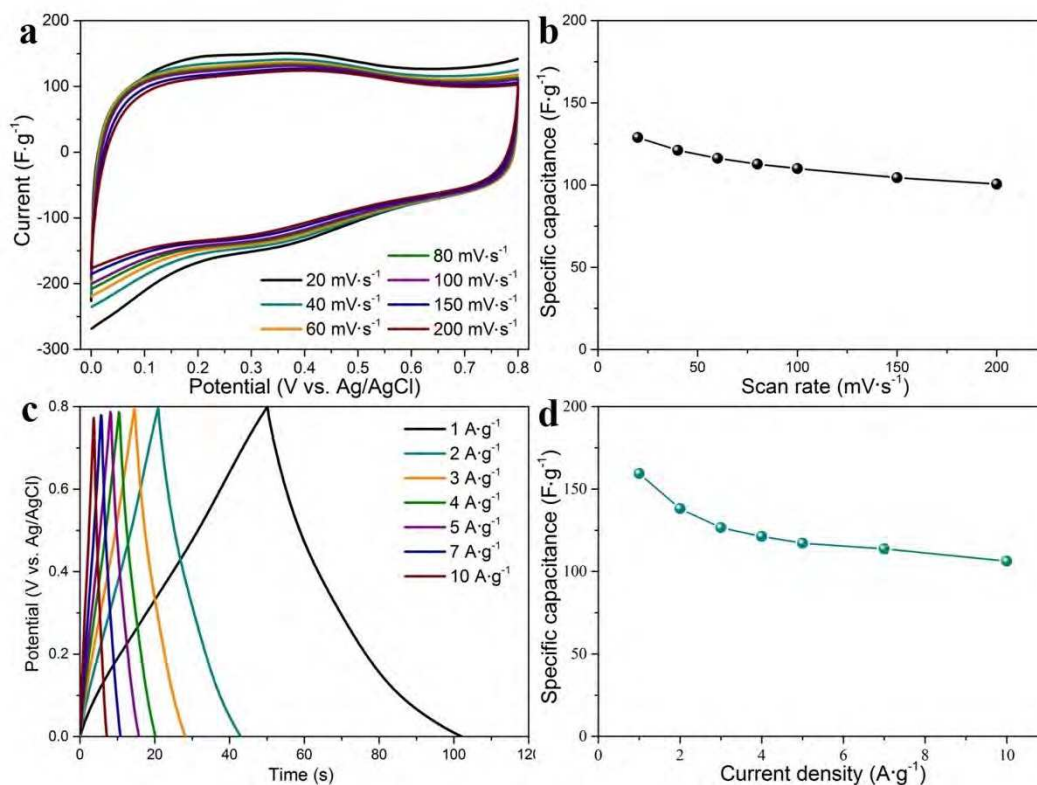


Figure 4.6 (a) Cyclic voltammograms with a potential sweep rate ranging from 20 to 200 $\text{mV}\cdot\text{s}^{-1}$, (b) specific capacitance values calculated from the cyclic voltammogram curves at different scan rates, (c) galvanostatic charge-discharge curves with a current density ranging from 1 to 10 $\text{A}\cdot\text{g}^{-1}$, and (d) specific capacitance values calculated from the galvanostatic charge-discharge curves at different current densities. All measurements were carried out in 1.0 M H_2SO_4 using a three-electrode system.

NHCS-LM synthesized by the dual-templating method in this study have a mesoporous shell with a large pore size (~ 20 nm) which has never been reported before. Combined with their large internal void space, abundant nitrogen functional groups, and large specific surface area and pore volume, NHCS-LM have a wide spectrum of potential applications. The NHCS-LM can be used, for example, as electrode materials in electric double-layer capacitors. The electrochemical properties of a NHCS-LM electrode implemented in a supercapacitor architecture were investigated by cyclic voltammetry (CV) and galvanostatic charge-discharge (GC-DC) measurements (**Figure 4.6**). The system was constructed in a three-electrode system

with a 1.0 M H₂SO₄ aqueous electrolyte. The CV curves were recorded at sweep rates ranging from 20 to 200 mV·s⁻¹. Galvanostatic charge-discharge measurements were obtained at various current densities ranging from 1 to 10 A·g⁻¹. It was observed that the NHCS-LM presented quasi-rectangular CV curves with a distinct hump (**Figure 4.6a**) and displayed quasi-linear charge-discharge curves accompanied by a slight bend (**Figure 4.6c**). These phenomena indicate that the capacitive response of NHCS-LM combines electric double-layer capacitance originating from the porous carbon with pseudo-capacitance originating from the doped nitrogen atoms.[38,39] It is noteworthy that the quasi-rectangular CV curves are only slightly distorted (**Figure 4.6a**), even at a high potential sweep rate of 200 mV·s⁻¹, implying an efficient ion transfer and rapid ion response inside the NHCS-LM electrode. The diffusion pathways and transport resistance of the electrolytes and ions are minimized due to the unique structural properties of NMCS-LM. This is because the macroporous core in NMCS-LM is able to build a buffer space for the electrolytes and the mesoporous thin wall provides free pathways for the ions, conditions favoring high-rate operation.[40,41] The specific capacitance values calculated from both the CV and GC-DC are plotted in **Figure 4.6b and d**. The NHCS-LM electrode shows a specific capacitance of 130 F·g⁻¹ and 160 F·g⁻¹ at a scan rate of 20 mV·s⁻¹ and a current density of 1 A·g⁻¹ respectively. In addition, NHCS-LM are promising candidates as drug-delivery carriers. Large-molecule drugs can easily ingress and egress the interior storage space through the large external mesoporous shell.[42] If the NHCS-LM were loaded with a sulfur element, moreover, they could be used as cathode materials in lithium-sulfur batteries. As reported in the previous work,[9] elemental sulfur can be encapsulated in the hollow core and sequestered by the shell, while the permeable mesoporous shell helps to fast-transport lithium ions to the internal sulfur.

4.4. Conclusion

In summary, I have described a dual-templating approach to N-doped hollow carbon spheres with macroporous cores and tailored large mesoporous shells (NHCS-LM). The sizes of the mesopores in the tunable shells can be easily adjusted by adopting diblock copolymers with different molecular weight. Due to the unique structural properties of NHCS-LM, including their possession of abundant nitrogen functional groups, high specific surface area of $427 \text{ m}^2 \cdot \text{g}^{-1}$, large tunable mesopores in the shell and confined internal space, NHCS-LM are expected to be promising materials for applications as adsorbents, catalyst supports, drug delivery cargos, and hosts for active substances.

References

- [1] R. J. White, K. Tauer, M. Antonietti, M.-M. Titirici, *J. Am. Chem. Soc.*, 2010, **132**, 17360.
- [2] J. Tang, J. J. Liu, N. L. Torad, T. Kimura, Y. Yamauchi, *Nano Today*, 2014, **9**, 305.
- [3] Y. Li, Y. Yang, J. Shi, M. Ruan, *Microporous Mesoporous Mater.*, 2008, **112**, 597.
- [4] S. Feng, W. Li, Q. Shi, Y. Li, J. Chen, Y. Ling, A. M. Asiri, D. Zhao, *Chem. Commun.*, 2014, **50**, 329.
- [5] J. Liu, N. P. Wickramaratne, S. Z. Qiao, M. Jaroniec, *Nat. Mater.*, 2015, **14**, 763.
- [6] J. Liu, T. Yang, D.-W. Wang, G. Q. (Max) Lu, D. Zhao, S. Z. Qiao, *Nat. Commun.*, 2013, **4**, 2798.
- [7] T. Yang, J. Liu, R. Zhou, Z. Chen, H. Xu, S. Z. Qiao, M. J. Monteiro, *J. Mater. Chem. A*, 2014, **2**, 18139.
- [8] A.-H. Lu, T. Sun, W.-C. Li, Q. Sun, F. Han, D.-H. Liu, Y. Guo, *Angew. Chem. Int. Ed.*, 2011, **50**, 11765.
- [9] N. Jayaprakash, J. Shen, S. S. Moganty, A. Corona, L. A. Archer, *Angew. Chem. Int. Ed.*, 2011, **50**, 5904.
- [10] Y. Han, X. Dong, C. Zhang, S. Liu, *J. Power Sources*, 2012, **211**, 92.
- [11] G. A. Ferrero, A. B. Fuertes, M. Sevilla, *J. Mater. Chem. A*, 2015, **3**, 2914.
- [12] Z. Lei, Z. Chen, X. S. Zhao, *J. Phys. Chem. C*, 2010, **114**, 19867.

- [13] J. Fu, Q. Xu, J. Chen, Z. Chen, X. Huang, X. Tang, *Chem. Commun.*, 2010, **46**, 6563.
- [14] C. Zhang, H. B. Wu, C. Yuan, Z. Guo, X. W. Lou, *Angew. Chem. Int. Ed.*, 2012, **51**, 9592.
- [15] Y. Meng, D. Gu, F. Q. Zhang, Y. F. Shi, H. F. Yang, Z. Li, C. Z. Yu, B. Tu, D. Y. Zhao, *Angew. Chem. Int. Ed.*, 2005, **44**, 7053.
- [16] T. Wang, C. Zhang, X. Sun, Y. Guo, H. Guo, J. Tang, H. Xue, M. Liu, X. Zhang, L. Zhu, Q. Xie, J. He, *J. Power Sources*, 2012, **212**, 1.
- [17] X. Bo, J. Bai, J. Ju, L. Guo, *J. Power Sources*, 2011, **196**, 8360.
- [18] Z.-A. Qiao, B. Guo, A. J. Binder, J. Chen, G. M. Veith, S. Dai, *Nano Lett.*, 2013, **13**, 207.
- [19] A. Chen, Y. Yu, H. Lv, Y. Wang, S. Shen, Y. Hu, B. Li, Y. Zhang, J. Zhang, *J. Mater. Chem. A*, 2013, **1**, 1045.
- [20] A.-H. Lu, W.-C. Li, G.-P. Hao, B. Spliethoff, H.-J. Bongard, B. B. Schaack, F. Schüth, *Angew. Chem. Int. Ed.*, 2010, **49**, 1615.
- [21] K. P. Gong, F. Du, Z. H. Xia, M. Durstock, L. M. Dai, *Science*, 2009, **323**, 760.
- [22] J. Tang, R. R. Salunkhe, J. Liu, N. L. Torad, M. Imura, S. Furukawa, Y. Yamauchi, *J. Am. Chem. Soc.*, 2015, **137**, 1572.
- [23] M. Zhong, E. K. Kim, J. P. McGann, S.-E. Chun, J. F. Whitacre, M. Jaroniec, K. Matyjaszewski, T. Kowalewski, *J. Am. Chem. Soc.*, 2012, **134**, 14846.
- [24] R. Liu, S. M. Mahurin, C. Li, R. R. Unocic, J. C. Idrobo, H. Gao, S. J. Pennycook, S. Dai, *Angew. Chem. Int. Ed.*, 2011, **50**, 6799.
- [25] H. Lee, S. M. Dellatore, W. M. Miller, P. B. Messersmith, *Science*, 2007, **318**, 426.
- [26] R. J. Li, K. Parvez, F. Hinkel, X. L. Feng, K. Müllen, *Angew. Chem. Int. Ed.*, 2013, **52**, 5535.
- [27] K. Ai, Y. L. Liu, C. P. Ruan, L. H. Lu, G. Q. Lu, *Adv. Mater.*, 2013, **25**, 998.
- [28] J. Tang, J. Liu, C. L. Li, Y. Q. Li, M. O. Tade, S. Dai, Y. Yamauchi, *Angew. Chem. Int. Ed.*, 2015, **54**, 588.
- [29] C. H. Xiao, X. C. Chu, Y. Yang, X. Li, X. H. Zhang, J. H. Chen, *Biosens. Bioelectron.*, 2011, **26**, 2934.

- [30] Y. M. Yu, J. H. Zhang, C. H. Xiao, J. D. Zhong, X. H. Zhang, J. H. Chen, *Fuel Cells*, 2012, **12**, 506.
- [31] Y. Fang, Y. Lv, F. Gong, Z. Wu, X. Li, H. Zhu, L. Zhou, C. Yao, F. Zhang, G. Zheng, D. Zhao, *J. Am. Chem. Soc.*, 2015, **137**, 2808.
- [32] S. Hong, Y. S. Na, S. Choi, I. T. Song, W. Y. Kim, H. Lee, *Adv. Funct. Mater.*, 2012, **22**, 4711.
- [33] F. Q. Zhang, Y. Meng, D. Gu, Y. Yan, C. Z. Yu, B. Tu, D. Y. Zhao, *J. Am. Chem. Soc.*, 2005, **127**, 13508.
- [34] J. Tang, T. Wang, X. C. Pan, X. Sun, X. L. Fan, Y. X. Guo, H. R. Xue, J. P. He, *J. Phys. Chem. C*, 2013, **117**, 16896.
- [35] J. Tang, N. L. Torad, R. R Salunkhe, J.-H. Yoon, M. S. A. Hossain, S. X. Dou, J. H. Kim, T. Kimura, Y. Yamauchi. *Chem. Asian J.*, 2014, **9**, 3238.
- [36] J. Tang, T. Wang, X. Sun, Y. X. Guo, H. R. Xue, H. Guo, M. Z. Liu, X. X. Zhang, J. P. He, *Microporous Mesoporous Mater.*, 2013, **177**, 105.
- [37] T. Wang, J. Tang, X. L. Fan, J. H. Zhou, H. R. Xue, H. Guo, J. P. He, *Nanoscale*, 2014, **6**, 5359.
- [38] F. W. Ma, H. Zhao, L. P. Sun, Q. Li, L. H. Huo, T. Xia, S. Gao, G. S. Pang, Z. Shi, S. H. Feng, *J. Mater. Chem.*, 2012, **22**, 13464.
- [39] L. F. Chen, X. D. Zhang, H. W. Liang, M. G. Kong, Q. F. Guan, P. Chen, Z. Y. Wu, S. H. Yu, *ACS Nano*, 2012, **6**, 7092.
- [40] D. W. Wang, F. Li, M. Liu, G. Q. Lu, H. M. Cheng, *Angew. Chem. Int. Ed.*, 2008, **47**, 373.
- [41] K. S. Xia, Q. M. Gao, J. H. Jiang, J. Hu, *Carbon*, 2008, **46**, 1718.
- [42] Y. Chen, P. F. Xu, M. Y. Wu, Q. S. Meng, H. R. Chen, Z. Shu, J. Wang, L. X. Zhang, Y. P. Li, J. L. Shi, *Adv. Mater.*, 2014, **26**, 4294.

Chapter 5

Thermal Conversion of Core–Shell Metal–Organic Frameworks: A New Method for Selectively Functionalized Nanoporous Hybrid Carbon

5.1. Introduction

Nanoporous carbons (NPCs), which have excellent chemical and mechanical stability, good electrical conductivity, a large specific surface area, and an adjustable pore structure, are attractive and significant materials for industrial applications as electrode materials, adsorbents, and catalyst supports.[1-6] To date, various carbon materials have been extensively studied for supercapacitor applications.[7-11] On the basis of previous research, high available surface areas are the predominant requirement for carbon-based electrodes used in supercapacitors.[12,13] Other factors such as accessible porous structures, good electrical conductivity, and surface functionalities also contribute to improve the capacitance.[14-16] Heteroatom doping (e.g., B, N, P) has been demonstrated as an effective strategy to enhance the capacitance of a carbon electrode through ameliorating the surface wettability and offering reversible pseudocapacitance effects.[17-22] Alternatively, the introduction of metals can provide additional functionalities in the carbon matrix and further promotes the applications of carbon materials, especially as electrode materials.[23-25] For example, the crystallinity and electrical conductivity of carbons can be remarkably improved by the incorporation of some specific metals (Fe, Co, and Ni) due to their effect of catalytic graphitization of amorphous carbon.[26-29] Therefore, heteroatom-doped and/or metal-modified carbons are very promising for future applications (e.g., supercapacitor) and attract much research interest.

Since the first report on metal–organic frameworks (MOFs) derived NPCs by Xu et al.,[30] several types of NPCs have been prepared by carbonization of MOFs. The parent MOFs assembled from metal ions (or clusters) with bridging organic linkers have many fascinating properties, such as an ultrahigh surface area, tunable compositions, and diverse structural topologies. In some cases, MOFs are considered as sacrificial templates, and additional carbon sources such as furfuryl alcohol are introduced into the micropores of MOFs, followed by polymerization and carbonization, to prepare NPCs.[31,32] In contrast, direct carbonization of MOFs is found to be a straightforward route for the preparation of NPCs possessing an extremely high surface area, heteroatom doping, and functional metal species.[33-37] In all the previous works, however, NPCs are prepared from a single MOFs precursor, and therefore the

expected functionalities are very limited.[38-42] In order to realize a high surface area, additional carbon sources (e.g., furfuryl alcohol) have been often filled in the MOFs, but the obtained NPCs are mainly composed of micropores, which suffer a diffusion limitation in supercapacitor application.[30,31,42] In addition, in the previous works, both high N content and highly graphitic structure are difficult to be realized at the same time because the N content largely decreases during the graphitization of NPCs.[36,41,43] The high porosity of NPCs is also seriously sacrificed during the graphitization process.[44] To overcome these issues, heterogeneous hybridization is an effective methodology to fuse the advantages of different materials and endows the hybrid materials with novel chemical and physical properties and interfacial functionality.[45-48] My target in this study is to realize selectively functionalized NPCs derived from core–shell MOFs, which can bring out novel chemical and physical properties that are not attainable from a single MOFs precursor.

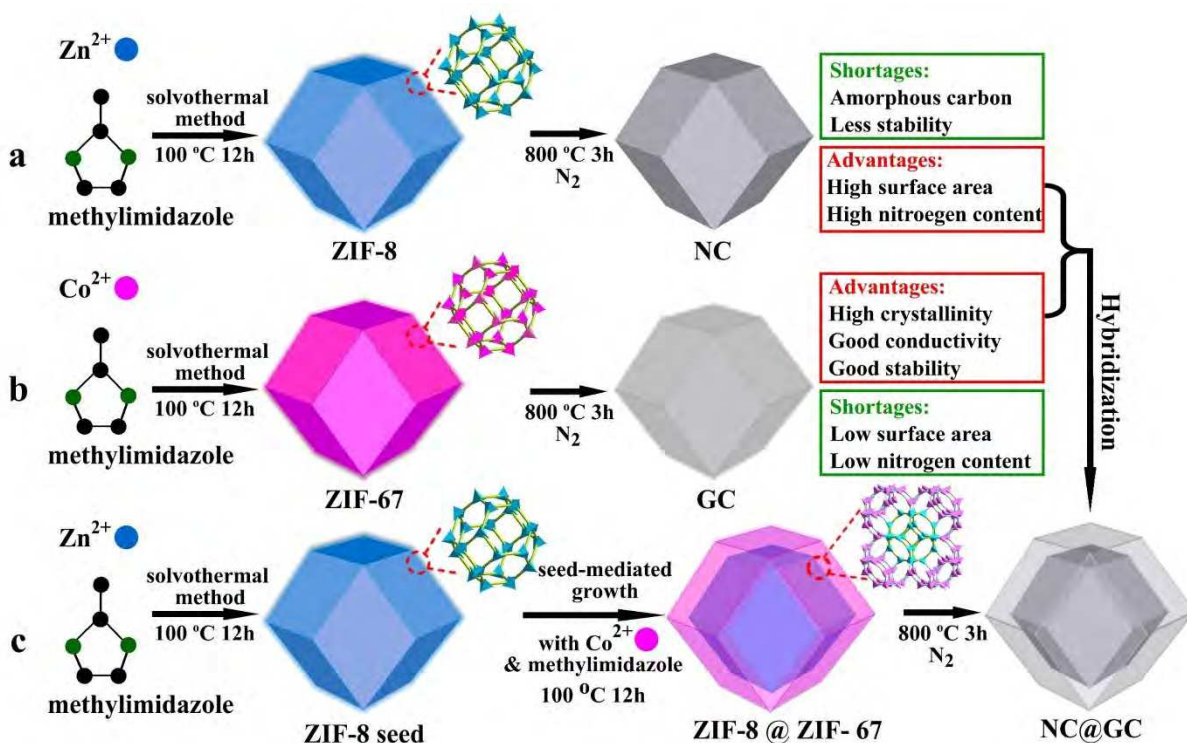


Figure 5.1 Synthetic scheme for the preparation of (a) ZIF-8 crystals and NC, (b) ZIF-67 crystals and GC, and (c) core–shell ZIF-8@ZIF-67 crystals and NC@GC.

A zeolite imidazole framework (ZIF) is a well-known subfamily of MOFs formed through the coordination interaction between the metal ions and the imidazole derivatives.[49,50] Therefore, I set out to prepare core–shell MOFs (ZIF-8@ZIF-67) crystals, which consist of ZIF-8 ($[\text{Zn}(\text{MeIm})_2]_n$) (MeIm=2-methylimidazole) crystals as the core and ZIF-67 ($[\text{Co}(\text{MeIm})_2]_n$) crystals as the shell, through a seed-mediated growth method that is usually adopted to prepare core–shell structured materials.[51-54] By thermal treatment of ZIF-8@ZIF-67 crystals, novel selectively functionalized nanoporous N-doped carbon@graphitic carbon (NC@GC) materials consisting of N-doped carbon (NC) as the core and highly graphitic carbon (GC) as the shell are successfully prepared (**Figure 5.1**). Nanoporous NC and GC materials have demonstrated different advantageous properties. Nanoporous NC prepared from ZIF-8 crystals has a relatively high N content of 16 wt% and a large specific surface area of $1499 \text{ m}^2 \cdot \text{g}^{-1}$, but the carbon is in an amorphous state. In contrast, nanoporous GC prepared from ZIF-67 crystals possesses highly graphitic walls with good conductivity due to the catalytic graphitization effect of well-dispersed Co species in the parent ZIF-67 crystals, but the specific surface area and N content are sacrificed. My novel NC@GC materials prepared from core–shell structured MOFs (ZIF-8@ZIF-67) reasonably integrate the advantageous properties of both NC and GC, including the high surface area, high N content, and graphitic structure. Furthermore, the NC@GC materials possess interconnected hierarchically micro/mesoporous structure originated from the core–shell ZIF-8@ZIF-67, which are favorable in supercapacitor. As expected, my nanoporous NC@GC electrode displayed a superior electrochemical performance in terms of capacitance and retention in comparison with nanoporous NC and GC electrodes prepared from single ZIF-8 and ZIF-67 crystals, respectively. This study not only bridges diverse carbon-based materials with infinite MOFs but also opens a new avenue for artificially designed nanoarchitectures with target functionalities.

5.2. Experimental Sections

5.2.1. Chemicals

Zinc nitrate hexahydrate ($\text{Zn}(\text{NO}_3)_2 \cdot 6\text{H}_2\text{O}$, 99%) and cobalt chloride (CoCl_2) were purchased from Sigma-Aldrich Chemical Co. 2-Methylimidazole (MeIm, purity 99%), hydrofluoric acid, and methanol were obtained from Nacalai Tesque Reagent Co. All the chemicals were used without further purification

5.2.2. Preparation of ZIF-8 Seeds with Different Particle Sizes

In a typical synthesis of ZIF-8 with a diameter of $\sim 4 \mu\text{m}$, methanolic solutions of zinc nitrate hexahydrate (810 mg, 40 mL) and methanolic solutions of MeIm (526 mg, 40 mL) were mixed under stirring. Then the mixture was transferred into an autoclave and was kept at 100 °C for 12 hours. The white powder was collected by centrifugation, washed several times with methanol, and dried at 80 °C. When the mixed methanolic solution of zinc nitrate hexahydrate and MeIm was kept at room temperature (22 °C) for 12 hours, the white particles of ZIF-8 with a diameter of 500 nm were precipitated. The size of ZIF-8 could be further decreased to ~ 50 nm by adding polyvinylpyrrolidone (PVP) as the capping agent and keeping the reaction at room temperature.

5.2.3. Preparation of ZIF-67

In the synthesis of ZIF-67 with a diameter of $\sim 5 \mu\text{m}$, a methanolic solutions (80 mL) of cobalt chloride (519 mg), polyvinylpyrrolidone (PVP) (600 mg) and MeIm (2630 mg) were mixed under stirring. Then the mixture was kept reaction at room temperature for 12 hours. The bright purple powder of ZIF-67 was collected by centrifugation, washed several times with methanol, and dried at 80 °C.

5.2.4. Preparation of Core–Shell ZIF-8@ZIF-67 Crystals

In a typical synthesis of core–shell ZIF-8@ZIF-67 crystals with micrometer-size, ZIF-8 seeds (80 mg) with diameter of $\sim 4 \mu\text{m}$ were first well-dispersed in methanol (10 mL) under sonication for 30 mins. After stirring for 20 mins, a methanolic solution of cobalt chloride (177 mg, 3 mL) and a methanolic solution of MeIm (895 mg, 3 mL) were stepwise injected into the above mixture. After stirring for another 5 mins, the mixture was transferred into an autoclave

and kept at 100 °C for 12 hours. During this time, the core–shell ZIF-8@ZIF-67 crystals were obtained. After cooling to room temperature, the resulting sample was collected by centrifugation, washed several times with methanol, and dried at 80 °C. The molar ratio of $\text{Co}^{2+}/\text{Zn}^{2+}$ in the obtained ZIF-8@ZIF-67 crystals under these typical conditions was 0.26. The shell thickness of ZIF-67 can be tuned by changing the amounts of methanolic solutions of cobalt chloride and MeIm. The obtained core–shell ZIF-8@ZIF-67 crystals with micrometer-size are noted as ZIF-8@ZIF-67(x), where x indicates the molar ratio of $\text{Co}^{2+}/\text{Zn}^{2+}$ in the product.

5.2.5. Carbonization of Core–Shell ZIF-8@ZIF-67 Crystals

Core–shell ZIF-8@ZIF-67 crystals with micrometer-size were thermally converted to NC@GC materials through carbonization under a N_2 flow at 800 °C for 3 hours, with a heating rate of 2 °C·min⁻¹. After that, the obtained samples were washed extensively by HF solution (10 wt%) to remove the deposited Zn and Co species. As a control experiment, two types of NPCs were prepared by single precursors (ZIF-8 and ZIF-67 with micrometer-size) under the same thermal conditions, which are noted as NC and GC, respectively.

5.2.6. Characterization

The morphology of the samples was characterized using a Hitachi SU-8000 field-emission scanning electron microscope (SEM) at an accelerating voltage of 5 kV. Transmission electron microscopy (TEM) and elemental mapping analysis were measured by a JEM-2100 operated at 200 kV. Wide-angle powder X-ray diffraction (PXRD) patterns were measured by a Rigaku Rint 2000 X-ray diffractometer using monochromated Cu $K\alpha$ radiation (40 kV, 40 mA) via continuous scan. In order to calculate the unit cell parameters of metal–organic framework by using Braggs' law, wide-angle powder X-ray diffraction (XRD) analysis was conducted via continuous scan by using a scan rate (angular velocity) of 0.5° min⁻¹ and step (sampling interval) of 0.02°. To get a higher quality XRD pattern, determining more precise peak position and alleviating background noise, further research can set a much slower scan rate and smaller step, such as 0.1° min⁻¹ with step of 0.01°. Carbon materials were analyzed by XRD at a scan rate of 2°·min⁻¹ with step of 0.02°. N_2 adsorption–desorption isotherms were

obtained using a Quantachrome Autosorb-iQ Automated Gas Sorption System at 77 K. The surface areas of ZIF-8, ZIF-67 and core–shell ZIF-8@ZIF-67 crystals were estimated based on the Brunauer–Emmett–Teller (BET) model and Langmuir model, respectively, by using the adsorption branch data in the relative pressure (P/P_0) range of 0.01–0.1. The surface areas of NC, GC, and NC@GC were obtained based on the BET model by using the data of adsorption branches in the relative pressure (P/P_0) range of 0.05–0.5. The total pore volumes and pore-size distributions were calculated from the adsorption branches of isotherms based on the density functional theory (DFT) method. Thermogravimetric (TG) analysis was carried out using a Hitachi HT-Seiko Instrument Exter 6300 TG/DTA in N₂ heating from room temperature to 900 °C at 5 °C·min⁻¹. X-ray photoelectron spectroscopy (XPS) spectra were measured at room temperature using a PHI Quantera SXM (ULVAC-PHI) instrument with an Al K α X-ray source. The region of survey spectra is 0 to 1400 eV and the region of high-resolution N 1s spectra is 392 to 412 eV. The percentage of N was calculated from the XPS survey spectrum by using N 1s peak. All the binding energies were calibrated via referencing to C 1s binding energy (285.0 eV). The peaks of the N 1s spectrum were fitted with a Gaussian-Lorentzian sum function and a Shirley background.

5.2.7. Electrochemical Measurements

The electrochemical measurements were conducted in a standard three-electrode electrochemical cell. Platinum and Ag/AgCl (3 M KCl) electrodes were selected as the counter electrode and reference electrode, respectively. The working electrode was prepared according to the following process. 1 mg of NC@GC materials derived from core–shell ZIF-8@ZIF-67 crystals was mixed with poly(vinylidene fluoride) (0.1 mg) and then dissolved in N-methyl-2-pyrrolidone solvent (0.5 mL). The obtained slurry was homogenized by ultrasonication, dropped onto graphite substrates (1 cm²), and dried under infrared lamp to form the thin film on the electrodes. For comparison, nanoporous NC and GC materials were prepared from single ZIF-8 and ZIF-67 crystals, respectively. The electrochemical measurements were carried out using an electrochemical workstation (CHI 660E CH Instruments) in acid electrolyte (1.0 M H₂SO₄). The electrochemical properties of the supercapacitor investigated by cyclic

voltammetry (CV) and galvanostatic charge-discharge measurements. The charge-discharge current density varied from 2 to 20 A·g⁻¹. The specific capacitance was calculated from the galvanostatic charge-discharge curves using the following equation, $C = ((I \times \Delta t)/(m \times \Delta V))$, where I is charge-discharge current at a discharge time Δt (s), ΔV is the potential range, and m is the mass of active electrode materials.

5.3. Results and Discussion

5.3.1. Synthesis and Characterization of Core–Shell ZIF-8@ZIF-67 Crystals

The core–shell MOFs (ZIF-8@ZIF-67) were prepared by a seed-mediated growth technique, as illustrated in **Figure 5.1c**. ZIF-8 and ZIF-67 are possible candidates for the preparation of core–shell MOFs (ZIF-8@ZIF-67) due to their isoreticular structures as $[M(\text{MeIm})_2]_n$ ($M = \text{Zn}$ for ZIF-8 and Co for ZIF-67) and their similar unit cell parameters between ZIF-8 ($a = b = c = 16.9910 \text{ \AA}$)[49] and ZIF-67 ($a = b = c = 16.9589 \text{ \AA}$),[50] which were determined by single crystal X-ray diffraction studies. To achieve this goal, uniformly sized ZIF-8 seeds were first synthesized by the coordination reaction of Zn^{2+} ions and MeIm. Scanning electron microscope (SEM) images confirmed that the obtained ZIF-8 consisted of uniformly dispersed crystals of rhombic dodecahedral shape, and the diameters of ZIF-8 were successfully tuned from 50 nm to 4 μm by tailoring the synthetic conditions (**Figure 5.2a-c**). As mentioned in the Experimental section, in a typical synthesis, the methanolic solution containing zinc nitrate hexahydrate and MeIm was kept at room temperature, and the ZIF-8 crystals with a diameter of around 500 nm were precipitated. When PVP was added as the capping agent, the size of the ZIF-8 crystals was significantly decreased to around 50 nm. When the methanolic solution containing zinc nitrate hexahydrate and MeIm was transferred into an autoclave and the reaction was kept at 100 °C, the micrometer-sized ZIF-8 crystals were precipitated. The ZIF-67 crystals of rhombic dodecahedral shape with a diameter of 5 μm were obtained by mixing a methanolic solutions of cobalt chloride, PVP, and MeIm and keeping the reaction at room temperature (**Figure 5.2d**).

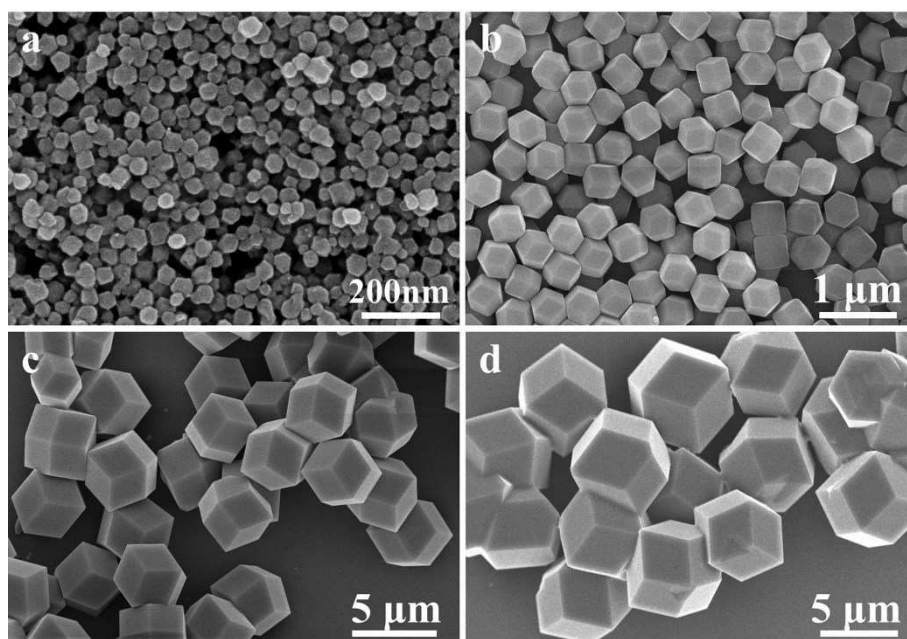


Figure 5.2 (a–c) SEM images of ZIF-8 with different diameters: (a) 50 nm, (b) 500 nm, and (c) 4 μm. (d) SEM images of ZIF-67 with diameter of 5 μm.

For the preparation of core–shell ZIF-8@ZIF-67 crystals, here I selected ZIF-8 seeds with a diameter of 500 nm or 4 μm due to their better dispersity than ZIF-8 with a diameter of 50 nm. The good dispersity is quite important for uniform coating with the ZIF-67 shell. After adding a methanolic solution of CoCl_2 , the Co^{2+} ions were immobilized on the surface of ZIF-8 seeds through the coordinative interaction with MeIm units exposed on the surface, followed by the growth of the ZIF-67 shell via the interaction with additive MeIm linkers. It is noted that ZIF-8 crystals are white, while ZIF-67 crystals are bright purple. After increasing the feeding ratio of $\text{Co}^{2+}/\text{Zn}^{2+}$ during synthesis, the color of core–shell ZIF-8@ZIF-67 crystals gradually changed from white to pink, lavender, and bright purple (**Figure 5.3**), indicating the increased shell thicknesses of the ZIF-67 layer. The obtained core–shell MOFs crystals by using ZIF-8 seeds with a diameter of 4 μm were abbreviated as ZIF-8@ZIF-67(x), where x represented the corresponding molar ratios of $\text{Co}^{2+}/\text{Zn}^{2+}$ in the products that were precisely determined by inductively coupled plasma (ICP) analysis.

In another experiment, I attempted to prepare core–shell ZIF-67@ZIF-8 crystals using the same protocol. However, no core–shell structures were observed. As seen in **Figure 5.4a**,

a mixture of ZIF-8 crystals (300 nm) and ZIF-67 crystals (5 μm) was obtained. After shaking and standing the mixture for some time (**Figure 5.4b,c**), the micrometer-sized ZIF-67 crystals first precipitated and separated with ZIF-8 crystals, suggesting the failure of preparation of core–shell ZIF-67@ZIF-8. This was most likely due to the fast nucleation reaction of ZIF-8 crystals, which did not favor heterogeneous seed-induced nucleation on the surface of ZIF-67 seeds. Thus, it is difficult to coat the ZIF-67 seeds with the ZIF-8 layer under the similar synthetic condition.

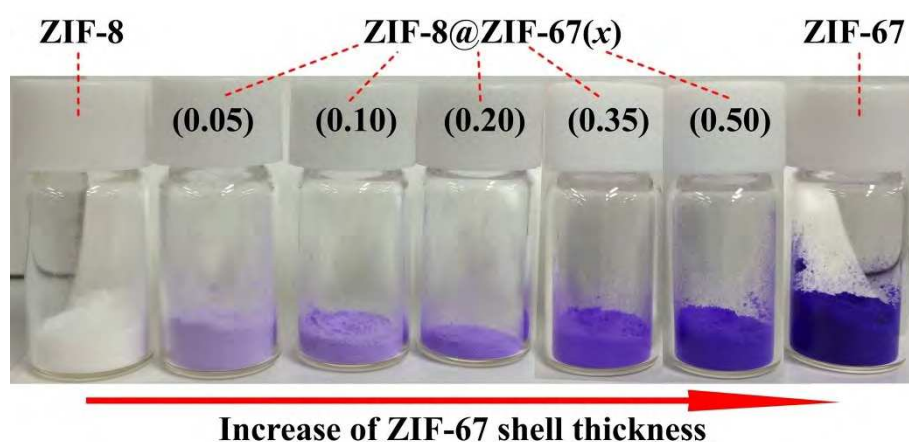


Figure 5.3 Photograph of ZIF-8, ZIF-67, and core–shell ZIF-8@ZIF-67(x) crystals prepared by using different feeding molar ratios of $\text{Co}^{2+}/\text{Zn}^{2+}$. The exact molar ratios of $\text{Co}^{2+}/\text{Zn}^{2+}$ are determined by ICP analysis and are labelled on the bottles.

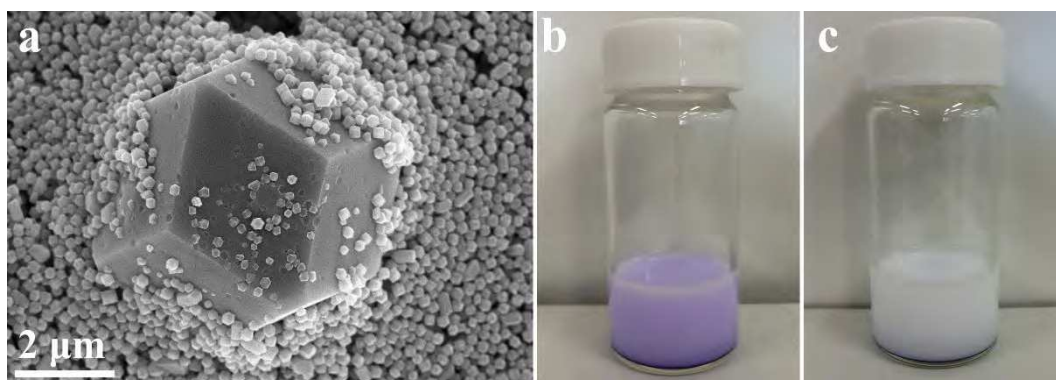


Figure 5.4 (a) SEM image of the products used to try to prepare core–shell ZIF-67@ZIF-8 crystals by using ZIF-67 (5 μm) as the seed. (b,c) Photographs of the product standing for 30 mins and 3 hours, respectively, after shaking.

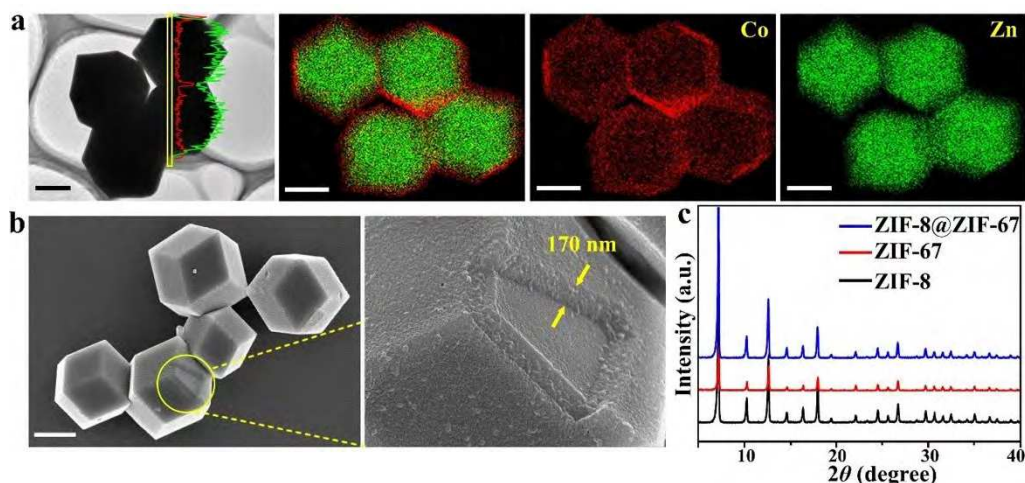


Figure 5.5 TEM image and elemental mappings of the core–shell ZIF-8@ZIF-67(0.26) crystals, (b) SEM images of core–shell ZIF-8@ZIF-67(0.26) crystals, and (c) wide-angle PXRD patterns of as-synthesized ZIF-8, ZIF-67, and ZIF-8@ZIF-67(0.26) crystals. The scale bars are all 2 μm .

The obtained core–shell ZIF-8@ZIF-67 crystals were carefully characterized. **Figure 5.5a** shows the TEM image, line scan, and elemental mappings for the representative ZIF-8@ZIF-67(0.26) crystals consisting of ZIF-8 cores and ZIF-67 shells. The molar ratio of $\text{Co}^{2+}/\text{Zn}^{2+}$ detected by energy dispersive X-ray (EDX) analysis was 0.26, which coincided with ICP data. As further proven by elemental mapping analysis (**Figure 5.6**), the core size and the shell thickness of ZIF-8@ZIF-67 crystals were easily controlled by using different sizes of ZIF-8 seeds and changing the feeding ratios of $\text{Co}^{2+}/\text{Zn}^{2+}$ during the synthesis, respectively. As shown in **Figure 5.5b**, core–shell ZIF-8@ZIF-67(0.26) crystals show well-defined rhombic dodecahedral morphology, which corresponds to the original morphology of ZIF-8 seeds (**Figure 5.2**). As shown in **Figure 5.5b**, when the edge part with cracks was observed, it was found that the ZIF-67 shell uniformly coated ZIF-8 core with a thickness of 170 nm. The wide-angle PXRD patterns of ZIF-8, ZIF-67, and core–shell ZIF-8@ZIF-67(0.26) crystals provide a better understanding of the core–shell crystals (**Figure 5.5c**). The positions of diffraction peaks of my prepared ZIF-8 and ZIF-67 crystals correspond to the PXRD patterns simulated from single crystal structures of ZIF-8[49] and ZIF-67.[50] The unit cell parameters estimated from my experimental PXRD pattern were $a = b = c = 17.1 \text{ \AA}$ for the prepared ZIF-8 crystals and were $a = b = c = 17.0 \text{ \AA}$ for the prepared ZIF-67 crystals. Because of the similar unit cell

parameters of ZIF-8 and ZIF-67 crystals, I can anticipate that the core–shell ZIF-8@ZIF-67 crystals are successfully prepared most likely via epitaxial growth and exhibit topological information identical to those of the ZIF-8 and ZIF-67 crystals. The unit cell parameters of ZIF-8@ZIF-67(0.26) crystals ($a = b = c = 17.0 \text{ \AA}$) are similar to those of ZIF-8 ($a = b = c = 17.1 \text{ \AA}$) and ZIF-67 ($a = b = c = 17.0 \text{ \AA}$), which were all calculated from the experimental PXRD patterns.

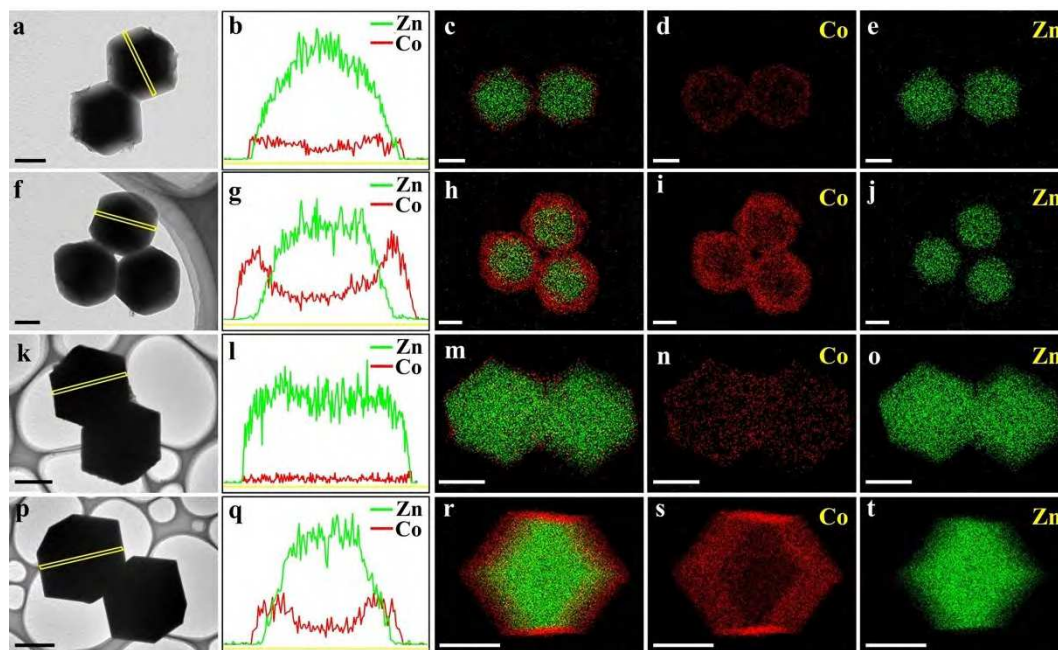


Figure 5.6 (a, f, k, and p) TEM images, (b, g, l, and q) line scans, and (c-e, h-j, m-o, and r-t) elemental mappings of the four kinds of core–shell ZIF-8@ZIF-67 crystals with different core sizes and shell thicknesses. The scale bars are all 200 nm for (a-j) and 2 μm for (k-t). The molar ratios of $\text{Co}^{2+}/\text{Zn}^{2+}$ detected by EDX analyses, core sizes, and shell thicknesses of the four samples are summarized in **Table 5.1**.

Table 5.1 Summary on the molar ratios of $\text{Co}^{2+}/\text{Zn}^{2+}$, core sizes, and shell thicknesses of the four kinds of core–shell ZIF-8@ZIF-67 crystals shown in **Figure 5.6**.

Figure No.	Molar ratio of $\text{Co}^{2+}/\text{Zn}^{2+}$	Core size (nm)	Shell thickness (nm)
Figure 5.6a-e	0.2	500	15
Figure 5.6f-j	1.5	500	89
Figure 5.6k-o	0.05	4000	33
Figure 5.6p-t	0.5	4000	290

The porosity of ZIF-8, ZIF-67, and core–shell ZIF-8@ZIF-67(0.26) crystals was measured by N₂ adsorption–desorption isotherms. As shown in **Figure 5.7a**, all of the samples displayed type I isotherms with steep N₂ uptakes at low relative pressure, which is typically associated with microporosity. The Brunauer–Emmett–Teller (BET) surface areas (S_{BET}), Langmuir surface areas (S_{Langmuir}), total pore volumes (V_{pore}), and pore sizes are summarized in **Table 5.2**. It is observable that the pore sizes for all three samples are the same. The specific surface area and the pore volume of ZIF-8@ZIF-67(0.26) crystals increase almost 10% in comparison to those of ZIF-8 and ZIF-67 crystals. Thus, there is no serious pore blocking at the interface between core ZIF-8 and shell ZIF-67 crystals. As clearly seen in wide-angle PXRD results (**Figure 5.5c**), the crystal structure and its lattice constant of ZIF-8 (core) are almost the same as those of ZIF-67 (shell). Therefore, the ZIF-67 shell can grow well on the surface of ZIF-8 crystals. As far as I know, the seed-mediated growth method reported here, for the first time, realized the preparation of novel core–shell ZIF-8@ZIF-67 crystals with controllable core sizes and adjustable shell thicknesses at the nanometer scale.

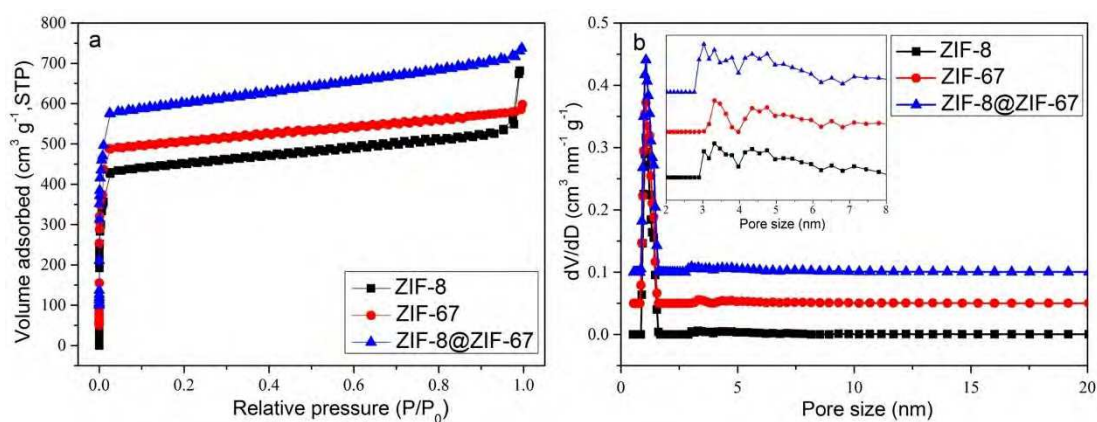


Figure 5.7 (a) N₂ adsorption–desorption isotherms and (b) pore-size distribution curves of ZIF-8, ZIF-67, and ZIF-8@ZIF-67(0.26) crystals. The region of mesopores was enlarged as inset. For clarity, the isotherms of ZIF-67 and ZIF-8@ZIF-67(0.26) are offset for 50 and 100 cm³·g⁻¹. The pore-size distribution curves for ZIF-67 and ZIF-8@ZIF-67(0.26) are offset vertically by 0.05 and 0.1 cm³·nm⁻¹·g⁻¹, respectively.

Table 5.2 Summary on the surface areas, total pore volumes, and pore sizes of ZIF-8, ZIF-67, and ZIF-8@ZIF-67(0.26) crystals.

Sample	S_{BET} ($\text{m}^2 \cdot \text{g}^{-1}$)	S_{Langmuir} ($\text{m}^2 \cdot \text{g}^{-1}$)	V_{pore} ($\text{cm}^3 \cdot \text{g}^{-1}$)	Pore size (nm)
ZIF-8	1727	1955	0.76	1.1
ZIF-67	1738	1963	0.73	1.1
ZIF-8@ZIF-67(0.26)	1910	2159	0.85	1.1

5.3.2. Thermal Conversion of Core–Shell ZIF-8@ZIF-67 Crystals to Nanoporous NC@GC Materials

The obtained ZIF-8@ZIF-67 crystals were thermally treated at 800 °C under a N₂ flow. Thermogravimetric (TG) curves for ZIF-8, ZIF-67, and ZIF-8@ZIF-67(0.26) crystals measured under a N₂ atmosphere are shown in **Figure 5.8**. Core–shell ZIF-8@ZIF-67(0.26) crystals were thermally stable up to 470 °C. This stability was almost the same as ZIF-67 crystals (460 °C) but was lower than ZIF-8 crystals (550 °C). Then the weight of the crystals decreased rapidly along with the continued increase of temperature. During the heat treatment under N₂ atmospheres, organic linkers thermally carbonized into carbon networks, and parts of organic linkers decomposed and evaporated in the form of small molecules (e.g., H₂O, CO₂).[40,55] Compared to the initial weight of ZIF-8, ZIF-67, and ZIF-8@ZIF-67(0.26) crystals, a 49–56 wt% loss (**Table 5.3**) was detected at 900 °C by TG analysis. After the carbonization, the products were washed with an HF solution to remove the residual Zn and/or Co species. NC, GC, and NC@GC(*x*) samples were prepared from ZIF-8, ZIF-67, and ZIF-8@ZIF-67(*x*), respectively.

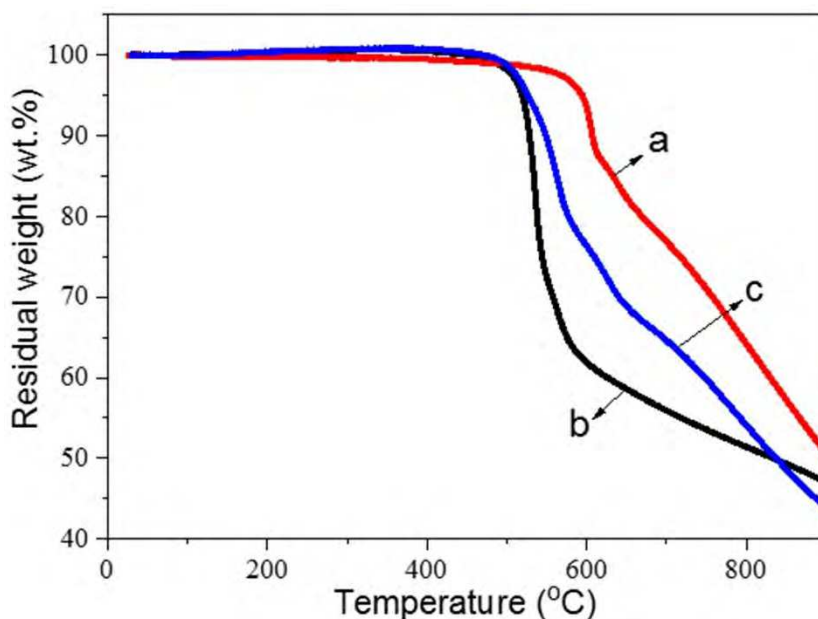


Figure 5.8 TG curves of (a) ZIF-8, (b) ZIF-67, and (c) ZIF-8@ZIF-67(0.26) crystals measured under N₂ atmosphere.

Table 5.3 Summary on the maximum temperature before the decomposition of ZIFs begins and the remaining weight (%) of ZIFs at 900 °C during TG analysis shown in **Figure 5.8**, assigned as T_{\max} and $W_{900\%}$, respectively.

Sample	T_{\max} (°C)	$W_{900\%}$
ZIF-8	550	50.6
ZIF-67	460	47.1
ZIF-8@ZIF-67(0.26)	470	43.8

As revealed by SEM images (**Figure 5.9a**), the obtained nanoporous NC particles retain the original rhombic dodecahedron shape from the parent ZIF-8 and exhibit a smooth surface without any large pores or cracks. In contrast, the nanoporous GC particles prepared from ZIF-67 shrink significantly and show a distorted, bumpy surface (**Figure 5.9d**). A similar situation was observed with NC@GC particles prepared from ZIF-8@ZIF-67 crystals (**Figure 5.9g,j**). With the increase of ZIF-67 shell thickness, the NC@GC(0.35) particles that carbonized from ZIF-8@ZIF-67(0.35) with a thick ZIF-67 shell display a more seriously distorted surface than NC@GC(0.05) carbonized from ZIF-8@ZIF-67(0.05) with a thin ZIF-67 shell (**Figure 5.9g**,

j). A more detailed porous structure and graphitic degree of the samples were investigated by TEM and high-resolution TEM (HRTEM). As seen in **Figure 5.9c**, no graphitic carbon structures are observed in NC particles, indicating that the particles are composed of disordered carbon (amorphous carbon) networks.

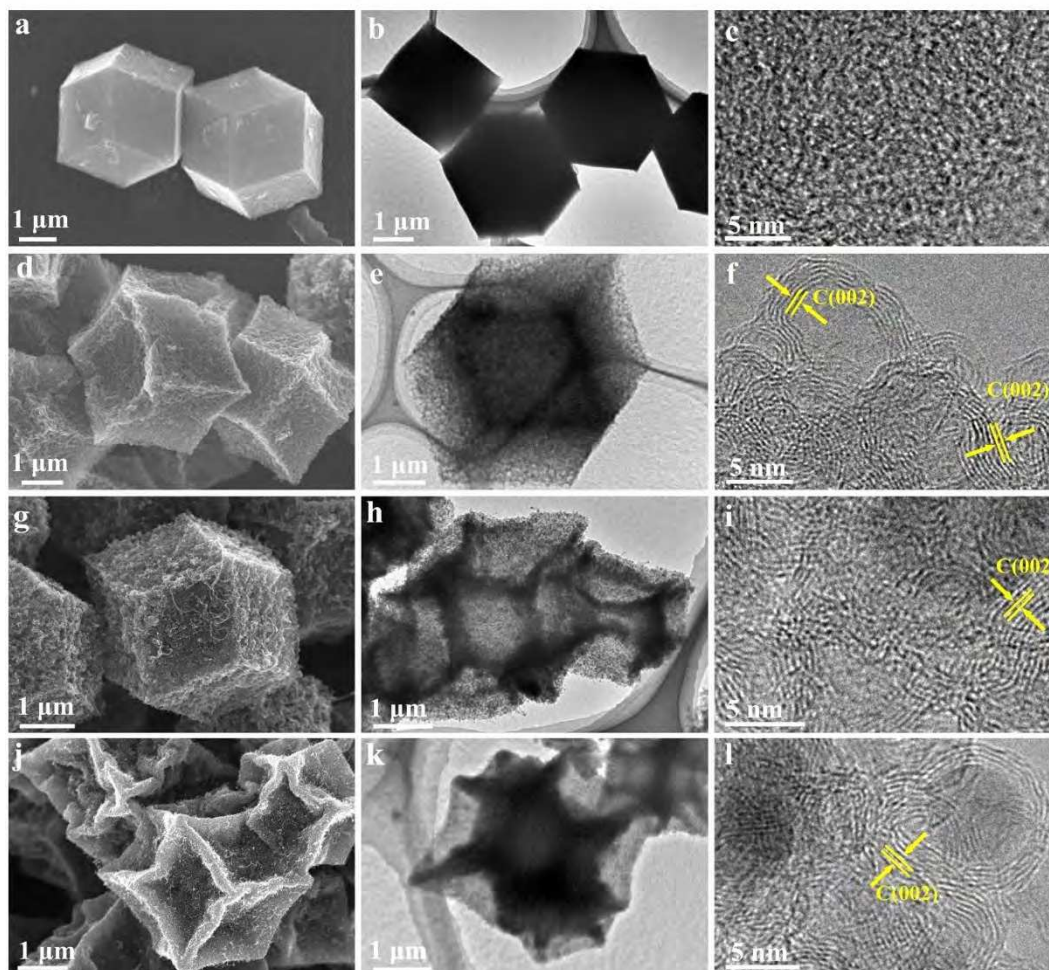


Figure 5.9 SEM images (a,d,g,j), TEM images (b,e,h,k), and HRTEM images (c,f,i,l) of NC (a-c), GC (d-f), NC@GC(0.05) (g-i), and NC@GC(0.35) (j-l).

Furthermore, there are no distinct pores shown in NC (**Figure 5.10a**) due to the mainly micropores with size smaller than 2 nm. In contrast, both GC and NC@GC particles show distinct mesopores over the particle surface and abundant layered graphitic carbon structures with a typical distance value of graphite (0.334 nm), as revealed in **Figure 5.9f,i,l** and **Figure 5.10b-d**. Through careful observation by HRTEM, it is found that the graphitic carbons are formed by catalytic graphitization of amorphous carbon on the deposited Co nanoparticles.[56,57] Most of the Co nanoparticles are in uniform size and spherical shape

(with diameter of around 3–4 nm) and they are easily removed by chemical etching (**Figure 5.9f** and **Figure 5.10b–d**), but there are some remaining Co nanoparticles with large size (over 7 nm) enclosed by well-developed graphitic layers. Because of such protection, it is difficult to completely remove the Co nanoparticles. The graphitization of amorphous carbon and the removal of Co species are supposed to induce the creation of a bumpy (rough) surface, as mentioned above (**Figure 5.9**). The particle shapes observed from TEM images (**Figure 5.9b,e,h,k**) are in accordance with SEM images (**Figure 5.9a,d,g,j**). From the elemental mapping analysis, it is revealed that the N content is more concentrated at the center of the particles, while the remaining Co nanoparticles are mostly observed only in the shell region (**Figure 5.11**). Thus, NC@GC particles with N-doped amorphous carbon cores and highly graphitic carbon shells are successfully obtained.

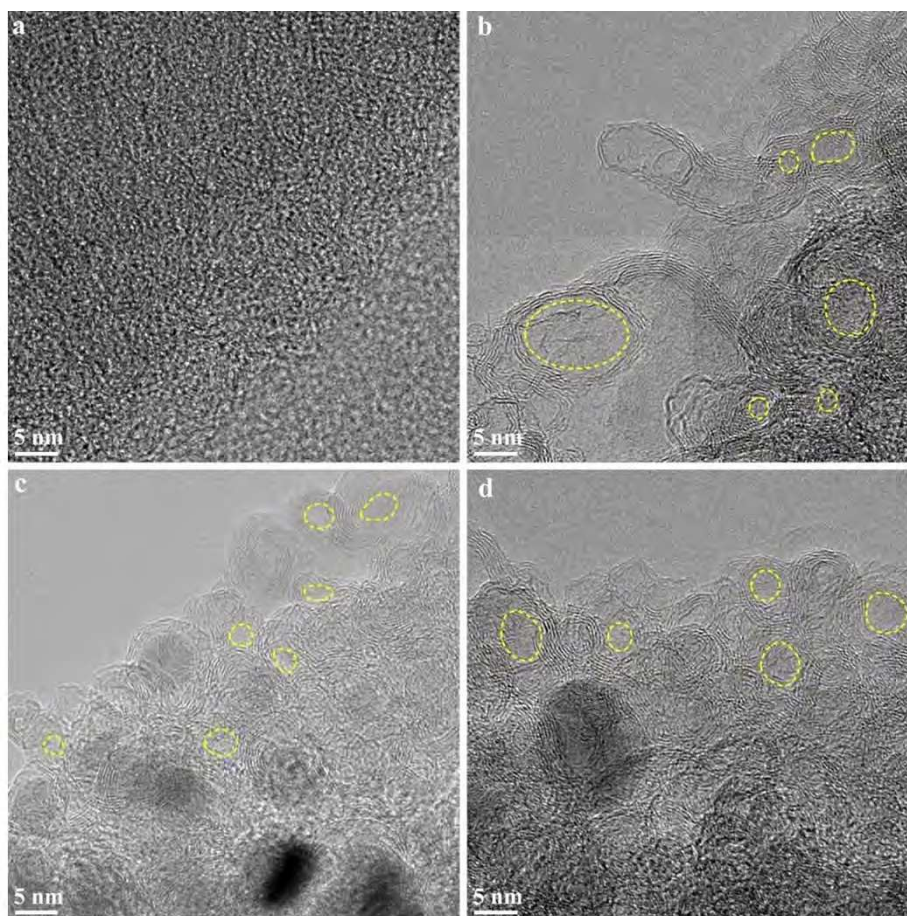


Figure 5.10 High resolution TEM images of the NC (a), GC (b), NC@GC(0.05) (c), and NC@GC(0.35) (d). The formed mesopores are indicated by circles.

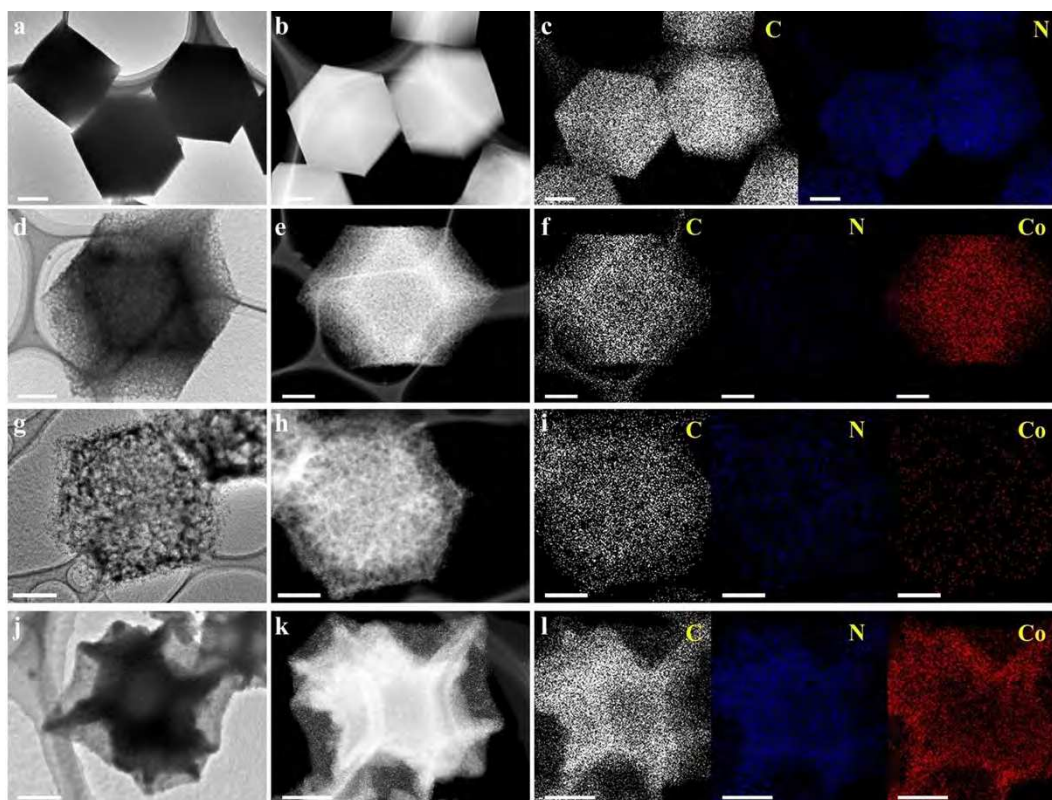


Figure 5.11 (a,d,g,j) TEM, (b,e,h,k) high-angle annular dark-field scanning TEM (HAADF-STEM) images, and (c,f,i,l) elemental mappings of (a-c) NC, (d-f) GC, (g-i) NC@GC(0.05), and (j-l) NC@GC(0.35). The scale bars are 1 μm .

Wide-angle XRD patterns for nanoporous NC exhibited two broad diffraction peaks at 25° and 44° that are identical to the (002) and (101) diffractions of amorphous carbon (**Figure 5.12a**). In the case of GC, NC@GC(0.05), and NC@GC(0.35), the (002) diffraction peaks were significantly shifted toward 26° , suggesting the formation of a graphitic carbon structure (**Figure 5.12b**).^[58,59] The other intense diffraction peaks located at around 44° and 51° were indexed to the (111) and (200) diffractions of face-centered-cubic (*fcc*) Co crystal (**Figure 5.12a**).^[56,57] The average particle sizes of the remaining Co nanoparticles not completely dissolved by HF treatment are estimated to be around 7-8 nm, which coincides with the TEM data (**Figure 5.9l**).

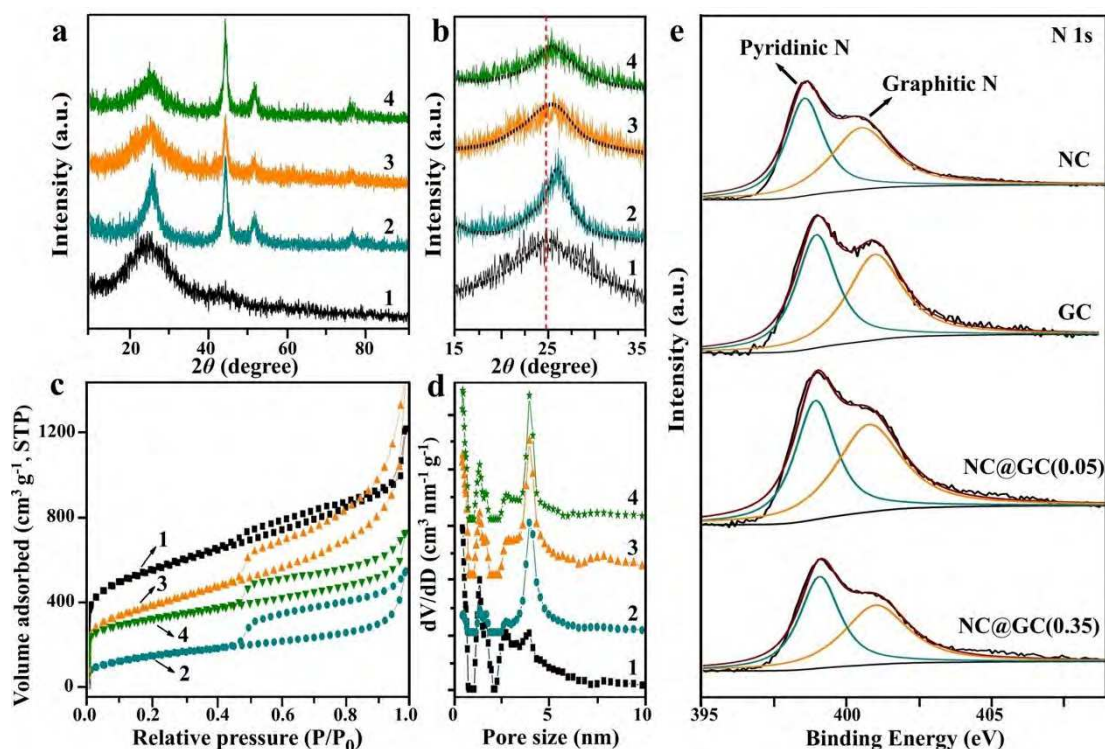


Figure 5.12 (a) Wide-angle XRD patterns, (b) enlarged XRD diffraction peaks, (c) N_2 adsorption–desorption isotherms, (d) pore-size distributions, and (e) high-resolution N 1s spectrum of the (1) NC, (2) GC, (3) NC@GC(0.05), and (4) NC@GC(0.35) samples. For clarity, the isotherms for (1) and (4) are offset by 100 and 50 $\text{cm}^3 \cdot \text{g}^{-1}$, respectively. The pore-size distribution curves for (2), (3), and (4) are offset vertically by 0.05, 0.10, and 0.15 $\text{cm}^3 \cdot \text{nm}^{-1} \cdot \text{g}^{-1}$, respectively.

Table 5.4 Surface areas and total pore volumes of NC, GC, NC@GC(0.05), and NC@GC(0.35)

Sample	S_{BET} ($\text{m}^2 \cdot \text{g}^{-1}$)	S_{micro} ($\text{m}^2 \cdot \text{g}^{-1}$)	$S_{\text{micro}}/S_{\text{BET}}$ (%)	V_{pore} ($\text{cm}^3 \cdot \text{g}^{-1}$)	V_{micro} ($\text{cm}^3 \cdot \text{g}^{-1}$)	$V_{\text{micro}}/V_{\text{pore}}$ (%)	N content (atomic %)
NC	1499	378	25.2	1.31	0.18	13.7	16.1
GC	496	49	10.0	0.71	0.02	2.8	5.7
NC@GC(0.05)	1276	274	21.5	1.78	0.13	7.3	10.6
NC@GC(0.35)	813	120	14.7	0.89	0.04	4.5	8.5

The surface areas and pore-size distributions were investigated by N_2 adsorption–desorption isotherms (**Figure 5.12c–d**). The sharp uptakes at low relative pressure (< 0.05) indicate the presence of micropores. The hysteresis loops and the gradual uptakes at a

relative pressure range from 0.45 to 0.95, which are caused by the capillary condensation of N₂ in the mesopores with wide size distributions, are more distinct in the GC and NC@GC samples. Such hysteresis loops have often been observed in mesoporous materials (e.g., SBA-type mesoporous silica).[60,61] The mesopores in the ZIF-derived carbons are bumpy, random and interconnected. The sizes of the mesopores are also not uniform. During the adsorption process along with the increased relative pressure, the nitrogen was condensed first within the smallest dimensions. The pressure increased until all pores were filled with nitrogen. Then the pressure decreased and induced desorption of nitrogen. Because the last filled large mesopores were connected with a few small mesopores, the nitrogen desorption in the same large mesopores happened at a lower relative pressure compared with adsorption process, leading to the formation of a hysteresis loop. Thus, the interconnected hierarchically micro/mesoporous structures are well-developed, as confirmed by the pore size distributions for each sample. The mesopores in GC and NC@GC are mainly generated by the carbonization process and the subsequent removal of Co nanoparticles with relatively small size (3-4 nm). Therefore, the mesopores are not uniform. The specific surface area (S_{BET}) and pore volume (V_{pore}) for the samples are summarized in **Table 5.4**. The NC sample possesses a high specific surface area of 1499 m²·g⁻¹, which is a bit lower than that of the parent ZIF-8 crystals (1727 m²·g⁻¹). However, the specific surface area of the GC sample with a highly graphitic structure is dramatically decreased to 496 m²·g⁻¹. The value is extremely low in comparison to the original ZIF-67 crystals (1738 m²·g⁻¹) due to the collapse of the well-defined microporous structure of ZIF-67 caused by the graphitization of amorphous carbon.[36,40] Furthermore, the ratio of the microporous surface area ($S_{\text{micro}}/S_{\text{BET}}$) in NC (25.2%) is much higher than that in GC (10.0%), confirming the presence of a large amount of mesopores in GC. As I expected, the surface areas of the NC@GC samples are the intermediate value between NC and GC. The NC@GC(0.05) sample with a thin GC shell show a higher specific surface area (1276 m²·g⁻¹) than the NC@GC(0.35) sample with a thick GC shell (813 m²·g⁻¹), which also indirectly proves a successful tuning of the GC shell thickness.

The electric state of N in the carbon matrix was carefully investigated by X-ray photoelectron spectroscopy (XPS). The N 1s spectra of all the samples can be mainly deconvoluted into two peaks centered at ~ 398.8 and ~ 400.8 eV, which are assignable to pyridinic-N and graphitic-N, respectively (**Figure 5.12e**). Pyridinic-N, referring to the sp^2 -hybridized N atoms bonded with two sp^2 -hybridized C neighbours via σ -bonds, possesses one lone-pair of electrons in the graphene plane, and contributes one electron to the conjugated π system.[62] In the graphitic-N configuration, three sp^2 -hybridized N valence electrons form three σ -bonds with three sp^2 -hybridized C neighbours, one electron fills the π -orbitals, and the fifth electron enters the π^* -states of the conduction band.[63] According to another report, the fifth electron is distributed in the local network of the carbon π -system whereas a part of the charge localizes on the graphitic-N dopant and electronically couples to its nearest C neighbours.[64] It is revealed that the N atoms in the pentagonal ring of the original imidazole units are mostly converted into two types of N states during the carbonization process. The N atoms are steadily doped into the carbon structure. The percentages of doped N content estimated from the XPS spectrum are 16.1 atomic% (for NC), 5.7 atomic% (for GC), 10.6 atomic% (for NC@GC(0.05)), and 8.5 atomic% (for NC@GC(0.35)). It is likely that the C-N bonds are partially destroyed during the catalytic graphitization process in the ZIF-67 crystals, thereby leading to the lower N content in the GC and NC@GC samples.[41,43,65]

5.3.3. Electrochemical Supercapacitors with NC@GC Electrodes

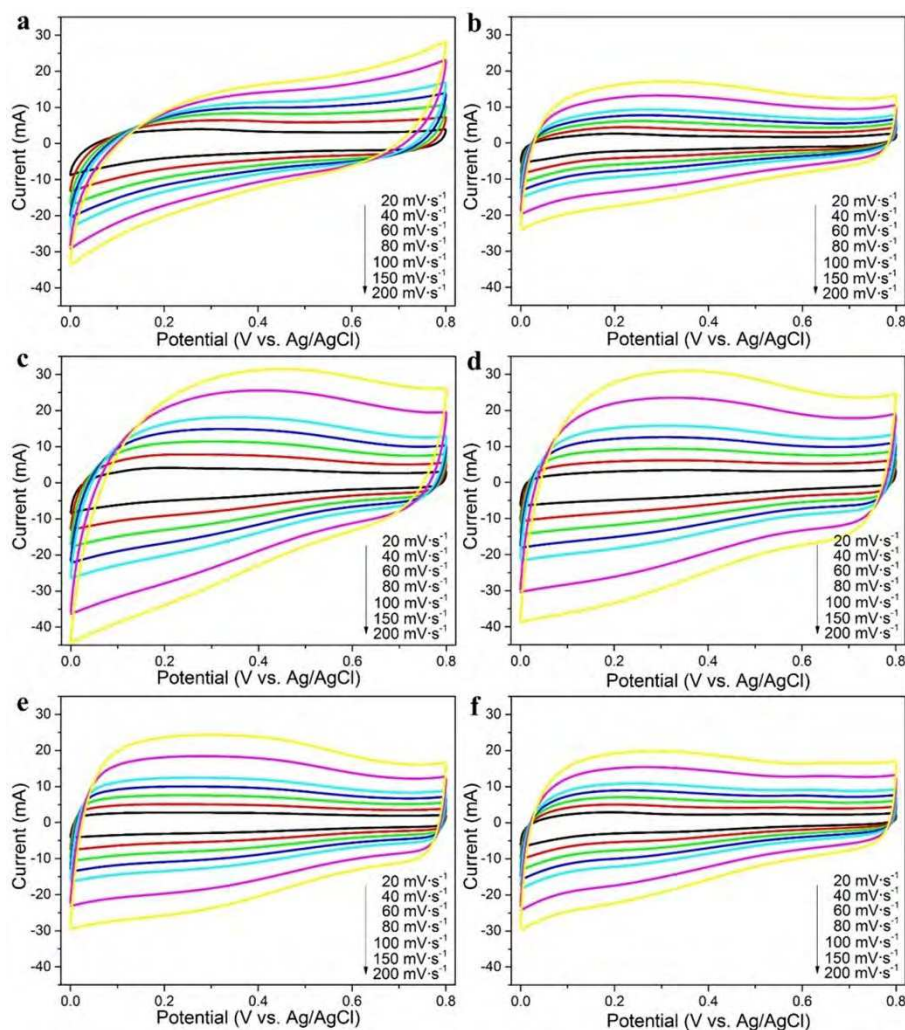


Figure 5.13 Cyclic voltammograms of (a) NC, (b) GC, (c) NC@GC(0.05), (d) NC@GC(0.15), (e) NC@GC(0.35), and (f) NC@GC(0.5) electrodes at various scan rates in a range from 20 to 200 $\text{mV}\cdot\text{s}^{-1}$. All measurements were conducted in 1.0 M H_2SO_4 .

A supercapacitor is an electrochemical energy-storage device that can rapidly store and give out energy over a number of repeated cycles.[66,67] This unique feature makes it a promising candidate to meet the increasing power demands in the field of portable electronic devices, hybrid electric vehicles, and memory backup. To evaluate the electrochemical properties NC, GC, and NC@GC electrodes, the cyclic voltammetry (CV) measurements using a standard three-electrode system were carried out in a 1.0 M H_2SO_4 aqueous electrolyte. The CV curves of NC, GC, and NC@GC electrodes conducted at different potential scan rates are

shown in **Figure 5.13**. The distinct appearance of humps in the rectangular-like shape CV curves reveals that the capacitive response derived from the combination of electric double-layer capacitance (EDLC) and pseudocapacitance due to the nitrogens doped in carbons.[21, 68, 71]

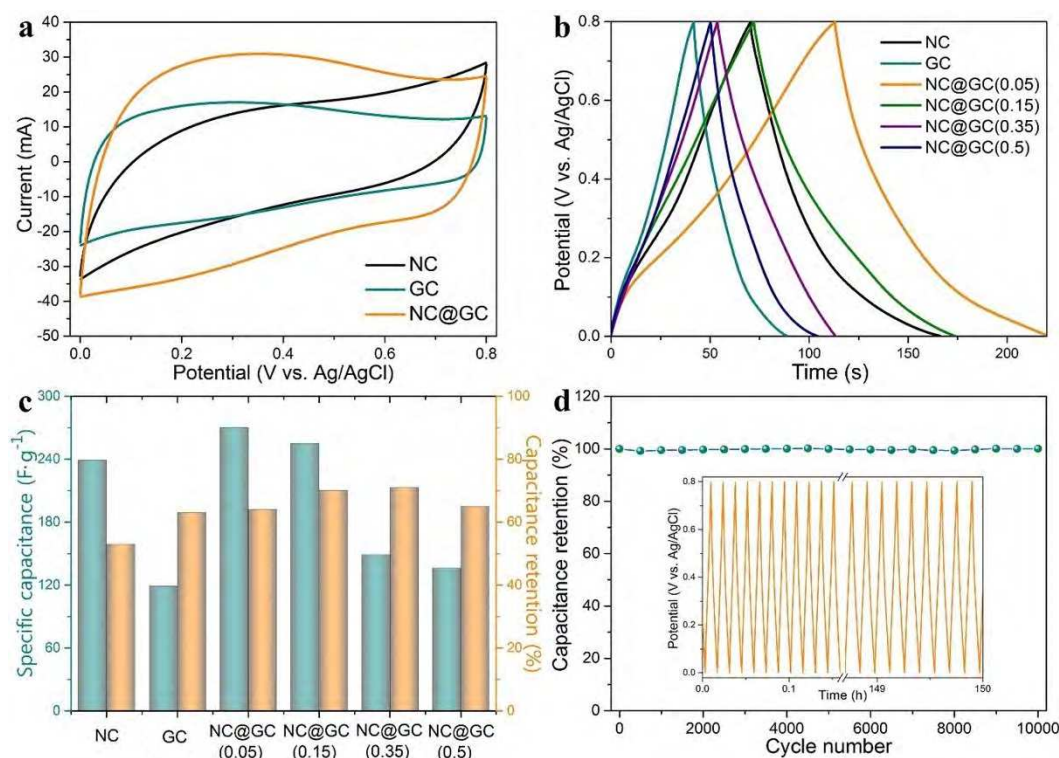


Figure 5.14 (a) Cyclic voltammograms at a potential scan rate of $200 \text{ mV} \cdot \text{s}^{-1}$ for NC, GC, and NC@GC(0.15). (b) Charge-discharge curves of NC, GC, NC@GC(0.05), NC@GC(0.15), NC@GC(0.35), and NC@GC(0.5) electrodes at a current density of $2 \text{ A} \cdot \text{g}^{-1}$. (c) The specific capacitance values obtained at a current density of $2 \text{ A} \cdot \text{g}^{-1}$ and the respective capacitance retention ratios at a higher current density of $10 \text{ A} \cdot \text{g}^{-1}$ for NC, GC, NC@GC(0.05), NC@GC(0.15), NC@GC(0.35), and NC@GC(0.5) electrodes. (d) Cyclic stability of NC@GC(0.15) at a charge-discharge current density of $5 \text{ A} \cdot \text{g}^{-1}$ for 10000 cycles. Inset shows the galvanostatic charge-discharge curves. All measurements were conducted in $1.0 \text{ M H}_2\text{SO}_4$ by using a three-electrode system.

The CV curves of NC, GC, and the representative NC@GC(0.15) electrodes at a high potential scan rate of $200 \text{ mV} \cdot \text{s}^{-1}$ are shown in **Figure 5.14a**. It is observed that NC displays a

distorted rectangular CV shape, whereas GC and NC@GC(0.15) electrodes present a quasi-rectangular CV shape. I infer that the ion-diffusion limitation in micropores is the predominant factor that leads to distorted rectangular CV shape at high potential scan rate.[11,15,72] As concluded in **Table 5.4**, although NC possesses a higher specific surface area than GC and NC@GC, the ratio of micropores/mesopores is much higher in NC. Therefore, the serious ion-transfer resistance in the inner micropores, especially at a high potential scan rate, leads to the distorted CV shape.[11,30,72] In addition, nanoporous NC prepared from ZIF-8 crystals is in an amorphous state; therefore, the electrical conductivity mainly controlled by the crystallinity of carbon is not as satisfied as GC and NC@GC under high-rate operation.[68]

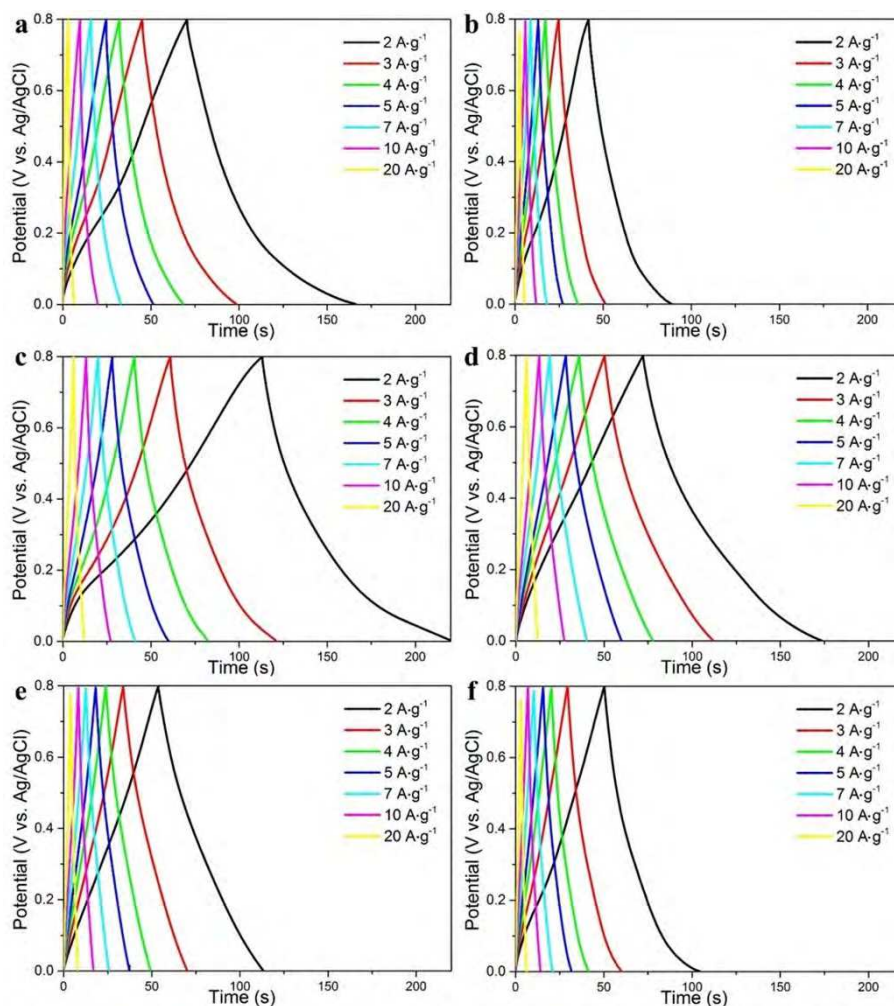


Figure 5.15 Charge-discharge curves of (a) NC, (b) GC, (c) NC@GC(0.05), (d) NC@GC(0.15), (e) NC@GC(0.35), and (f) NC@GC(0.5) electrodes at different current densities ranges from 2 to 20 $\text{A}\cdot\text{g}^{-1}$. All measurements were conducted in 1.0 M H_2SO_4 .

In order to evaluate the specific capacitance and get further insight into the electrochemical performance of the NC, GC, and NC@GC electrodes, a galvanostatic charge-discharge measurement that is a frequently-used technique for capacitance evaluation was carried out at various current densities in a three-electrode system (**Figure 5.15**). The galvanostatic charge-discharge curves of all electrodes conducted at a current density of $2 \text{ A} \cdot \text{g}^{-1}$ are shown in **Figure 5.14b**. All of the electrodes display a quasi-linear appearance with a slight bend, implying the impact of pseudocapacitance derived from N doping.[11,21,68,71,72] The specific capacitance values are calculated from the galvanostatic charge-discharge curves since it is considered to be a more accurate technique especially for EDLC materials.[31,71,72] As shown in the **Figure 5.14c**, the specific capacitance values obtained at a current density of $2 \text{ A} \cdot \text{g}^{-1}$ are NC ($239 \text{ F} \cdot \text{g}^{-1}$), GC ($119 \text{ F} \cdot \text{g}^{-1}$), NC@GC(0.05) ($270 \text{ F} \cdot \text{g}^{-1}$), NC@GC(0.15) ($255 \text{ F} \cdot \text{g}^{-1}$), NC@GC(0.35) ($149 \text{ F} \cdot \text{g}^{-1}$), and NC@GC(0.5) ($136 \text{ F} \cdot \text{g}^{-1}$). The retention in specific capacitance at a higher current density of $10 \text{ A} \cdot \text{g}^{-1}$ for NC, GC, NC@GC(0.05), NC@GC(0.15), NC@GC(0.35), and NC@GC(0.5) is 53, 63, 64, 70, 71, and 65%, respectively. It is well known that the high specific surface area of carbon materials usually leads to high capacitance, and N doping is able to increase the capacitance by bringing about pseudocapacitance and ameliorating surface wettability.[17,69-72] Electrical conductivity, which is determined by the graphitic degree in carbon materials, is also crucial for capacitance by reducing the internal resistance. As discussed above, the NC@GC materials integrate the advantages of a high specific surface area and high N content in the NC core and a high graphitic degree in the GC shell, which can synergistically contribute to the high capacitance of a NC@GC electrode. Furthermore, the developed network of mesopores are also able to be accessed more freely and quickly by electrolyte ions,[73,74] even though the micropores are responsible for charge accommodation.[17,18,44,74-76] Thus, the NC@GC(0.15) electrode consisting of the mediate graphitic carbon shell and highly porous carbon core exhibits the best electrochemical performance (specific capacitance of $255 \text{ F} \cdot \text{g}^{-1}$ with retention of 70 %) compared to the other samples (**Figure 5.14c**) due to its optimized physicochemical properties. For a thinner GC shell, the capacitance value of the NC@GC(0.05) electrode is a bit higher ($270 \text{ F} \cdot \text{g}^{-1}$); however, the

retention in capacitance of NC@GC(0.05) electrode (64%) is much lower than that of the NC@GC(0.15) electrode (70%). Moreover, as I continue increasing the thickness of the GC shell, the specific capacitance value is found to be decreased in NC@GC(0.35) and NC@GC(0.5) electrodes. As demonstrated by the N₂ adsorption–desorption analysis (**Table 5.4**), the effective specific surface areas of NC@GC derived from ZIF-8@ZIF-67 crystals with a thicker ZIF-67 shell drastically decline due to the excessive graphitization of amorphous carbon in the thick GC shell, which ultimately decreases the capacitance value. The long-term cyclic stability of the representative NC@GC(0.15) electrode was investigated by using galvanostatic charge-discharge experiments at a current density of 5 A·g⁻¹ within a potential window of 0–0.8 V (vs. Ag/AgCl). As shown in **Figure 5.14d**, the capacitance retention is almost 100% during all 10000 cycles, indicating an excellent stability of NC@GC(0.15).

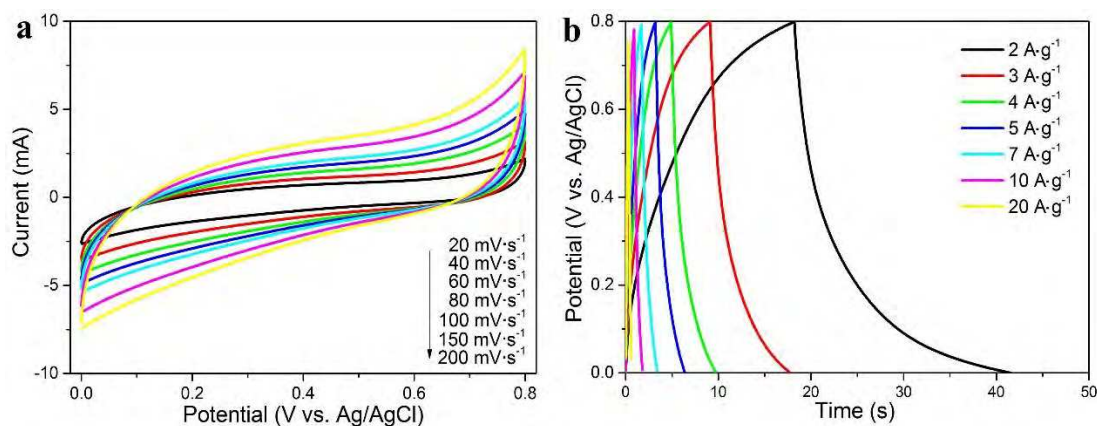


Figure 5.16 (a) Cyclic voltammograms at various scan rates in a range from 20 to 200 mV·s⁻¹ and (b) charge-discharge curves at different current densities ranges from 2 to 20 A·g⁻¹ of mixed NC and GC electrode. The mass ratio of NC in the mixture of NC and GC is 0.9. All measurements were conducted in 1.0 M H₂SO₄.

Further to demonstrate the importance of my hybrid structure (NC@GC), I simply mixed the NC and GC (mass ratio of NC is 0.9), and investigated their capacitive performance by CV and galvanostatic charge-discharge measurements (**Figure 5.16**). The specific capacitance value estimated from galvanostatic charge-discharge curve at a current density of 2 A·g⁻¹ is only 69 F·g⁻¹, which is much lower than NC@GC (270 F·g⁻¹).

To the best of my knowledge, this capacitance value obtained from my study is significantly higher or comparable in comparison with the previously reported heteroatom-doped carbon materials, especially N-doped carbon materials (**Table 5.5**). Some reports show a little higher capacitances than my materials, but their current densities are too low (only $0.2 \text{ A}\cdot\text{g}^{-1}$). [17,39] To obtain high performance EDLC supercapacitor, I should consider a proper balance between surface area, pore volume, pore size distribution, graphitic degree, and N content. Although the specific surface area of NC@GC is not exceptionally good enough compared with previous reports, I believe that the overall performance of my NC@GC material is due to the synergy of high specific surface area ($1276 \text{ m}^2\cdot\text{g}^{-1}$), interconnected hierarchically micro/mesoporous structure, moderate N content (10.6 atomic%), as well as optimized graphitic carbon shell thickness which allows easy and rapid diffusion of ions. As seen in the **Table 5.5**, other reported materials are not able to simultaneously possess so many kinds of excellent properties. Actually, practically improving one property will hamper other properties which results into decreased performance. In this study, the structure properties in my hybrid NC@GC material can be easily adjusted by tuning the shell thickness in the parent ZIF-8@ZIF-67 crystals, thus, superior electrochemical performance can be optimized successfully.

Table 5.5 Specific capacitances of porous carbons reported in the representative literatures in aqueous electrolytes using three-electrode systems.

Materials	Surface area (m ² ·g ⁻¹)	Pore volume (cm ³ ·g ⁻¹)	Pore size (nm)	Graphitization degree	Heteroatom content (wt%)	Electrolyte	Potential range (V)	Current density (A·g ⁻¹)	Capacitance (F·g ⁻¹)	Reference
Nanoporous NC@GC	1276	1.78	1-5	Partially graphitic	N: 10.6	1.0 M H ₂ SO ₄	0.8	2.0	270	This study
Nanoporous GC derived from ZIF-67	943	0.84	4-8	Partially graphitic	N: 0.8	0.5 M H ₂ SO ₄	0.8	--	238*	<i>Chem. Eur. J.</i> 2014 , <i>20</i> , 7895.
Nitrogen-doped hollow carbon spheres	753	--	< 2	Partially graphitic	N: 6.0	2.0 M H ₂ SO ₄	0.8	2.0	245	<i>J. Mater. Chem.</i> 2012 , <i>22</i> , 13464.
Nitrogen-doped porous nanofibers	563	0.51	3.64	Partially graphitic	N: 7.2	6.0 M KOH	1.0	1.0	202	<i>ACS Nano</i> , 2012 , <i>6</i> , 7092.
Vertically aligned BCN nanotubes	347	--	--	Graphitic	B: 27 N: 31	1.0 M H ₂ SO ₄	1.3	2.0	265	<i>ACS Nano</i> , 2012 , <i>6</i> , 5259.
Nitrogen and boron co-doped graphene	249	--	Meso-macro pores	Graphitic	B: 0.6 N: 3.0	1.0 M H ₂ SO ₄	0.8	--	215*	<i>Adv. Mater.</i> 2012 , <i>24</i> , 5130.
MOF-templated carbon	2222	1.14	0.68	Amorphous	--	6.0 M KOH	1.0	0.25	274	<i>Carbon</i> 2010 , <i>48</i> , 3599.
Nitrogen-doped microporous carbon	1680	0.86	1-1.2	Amorphous	N: 6.0	1.0 M H ₂ SO ₄	1.2	0.2	310	<i>Adv. Funct. Mater.</i> 2007 , <i>17</i> , 1828.
Heteroatom-doped carbon	1578	1.09	< 2	Amorphous	N: 0.7	1.0 M H ₂ SO ₄	1.0	2.0	245	<i>Adv. Funct. Mater.</i> 2013 , <i>23</i> , 1305.
Nitrogen enriched mesoporous carbon spheres	1330	--	29	Amorphous	N: 10.0	5.0 M H ₂ SO ₄	0.8	1.0	211	<i>Electrochem. Commu.</i> 2007 , <i>9</i> , 569.
Phosphorus-enriched carbon	633	0.31	0.6-1.3	Amorphous	P: 6.2	1.0 M H ₂ SO ₄	1.0	1.0	220	<i>J. Am. Chem. Soc.</i> 2009 , <i>131</i> , 5026.
N-containing hydrothermal carbons	571	0.32	1.1	Amorphous	N: 4.4	1.0 M H ₂ SO ₄	0.8	2.0	245	<i>Adv. Mater.</i> 2010 , <i>22</i> , 5202.
Melamine-based carbon	442	0.30	< 2	Amorphous	N: 20.0	1.0 M H ₂ SO ₄	1.0	0.02	205	<i>Chem. Mater.</i> 2005 , <i>17</i> , 1241.

***Note:** The specific capacitance value was calculated from CV curves by using following equation:

$C = \frac{1}{ms(V_f - V_i)} \int_{V_i}^{V_f} I(V) dv$, where m is the mass of active electrode material, s is the potential scan rate, V_f and V_i are the integration limits of the voltammetric curve, and $I(V)$ denotes the current density.

5.4. Conclusion

Core–shell ZIF-8@ZIF-67 crystals, which integrate the properties of single ZIF-8 and ZIF-67, are elaborately designed for the first time by applying a seed-mediated growth technique. The core sizes of ZIF-8 and the shell thicknesses of ZIF-67 can be tuned simply by using different sizes of ZIF-8 seeds and varying the feeding molar ratios of $\text{Co}^{2+}/\text{Zn}^{2+}$. After the direct carbonization of core–shell ZIF-8@ZIF-67 crystals, a new type of selectively functionalized NC@GC materials retain both the high specific surface area (up to $1276 \text{ m}^2 \cdot \text{g}^{-1}$) and high N content (10.6 atomic%) derived from core ZIF-8 and superior graphitic structure originated from shell ZIF-67. The optimized NC@GC exhibits a distinguished electrochemical performance as an electrode in supercapacitors. This study bridges infinite MOFs with diverse functional carbon-based materials and provides new insight into artificially designed nanomaterials.

References

- [1] C. D. Liang, Z. J. Li, Dai. S, *Angew. Chem. Int. Ed.*, 2008, **47**, 3696.
- [2] Z. X. Wu, W. D. Wu, W. J. Liu, C. Selomulya, X. D. Chen, D. Y. Zhao, *Angew. Chem. Int. Ed.*, 2013, **52**, 13764.
- [3] Y. Fang, G. F. Zheng, J. P. Yang, H. S. Tang, Y. F. Zhang, B. Kong, Y. Y. Lv, C. J. Xu, A. M. Asiri, J. Zi, F. Zhang, D. Y. Zhao, *Angew. Chem. Int. Ed.*, 2014, **53**, 5366.
- [4] P. F. Fulvio, R. T. Mayes, X. Q. Wang, S. M. Mahurin, J. C. Bauer, V. Presser, J. McDonough, Y. Gogotsi, S. Dai, *Adv. Funct. Mater.*, 2011, **21**, 2208.
- [5] H. Chang, S. H. Joo, C. J. Pak, *Mater. Chem.*, 2007, **17**, 3078.
- [6] J. Tang, J. Liu, N. L. Torad, T. Kimura, Y. Yamauchi, *Nano Today*, 2014, **9**, 305.
- [7] M. J. Zhong, E. K. Kim, J. P. McGann, S.-E. Chun, J. F. Whitacre, M. Jaroniec, K. Matyjaszewski, T. Kowalewski, *J. Am. Chem. Soc.*, 2012, **134**, 14846.
- [8] J. Jin, S. Tanaka, Y. Egashira, N. Nishiyama, *Carbon*, 2010, **48**, 1985.
- [9] Z. B. Lei, D. Bai, X. S. Zhao, *Microporous Mesoporous Mater.*, 2012, **147**, 86.
- [10] H. L. Guo, Q. M. Gao, *J. Power Sources*, 2009, **186**, 551.

- [11] H. Zhu, J. Yin, X. Wang, H. Wang, X. Yang, *Adv. Funct. Mater.*, 2013, **23**, 1305.
- [12] A. G. Pandolfo, A. F. Hollenkamp, *J. Power Sources*, 2006, **157**, 11.
- [13] A. S. Aricò, P. Bruce, B. Scrosati, J. M. Tarascon, W. V. Schalkwijk, *Nat. Mater.*, 2005, **4**, 366.
- [14] E. Frackowiak, F. Béguin, *Carbon*, 2001, **39**, 937.
- [15] D. W. Wang, F. Li, M. Liu, G. Q. Lu, H. M. Cheng, *Angew. Chem. Int. Ed.*, 2008, **47**, 373.
- [16] K. K. R. Datta, V. V. Balasubramanian, K. Ariga, T. Mori, A. Vinu, *Chem. Eur. J.*, 2011, **17**, 3390.
- [17] C. O. Ania, V. Khomenko, E. Raymundo-Pinero, J. B. Parra, F. Béguin, *Adv. Funct. Mater.*, 2007, **17**, 1828.
- [18] D. Hulicova-Jurcakova, A. M. Puziy, O. I. Poddubnaya, F. Suárez-García, J. M. D. Tascón, G. Q. Lu, *J. Am. Chem. Soc.*, 2009, **131**, 5026.
- [19] R. R. Salunkhe, Y. Kamachi, N. L. Torad, S. M. Hwang, Z. Q. Sun, S. X. Dou, J. H. Kim, Y. Yamauchi, *J. Mater. Chem. A*, 2014, **2**, 19848.
- [20] D. W. Wang, F. Li, Z. G. Chen, G. Q. Lu, H. M. Cheng, *Chem. Mater.*, 2008, **20**, 7195.
- [21] E. Iyyamperumal, S. Y. Wang, L. M. Dai, *ACS Nano*, 2012, **6**, 5259.
- [22] Z. S. Wu, A. Winter, L. Chen, Y. Sun, A. Turchanin, X. L. Feng, K. Müllen, *Adv. Mater.*, 2012, **24**, 5130.
- [23] C. C. Hu, K. H. Chang, M. C. Lin, Y. T. Wu, *Nano Lett.*, 2006, **6**, 2690.
- [24] Z. Chen, Y. C. Qin, D. Weng, Q. F. Xiao, Y. T. Peng, X. L. Wang, H. X. Li, F. Wei, Y. F. Lu, *Adv. Funct. Mater.*, 2009, **19**, 3420.
- [25] T. Wang, J. Tang, X. L. Fan, J. H. Zhou, H. R. Xue, H. Guo, J. P. He, *Nanoscale*, 2014, **6**, 5359.
- [26] M. Sevilla, A. B. Fuertes, *Carbon*, 2006, **44**, 468.
- [27] J. Tang, T. Wang, X. Sun, Y. X. Guo, H. R. Xue, H. Guo, M. Z. Liu, X. X. Zhang, J. P. He, *Microporous Mesoporous Mater.*, 2013, **177**, 105.
- [28] Z. L. Schaefer, M. L. Gross, M. A. Hickner, R. E. Schaak, *Angew. Chem. Int. Ed.*, 2010, **49**, 7045.

- [29] J. Y. Yuan, C. Giordano, M. Antonietti, *Chem. Mater.*, 2010, **22**, 5003.
- [30] B. Liu, H. Shioyama, T. Akita, Q. Xu, *J. Am. Chem. Soc.*, 2008, **130**, 5390.
- [31] H.-L. Jiang, B. Liu, Y.-Q. Lan, K. Kuratani, T. Akita, H. Shioyama, F. Q. Zong, Q. Xu, *J. Am. Chem. Soc.*, 2011, **133**, 11854.
- [32] A. Almasoudi, R. Mokaya, *J. Mater. Chem.*, 2012, **22**, 146.
- [33] M. Hu, J. Reboul, S. Furukawa, N. L. Torad, Q. M. Ji, P. Srinivasu, K. Ariga, S. Kitagawa, Y. Yamauchi, *J. Am. Chem. Soc.*, 2012, **134**, 2864.
- [34] H. B. Aiyappa, P. Pachfule, R. Banerjee, S. Kurungot, *Cryst. Growth Des.*, 2013, **13**, 4195.
- [35] W. Chaikittisilp, M. Hu, H. Wang, H. S. Huang, T. Fujita, K. C. W. Wu, L. C. Chen, Y. Yamauchi, K. Ariga, *Chem. Commun.*, 2012, **48**, 7259.
- [36] N. L. Torad, R. R. Salunkhe, Y. Q. Li, H. Hamoudi, M. Imura, Y. Sakka, C.-C. Hu, Y. Yamauchi, *Chem. Eur. J.*, 2014, **20**, 7895.
- [37] N. L. Torad, M. Hu, Y. Kamachi, K. Takai, M. Imura, M. Naito, Y. Yamauchi, *Chem. Commun.*, 2013, **49**, 2521.
- [38] S. Lim, L. Suh, Y. Kim, M. Y. Yoon, H. Park, D. N. Dybtsev, K. Kim, *Chem. Commun.*, 2012, **48**, 7447.
- [39] J. Hu, H. L. Wang, Q. M. Gao, H. L. Guo, *Carbon*, 2010, **48**, 3599.
- [40] N. L. Torad, M. Hu, S. Ishihara, H. Sukegawa, A. A. Belik, M. Imura, K. Ariga, Y. Yamauchi, Y. Sakka, *Small*, 2014, **10**, 2096.
- [41] S. Q. Ma, G. A. Goenaga, A. V. Call, D. J. Liu, *Chem. Eur. J.*, 2011, **17**, 2063.
- [42] A. J. Amali, J.-K. Sun, Q. Xu, *Chem. Commun.*, 2014, **50**, 1519.
- [43] D. Hulicova, M. Kodama, H. Hatori, *Chem. Mater.*, 2005, **17**, 1241.
- [44] J. Chmiola, G. Yushin, R. Dash, Y. Gogotsi, *J. Power Sources*, 2006, **158**, 765.
- [45] S. Furukawa, K. Hirai, K. Nakagawa, Y. Takashima, R. Matsuda, T. Tsuruoka, M. Kondo, R. Haruki, D. Tanaka, H. Sakamoto, S. Shimomura, O. Sakata, S. Kitagawa, *Angew. Chem. Int. Ed.*, 2009, **48**, 1766.
- [46] K. Koh, A. G. Wong-Foy, A. J. Matzger, *Chem. Commun.*, 2009, 6162.

- [47] X. Song, T. Kim, H. Kim, D. Kim, S. Jeong, H. R. Moon, M. S. Lah, *Chem. Mater.*, 2012, **24**, 3065.
- [48] T. Li, J. E. Sullivan, N. L. Rosi, *J. Am. Chem. Soc.*, 2013, **135**, 9984.
- [49] K. S. Park, Z. Ni, A. P. Côté, J. Y. Choi, R. D. Huang, F. J. Uribe-Romo, H. K. Chae, M. O’Keeffe, O. M. Yaghi, *Proc. Natl. Acad. Sci. U. S. A.*, 2006, **103**, 10186.
- [50] R. Banerjee, A. Phan, B. Wang, C. Knobler, H. Furukawa, M. O’Keeffe, O. M. Yaghi, *Science*, 2008, **319**, 939.
- [51] B. Xie, J. W. Song, L. M. Ren, Y. Y. Ji, J. X. Li, F.-S. Xiao, *Chem. Mater.*, 2008, **20**, 4533.
- [52] B. Xie, H. Y. Zhang, C. G. Yang, S. Y. Liu, L. M. Ren, L. Zhang, X. J. Meng, B. Yilmaz, U. Müller, F.-S. Xiao, *Chem. Commun.*, 2011, **47**, 3945.
- [53] J. C. MacDonald, P. C. Dorrestein, M. M. Pilley, M. M. Foote, J. L. Lundburg, R. W. Henning, A. J. Schultz, J. L. Manson, *J. Am. Chem. Soc.*, 2000, **122**, 11692.
- [54] J. C. Noveron, M. S. Lah, R. E. D. Sesto, A. M. Arif, J. S. Miller, P. J. Stang, *J. Am. Chem. Soc.*, 2000, **124**, 6613.
- [55] S. J. Yang, T. Kim, J. H. Im, Y. S. Kim, K. Lee, H. Jung, C. R. Park, *Chem. Mater.*, 2012, **24**, 464.
- [56] J. Tang, T. Wang, X. C. Pan, X. Sun, X. L. Fan, Y. X. Guo, H. R. Xue, J. P. He, *J. Phys. Chem. C*, 2013, **117**, 16896.
- [57] N. A. M. Barakat, B. Kim, S. J. Park, Y. H. Jo, M.-H. Jung, H. Y. Kim, *J. Mater. Chem.*, 2009, **19**, 7371.
- [58] J. Kim, R. Ryoo, K. J. Stevenson, K. P. Johnston, *J. Phys. Chem. C*, 2010, **114**, 10796.
- [59] Z. X. Yan, M. Cai, P. K. Shen, *J. Mater. Chem.*, 2012, **22**, 2133.
- [60] Y. Z. Zhao, J. L. Feng, Q. S. Huo, N. Melosh, G. H. Fredrickson, B. F. Chmelka, G. D. Stucky, *Science*, 1998, **279**, 548.
- [61] S. D. Shen, A. E. Garcia-Bennett, Z. Liu, Q. Y. Lu, Y. F. Shi, Y. Yan, C. Z. Yu, W. C. Liu, Y. Cai, O. Terasaki, D. Y. Zhao, *J. Am. Chem. Soc.*, 2005, **127**, 6780.
- [62] L. Lai, J. R. Potts, D. Zhan, L. Wang, C. K. Poh, C. Tang, H. Gong, Z. Shen, J. Lin, R. S. Ruoff, *Energy Environ. Sci.*, 2012, **5**, 7936.

- [63] D. Usachov, O. Vilkov, A. Grüneis, D. Haberer, A. Fedorov, V. K. Adamchuk, A. B. Preobrajenski, P. Dudin, A. Barinov, M. Oehzelt, C. Laubschat, D. V. Vyalikh, *Nano Lett.*, 2011, **11**, 5401.
- [64] T. Schiros, D. Nordlund, L. Pálová, D. Prezzi, L. Zhao, K. S. Kim, U. Wurstbauer, C. Gutiérrez, D. Delongchamp, C. Jaye, D. Fischer, H. Ogasawara, L. G. M. Pettersson, D. R. Reichman, P. Kim, M. S. Hybertsen, A. N. Pasupathy, *Nano Lett.*, 2012, **12**, 4025.
- [65] A. Ōya, S. Ōtani, *Carbon*, 1979, **17**, 131.
- [66] J. R. Miller, P. Simon, *Science*, 2008, **321**, 651.
- [67] P. Simon, Y. Gogotsi, *Nat. Mater.*, 2008, **7**, 845.
- [68] F. W. Ma, H. Zhao, L. P. Sun, Q. Li, L. H. Huo, T. Xia, S. Gao, G. S. Pang, Z. Shi, S. H. Feng, *J. Mater. Chem.*, 2012, **22**, 13464.
- [69] H. M. Jeong, J. W. Lee, W. H. Shin, Y. J. Choi, H. J. Shin, J. K. Kang, J. W. Choi, *Nano Lett.*, 2011, **11**, 2472.
- [70] D. Hulicova, M. Kodama, H. Hatori, *Chem. Mater.*, 2006, **18**, 2318.
- [71] L. Zhao, L. Z. Fan, M. Q. Zhou, H. Guan, S. Qiao, M. Antonietti, M.-M. Titirici, *Adv. Mater.*, 2010, **22**, 5202.
- [72] L. F. Chen, X. D. Zhang, H. W. Liang, M. G. Kong, Q. F. Guan, P. Chen, Z. Y. Wu, S. H. Yu, *ACS Nano*, 2012, **6**, 7092.
- [73] B. Liu, H. Shioyama, H. L. Jiang, X. B. Zhang, Q. Xu, *Carbon*, 2010, **48**, 456.
- [74] E. Frackowiak, G. Lota, J. Machnikowski, C. Vix-Guterl, F. Béguin, *Electrochim. Acta*, 2006, **51**, 2209.
- [75] J. Chmiola, G. Yushin, Y. Gogotsi, C. Portet, P. Simon, P. L. Taberna, *Science*, 2006, **313**, 1760.
- [76] E. Raymundo-Piñero, K. Kierzek, J. Machnikowski, F. Béguin, *Carbon*, 2006, **44**, 2498.

Chapter 6

Cage-Type Highly Graphitic Porous Carbon-Co₃O₄ Polyhedron as the Cathode of Lithium-Oxygen Batteries

6.1. Introduction

Considering global warming and other environmental issues caused by automobiles, electric vehicles are being developed to serve the next generation of urban commuters.[1] Thus, it is urgent to establish a rechargeable battery system with a high energy density, a good rate capability, and a long cycle life that can meet the requirements in commercial electric vehicles. The rechargeable Li–O₂ (air) battery, which has an extremely high theoretical energy density compared to any other practical electrochemical batteries, has attracted enormous research attention since its introduction by Abraham and Jiang in 1996.[2] Although various kinds of electrode materials have been developed to improve the performance of Li–O₂ batteries, carbon is still considered to be the most promising choice due to its comprehensive advantages, including low-cost, good conductivity, large pore volume, and tunable porous structures,[3,4] which are required properties for Li–O₂ cathode materials. Much effort has been made to reveal the favorable structural properties of carbon cathodes in Li–O₂ batteries.

To realize the practical application of a carbon-based cathode in a Li–O₂ battery, however, there are still many challenges to overcome. A principal problem is the insufficient catalysis activity toward the oxygen reduction reaction (ORR) and especially the oxygen evolution reaction (OER) during the discharge/charge process, which might result in high overpotentials, low round-trip efficiency, passivation of the O₂ electrode, low rate capability, and poor cycling performance.[5,6] Metals and compounds such as nanoporous gold,[7] TiC,[8] Ru nanoparticles,[9-12] and RuO₂[13-15] have been screen out to be effective catalyst materials for non-aqueous Li–O₂ battery with respect to accelerating the formation of Li₂O₂ during discharging, lower the charge potential during charging, and improve the cycling performance in the Li–O₂ battery. However, metals and compounds generally provide low overall electrical conductivity and a heavy molecular weight, resulting in low energy efficiency[16] and significantly reduced specific capacity.[17,18] Considering the above aspect, incorporating catalytically active materials into the carbon-based cathodes such as the Co₃O₄/carbon composite is an effective way to promote the ORR and OER in Li–O₂

batteries[19-21] and prevents the large discharge/charge overpotentials generally observed on carbon cathode.[22]

In recent years, since the first report by Xu *et al.*,[23] the direct carbonization of metal-organic frameworks (MOFs), which are assembled by bridging metal ions (or clusters) with organic linkers, has become an effective and popular method to prepare functional porous carbon-based composites. Our group mainly focuses on zeolitic imidazolate framework-derived carbon and has explored their potential application in various fields, including chemical sensor,[24] supercapacitor,[25-27] and electrocatalyst.[28] The metal ions that exist in the parent MOFs can be in situ incorporated into the resulting carbon matrix, offering an excellent electronic connection between the metals/metal oxides and the carbon frameworks.[29,30] In some cases, a graphitic carbon can be obtained due to the catalytic graphitization effect of some specific metals (e.g., Fe,[31] Co[32]) contained in the parent MOFs. Thus, the MOFs-derived carbon composites usually exhibit attractive electrocatalytic activity.[33] For example, a MOFs-derived Co₃O₄-embedded N-doped mesoporous carbon layer/multiwalled carbon nanotube hybrid is prepared as the bi-functional electrocatalyst for the oxygen evolution reaction and oxygen reduction reaction.[34]

Very recently, our group reported the design of core-shell structured MOFs and the derived first example of a selectively functionalized nanoporous hybrid carbon polyhedron, which consists of amorphous carbon as the core and highly graphitic carbon-Co as the shell.[35] Taking advantage of the different thermal stabilities of amorphous carbon cores and highly graphitic carbon shells under an air atmosphere[36,37] offers a good opportunity for us to obtain a cage-type extremely highly graphitic porous carbon-Co₃O₄ polyhedron by removal of the amorphous carbon cores and simultaneous oxidation of Co nanoparticles in the graphitic carbon shells via annealing of the selectively functionalized nanoporous hybrid carbon polyhedron in air. In this study, I report the fabrication of a cage-type extremely highly graphitic porous carbon-Co₃O₄ (GPC-Co₃O₄) polyhedron for the first time and employ it as an oxygen electrode without an additional conductive agent for the Li-O₂ battery cathode. The GPC-Co₃O₄ polyhedron integrates the favorable properties, including high electrical conductivity,

mesoporous structure, and well-dispersed catalytically active Co₃O₄ nanoparticles, resulting in a low charge potential and good cycling performance as the Li–O₂ battery cathode.

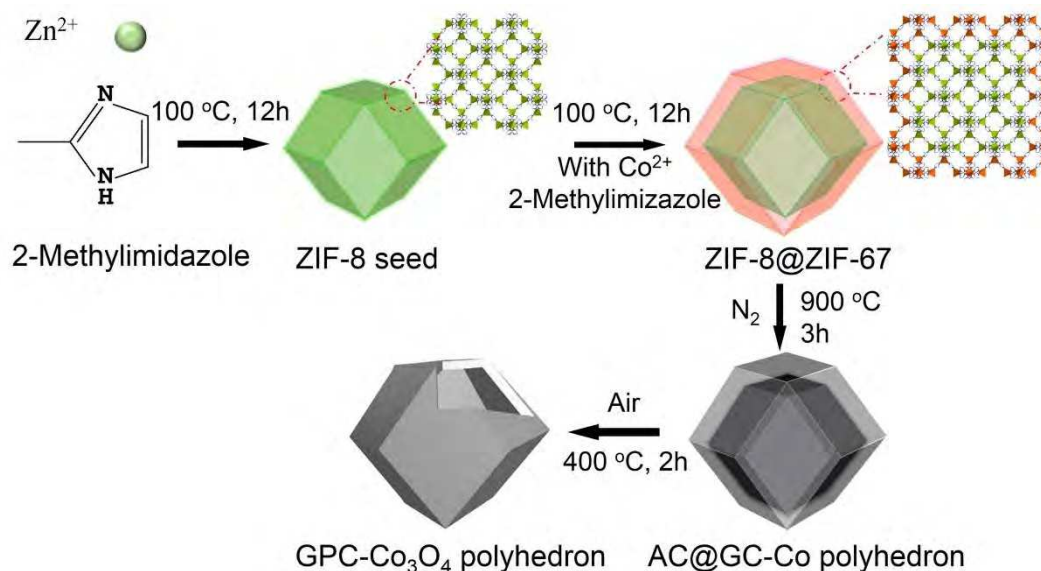


Figure 6.1 Synthetic scheme for the preparation of core-shell ZIF-8@ZIF-67 crystals, AC@GC-Co, and GPC-Co₃O₄.

The designed synthesis of the cage-type GPC-Co₃O₄ polyhedron is illustrated in **Figure 6.1**. The core-shell structured MOFs (ZIF-8@ZIF-67) are well designed and prepared through a seed-mediated growth method.[35] The core ZIF-8 is assembled from zinc ions and the organic linker of 2-methylimidazole, whereas the shell ZIF-67 is formed by cobalt ions and the organic linker of 2-methylimidazole. Thus, after the carbonization of ZIF-8@ZIF-67 crystals under an inert atmosphere, I demonstrate that a selectively functionalized porous carbon polyhedron consisting of amorphous carbon (AC) as the core and highly graphitic carbon-Co (GC-Co) composite as the shell can be successfully prepared (assigned as AC@GC-Co). Inspired by the different thermal stabilities of AC cores and GC-Co shells,[36,37] I thus intend to prepare a cage-type highly graphitic porous carbon-Co₃O₄ (assigned as GPC-Co₃O₄) polyhedron by executing an air calcination of the AC@GC-Co under an appropriate temperature.

6.2. Experimental Sections

6.2.1. Chemicals

Cobalt chloride (CoCl₂) and zinc nitrate hexahydrate (Zn(NO₃)₂·6H₂O, 99%) were obtained from Sigma-Aldrich Chemical Co. 2-Methylimidazole (MeIm, purity 99%), methanol, and hydrofluoric acid were purchased from Nacalai Tesque Reagent Co. All of the chemicals were utilized without further purification.

6.2.2. Synthesis of ZIF-8 Seeds

In a typical synthesis, methanolic solutions of Zn(NO₃)₂·6H₂O (810 mg, 40 mL) and methanolic solutions of MeIm (526 mg, 40 mL) were homogeneously mixed by stirring. Then the mixture was transferred into an autoclave and incubated for 12 hours at 100 °C. After cooling to room temperature, the white product was collected by centrifugation, washed with methanol, and dried at 80 °C.

6.2.3. Synthesis of Core-Shell ZIF-8@ZIF-67 Crystals

The core-shell ZIF-8@ZIF-67 crystals were prepared according to our previously reported method.[35] For details, the prepared ZIF-8 seeds (80 mg) were first dispersed in methanol (10 mL) under sonication. Then a methanolic solution of CoCl₂ (218 mg, 5 mL) was added to the above mixture under continuous stirring. After stirring for 10 mins, a methanolic solution of MeIm (1100 mg, 5 mL) was added into the above solution. After stirring for another 5 mins, the mixture was transferred into a 50 ml autoclave with a Teflon liner and incubated at 100 °C for 12 hours. After cooling, the lavender core-shell ZIF-8@ZIF-67 crystals were collected by centrifugation, washed with methanol, and dried at 80 °C.

6.2.4. Preparation of the Cage-Type Highly Graphitic Porous Carbon-Co₃O₄ (GPC-Co₃O₄) Polyhedron Composite

The cage-type highly graphitic porous carbon-Co₃O₄ (GPC-Co₃O₄) polyhedron composite was prepared through two-step annealing. First, core-shell ZIF-8@ZIF-67 crystals were thermally carbonized under a nitrogen flow at 900 °C for 3 hours with a controlled heating rate of 2 °C·min⁻¹. Then Zn species and most of the Co species retained in the obtained carbon

product were removed by using a hydrogen fluoride aqueous solution (10 wt%). For the moment, the nanoporous amorphous carbon@graphitic carbon-cobalt polyhedron composite (assigned as AC@GC-Co) consisting of amorphous carbon (AC) as the core and graphitic carbon-cobalt (GC-Co) as the shell was successfully prepared as demonstrated by our previous research. Finally, AC@GC-Co was further calcined under air flow at 400 °C for 2 hours to remove the amorphous carbon core and produced the target cage-type highly graphitic hollow porous carbon-CO₃O₄ polyhedron composite (assigned as GPC-CO₃O₄).

6.2.5. Characterization

Transmission electron microscopy (TEM), a line scan, elemental mapping, and energy-dispersive X-ray analysis were conducted using a JEM-2100 at a voltage of 200 kV. The morphology of the products was performed on a Hitachi SU-8000 field-emission scanning electron microscope (SEM) instrument at an accelerating voltage of 5 kV. Wide-angle powder X-ray diffraction (XRD) patterns were acquired on a Rigaku Rint 2000 X-ray diffractometer using monochromated Cu K α radiation (40 kV, 40 mA) at a scanning rate of 2°·min⁻¹. N₂ adsorption-desorption isotherms were measured using a Quantachrome Autosorb-iQ Automated Gas Sorption System at 77 K. The specific surface area of core-shell ZIF-8@ZIF-67 crystals was estimated based on the Langmuir model by using the adsorption branch data in the relative pressure (P/P_0) range of 0.01-0.1. The specific surface area of GPC-CO₃O₄ was estimated according to the Brunauer-Emmett-Teller (BET) model by using the adsorption branch data in the relative pressure (P/P_0) range of 0.05-0.3. The pore-size distributions were calculated from the adsorption branches of isotherms on the basis of the density functional theory (DFT) method. Thermogravimetric (TG) analysis was performed by using a Hitachi HT-Seiko Instrument Exter 6300 TG/DTA in a N₂/air atmosphere with a heating rate of 5 °C min⁻¹ from room temperature to target temperature. X-ray photoelectron spectroscopy (XPS) spectra were measured at room temperature using a PHI Quantera SXM (ULVAC-PHI) instrument with an Al K α X-ray source. All the binding energies were calibrated via referencing to C 1s binding energy (285.0 eV). The peaks of the N 1s spectrum was fitted with a Gaussian-Lorentzian sum function and a Shirley background.

6.2.6. Battery Assembly

The Li–O₂ battery assembly was conducted in a 2032 coin cell with holes on the top in an Ar-filled glove box (< 0.1 ppm of H₂O and 1 ppm of O₂). The electrolyte was 1 M LiTFSI dissolved in tetraglyme (TEGDME) and the amount of electrolytes in a coin cell was 50 μ L. The H₂O content in the electrolyte measured by the Karl-Fischer titration is \sim 10 ppm. A glass fiber (GFA, Whatman) was used as a separator. A Li metal was utilized as the anode. The oxygen electrode was prepared by pressing a film composed of the active material and PTFE with a ratio of 85:15 wt% onto a hydrophobic carbon paper as the cathode for the Li–O₂ battery. The electrodes were dried at 80 °C for 12 hours and then transferred to the glovebox without contact with air in a glass tube oven (GTO-200). The mass loading of the active material was 0.5–1.0 mg·cm⁻². The coin cell stored in a sealed glass chamber was purged with O₂ (99.999%) for 2 hours before electrochemical tests.

6.2.7. Electrochemical Measurements and Characterization

All of the electrochemical measurements were conducted at a constant room temperature. Galvanostatic discharge/charge was conducted on a Hokuto discharging/charging system. The specific capacities and current densities were based on the mass of the active material in electrodes. For ex situ X-ray diffraction (XRD) measurements and scanning electron microscope (SEM) measurements of the discharged/charged cathodes, batteries were disassembled in an Ar glovebox, and the cathodes were extracted and rinsed with dimethylethane (DME) to wash off the electrolyte salt. After being dried in a vacuum chamber connected to the glovebox, the cathodes were placed in a customer-built X-ray cell sealed with a kapton polyimide film. XRD measurements were performed on a Bruker D8 Advanced diffractometer with Cu K α ($\lambda = 1.5406 \text{ \AA}$) radiation. SEM was performed on Hitachi SU-8000 field-emission scanning electron microscope. The cathodes were taken to the SEM sample loading chamber in a sealed glass bottle with a piece of lithium metal. The time from opening the glass bottle to finishing the sample loading into the SEM machine was < 10 seconds.

6.3. Results and Discussion

6.3.1. Thermal Conversion of Core–Shell ZIF-8@ZIF-67 Crystals to Cage-Type GPC-Co₃O₄

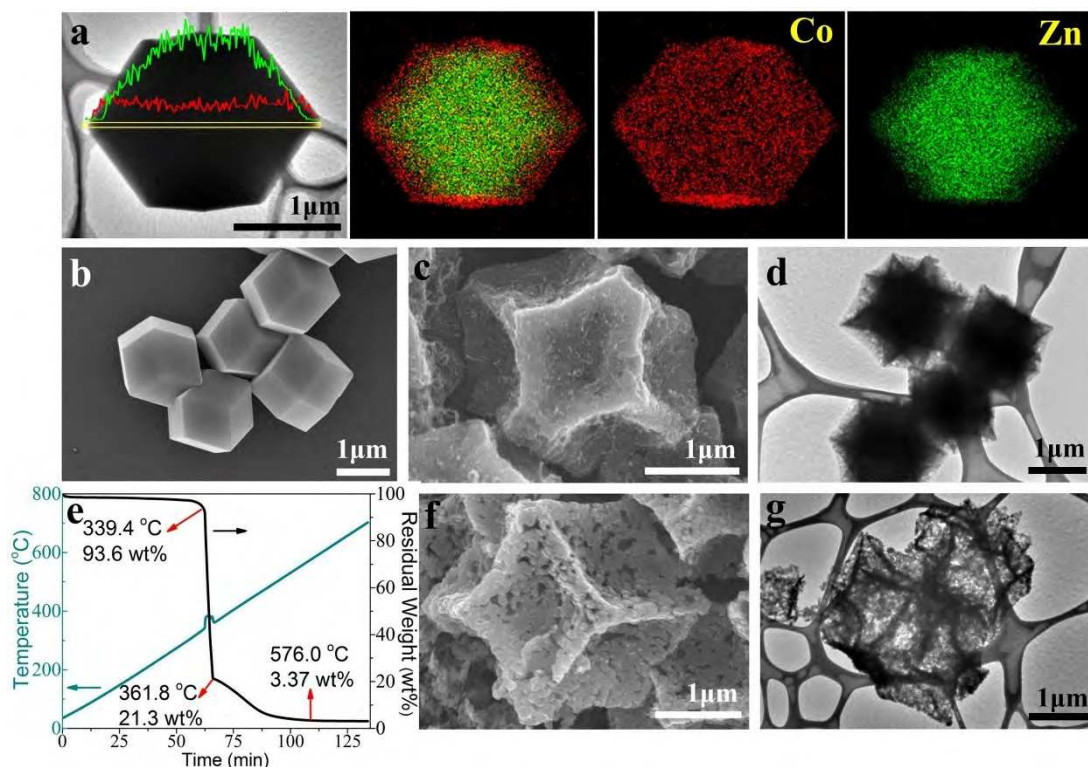


Figure 6.2 (a) TEM image, line scan, and elemental mappings of a ZIF-8@ZIF-67 crystal; (b) SEM image of ZIF-8@ZIF-67 crystals; (c) SEM image and (d) TEM image of AC@GC-Co; (e) TG curve of AC@GC-Co measured under air atmosphere from room temperature to 700 °C with a heating rate of 5 °C·min⁻¹; (f) SEM image and (g) TEM image of GPC-Co₃O₄.

The core–shell structure of the obtained MOFs (ZIF-8@ZIF-67) was carefully characterized by TEM, line scan, and elemental mappings (**Figure 6.2a**), showing the ZIF-8 core (zinc, green color) and the ZIF-67 shell (cobalt, red color). The molar ratio of Co²⁺/Zn²⁺ detected by energy-dispersive X-ray analysis was 0.3. The SEM image (**Figure 6.2b**) reveals that the prepared ZIF-8@ZIF-67 display a typical rhombic dodecahedral shape due to the seed growth of the parent rhombic dodecahedral ZIF-8. The crystal structure of core–shell ZIF-8@ZIF-67 was identified by the powder XRD and the nitrogen sorption analysis. As proved by **Figure 6.3a**, ZIF-8@ZIF-67 possess topology information similar to that of ZIF-8 seeds

and ZIF-67 shells, which is the most important reason for the successful formation of the core–shell structured ZIFs, most likely via epitaxial growth. The core–shell ZIF-8@ZIF-67 crystals retain the high microporosity from the ZIF-8 core and the ZIF-67 shell well (**Figure 6.3b**), exhibiting a high specific surface area of 2240 m²·g⁻¹ and a narrow pore size of 1.2 nm.

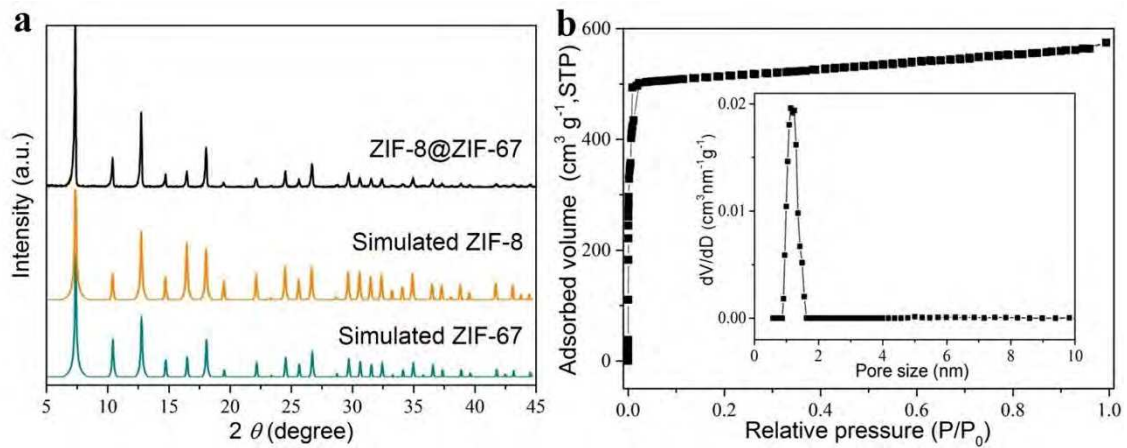


Figure 6.3 (a) The simulated XRD patterns of ZIF-8 and ZIF-67, the wide-angle powder XRD pattern of as-prepared ZIF-8@ZIF-67 crystals, and (b) the N₂ adsorption–desorption isotherm and pore-size distribution curve of ZIF-8@ZIF-67 crystals.

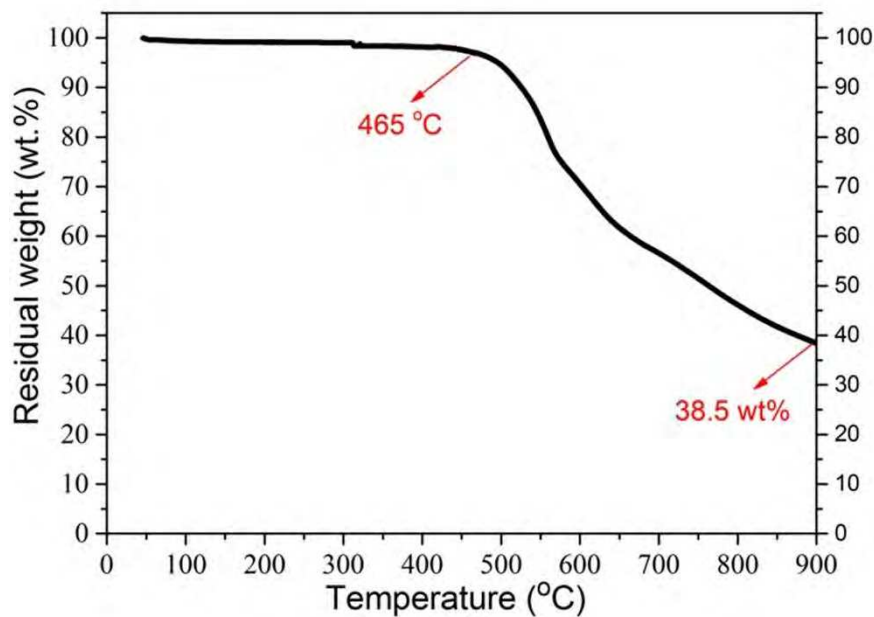


Figure 6.4 TG curve of core–shell ZIF-8@ZIF-67 crystals measured under a N₂ atmosphere from room temperature to 900 °C with a heating rate of 5 °C·min⁻¹.

The selectively functionalized porous carbon polyhedron (AC@GC-Co) was successfully prepared by carrying out the carbonization of ZIF-8@ZIF-67 at 900 °C under a N₂ atmosphere. As monitored by the TG analysis (**Figure 6.4**), a 38.5 wt% of the initial ZIF-8@ZIF-67 is retained at 900 °C under a N₂ atmosphere. During this process, the 2-methylimidazole in ZIF-8@ZIF-67 is converted to a carbon state, and the metal ions of Zn²⁺ in the core ZIF-8 and Co²⁺ in the shell ZIF-67 are thermally reduced to be metallic Zn and Co, respectively. Adding catalytic active transition metals into the carbon precursor, especially iron, nickel, and cobalt, has been examined to be an effective way for the graphitization of amorphous carbon through the solid-state transformation.[38] As a result, the carbons in the shells are catalytically graphitized by Co species whereas the carbons in the cores are still amorphous due to the weak catalytic activity of Zn species.[35] After washing with hydrofluoric acid (10 wt%), the metallic Zn and the most of Co nanoparticles can be removed. Some small Co nanoparticles well-enclosed by curved and layered graphitic carbon shells were protected against strong acid erosion and retained in carbon matrix.[39] Then I obtain the mediate product of AC@GC-Co, consisting of amorphous carbon (AC) as the cores and highly graphitic carbon-Co (GC-Co) composite as the shells. AC@GC-Co shows a solid rhombic dodecahedral morphology from the parent ZIF-8@ZIF-67 crystals (**Figure 6.2b**), as illustrated by SEM (**Figure 6.2c**, **Figure 6.5a**) and TEM images (**Figure 6.2d**).

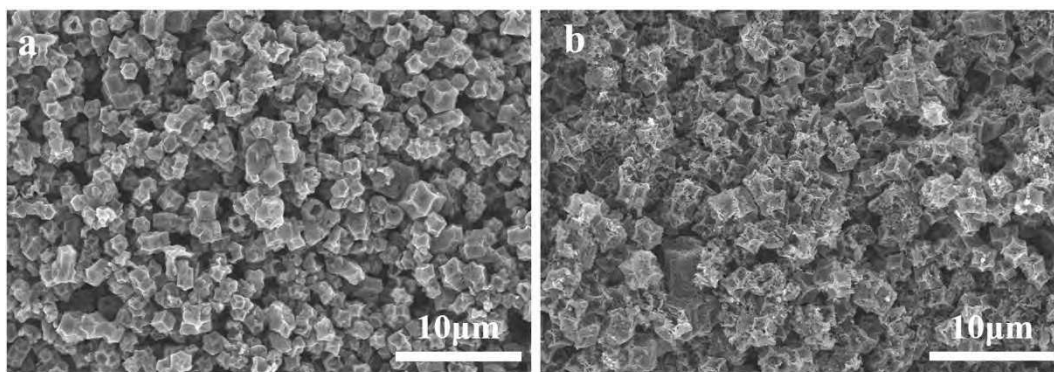


Figure 6.5 SEM images of (a) AC@GC-Co and (b) GPC-Co₃O₄.

Generally, the graphitic carbon is more thermally stable than amorphous carbon under air conditions.[36,37] The details of the thermal stability of AC@GC-Co were investigated using TG analysis, and the TG curve shown in **Figure 6.2e** was acquired under an air atmosphere. AC@GC-Co is stable up to 339.4 °C and then decomposes rapidly until 361.8 °C, accompanied by a weight loss of 78.7 wt%. During this moment, the amorphous carbons in AC@GC-Co burn out and release a large quantity of heat in a very short time. Thus, the temperature curve (blue line in **Figure 6.2e**) displays a peak at around the 62 min, showing that the temperature suddenly increases from 345.0 to 383.0 °C. The AC@GC-Co displays a secondary decomposition during the temperature range of 361.8 to 576.0 °C due to the burnout of the graphitic carbon. The weight of AC@GC-Co decreases slowly in this stage without disturbing the programmed increased temperature. The residual weight at 700.0 °C is only 3.37 wt%, proving the existence of an incombustible metal species. On the basis of the TG result, I determine to anneal the AC@GC-Co at 400.0 °C under air conditions to remove the amorphous carbon cores but reserve the graphitic carbon shells, and the metallic Co nanoparticles that exist in AC@GC-Co would be oxidized simultaneously to Co₃O₄. As demonstrated by the SEM (**Figure 6.2f**, **Figure 6.5b**) and TEM images (**Figure 6.2g**), the product retains the rhombic dodecahedral morphology and displays an expected hollow core. The detailed structural information on the obtained cage-type graphitic porous carbon-Co₃O₄ (assigned as GPC-Co₃O₄) polyhedron is investigated in the following section.

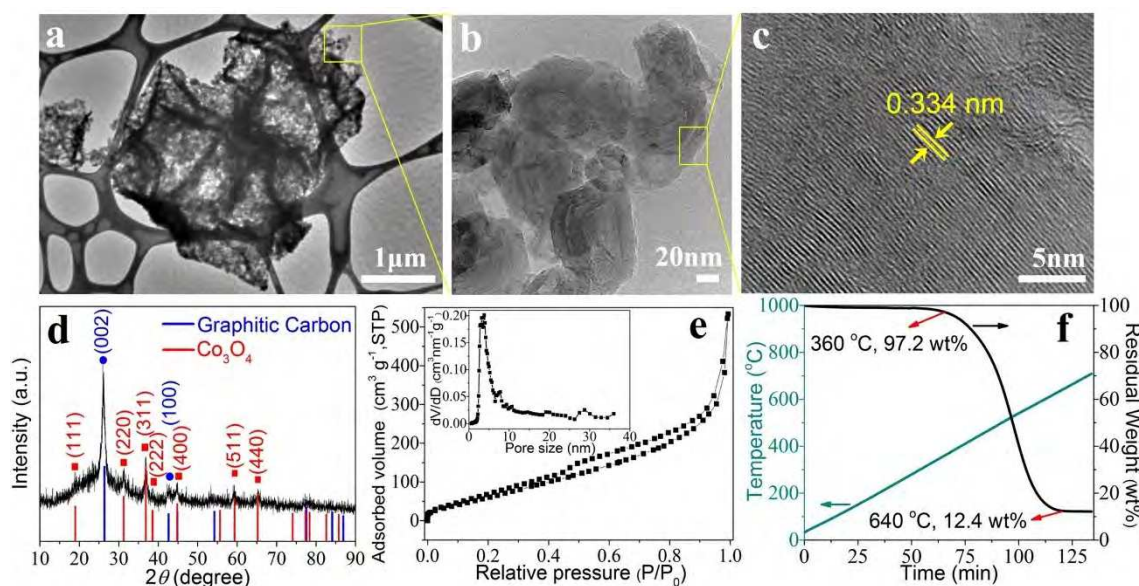


Figure 6.6 (a,b) TEM images with different magnification, (c) high-resolution TEM image, (d) wide-angle XRD pattern, (e) N₂ adsorption–desorption isotherm (the inset is the pore-size distribution curve), and (f) TG curve of GPC-Co₃O₄. The TG curve was obtained under an air atmosphere from room temperature to 700 °C with a heating rate of 5 °C·min⁻¹.

The crystallization of GPC-Co₃O₄ was carefully characterized by TEM, high-resolution TEM, and XRD analysis. As shown in **Figure 6.6a-c**, the shells of GPC-Co₃O₄ are composed of ring-like graphitic carbon layers with an interplanar spacing of 0.334 nm, which is the typical value of graphite.[40] It is well known that the uniformly distributed Co species in the parent ZIF-67 shell are able to graphitize catalytically the amorphous carbon at relatively low temperature (< 1000 °C), leading to a highly graphitic carbon structure.[32] The additional annealing in air atmosphere selectively remove the low-graphitic thermally unstable carbons, thus further increasing the degree of graphitization. The powder XRD pattern of GPC-Co₃O₄ (**Figure 6.6d**) displays a sharp diffraction peak at 26.3° that corresponds to the (002) diffractions of graphitic carbon. The other diffraction peaks located at 31.2°, 36.8°, 44.8°, 59.3°, and 65.2° are respectively indexed to the (220), (311), (400), (511), and (440) diffractions of the cubic Co₃O₄ crystal (**Figure 6.6d**).[41] The Co₃O₄ crystals show weak diffraction peaks, implying the small sizes of Co₃O₄ crystals. As demonstrated by previous studies, it is difficult to completely etch of Co nanoparticles, which are enclosed integrally by ring-like graphitic

carbon layers that formed during catalytic graphitization.[32,35] Thus, the traceable Co₃O₄ nanoparticles in GPC-Co₃O₄ are due to oxidation of the residual Co nanoparticles in AC@GC-Co. The uniform distributions of elements including carbon, oxygen, and cobalt in GPC-Co₃O₄ are shown in the elemental mapping images (**Figure 6.7**). However, it is difficult to distinguish the Co₃O₄ nanoparticles clearly in GPC-Co₃O₄ because they are quite small and are surrounded by graphitic carbon layers. I further acquired the X-ray photoelectron spectroscopy (XPS) spectrum to monitor the changes of elements before and after the secondary annealing in air. The full spectra and high-resolution N 1s spectra of AC@GC-Co and GPC-Co₃O₄ are shown in **Figure 6.8**. It is noteworthy that the N 1s spectrum of AC@GC-Co can be obviously fitted into two peaks, which are assignable to pyridinic-N (398.7 eV) and graphitic-N (400.8 eV), respectively (**Figure 6.8b**). However, nitrogen was not detected in GPC-Co₃O₄. The results suggest that the nitrogen was removed from AC@GC-Co during the secondary air annealing.

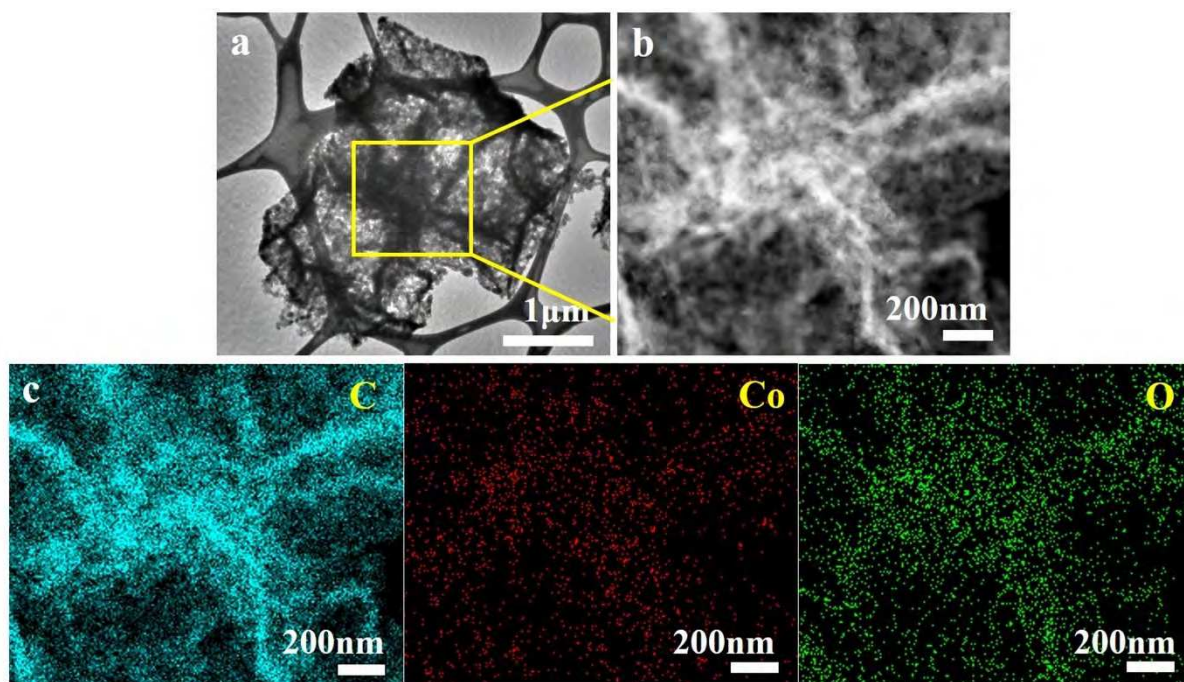


Figure 6.7 (a) TEM, (b) high-angle annular dark-field scanning TEM (HAADF-STEM) images, and (c) elemental mappings of GPC-Co₃O₄.

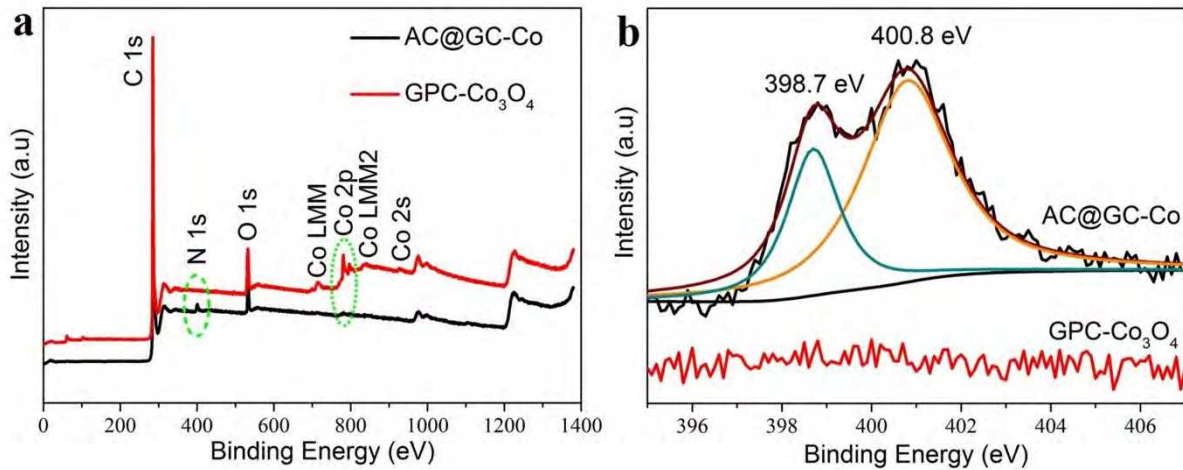


Figure 6.8 X-ray photoelectron spectroscopy (XPS) spectra and high-resolution N 1s spectra of AC@GC-Co and GPC-Co₃O₄.

The porosity of GPC-Co₃O₄ was measured by a N₂ adsorption–desorption isotherm. As shown in **Figure 6.6e**, the isotherm displays a type IV curve with a hysteresis loop, which is generally induced by the capillary condensation of N₂ in the mesopores.[42] The mesopores in GPC-Co₃O₄ have various sizes and distribute randomly. During the adsorption process along with the increased relative pressure, the nitrogen was condensed first within the smallest mesopores. The pressure increased until all pores were filled with nitrogen. Then, the pressure decreased and induced desorption of nitrogen. Because the last filled large mesopores were connected with the small mesopores, the nitrogen desorption in the same large mesopores happened at a lower relative pressure compared with adsorption process, leading to the formation of a hysteresis loop. The unsaturated N₂ uptake in the high relative pressure of 0.9 to 1.0 indicates the existence of macropores, which relates to the interior void generated from the removal of the amorphous carbon core.[43] The specific surface area calculated from the adsorption branch database on the BET model is 282 m²·g⁻¹. The pore-size distribution inset in **Figure 6.6e** clearly reveals that the graphitic carbon shells have abundant mesopores with diameters mostly concentrated at 3.8, 7.8, and 28 nm. The thermal stability of GPC-Co₃O₄ was investigated via TG analysis (**Figure 6.6f**). GPC-Co₃O₄ shows no remarkable weight loss below the temperature of 360.0 °C; weight loss occurs gradually from 360.0 to 640.0 °C. The process corresponds well to the second decomposition of AC@GC-Co from 361.8 to 576.0 °C

(**Figure 6.2e**) after the rapid decomposition of the amorphous carbons in the first stage from 339.4 to 361.8 °C (**Figure 6.2e**). The results reveal that GPC-CO₃O₄ has a higher decomposition temperature in comparison to AC@GC-Co due to the better stability of graphitic carbons in GPC-CO₃O₄ after the removal of amorphous carbon in AC@GC-Co via annealing at 400 °C under an air atmosphere. After the full decomposition of carbons above 640.0 °C, the content of CO₃O₄ was detected to be 12.4 wt % in GPC-CO₃O₄ (**Figure 6.6f**).

6.3.2. Electrochemical Performance of the Li-O₂ Battery with a GPC-CO₃O₄ Electrode

The successful cycling operation of a non-aqueous Li-O₂ battery is widely considered to rely on the formation of insoluble discharge product of Li₂O₂ on the cathode during discharging, and the decomposition of Li₂O₂ during charging.[44] As demonstrated by many studies, the discharge capacity of a Li-O₂ battery is linearly proportional to the amount of discharge product of Li₂O₂ deposited on the O₂ electrode.[45] The mesopore volume of the porous carbon cathode is far more efficient for accommodating the reduction product of Li₂O₂ compared to the micropore volume.[1,45] In addition, the mesopores facilitate the electrolyte immersion and electron/ion transfer.[46,47] Thus, compared to microporous carbon, mesoporous carbon is more suitable for achieving higher specific capacitance during discharge.[48,49] Furthermore, considering the gradual blockage of the O₂ pathway caused by the deposited insoluble discharge products, the mesopores provide an open framework allowing for the rapid transfer of O₂. [45] Also, the highly conductive carbons (e.g., graphene, carbon nanocage, carbon onions) are able to provide a low-resistance pathway for electron transfer. Inspired by the high graphitic degree, advantageous mesoporous and cage-type structure, and additional catalyst of CO₃O₄, GPC-CO₃O₄ was assembled as the oxygen electrode of a Li-O₂ battery without adding an extra conductive agent. The cage-type extremely highly graphitic porous carbon-CO₃O₄ polyhedron serves as not only the current collector but also the catalyst, as well as the substrate of the CO₃O₄ catalyst. To evaluate the performance, discharge and charge tests were conducted. The cutoff voltage window was 2.0–4.5 V vs Li/Li⁺.

The initial discharge and charge profiles of the Li-O₂ battery with a GPC-Co₃O₄ electrode are shown in **Figure 6.9a**. The green points of i, ii, iii and iv represent the pristine, mediate discharge, full discharge, and full charge of Li-O₂ batteries, respectively. The Li-O₂ battery with a GPC-Co₃O₄ electrode delivers a high average discharge plateau at 2.7 V vs. Li/Li⁺, indicating strong ORR catalytic activity. The discharge capacity is calculated to be 1575 mAh·g⁻¹ at a current density of 125 mA·g⁻¹ based on the mass of GPC-Co₃O₄ in the electrodes (**Figure 6.9a**). Remarkably, the charge profile exhibits an obvious plateau at 3.5 V vs. Li/Li⁺, corresponding to the charge overpotential of ~0.58 V, which is considerably lower than that of the common carbon cathode (~1.0 V vs. Li/Li⁺).^[19,50] During the charging process, reactions are mainly related to the oxidation of amorphous Li₂O₂ at low potentials (~3.6 V). The increased potential at the latter part of the charging profile (**Figure 6.9a**) is probably due to the decomposition of crystalline Li₂O₂ via a Li deficient solid solution reaction.^[51] The good performance is likely attributable to the high conductivity of carbon frameworks, which promotes the transport of electrons during redox reactions, and associates with the embedded catalytic sites of Co₃O₄, which facilitates the formation and decomposition of Li₂O₂ during the discharge and charge processes in the Li-O₂ battery.

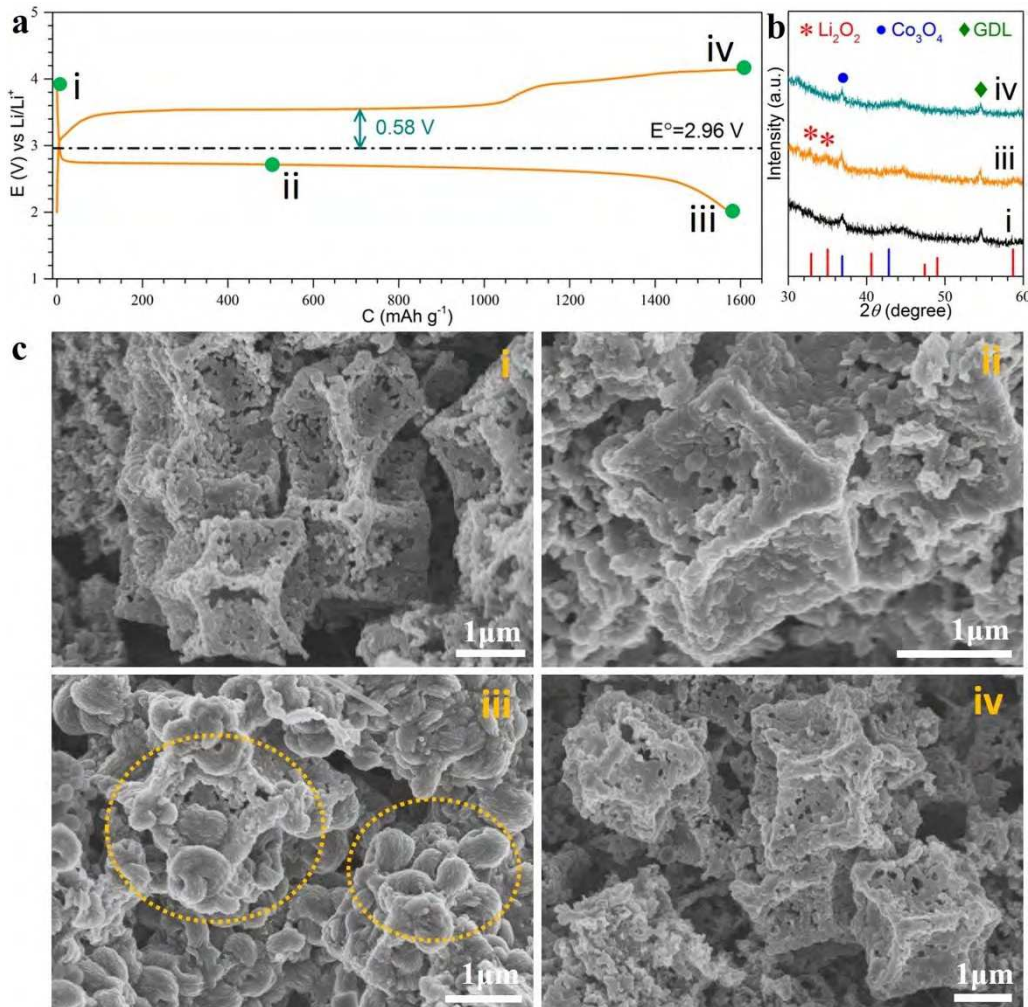


Figure 6.9 (a) The initial discharge and charge profiles of the Li–O₂ battery with a GPC–Co₃O₄ electrode at a current density of 125 mA · g⁻¹, (b) ex situ XRD patterns, and (c) SEM images of the GPC–Co₃O₄ cathodes after discharge and charge of the Li–O₂ battery. The number coding marks of i, ii, iii, and iv represent the pristine, mediate discharge, full discharge, and full charge of Li–O₂ batteries, respectively.

To identify the products after discharge and charge of the Li–O₂ battery, ex situ XRD analysis was performed to characterize the GPC–Co₃O₄ electrode after disassembling the battery at the states of pristine (i), full discharge (iii), and full charge (iv). In contrast to the pristine electrode (**Figure 6.9b, i**) and fully charged electrode (**Figure 6.9b, iv**), the XRD pattern of the electrodes after full discharging (**Figure 6.9b, iii**) exhibits extra weak reflections at 2θ of 33° and 35° indexing to the diffractions of Li₂O₂.^[52] Neither Li₂O nor LiOH was

detected from the XRD patterns (**Figure 6.9b**). The XRD analysis reveals that Li₂O₂ is the main discharge product and will reversibly decompose after being fully charged.

To figure out the morphologies of the discharge products formed on the GPC-Co₃O₄ electrode, I disassembled the battery at the stages of pristine (i), partly discharged (ii), fully discharged (iii), and fully charged (iv) and examined the GPC-Co₃O₄ electrode via SEM images. As revealed in **Figure 6.9c i, ii, iii**, the typical toroid-like lithium peroxide appears along with the discharging time and deposits definitely on the surface and in the pores of cage-type GPC-Co₃O₄ polyhedron.[53] After a sufficient charge, the toroid-like lithium peroxide disappears (**Figure 6.9c, iv**), indicating the high reversibility of the electrodes. It is noteworthy that the morphology of the GPC-Co₃O₄ polyhedron is well-preserved after suffering the charge and discharge (**Figure 6.9c, iv**). The cage-type structure consists of the mesoporous walls, and the interior void enables the GPC-Co₃O₄ polyhedron to sustain the volume expansion and contraction during the deposition and release of Li₂O₂, which would help to keep the integrity of the GPC-Co₃O₄ electrode and increase the cycle life. Both XRD patterns and SEM images demonstrate the efficient generation of Li₂O₂ during discharging and the reversible decomposition of Li₂O₂ during charging, which is one of the pivotal factors for a successful rechargeable Li-O₂ battery.

The rate capability and cycling stability of the Li-O₂ batteries with a GPC-Co₃O₄ electrode were studied with a limited specific capacity of 500 mAh·g⁻¹. The discharge and charge profiles at the current densities of 250, 375, 500, and 1250 mA·g⁻¹ are shown in **Figure 6.10a**. During the discharging and charging process, the overpotentials increase in proportion to the increased current densities, whereas the Coulombic efficiencies remain ~100%. The result indicates the good rate capability of Li-O₂ batteries. The cycling performance of the GPC-Co₃O₄ electrode was further investigated at a current density of 250 mA·g⁻¹ for 50 cycles. **Figure 6.10b** shows the selected discharge and charge profiles of the battery at the 1st, 25th, and 50th cycles. The profiles are overlapped and show no increase in discharge and charge overpotentials. As illustrated in **Figure 6.10c**, there is no variation and decay of the specific capacity over 50 cycles. The discharge and charge terminal voltages maintain well. After 50

cycles, the terminal voltages are still 2.62 V and 4.16 V, respectively. Commercial carbon material Super P (SP) was employed as the oxygen electrode and its performance was evaluated for comparison with GPC-Co₃O₄. The discharge and charge profiles of commercial carbon Super P electrode at first and 10th cycles are provided in **Figure 6.10b**. SP electrode shows a much higher charge potential of ~ 4.22 V and the corresponding charge overpotential is ~ 1.26 V, which is much higher than that of the GPC-Co₃O₄ electrode (~ 0.58 V). The charge terminal voltage of SP increases gradually during cycling and reaches the cutoff voltage of 4.5 V after 10 cycles (**Figure 6.10c**). The capacity also decreases below 500 mAh g⁻¹ after 10 cycles, which indicating the poor reversibility. These results imply the outstanding cycling stability of the Li-O₂ batteries with this unique GPC-Co₃O₄ electrode.

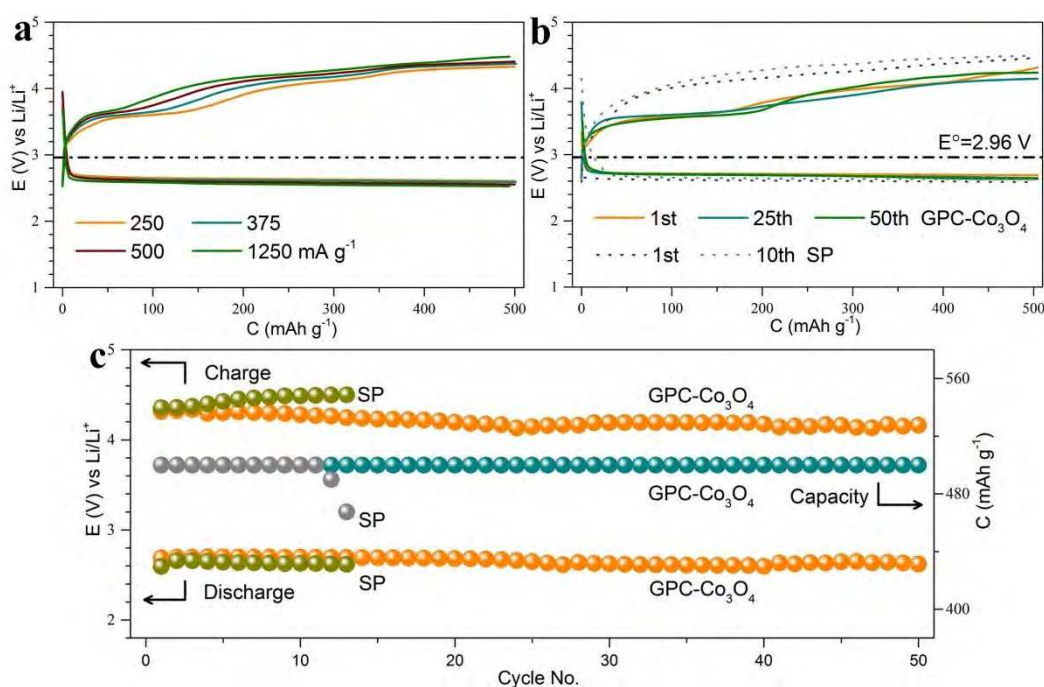


Figure 6.10 (a) Rate capability of Li-O₂ batteries with a GPC-Co₃O₄ electrode, (b) discharge/charge profiles of the selected 1st, 25th, and 50th cycles of GPC-Co₃O₄ electrode and the selected 1st and 10th cycles of Super P electrode at 250 mA g⁻¹, and (c) the terminal voltages and capacities of charge and discharge against cycle number.

6.4. Conclusion

A cage-type highly graphitic carbon-Co₃O₄ polyhedron was fabricated by the annealing of core-shell structured MOFs (ZIF-8@ZIF-67) in a N₂ atmosphere first and subsequently in an air atmosphere. After first annealing in the N₂ atmosphere, a solid AC@GC-Co polyhedron consisting of the amorphous carbon cores (AC) and the graphitic carbon-Co shells (GC-Co) was obtained. By making use of the different thermal stabilities of amorphous carbon cores and highly graphitic carbon shells, a secondary annealing of AC@GC-Co in an air atmosphere was conducted to remove the low-graphitic carbons that were distributed mainly in the cores. Thus, a cage-type highly graphitic porous carbon-Co₃O₄ (GPC-Co₃O₄) polyhedron was obtained for the first time and was employed as an oxygen electrode without an additional conductive agent for the Li-O₂ battery. The cage-type GPC-Co₃O₄ polyhedron cathode displays a low charge potential and long cycle life benefit from the structural properties, including high electrical conductivity, cage-type and mesoporous structure, and well-dispersed catalytically active Co₃O₄ nanoparticles.

References

- [1] C. Tran, X.-Q. Yang, D. Qu, *J. Power Sources*, 2010, **195**, 2057.
- [2] K. M. Abraham, Z. Jiang, *J. Electrochem. Soc.*, 1996, **143**, 1.
- [3] G. Wu, N. H. Mack, W. Gao, S. Ma, R. Zhong, J. Han, J. K. Baldwin, P. Zelenay, *ACS Nano*, 2012, **6**, 9764.
- [4] E. Yoo, H. Zhou, *ACS Nano*, 2011, **5**, 3020.
- [5] Y. Li, X. Li, D. Geng, Y. Tang, R. Li, J. Dodelet, M. Lefevre, X. Sun, *Carbon*, 2013, **64**, 170.
- [6] H. Nie, H. Zhang, Y. Zhang, T. Liu, J. Li, Q. Lai, *Nanoscale*, 2013, **5**, 8484.
- [7] Z. Peng, S. A. Freunberger, Y. Chen, P. G. Bruce, *Science*, 2012, **373**, 563.
- [8] M. M. O. Thotiyl, S. A. Freunberger, Z. Peng, Y. Chen, Z. Liu, P. G. Bruce, *Nat. Mater.*, 2013, **12**, 1050.

- [9] F. Li, D.-M. Tang, Y. Chen, D. Golberg, H. Kitaura, T. Zhang, A. Yamada, H. Zhou, *Nano Lett.*, 2013, **13**, 4702.
- (10) F. Li, D.-M. Tang, Z. Jian, D. Liu, D. Golberg, A. Yamada, H. Zhou, *Adv. Mater.*, 2014, **26**, 4659.
- (11) K. Liao, T. Zhang, Y. Wang, F. Li, Z. Jian, H. Yu, H. Zhou, *ChemSusChem*, 2015, **8**, 1429.
- (12) D. W. Su, S. X. Dou, G. X. Wang, *J. Mater. Chem.*, 2015, **3**, 18384.
- (13) Z. Jian, P. Liu, F. Li, P. He, X. Guo, M. Chen, H. Zhou, *Angew. Chem. Int. Ed.*, 2014, **53**, 442.
- (14) K. Liao, X. Wang, Y. Sun, D. Tang, M. Han, P. He, X. Jiang, T. Zhang, H. Zhou, *Energy Environ. Sci.*, 2015, **8**, 1992.
- (15) F. Li, D.-M. Tang, T. Zhang, K. Liao, P. He, D. Golberg, A. Yamada, H. Zhou, *Adv. Energy Mater.*, 2015, **5**, 1500294.
- (16) A. Debart, A. J. Paterson, J. Bao, P. G. Bruce, *Angew. Chem. Int. Ed.*, 2008, **47**, 4521.
- (17) H. Cheng, K. Scott, *J. Power Sources*, 2010, **195**, 1370.
- (18) Y. Cui, Z. Wen, S. Sun, Y. Lu, J. Jin, *Solid State Ionics*, 2012, **225**, 598.
- (19) A. Débart, J. Bao, G. Armstrong, P. G. Bruce, *J. Power Sources*, 2007, **174**, 1177.
- (20) C. Sun, F. Li, C. Ma, Y. Wang, Y. Ren, W. Yang, Z. Ma, J. Li, Y. Chen, Y. Kim, L. Chen, *J. Mater. Chem. A*, 2014, **2**, 7188.
- (21) X. Ren, S. S. Zhang, D. T. Tran, J. Read, *J. Mater. Chem.*, 2011, **21**, 10118.
- (22) R. R. Mitchell, B. M. Gallant, C. V. Thompson, Y. Shao-Horn, *Energy Environ. Sci.*, 2011, **4**, 2952.
- (23) H.-L. Jiang, B. Liu, Y.-Q. Lan, K. Kuratani, T. Akita, H. Shioyama, F. Zong, Q. Xu, *J. Am. Chem. Soc.*, 2011, **133**, 11854.
- (24) N. L. Torad, M. Hu, Y. Kamachi, K. Takai, M. Imura, M. Naito, Y. Yamauchi, *Chem. Commun.*, 2013, **49**, 2521.
- (25) W. Chaikittisilp, M. Hu, H. Wang, H.-S. Huang, T. Fujita, K. C.-W. Wu, L.-C. Chen, Y. Yamauchi, K. Ariga, *Chem. Commun.*, 2012, **48**, 7259.

- (26) N. L. Torad, R. R. Salunkhe, Y. Li, H. Hamoudi, M. Imura, Y. Sakka, C.-C. Hu, Y. Yamauchi, *Chem. Eur. J.*, 2014, **20**, 7895.
- (27) R. R. Salunkhe, J. Tang, Y. Kamachi, T. Nakato, J. H. Kim, Y. Yamauchi, *ACS Nano*, 2015, **9**, 6288.
- (28) W. Chaikittisilp, N. L. Torad, C. Li, M. Imura, N. Suzuki, S. Ishihara, K. Ariga, Y. Yamauchi, *Chem. - Eur. J.*, 2014, **20**, 4217.
- (29) S. Ma, G. A. Goenaga, A. V. Call, D.-J. Liu, *Chem. - Eur. J.*, 2011, **17**, 2063.
- (30) W. Yin, Y. Shen, F. Zou, X. Hu, B. Chi, Y. Huang, *ACS Appl. Mater. Interfaces*, 2015, **7**, 4947.
- (31) Y. Hou, T. Huang, Z. Wen, S. Mao, S. Cui, J. Chen, *Adv. Energy Mater.*, 2014, **4**, 1400337.
- (32) N. L. Torad, M. Hu, S. Ishihara, H. Sukegawa, A. A. Belik, M. Imura, K. Ariga, Y. Sakka, Y. Yamauchi, *Small*, 2014, **10**, 2096.
- (33) T. Y. Ma, S. Dai, M. Jaroniec, S. Z. Qiao, *J. Am. Chem. Soc.*, 2014, **136**, 13925.
- (34) X. Li, Y. Fang, X. Lin, M. Tian, X. An, Y. Fu, R. Li, J. Jin, J. Ma, *J. Mater. Chem. A*, 2015, **3**, 17392.
- (35) J. Tang, R. R. Salunkhe, J. Liu, N. L. Torad, M. Imura, S. Furukawa, Y. Yamauchi, *J. Am. Chem. Soc.*, 2015, **137**, 1572.
- (36) J. Tang, N. L. Torad, R. R. Salunkhe, J.-H. Yoon, M. S. A. Hossain, S. X. Dou, J. H. Kim, T. Kimura, Y. Yamauchi, *Chem. Asian J.*, 2014, **9**, 3238.
- (37) Y. C. Sui, D. R. Acosta, J. A. González-León, A. Bermúdez, J. Feuchtwanger, B. Z. Cui, J. O. Flores, J. M. Saniger, *J. Phys. Chem. B*, 2001, **105**, 1523.
- (38) G. C. Loh, D. Baillargeat, *J. Appl. Phys.*, 2013, **114**, 033534.
- (39) A.-H. Lu, W.-C. Li, N. Matoussevitch, B. Spliethoff, H. Bönemann, F. Schüth, *Chem. Commun.*, 2005, 98.
- (40) J. Tang, T. Wang, X. C. Pan, X. Sun, X. L. Fan, Y. X. Guo, H. R. Xue, J. P. He, *J. Phys. Chem. C*, 2013, **117**, 16896.
- (41) H. Lee, Y.-J. Kim, D. J. Lee, J. Song, Y. M. Lee, H.-T. Kim, J.-K. Park, *J. Mater. Chem. A*, 2014, **2**, 11891.

- (42) K. S. W. Sing, D. H. Everett, R. A. W. Haul, L. Moscou, R. A. Pierotti, J. Rouquérol, T. Siemie-niewska, *Pure Appl. Chem.*, 1985, **57**, 603.
- (43) X. Bo, J. Bai, J. Ju, L. Guo, *J. Power Sources*, 2011, **196**, 8360.
- (44) Y. Cui, Z. Wen, Y. Liu, *Energy Environ. Sci.*, 2011, **4**, 4727.
- (45) S. B. Ma, D. J. Lee, V. Røev, D. Im, S.-G. Doo, *J. Power Sources*, 2013, **244**, 494.
- (46) Z. Guo, D. Zhou, X. Dong, Z. Qiu, Y. Wang, Y. Xia, *Adv. Mater.*, 2013, **25**, 5668.
- (47) Z. Guo, D. Zhou, H. Liu, X. Dong, S. Yuan, A. Yu, Y. Wang, Y. Xia, *J. Power Sources*, 2015, **276**, 181.
- (48) T. Kuboki, T. Okuyama, T. Ohsaki, N. Takami, *J. Power Sources*, 2005, **146**, 766.
- (49) X.-H. Yang, P. He, Y.-Y. Xia, *Electrochem. Commun.*, 2009, **11**, 1127.
- (50) Y.-C. Lu, Z. Xu, H. A. Gasteiger, S. Chen, K. Hamad-Schifferli, Y. Shao-Horn, *J. Am. Chem. Soc.*, 2010, **132**, 12170.
- (51) S. Ganapathy, B. D. Adams, G. Stenou, M. S. Anastasaki, K. Goubitz, X. F. Miao, L. F. Nazar, *J. Am. Chem. Soc.*, 2014, **136**, 16335.
- (52) H.-G. Jung, J. Hassoun, J.-B. Park, Y.-K. Sun, B. Scrosati, *Nat. Chem.*, 2012, **4**, 579.
- (53) S. Wu, J. Tang, F. Li, X. Liu, H. Zhou, *Chem. Commun.*, 2015, **51**, 16860.

Chapter 7

Bimetallic Metal–Organic Frameworks for Controlled Catalytic Graphitization of Nanoporous Carbons

7.1. Introduction

Hybrid nanoporous carbon materials with controllable pore sizes, shapes, and surface properties have attracted considerable attention for the development of next-generation high performance electronic devices. Up to now, various types of carbon materials with different dimensionality (D), such as carbon-onions (0-D),[1] carbon nanotubes (1-D),[2] graphene (2-D),[3] activated carbons (3-D),[4] and templated carbons (3-D),[5] have been explored extensively. The advantageous properties such as suitable pore size distribution,[6-8] large specific surface area,[9] high electrical conductivity,[10] and doped heteroatoms,[11] are favorable for energy conversion and storage applications. Practical improvements related to a specific property causes, however, the performance associated to other properties to decrease. Thus, the rational design and synthesis of hybrid carbon materials with controlled physical and chemical properties is still a challenge and is of great interest from the viewpoint of synthetic chemistry.

In recent years, metal–organic frameworks (MOFs) have been scrutinized as convenient precursors for preparing diverse porous-carbon-based materials[12,13] or metal oxides[14,15] due to their regular nano-architecture constructed from various metal ions/clusters and organic ligands. Even though great progress has been made in using MOFs as precursors, the properties of the resulting porous carbons or metal oxides are limited by using only simple MOFs. As a subfamily of MOFs, zeolitic imidazolate frameworks (ZIFs), constructed from the coordination between zinc (Zn^{2+}) or cobalt ions (Co^{2+}) and imidazolate-type linkers,[16] have proved to be great candidates for fabricating morphology-inherited porous carbon materials. The zinc-based ZIF (ZIF-8) or cobalt-based ZIF (ZIF-67) derived carbons exhibit many advantageous properties, along with specific limitations. In detail, nanoporous carbons derived from the typical single-metal ZIFs composed of zinc ions (e.g., ZIF-8) usually possess a microporous structure, large specific surface area, and high degree of nitrogen doping, but also a low degree of graphitization.[17] On the other hand, nanoporous carbons derived from the single-metal ZIFs composed of cobalt ions (e.g., ZIF-67) generally possess mesoporous structure and a high degree of graphitization, but a low specific surface

area and nitrogen content.[18] These examples suggest that having only a single type of metal ions in the ZIFs comes with both advantages and disadvantages. In contrast to zinc, cobalt is able to catalytically promote the graphitization of amorphous carbon at high temperature, but at the expense of decreasing the surface area[19] and concentration of doped heteroatoms.[20,21] Therefore, it is desirable to combine the advantages of zinc and cobalt ions in one single crystal (bimetallic ZIFs) in order to achieve porous carbon materials with tailored functionalities.

According to our previous research, ZIF-8 ($\text{Zn}(\text{MeIm})_2$, MeIm = 2-methylimidazolate) and ZIF-67 ($\text{Co}(\text{MeIm})_2$) are highly compatible due to their isoreticular structure and similar lattice parameters.[16,22] As a result, our group successfully synthesized core–shell ZIFs (ZIF-8@ZIF-67) by using ZIF-8 as seeds and further coating with ZIF-67 via epitaxial growth.[23] The fabrication of hetero-bimetallic ZIFs was also recently achieved via the co-precipitation of zinc and cobalt ions with MeIm.[24,25] Unlike the single-metal ZIFs, which only contain zinc or cobalt ions, here the zinc and cobalt ions coexist indiscriminately in the bimetallic ZIFs. As mentioned above, the zinc and cobalt ions exhibit different functionalities during carbonization. The MeIm coordinated with zinc ions can be converted into N-doped carbons, and the micropores formed between the MeIm and zinc ions can be mostly retained. In contrast, the MeIm coordinated with cobalt ions tends to yield graphitic carbon, while sacrificing the microporosity and doped nitrogen. Considering this background, in the present work, I study the synthesis of nanoporous carbons by using bimetallic ZIFs as precursor. The properties of the bimetallic-ZIF-derived carbons, including the specific surface area, porosity, degree of graphitization, and nitrogen doping, are precisely controlled by finely tuning the composition of the bimetallic ZIF precursors.

7.2. Experimental Sections

7.2.1. Chemicals

Zinc nitrate hexahydrate ($\text{Zn}(\text{NO}_3)_2 \cdot 6\text{H}_2\text{O}$, 99%) and cobalt nitrate hexahydrate ($\text{Co}(\text{NO}_3)_2 \cdot 6\text{H}_2\text{O}$, 99%), 2-methylimidazole (purity 99%), methanol, and hydrofluoric acid were purchased from Nacalai Tesque Reagent Co. All the chemicals were used without further purification.

7.2.2. Preparation of Bimetallic ZIFs ($\text{Co}_x \cdot \text{Zn}_{1-x}(\text{MeIm})_2$)

In a typical synthesis, $\text{Co}(\text{NO}_3)_2 \cdot 6\text{H}_2\text{O}$ and $\text{Zn}(\text{NO}_3)_2 \cdot 6\text{H}_2\text{O}$ were dissolved in 30 mL of methanol to form a clear solution, followed by the addition of 2-methylimidazole (984 mg, 12 mmol) dissolved in 10 mL of methanol. After thoroughly mixing by continuous stirring for 10 mins, the solution was then transferred into an autoclave and was incubated at 100 °C for 12 hours. After cooling to room temperature, the resulting crystals were collected by centrifugation, washed with methanol, and dried at 60 °C. The molar ratio of $\text{Co}^{2+}/\text{Zn}^{2+}$ in the obtained bimetallic crystals was adjustable over a wide range by varying the initial metallic precursor ratio. The total molarity of Co^{2+} and Zn^{2+} was fixed to be 3 mmol during the synthesis. As a result, a series of bimetallic ZIFs were prepared and categorized as $\text{Co}_x \cdot \text{Zn}_{1-x}(\text{MeIm})_2$, where $x/1-x$ represents the corresponding initial molar ratio of $\text{Co}^{2+}/\text{Zn}^{2+}$ and the obtained bimetallic ZIFs are denoted as $\text{Co}_{0.05} \cdot \text{Zn}_{0.95}(\text{MeIm})_2$, $\text{Co}_{0.1} \cdot \text{Zn}_{0.9}(\text{MeIm})_2$, $\text{Co}_{0.33} \cdot \text{Zn}_{0.67}(\text{MeIm})_2$, and $\text{Co}_{0.67} \cdot \text{Zn}_{0.33}(\text{MeIm})_2$, respectively. Two single-metal ZIFs, ZIF-8 ($\text{Zn}(\text{MeIm})_2$) and ZIF-67 ($\text{Co}(\text{MeIm})_2$), were also prepared by adding only Zn^{2+} or Co^{2+} , respectively.

7.2.3. Carbonization of Bimetallic ZIFs ($\text{Co}_x \cdot \text{Zn}_{1-x}(\text{MeIm})_2$)

Bimetallic ZIFs ($\text{Co}_x \cdot \text{Zn}_{1-x}(\text{MeIm})_2$), ZIF-8, and ZIF-67 crystals were thermally converted into nanoporous carbon through carbonization under flowing argon at 900 °C for 3 hours with a heating rate of 2 °C·min⁻¹. The Zn and Co species were removed by extensive washing with HF solution (10 wt%). The nanoporous carbons converted from bimetallic ZIFs ($\text{Co}_x \cdot \text{Zn}_{1-x}(\text{MeIm})_2$) are denoted as C- y ($y = x/1-x$, in the form of an irreducible fraction). Thus, the nanoporous carbons converted from the bimetallic ZIFs $\text{Co}_{0.05} \cdot \text{Zn}_{0.95}(\text{MeIm})_2$, $\text{Co}_{0.1} \cdot \text{Zn}_{0.9}(\text{MeIm})_2$, $\text{Co}_{0.33} \cdot \text{Zn}_{0.67}(\text{MeIm})_2$, and $\text{Co}_{0.67} \cdot \text{Zn}_{0.33}(\text{MeIm})_2$ are designated as C-1/19,

C-1/9, C-1/2, and C-2/1, respectively. C-ZIF-8 and C-ZIF-67 are also prepared for comparison by using ZIF-8 and ZIF-67 as the precursors, respectively.

7.2.4. Characterization

The morphology of the products was investigated by a Hitachi SU-8000 field-emission scanning electron microscope (SEM) at an accelerating voltage of 5 kV. Transmission electron microscopy (TEM), high-angle annular dark-field scanning transmission electron microscopy (HAADF STEM), and elemental mapping analysis were conducted on a JEM-2100 at voltage of 200 kV. N₂ adsorption–desorption isotherms were measured with a Quantachrome Autosorb-iQ Automated Gas Sorption System at 77 K. The surface areas of C- γ , C-ZIF-8, and C-ZIF-67 were calculated according to the Brunauer–Emmett–Teller (BET) model by using the adsorption branch data in the relative pressure (P/P_0) range of 0.05–0.35. The total pore volumes and pore-size distributions were estimated from the adsorption branches of the N₂ isotherms on the basis of the density functional theory (DFT). Wide-angle powder X-ray diffraction (PXRD) patterns were acquired on a Rigaku Rint 2000 X-ray diffractometer using monochromated Cu K α radiation (40 kV, 40 mA) at a scanning rate of 2°·min⁻¹. Raman spectra were collected on a Horiba-Jovin Yvon T64000 instrument with an excitation laser wavelength of $\lambda = 514.5$ nm. CHN analysis was measured by Perkin Elmer 2400 CHNO Series II System. Thermogravimetric (TG) analysis was conducted on Hitachi HT-Seiko Instrument Exter 6300 TG/DTA in N₂ atmospheres and heated from room temperature to 900 °C at 5 °C·min⁻¹. X-ray photoelectron spectroscopy (XPS) spectra were measured at room temperature using a PHI Quantera SXM (ULVAC-PHI) instrument with an Al K α X-ray source. The region of high-resolution N 1s spectrum ranges from 392 to 412 eV. The binding energies were calibrated via referencing to C 1s binding energy located at 285.0 eV. The peaks of the N 1s spectrum were fitted with a Gaussian-Lorentzian sum function and a Shirley background.

7.2.5. Electrochemical Measurements

The electrochemical measurements were carried out using an electrochemical workstation (CHI 660e, CH Instruments). Firstly, the electrochemical analysis was carried out using standard three-electrode measurements. Ag/AgCl and platinum were used as the reference and the counter electrode, respectively. The electrolyte used for the present measurement was 1.0 M H₂SO₄. The working electrode was prepared as following description. 1 mg of bimetallic-ZIF-derived carbon material was mixed with 0.1 mg of poly(vinylidene fluoride). After adding 200 μL of N-methyl-2-pyrrolidone, the mixture was treated with ultrasonication for 20 mins. The obtained homogeneous black slurry was dropped stepwise onto a graphite substrate (1 cm²) and dried under an infrared lamp to form a thin film. For all the samples, the mass loading per electrode was 1 mg. The thickness of the thin film estimated by cross-section SEM image is around 25 μm, the density of the active electrode material corresponds to 0.5 g·cm⁻³. For the symmetric supercapacitor cell (SSC) measurements, two electrodes with the same weight loadings were used. The positive and negative electrodes were separated from each other by a distance of 0.3 cm, without a separator, and used for the electrochemical measurements. Thus the total weight loadings for both electrodes were 2 mg. The electrochemical properties of the electrodes were investigated by cyclic voltammetry (CV) and galvanostatic charge-discharge (GC-DC) measurements. The gravimetric and volumetric capacitance values were calculated using cyclic voltammetry and galvanostatic charge-discharge measurements and the following equations:

$$C_g = \frac{1}{ms(V_f - V_i)} \int_{V_i}^{V_f} I(V) dV \quad (1)$$

$$C_g = \frac{I \times \Delta t}{m \times \Delta V} \quad (2)$$

$$C_v = C_g \times \rho \quad (3)$$

Where C_g is gravimetric capacitance (F·g⁻¹), C_v volumetric capacitance (F·cm⁻³), s is the potential scan rate, V the is potential window, I is the current (A), t is the discharge time, m is the mass in grams, and ρ is the density of the active electrode material.

7.3. Results and Discussion

7.3.1. Synthesis and Characterization of Bimetallic ZIFs ($\text{Co}_x \cdot \text{Zn}_{1-x}(\text{MeIm})_2$)

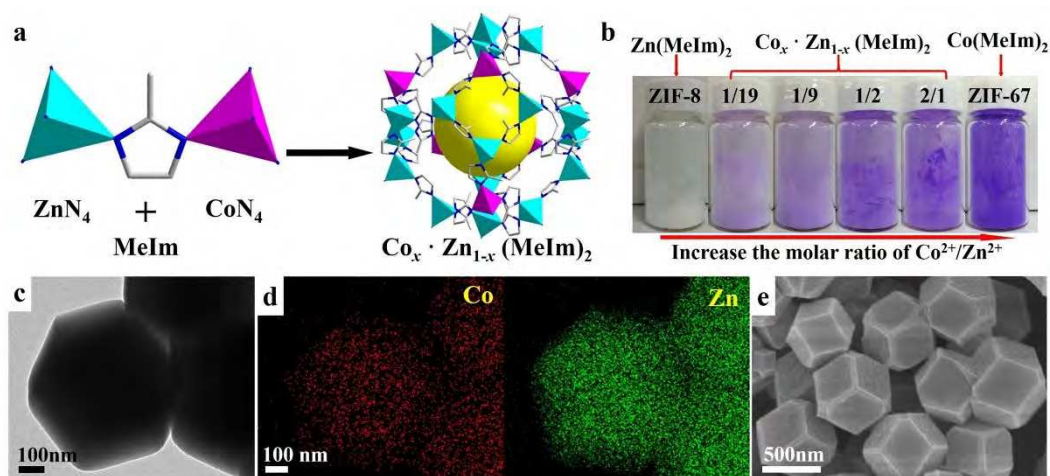


Figure 7.1 (a) Schematic illustration of the crystal structure of the bimetallic ZIFs ($\text{Co}_x \cdot \text{Zn}_{1-x}(\text{MeIm})_2$). (b) Photograph of ZIF-8, ZIF-67, and the bimetallic ZIF ($\text{Co}_x \cdot \text{Zn}_{1-x}(\text{MeIm})_2$) crystals. The initial molar ratios of $\text{Co}^{2+}/\text{Zn}^{2+}$ for the synthesis of each bimetallic ZIF is shown on top of the bottles in the form of an irreducible fraction. (c) TEM image, (d) elemental mapping, and (e) SEM image of the $\text{Co}_{0.1} \cdot \text{Zn}_{0.9}(\text{MeIm})_2$.

Table 7.1 Summary of the molar ratios of $\text{Co}^{2+}/\text{Zn}^{2+}$ in bimetallic ZIFs.

Sample	ICP determined molar ratio of $\text{Co}^{2+}/\text{Zn}^{2+}$	Feeding molar ratio of $\text{Co}^{2+}/\text{Zn}^{2+}$
$\text{Co}_{0.05} \cdot \text{Zn}_{0.95}(\text{MeIm})_2$	0.027	0.053
$\text{Co}_{0.1} \cdot \text{Zn}_{0.9}(\text{MeIm})_2$	0.065	0.111
$\text{Co}_{0.33} \cdot \text{Zn}_{0.67}(\text{MeIm})_2$	0.356	0.500
$\text{Co}_{0.67} \cdot \text{Zn}_{0.33}(\text{MeIm})_2$	1.886	2.000

A series of bimetallic ZIFs were prepared by reacting Co^{2+} and Zn^{2+} ions with 2-methylimidazolate (MeIm) in methanolic solution. The proposed crystal structure of bimetallic ZIFs is shown in **Figure 7.1a**, which is formed by the mixed-coordination of MeIm with Zn^{2+} and Co^{2+} , respectively, based on the nets of ZnN_4 [16] or CoN_4 [22] tetrahedra. The bimetallic ZIF crystals are denoted as $\text{Co}_x \cdot \text{Zn}_{1-x}(\text{MeIm})_2$, where $x/1-x$ represent the corresponding initial molar ratio of $\text{Co}^{2+}/\text{Zn}^{2+}$ used for the synthesis, as listed in **Table 7.1**. It should be noted that

ZIF-8 crystals, only consisting of zinc ions, are white. When the zinc ions are replaced by cobalt ions, the color of the obtained bimetallic ZIFs gradually changes from white to pink, lavender, and ultimately to purple (ZIF-67), as illustrated in **Figure 7.1b**. The metal content in each bimetallic ZIF sample was precisely determined by inductively coupled plasma (ICP) analysis. As summarized in **Table 7.1**, the actual molar ratio of $\text{Co}^{2+}/\text{Zn}^{2+}$ is slightly less than the feeding molar ratio used for the synthesis, implying that the coordination interaction between zinc and MeIm is stronger than that between cobalt and MeIm. The successful preparation of bimetallic ZIFs by incorporation of Zn^{2+} and Co^{2+} into one crystal are directly demonstrated by transmission electron microscopy (TEM) and element mapping. As shown in **Figure 7.1c,d**, the zinc and cobalt species coexist and are dispersed uniformly throughout the bimetallic $\text{Co}_{0.1}\cdot\text{Zn}_{0.9}(\text{MeIm})_2$ crystals. The adjustable molar ratio of $\text{Co}^{2+}/\text{Zn}^{2+}$ in the other bimetallic ZIFs samples is also confirmed by elemental mapping (**Figure 7.2**). As discussed above, ZIF-8 and ZIF-67 are compatible thus, the resulting bimetallic ZIFs inherit the topology from both parent structures. According to the powder X-ray diffraction (XRD) patterns (**Figure 7.3**), the diffraction peaks of the bimetallic ZIFs match well with the single-metal ZIF-8 and ZIF-67. The absence of shifted peaks reflects the crystal compatibility between the parent structures as the lattice seems not to suffer from any distortions. The SEM images in **Figure 7.1e** and **Figure 7.4b-e** show that the series of bimetallic ZIFs have a rhombic dodecahedral shape identical to single-metal ZIF-8 and ZIF-67 (**Figure 7.4a,f**).

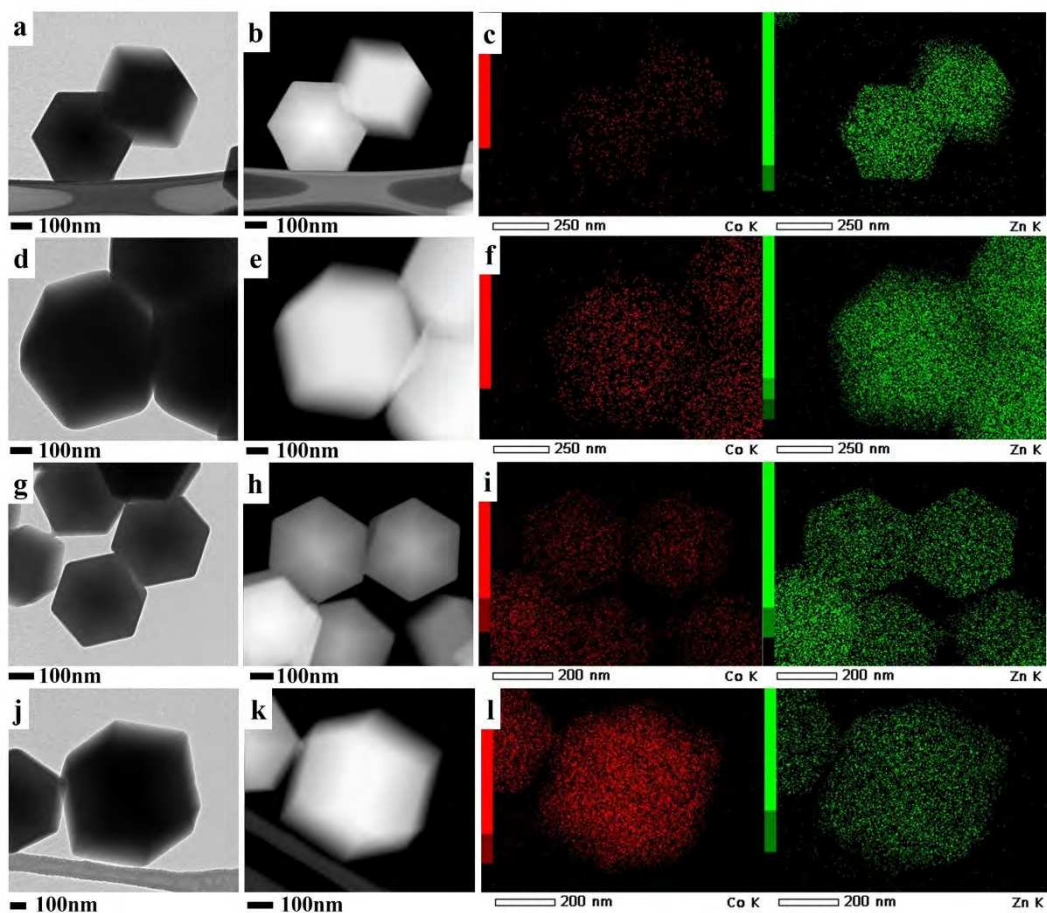


Figure 7.2 (a, d, g, j) TEM images, (b, e, h, k) HAADF STEM images, and (c, f, i, l) elemental mappings of the bimetallic ZIFs. (a-c) $\text{Co}_{0.05}\cdot\text{Zn}_{0.95}(\text{MeIm})_2$, (d-f) $\text{Co}_{0.1}\cdot\text{Zn}_{0.9}(\text{MeIm})_2$, (g-i) $\text{Co}_{0.33}\cdot\text{Zn}_{0.67}(\text{MeIm})_2$, and (j-l) $\text{Co}_{0.67}\cdot\text{Zn}_{0.33}(\text{MeIm})_2$.

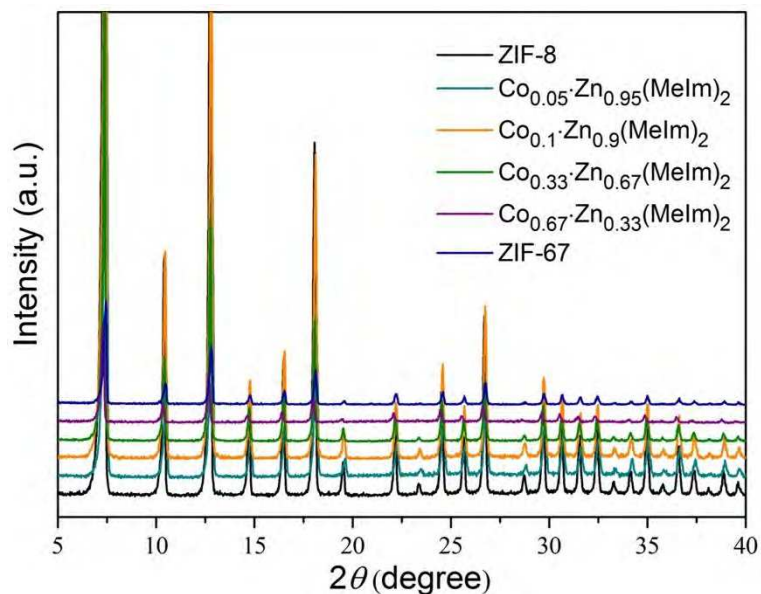


Figure 7.3 Wide-angle powder XRD patterns of the as-prepared ZIF-8, ZIF-67, and bimetallic ZIF ($\text{Co}_x\text{Zn}_{1-x}(\text{MeIm})_2$) crystals.

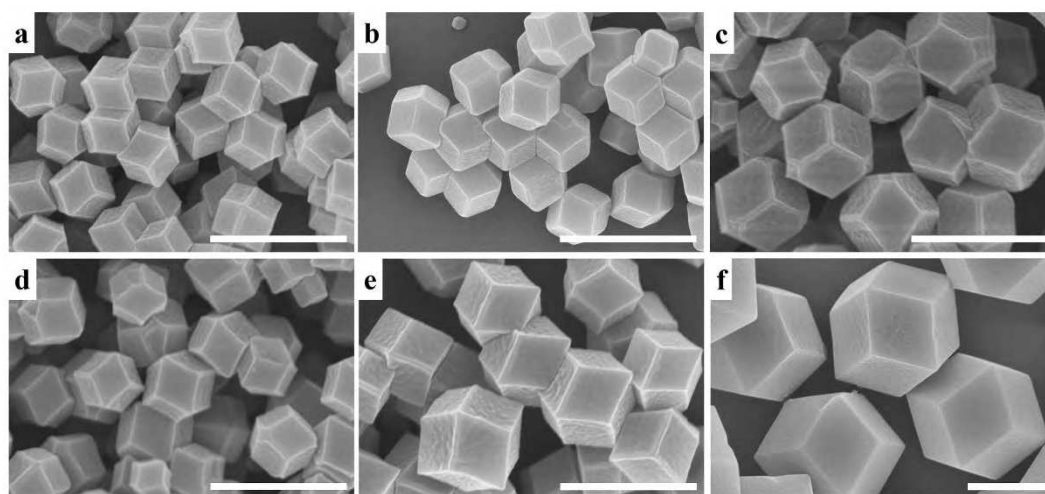


Figure 7.4 SEM images of the as-synthesized (a) ZIF-8, (b) $\text{Co}_{0.05}\text{Zn}_{0.95}(\text{MeIm})_2$, (c) $\text{Co}_{0.1}\text{Zn}_{0.9}(\text{MeIm})_2$, (d) $\text{Co}_{0.33}\text{Zn}_{0.67}(\text{MeIm})_2$, (e) $\text{Co}_{0.67}\text{Zn}_{0.33}(\text{MeIm})_2$, and (f) ZIF-67. The scale bars are all 1 μm.

7.3.2. Thermal Conversion of Bimetallic ZIFs to Nanoporous Carbon Materials

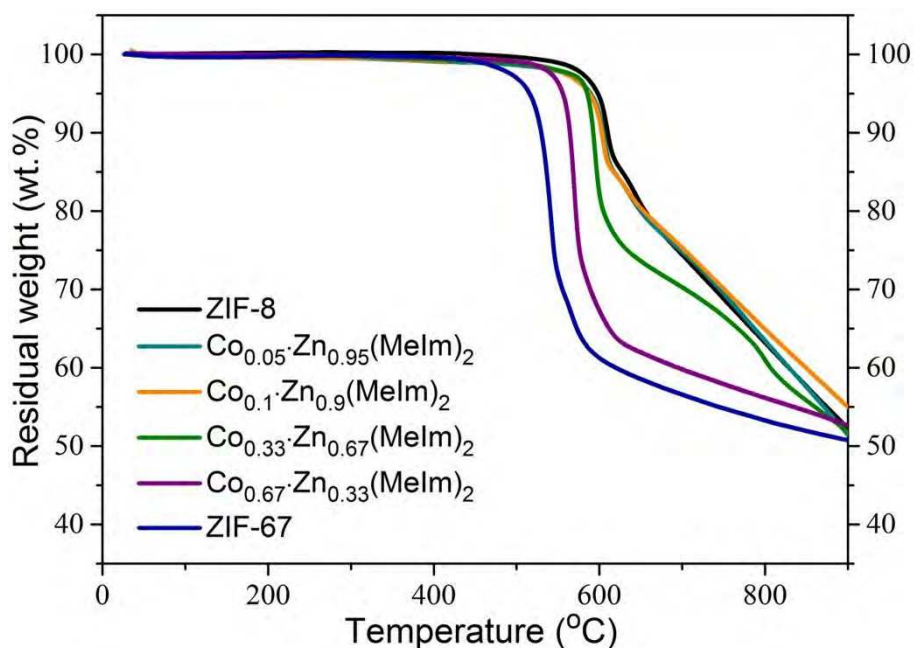


Figure 7.5 TG curves of ZIF-8, ZIF-67, and bimetallic ZIF ($\text{Co}_x\cdot\text{Zn}_{1-x}(\text{MeIm})_2$) crystals measured under N_2 atmosphere at a heating rate of $5\text{ }^\circ\text{C}\cdot\text{min}^{-1}$.

In order to investigate the effect of the $\text{Co}^{2+}/\text{Zn}^{2+}$ molar ratio on the degree of graphitization, specific surface area, and pore size distribution of the bimetallic-ZIF-derived carbon, the series of bimetallic ZIFs were carbonized at an elevated temperature. As shown in the thermogravimetric (TG) curves (**Figure 7.5**), the thermal stability of bimetallic ZIF crystals under a N_2 atmosphere gradually becomes lower along with the increased $\text{Co}^{2+}/\text{Zn}^{2+}$ ratios, which corresponds to the decreased thermal stability from single-metal ZIF-8 to ZIF-67. The weight of ZIF-8, ZIF-67, and bimetallic ZIF ($\text{Co}_x\cdot\text{Zn}_{1-x}(\text{MeIm})_2$) crystals decreases rapidly as the temperature increases, ultimately yielding to $\sim 50\text{ wt}\%$ at $900\text{ }^\circ\text{C}$. During heat treatment under inert atmospheres, most the organic linkers thermally converted into the carbon matrix, while some parts also decomposed and evaporated as small molecules. The porous carbon materials derived from the bimetallic ZIFs ($\text{Co}_x\cdot\text{Zn}_{1-x}(\text{MeIm})_2$) were labelled as C- y ($y = x/1-x$). C-ZIF-8 and C-ZIF-67 are also prepared for comparison by respectively using single-metal ZIF-8 and ZIF-67 as the precursors.

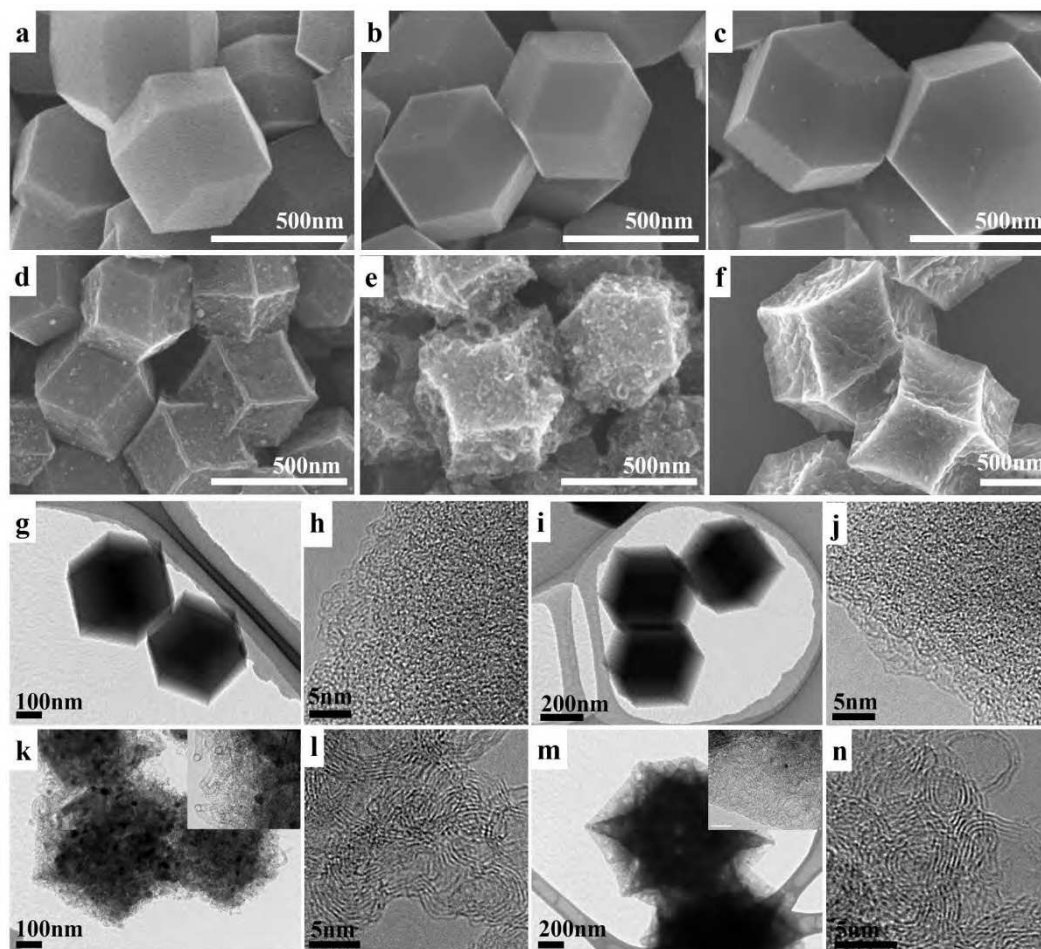


Figure 7.6 SEM images of the (a) C-ZIF-8, (b) C-1/19, (c) C-1/9, (d) C-1/2, (e) C-2/1 and (f) C-ZIF-67. TEM and high-resolution TEM images of the representative samples (g,h) C-ZIF-8, (i,j) C-1/9, (k,l) C-2/1 and (m,n) C-ZIF-67. The insets in (k) and (m) show higher magnification images of the edges.

As shown in the SEM images (**Figure 7.6a-f**), all of the carbon materials kept the rhombic dodecahedral morphology inherited from the parent ZIFs. It is worth mentioning that the surfaces of C-ZIF-8, C-1/19, and C-1/9 are smooth (**Figure 7.6a-c**). When the molar ratio of $\text{Co}^{2+}/\text{Zn}^{2+}$ increases above 1/2, however, the derived carbon materials C-1/2, C-2/1, and C-ZIF-67 are found to have a rough surface and shrunken facets (**Figure 7.6d-f**). A detailed characterization by TEM and high-resolution TEM reveals that the smooth samples of C-ZIF-8 and C-1/9 only consist of amorphous carbon (**Figure 7.6g-j**) whereas the rough samples of C-2/1 and C-ZIF-67 are composed of graphitic carbon sheets (**Figure 7.6k-n**). These results

suggest that the carbonized bimetallic ZIFs can be effectively graphitized in the presence of enough cobalt species, which explains the rough surface and distorted facets.

During carbonization, the MeIm from the bimetallic ZIF is converted into a carbon state and the coexisting Zn^{2+} and Co^{2+} ions are thermally reduced to metallic Zn and Co nanoparticles, respectively. Incorporating catalytic active transition metals into the carbon precursor (e.g., Fe, Ni, Co) has been demonstrated as an effective approach for catalytic graphitization of amorphous carbon via solid-state transformation process.[26,27] As a result, the MeIm organic linkers that surround the cobalt ions tend to be catalytically converted into graphitic carbon. However, the organic linkers that surround zinc ions tend to yield amorphous carbon because a part of the zinc evaporates during the high temperature treatment and the residual zinc nanoparticles have a weak catalytic graphitization effect.[25] In other words, the degree of graphitization of C- γ can be easily controlled by adjusting the molar ratio of $\text{Co}^{2+}/\text{Zn}^{2+}$ in the parent bimetallic ZIFs.

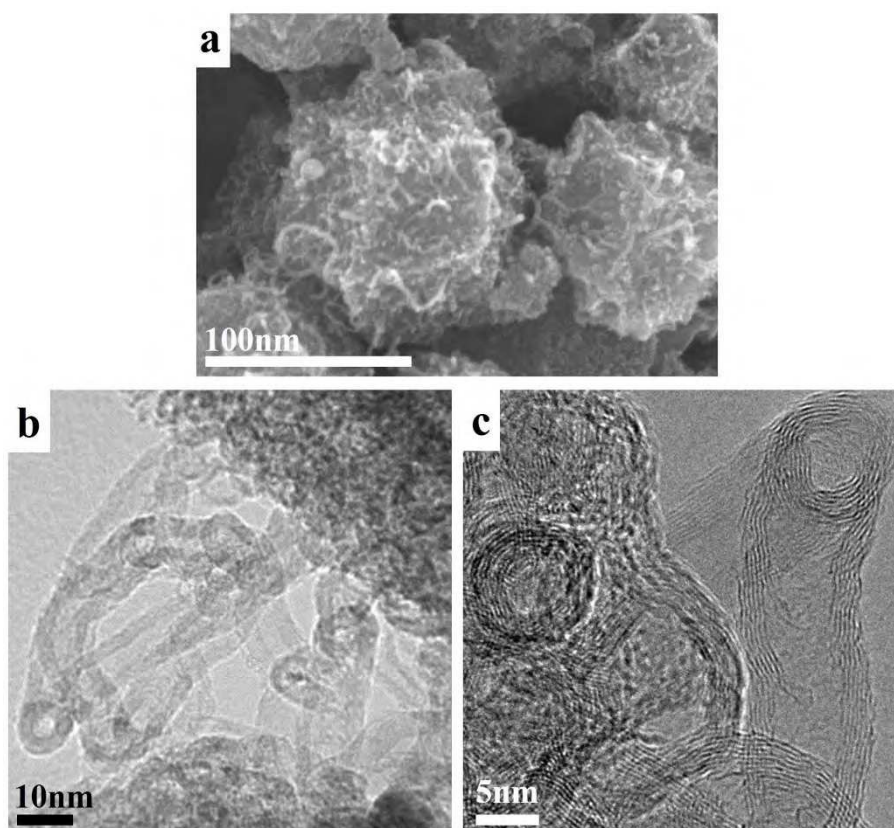


Figure 7.7 (a) SEM image, (b, c) high-resolution TEM images of sample C-2/1.

A close observation of sample C-2/1 by high magnification SEM and TEM images (**Figure 7.7**) confirms the presence of thin graphitic carbon nanotubes grown on the surfaces of C-2/1. Although C-1/2 and C-ZIF-67 also consist of graphitic carbon, the presence of carbon nanotubes could not be observed (**Figure 7.6d,f**). This suggests that there is an optimal ratio of $\text{Co}^{2+}/\text{Zn}^{2+}$ in the bimetallic ZIFs to favor the growth of carbon nanotubes under inert atmosphere only. In this case, the zinc species in the bimetallic ZIFs separate from the cobalt species and prevent the excessive growth of cobalt nanoparticles during carbonthermal reduction of cobalt ions, resulting in the formation of abundant, dispersed, and catalytically active cobalt nanoparticles. At the same time, these cobalt nanoparticles are surrounded by a suitable amount of carbon atoms that will be effectively catalytically converted to be carbon nanotubes.[28]

The degree of graphitization of carbon materials can be characterized by XRD patterns and Raman spectra. As shown in **Figure 7.8a**, the C-ZIF-8, C-1/19, and C-1/9 samples only exhibit two broad diffraction peaks at 23° and 44° , which are indexed to the (002) and (101) diffractions of amorphous carbon.[23] The broad diffraction peak at around 23° shift slightly toward higher angles as the cobalt content is increased from C-ZIF-8 to C-1/19, and to C-1/9, indicating the gradual formation of graphitized carbon. In the case of C-1/2, C-2/1, and C-ZIF-67, which have higher ratios of cobalt, the (002) diffraction peak is observed at 26° , indicating highly graphitic carbon states.[28] The results confirm the importance of cobalt ions on the degree of graphitization in the bimetallic-ZIF-derived carbon. In addition, as revealed by the XRD patterns in **Figure 7.9**, the elevated calcination temperature from 800 to 900 °C also is quite critical to promote the graphitization of carbon, thus helps to magnify the distinction of graphitization degree in the series of bimetallic-ZIF-derived carbons in this study. The increased degree of graphitization from C-ZIF-8, to C-1/19, C-1/9, C-1/2, C-2/1, and C-ZIF-67 was further observed by Raman spectroscopy (**Figure 7.8b**). Each carbon sample displays two vibration bands. The D band located at 1360 cm^{-1} corresponds to the vibrations of disordered carbon or defects, while the G band located at 1590 cm^{-1} is related to the vibrations of sp^2 -bonded graphitic carbon sheets.[29] The intensity ratio between the D and G band (I_D/I_G)

provides a good insight on the degree of graphitization for comparative studies. As shown in **Table 7.2**, the value of I_D/I_G for C-ZIF-8, C-y, and C-ZIF-67 decreases with increasing the cobalt content in the bimetallic ZIF precursors, suggesting an improved graphitization.

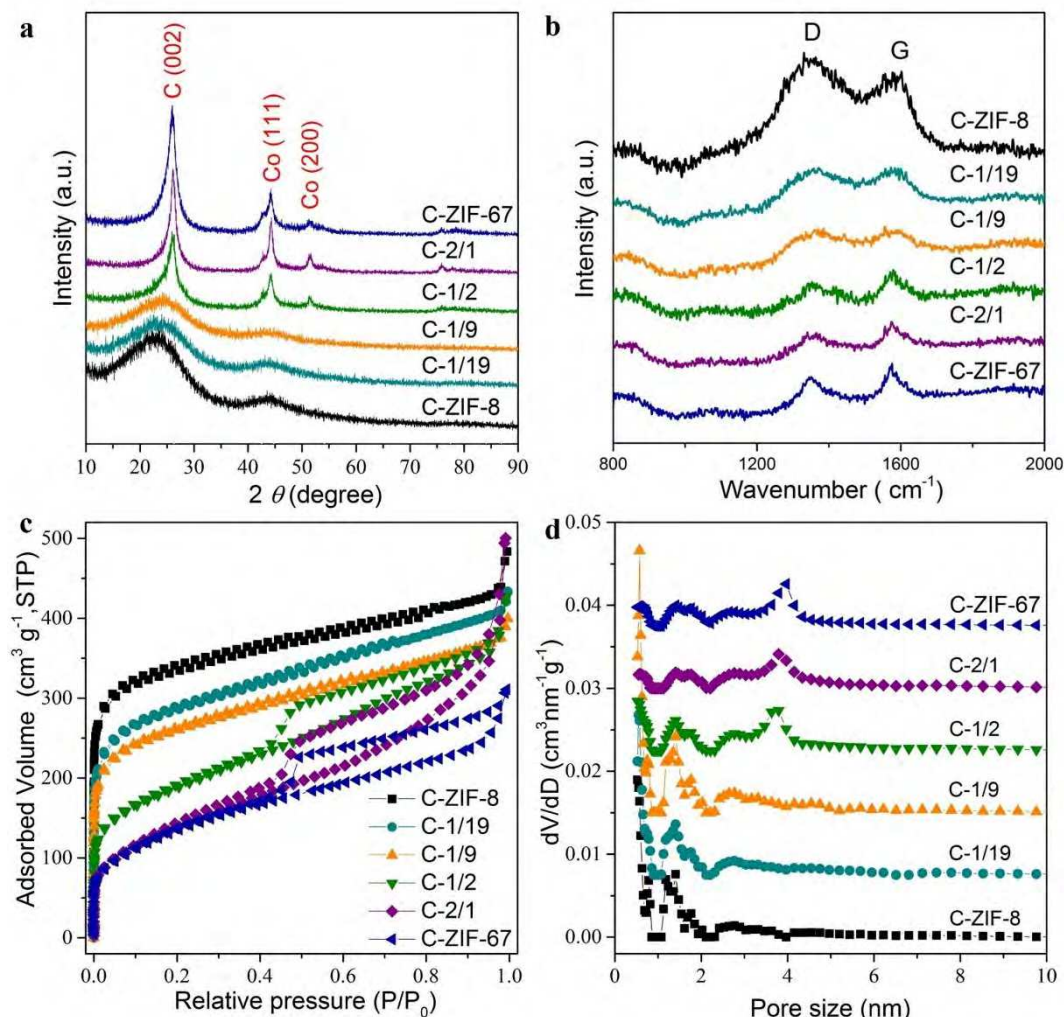


Figure 7.8 (a) Wide-angle PXRD patterns, (b) Raman spectra, (c) N_2 adsorption–desorption isotherms, (d) pore-size distributions, as estimated by the DFT method, of the C-ZIF-8, C-y, and C-ZIF-67 samples. For clarity, the isotherms for C-ZIF-8 are offset by $40 \text{ cm}^3 \cdot \text{g}^{-1}$. The pore-size distribution curves for C-1/19, C-1/9, C-1/2, C-2/1, and C-ZIF-67 are offset vertically by 0.0075 , 0.015 , 0.0225 , 0.03 , and $0.0375 \text{ cm}^3 \cdot \text{nm}^{-1} \cdot \text{g}^{-1}$, respectively.

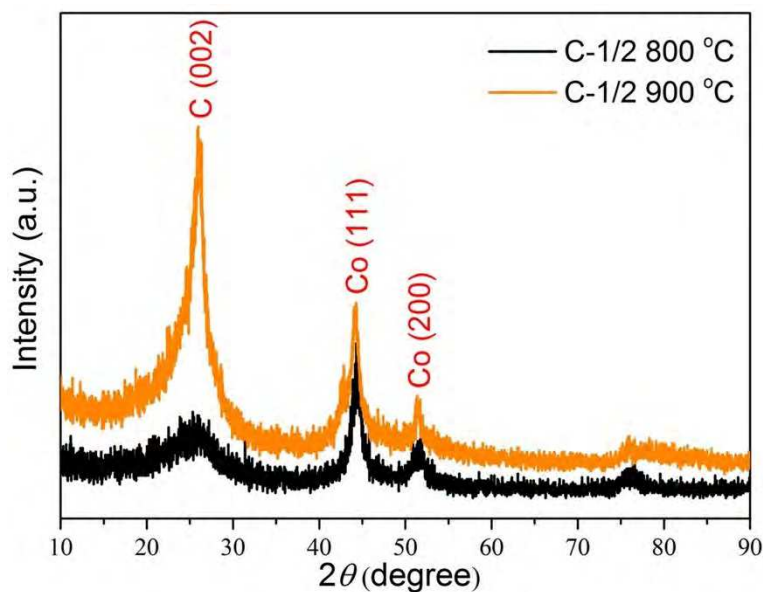


Figure 7.9 Wide-angle powder XRD patterns of the bimetallic-ZIF of $\text{Co}_{0.33}\cdot\text{Zn}_{0.67}(\text{MeIm})_2$ derived carbon carbonized at 800 and 900 °C, respectively.

In addition to the diffraction peaks of carbon, C-1/2, C-2/1, and C-ZIF-67 display other intense diffraction peaks at 44° and 51°, which can be attributed to the (111) and (200) diffractions of face-centered-cubic metallic Co nanoparticles (**Figure 7.8a**). The average size of Co nanoparticles is estimated to be 9.2, 11.8, and 11.9 nm for C-1/2, C-2/1, and C-ZIF-67, respectively, by using the Scherrer equation.[30] Although most of the cobalt nanoparticles in the carbon matrix can be removed via acid etching to form the pores, some Co nanoparticles wrapped in circular graphitic carbon layers which formed during the catalytic graphitization, are protected from acid erosion and kept embedded in the carbon matrix.[31,32] The spatial distribution of carbon, nitrogen, and cobalt was detected by elemental mapping (**Figure 7.10**). Zinc completely disappeared from each carbon sample, and cobalt was also rarely observed. Even when the ZIFs containing high content of Co ions are used as the precursor, the resulting cobalt content is only 2.15 wt% and 1.90 wt% in C-2/1 and C-ZIF-67, respectively. From CHN analysis, it is found that the level of doped nitrogen (relative weight ratio of nitrogen to carbon) is 24.0, 23.4, 23.0, 6.2, 3.5, and 2.7%, for C-ZIF-8, C-1/19, C-1/9, C-1/2, C-2/1, and C-ZIF-67, respectively. This confirms that the nitrogen heteroatoms, originating from the MeIm organic linker, are preserved in the carbon matrix after the high temperature treatment. However, the

content of nitrogen decreases along with the increased cobalt ratios in the bimetallic ZIF precursors which is probably due to the breakdown of C-N bond during the catalytically graphitization promoted by cobalt nanoparticles.

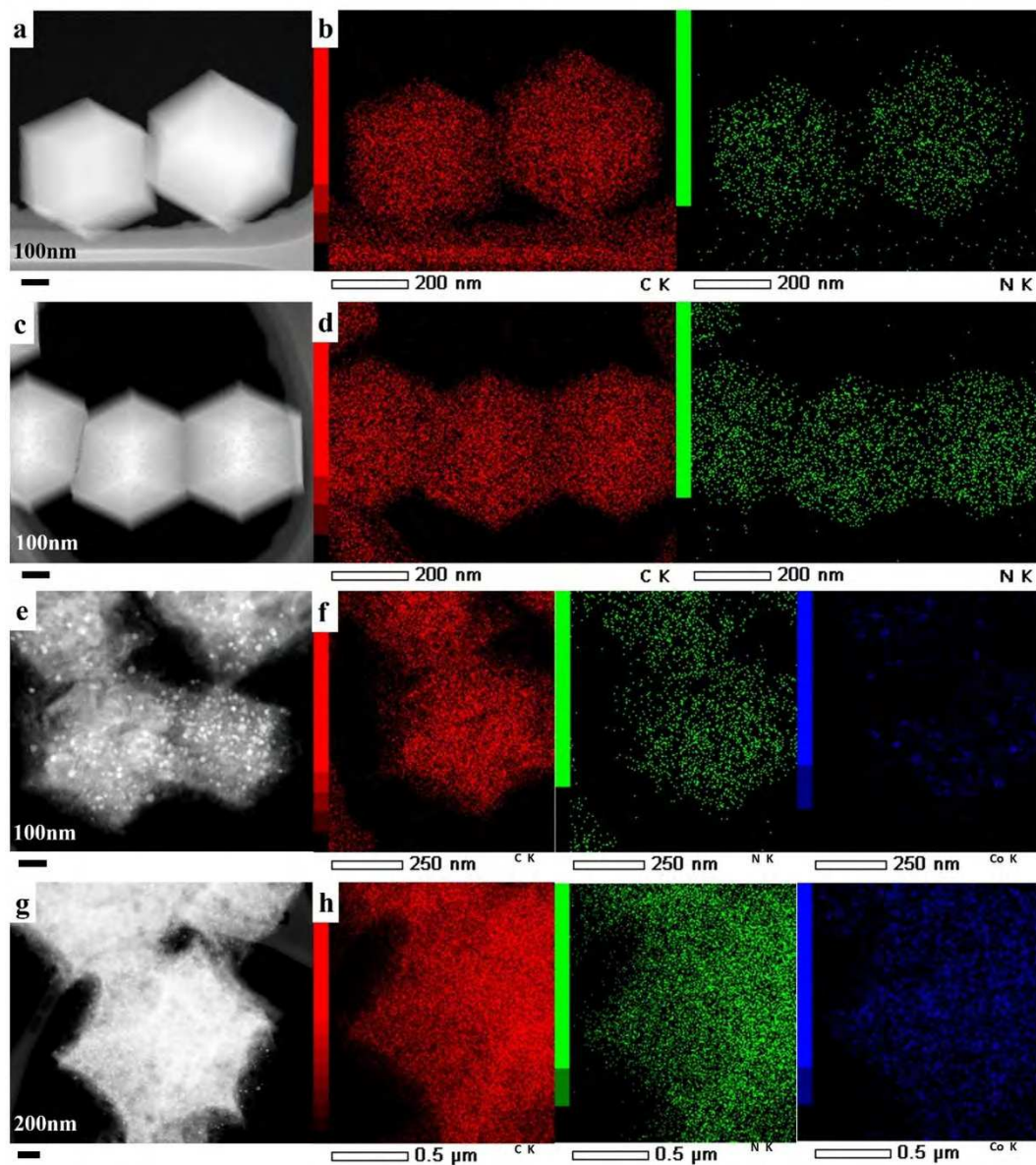


Figure 7.10 (a, c, e, g) HAADF STEM and (b, d, f, h) elemental mappings of (a, b) C-ZIF-8, (c, d) C-1/9, (e, f) C-2/1, and (g, h) C-ZIF-67.

The porosity of the carbon samples was investigated by N_2 adsorption–desorption isotherms. The sharp nitrogen uptake at low relative pressure stage ($P/P_0 < 0.05$) is generally attributed to the strong nitrogen adsorption into micropores. As shown in **Figure 7.8c**, the C-ZIF-8, C-1/19, and C-1/9 samples exhibit a much higher nitrogen uptake at low relative

pressure compared with the C-1/2, C-2/1, and C-ZIF-67 samples, indicating higher microporosity. All of the samples have gradual nitrogen uptakes in the middle relative pressure ranges from 0.3 to 0.9, implying the presence of mesopores with wide size distributions. Unlike C-ZIF-8, C-1/19, and C-1/9, the C-1/2, C-2/1, and C-ZIF-67 samples display a clear hysteresis loop, which is generally due to presence of abundant, random, bumpy, and non-uniform mesopores.[33] During the adsorption process, the nitrogen was condensed first within the smallest dimensions. The pressure increased until all pores were filled with nitrogen. Then, the pressure decreased and induced desorption of nitrogen. Because the last filled large mesopores were connected with the small mesopores, the nitrogen desorption in the same large mesopores happened at a lower relative pressure compared with adsorption process, leading to the formation of a hysteresis loop. The pore size distributions (**Figure 7.8d**), calculated by the density functional theory (DFT) method, further prove that the pores in C-*y* gradually move from micropores towards mesopores with increasing the cobalt content in the bimetallic ZIF precursors.

Table 7.2 The surface areas and total pore volumes calculated from N₂ adsorption-desorption isotherms, and the ratios of D band to G band estimated from Raman spectra are summarized.

Sample	S_{BET} ($\text{m}^2 \cdot \text{g}^{-1}$)	S_{micro} ($\text{m}^2 \cdot \text{g}^{-1}$)	$S_{\text{micro}}/S_{\text{BET}}$	V_{pore} ($\text{cm}^3 \cdot \text{g}^{-1}$)	V_{micro} ($\text{cm}^3 \cdot \text{g}^{-1}$)	$V_{\text{micro}}/V_{\text{pore}}$	$I_{\text{D}}/I_{\text{G}}$
C-ZIF-8	925	541	58.5%	0.57	0.29	50.9%	1.19
C-1/19	890	426	47.9%	0.58	0.23	39.7%	1.00
C-1/9	781	250	32.0%	0.52	0.14	26.9%	1.00
C-1/2	643	123	19.1%	0.54	0.06	11.1%	0.67
C-2/1	502	57	11.4%	0.53	0.03	5.7%	0.67
C-ZIF-67	450	41	9.1%	0.43	0.01	2.3%	0.67

The specific surface areas of C-*y* are also closely related to the cobalt ratios in the bimetallic ZIFs. As summarized in **Table 7.2**, the surface areas decrease from C-ZIF-8 (925 $\text{m}^2 \cdot \text{g}^{-1}$), to C-1/19 (890 $\text{m}^2 \cdot \text{g}^{-1}$), C-1/9 (781 $\text{m}^2 \cdot \text{g}^{-1}$), C-1/2 (643 $\text{m}^2 \cdot \text{g}^{-1}$), C-2/1 (502 $\text{m}^2 \cdot \text{g}^{-1}$), and

finally to C-ZIF-67 ($450 \text{ m}^2 \cdot \text{g}^{-1}$). The specific surface area of C-ZIF-8 ($925 \text{ m}^2 \cdot \text{g}^{-1}$, carbonized at $900 \text{ }^\circ\text{C}$) is lower than that of our previously reported ZIF-8-derived-carbon ($1499 \text{ m}^2 \cdot \text{g}^{-1}$, carbonized at $800 \text{ }^\circ\text{C}$),^[23] probably due to the collapse of some nanopores during the calcination at higher temperature. In addition, the ratio of the microporous surface area to the total surface area gradually decreases as the $\text{Co}^{2+}/\text{Zn}^{2+}$ molar ratio increases (**Table 7.2**). These results suggest that the microporosity in the carbons is inherited from the microporous ZIF precursor and that it is sacrificed during the graphitization of amorphous carbon catalyzed by the cobalt nanoparticles. Meanwhile, the mesopores are generated by the carbonization process and the subsequent removal of metal nanoparticles. Thus, hierarchically crosslinked micro/mesoporous structures are developed, and are expected to promote electrolyte penetration and to lower the diffusion resistance when used as electrode materials in electrochemical devices.

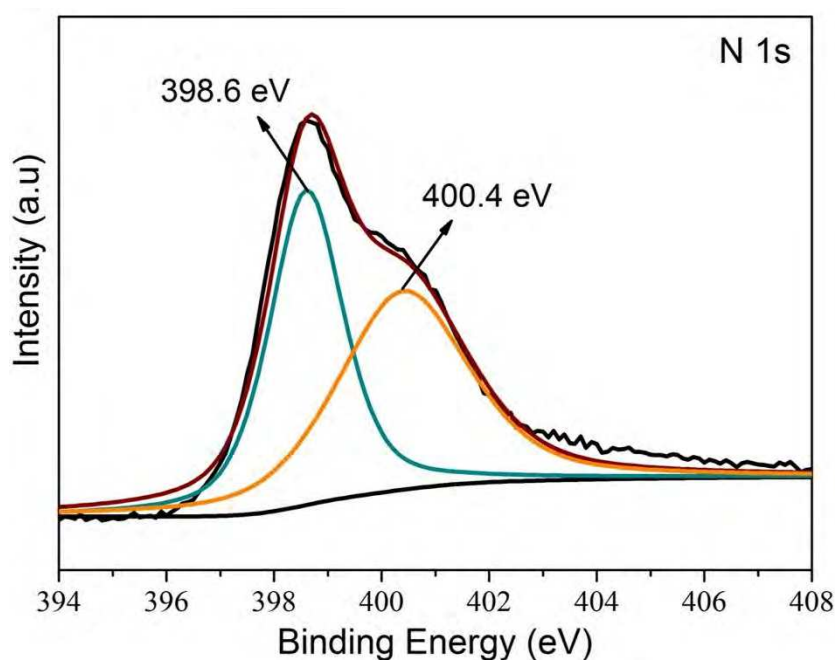


Figure 7.11. High-resolution XPS spectrum centered on the N 1s peak of the representative C-1/19 sample.

The electric state of N in the carbon was investigated by X-ray photoelectron spectroscopy (XPS). As shown in **Figure 7.11**, the high resolution spectrum of the N 1s peak of the representative C-1/19 sample can be mainly fitted with two peaks centered at ~ 398.6 and

~400.4 eV, which are assignable to pyridinic-N and graphitic-N, respectively.[34] The result demonstrates that the N atoms in the original pentagonal ring of the imidazole units are mainly doped into the carbon framework through two distinct mechanisms following the carbonization process. Pyridinic-N, referring to the sp^2 -hybridized N atoms bonded with two sp^2 -hybridized C neighbours via σ -bonds, possesses one lone-pair of electrons in the graphene plane, and contributes one electron to the conjugated π system.[35] In the graphitic-N configuration, three sp^2 -hybridized N valence electrons form three σ -bonds with three sp^2 -hybridized C neighbours, one electron fills the π -orbitals, and the fifth electron enters the π^* -states of the conduction band.[36] According to another report, the fifth electron is distributed in the local network of the carbon π -system whereas a part of the charge localizes on the graphitic-N dopant and electronically couples to its nearest C neighbours.[37]

7.3.3. Electrochemical Supercapacitors with Bimetallic-ZIF-Derived Carbon Electrodes

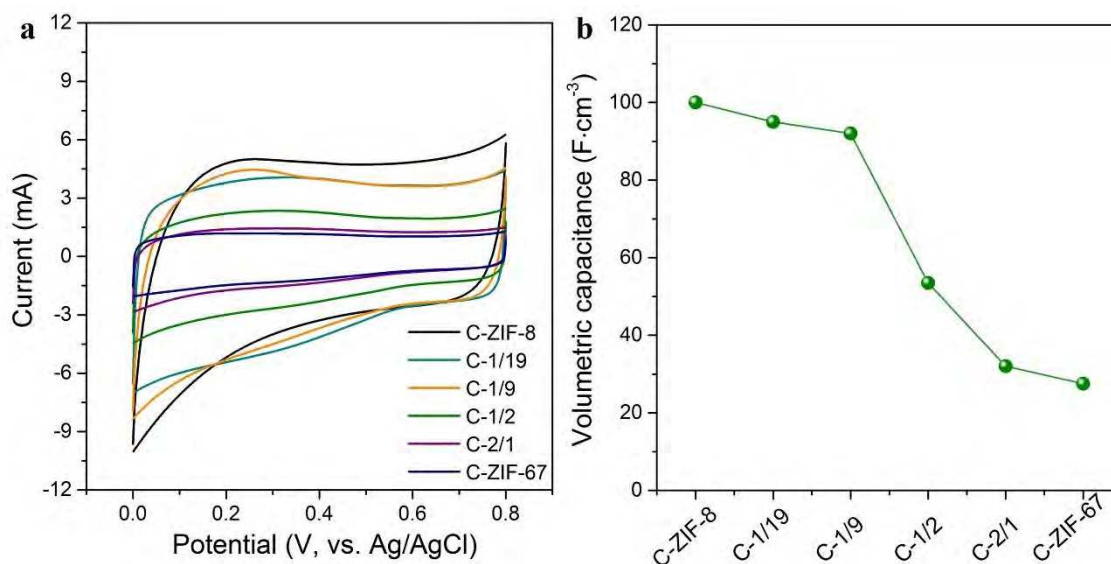


Figure 7.12. (a) CV curves and (b) volumetric capacitance for C-ZIF-8, C-y, and C-ZIF-67 samples at a scan rate of $20 \text{ mV}\cdot\text{s}^{-1}$.

To the best of my knowledge, this is the first example of a facile control over the degree of graphitization, pore size distribution, and nitrogen doping in carbons by utilizing bimetallic

MOFs with adjustable compositions. Furthermore, the series of bimetallic-MOF-derived nanoporous carbons doped with heteroatoms, which feature high surface area and a continuous conductive framework, have been investigated as promising compounds for electrodes in supercapacitor application using a standard three-electrode system. Cyclic voltammetry (CV) studies were carried out in a potential window ranging from 0.0 to 0.8 V. The CV curves for the samples show a quasi-rectangular shape (**Figure 7.12a**). The volumetric performance is an important technological metric for energy storage devices to meet realistic application. The variation of the volumetric capacitance values obtained for different samples is shown in **Figure 7.12b**. The volumetric capacitances are calculated to be 100, 95, 93, 54, 33, and 29 $\text{F}\cdot\text{cm}^{-3}$ for C-ZIF-8, C-1/19, C-1/9, C-1/2, C-2/1, and C-ZIF-67, respectively, at a scan rate of $20 \text{ mV}\cdot\text{s}^{-1}$. From these values, it can be clearly found that the capacitance decreases as the $\text{Co}^{2+}/\text{Zn}^{2+}$ ratio in the bimetallic ZIF precursor is increased. These results are consistent with the N_2 adsorption–desorption data, which indicates that the surface area as well as the number of micropores decrease as the cobalt content increases (**Table 7.2**). The capacitance retention at a high scan speed is one of the most important parameters for high performance supercapacitors. As shown in **Figure 7.13**, the capacitance retention for the C-ZIF-8 sample is found to be only 38% after cycling at a $200 \text{ mV}\cdot\text{s}^{-1}$, which is significantly lower than 71%, 85%, and 84% for the C-1/19, C-1/2, and C-ZIF-67 samples, respectively. The increased retention values can be explained by (i) the decreased concentration of micropores and increased concentration of mesopores which allow fast intercalation/de-intercalation of ions in the material, and (ii) the higher conductivity of the carbon matrix, owing to the increased degree of carbon graphitization.[38,39]

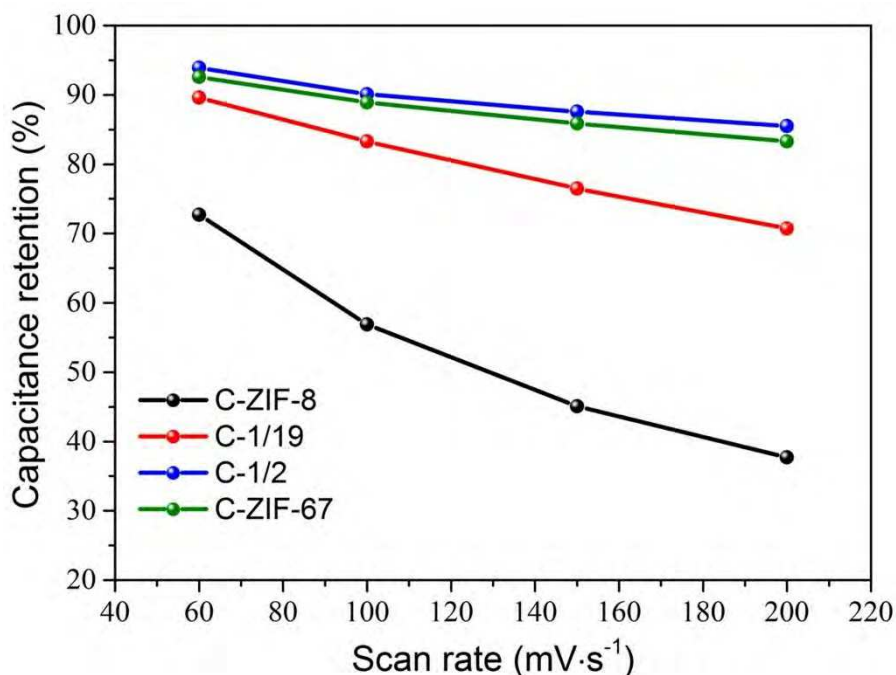


Figure 7.13 Volumetric capacitance retention of C-ZIF-8, C-1/19, C-1/2, and C-ZIF-67 samples as a function of the applied scan rates. The capacitance retention is the volumetric capacitance calculated at a higher scan rate compared to the initial scan rate of 20 mV·s⁻¹.

Among all of the samples, C-1/19 shows the high volumetric capacitance (95 F·cm⁻³) with good capacitance retention (71%), further supercapacitor studies were carried out using this sample. A symmetric supercapacitor cell (SSC) was fabricated using C-1/19 for the positive and negative electrodes. **Figure 7.14a** shows the CV curves for the SSC at various scan rates ranging from 10-300 mV·s⁻¹. The CV shape is unaltered, even at high scan rates. This shows high stability and good capacitance retention for capacitor materials. The galvanostatic charge-discharge analysis were carried out at various applied current densities (**Figure 7.14b**). More interestingly, the charge-discharge curves show no electrode-potential drop (*IR* drop) even when the applied current density is increased up to 5 A·g⁻¹ (~15 times the initial current density), indicating the low internal ion-transport resistance.[6] The capacitance values are found to be 21.1, 20.4, 20.3, 18.7, 18.2, 17.9, 17.9, and 15.6 F·cm⁻³ at the current densities of 0.35, 0.4, 0.45, 0.5, 1.0, 1.5, 3.5, and 5 A·g⁻¹, respectively (**Figure 7.14c**). This clearly reveals that this carbon material can be used in high-rate operating devices with high volumetric capacitance and capacitance retention. In addition to supercapacitor, carbon-based

materials are widely used in various fields (e.g., including Li-ion battery, fuel cell, catalysis), which request different properties of carbon. In this study, the physical and chemical properties of my bimetallic-ZIF-derived carbon can be precisely adjusted by tuning the ratio of $\text{Co}^{2+}/\text{Zn}^{2+}$ in the bimetallic ZIF precursor, providing an opportunity for us to screen out the optimal carbon materials for the specific applications.

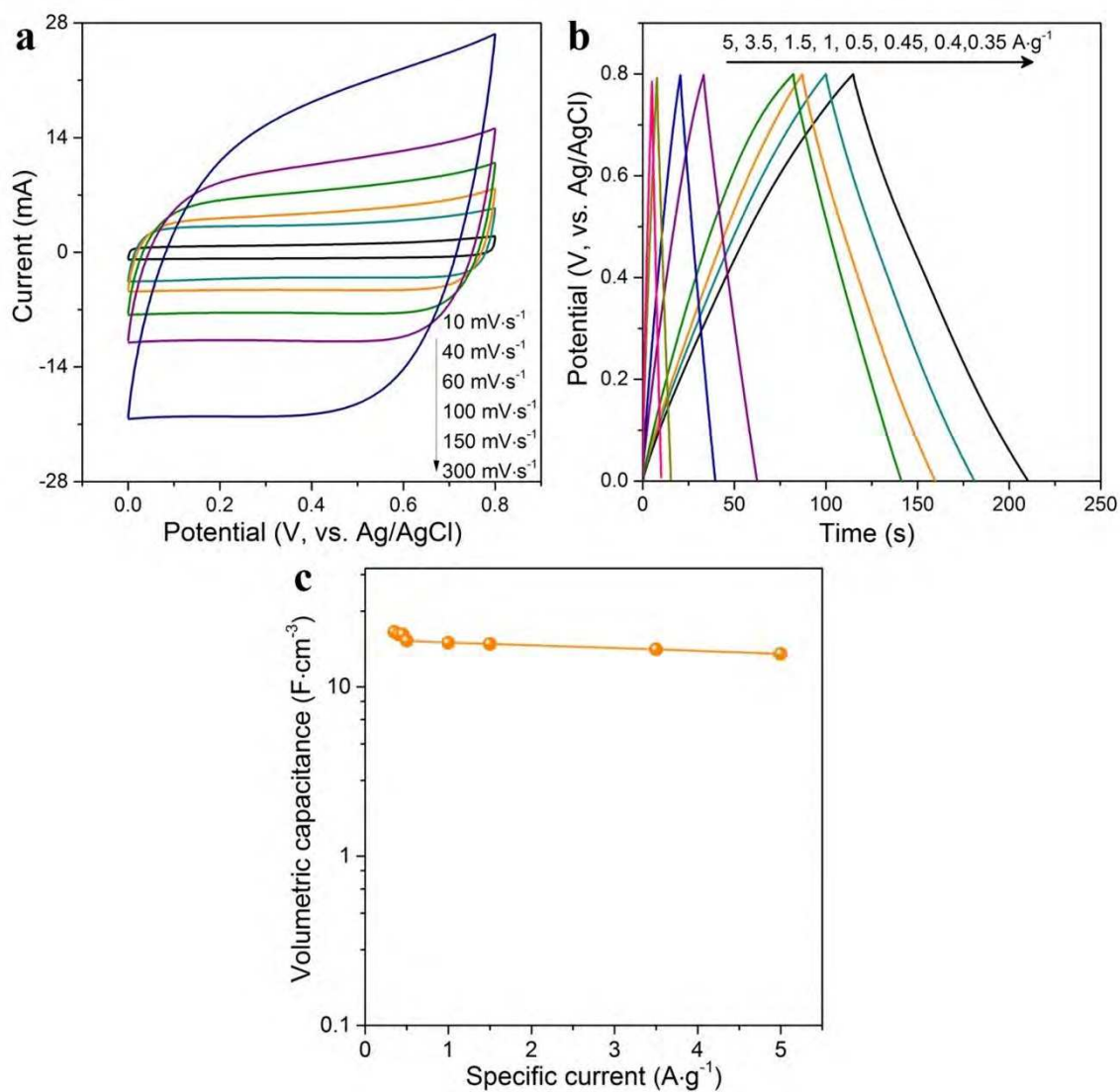


Figure 7.14 (a) CV curves at different scan rates of symmetric supercapacitor cell (SSC) with nanoporous carbon (C-1/19 sample) positive and negative electrodes. The device was cycled within the potential window of 0 to 0.8 V. (b) Galvanostatic charge-discharge curves with current density for the SSC. (c) Volumetric capacitance of SSC as a function of the applied current densities.

7.4. Conclusion

In summary, bimetallic ZIFs ($\text{Co}_x\text{Zn}_{1-x}(\text{MeIm})_2$) have been successfully prepared due to the crystal compatibility between ZIF-8 ($\text{Zn}(\text{MeIm})_2$) and ZIF-67 ($\text{Co}(\text{MeIm})_2$). Unlike the single-metal ZIFs, which only contain zinc or cobalt ions, the zinc and cobalt ions coexist in the bimetallic ZIFs and support different functionalities during the carbonization process. As a result, the physical and chemical properties of the bimetallic-ZIF-derived carbon can be designed via simply and precisely adjusting the ratio of $\text{Co}^{2+}/\text{Zn}^{2+}$ in the bimetallic ZIF precursor. Therefore, this work offers a practical way to achieve optimal properties in carbon materials for specific applications by easily tailoring the components of the bimetallic ZIFs precursors.

References

- [1] D. Pech, M. Brunet, H. Durou, P. Huang, V. Mochalin, Y. Gogotsi, P. Taberna, P. Simon, *Nat. Nanotechnol.*, 2010, **5**, 651.
- [2] K. H. An, W. S. Kim, Y. S. Park, J.-M. Moon, D. J. Bae, S. C. Lim, Y. S. Lee, Y. H. Lee, *Adv. Funct. Mater.*, 2001, **11**, 387.
- [3] X. Wang, Y. Zhang, C. Zhi, X. Wang, D. Tang, Y. Xu, Q. Weng, X. Jiang, M. Mitome, D. Golberg, Y. Bando, *Nat. Commun.*, 2013, **4**, 2905.
- [4] D. Hulicova-Jurcakova, M. Seredych, G. Q. Lu, T. J. Bandoz, *Adv. Funct. Mater.*, 2009, **19**, 438.
- [5] Z.-A. Qiao, B. Guo, A. J. Binder, J. Chen, G. M. Veith, S. Dai, *Nano Lett.*, 2013, **13**, 207.
- [6] D.-W. Wang, F. Li, M. Liu, G. Q. Lu, H.-M. Cheng, *Angew. Chem. Int. Ed.*, 2008, **47**, 373.
- [7] J. Chmiola, G. Yushin, Y. Gogotsi, C. Portet, P. Simon, P. L. Taberna, *Science*, 2006, **313**, 1760.
- [8] L. Zhang, X. Yang, F. Zhang, G. Long, T. Zhang, K. Leng, Y. Zhang, Y. Huang, Y. Ma, M. Zhang, Y. Chen, *J. Am. Chem. Soc.*, 2013, **135**, 5921.
- [9] A. S. Aricò, P. Bruce, B. Scrosati, J. M. Tarascon, W. V. Schalkwijk, *Nat. Mater.*, 2005, **4**, 366.

- [10] J. Hu, P. Tao, S. Wang, Y. Liu, Y. Tang, H. Zhong, Z. Lu, *J. Mater. Chem. A*, 2013, **1**, 6558.
- [11] D. Hulicova-Jurcakova, A. M. Puziy, O. I. Poddubnaya, F. Suárez-García, J. M. D. Tascón, G. Q. Lu, *J. Am. Chem. Soc.*, 2009, **131**, 5026.
- [12] B. Liu, H. Shioyama, T. Akita, Q. Xu, *J. Am. Chem. Soc.*, 2008, **130**, 5390.
- [13] H.-L. Jiang, B. Liu, Y.-Q. Lan, K. Kuratani, T. Akita, H. Shioyama, F. Zong, Q. Xu, *J. Am. Chem. Soc.*, 2011, **133**, 11854.
- [14] X. Cao, B. Zheng, X. Rui, W. Shi, Q. Yan, H. Zhang, *Angew. Chem. Int. Ed.*, 2014, **53**, 1404.
- [15] R. R. Salunkhe, J. Tang, Y. Kamachi, T. Nakato, J. H. Kim, Y. Yamauchi, *ACS Nano*, 2015, **9**, 6288.
- [16] K. S. Park, Z. Ni, A. P. Côté, J. Y. Choi, R. Huang, F. J. Uribe-Romo, H. K. Chae, M. O’Keeffe, O. M. Yaghi, *Proc. Natl. Acad. Sci. USA*, 2006, **103**, 10186.
- [17] N. L. Torad, M. Hu, Y. Kamachi, K. Takai, M. Imura, M. Naito, Y. Yamauchi, *Chem. Commun.*, 2013, **49**, 2521.
- [18] N. L. Torad, M. Hu, S. Ishihara, H. Sukegawa, A. A. Belik, M. Imura, K. Ariga, Y. Sakka, Y. Yamauchi, *Small*, 2014, **10**, 2096.
- [19] J. Chmiola, G. Yushin, R. Dash, Y. Gogotsi, *J. Power Sources*, 2006, **158**, 765.
- [20] X.-H. Li, S. Kurasch, U. Kaiser, M. Antonietti, *Angew. Chem. Int. Ed.*, 2012, **51**, 9689.
- [21] D. Hulicova, J. Yamashita, Y. Soneda, H. Hatori, M. Kodama, *Chem. Mater.*, 2005, **17**, 1241.
- [22] R. Banerjee, A. Phan, B. Wang, C. Knobler, H. Furukawa, M. O’Keeffe, O. M. Yaghi, *Science*, 2008, **319**, 939.
- [23] J. Tang, R. R. Salunkhe, J. Liu, N. L. Torad, M. Imura, S. Furukawa, Y. Yamauchi, *J. Am. Chem. Soc.*, 2015, **137**, 1572.
- [24] R. Wu, X. Qian, K. Zhou, J. Wei, J. Lou, P. M. Ajayan, *ACS Nano*, 2014, **8**, 6297.
- [25] Y.-Z. Chen, C. Wang, Z.-Y. Wu, Y. Xiong, Q. Xu, S.-H. Yu, H.-L. Jiang, *Adv. Mater.*, 2015, **27**, 5010.

- [26] G. C. Loh, D. Baillargeat, *J. Appl. Phys.*, 2013, **114**, 033534.
- [27] P. Su, H. Xiao, J. Zhao, Y. Yao, Z. Shao, C. Li, Q. Yang, *Chem. Sci.*, 2013, **4**, 2941.
- [28] B. Y. Xia, Y. Yan, N. Li, H. B. Wu, X. W. Lou, X. Wang, *Nat. Energy*, 2016, **1**, 15006.
- [29] R. Zhang, Y. Liu, L. Yu, Z. Li, S. Sun, *Nanotechnology*, 2013, **24**, 225601.
- [30] J. Tang, T. Wang, X. Pan, X. Sun, X. Fan, Y. Guo, H. Xue, J. He, *J. Phys. Chem. C*, 2013, **117**, 16896.
- [31] A.-H. Lu, W.-C. Li, N. Matoussevitch, B. Spliethoff, H. Bönemann, F. Schüth, *Chem. Commun.*, 2005, 98.
- [32] J. Tang, S. Wu, T. Wang, H. Gong, H. Zhang, S. M. Alshehri, T. Ahamad, H. Zhou, Y. Yamauchi, *ACS Appl. Mater. Interfaces*, 2016, **8**, 2796.
- [33] K. S. W. Sing, D. H. Everett, R. A. W. Haul, L. Moscou, R. A. Pierotti, J. Rouquérol, T. Siemieniowska, *Pure Appl. Chem.*, 1985, **57**, 603.
- [34] F. Zheng, Y. Yang, Q. Chen, *Nat. Commun.*, 2014, **5**, 5261.
- [35] L. Lai, J. R. Potts, D. Zhan, L. Wang, C. K. Poh, C. Tang, H. Gong, Z. Shen, J. Lin, R. S. Ruoff, *Energy Environ. Sci.*, 2012, **5**, 7936.
- [36] D. Usachov, O. Vilkov, A. Grüneis, D. Haberer, A. Fedorov, V. K. Adamchuk, A. B. Preobrajenski, P. Dudin, A. Barinov, M. Oehzelt, C. Laubschat, D. V. Vyalikh, *Nano Lett.*, 2011, **11**, 5401.
- [37] T. Schiros, D. Nordlund, L. Pálová, D. Prezzi, L. Zhao, K. S. Kim, U. Wurstbauer, C. Gutiérrez, D. Delongchamp, C. Jaye, D. Fischer, H. Ogasawara, L. G. M. Pettersson, D. R. Reichman, P. Kim, M. S. Hybertsen, A. N. Pasupathy, *Nano Lett.*, 2012, **12**, 4025.
- [38] B. Liu, H. Shioyama, H. Jiang, X. Zhang, Q. Xu, *Carbon*, 2010, **48**, 456.
- [39] H. Zhu, J. Yin, X. Wang, H. Wang, X. Yang, *Adv. Funct. Mater.*, 2013, **23**, 1305.

Chapter 8

General Conclusions and Future Perspective

8.1. Overview of the Achievements

Nanoporous carbon materials have attracted considerable attention for the development of next-generation high-performance electronic devices. In an overview of the whole work, I focus on rational design and synthesis of carbon-based materials with controlled physical and chemical properties, especially paying attention to the pore size distribution, nitrogen-doping, and degree of graphitization. The researches and main achievements are summarized in two sections below.

(I) Synthesis of N-Doped Porous Carbon based on a Templating Method and Using Nitrogenous Dopamine as the Precursor

The nanoscale mesoporous structure and spherical morphology are fascinating properties in carbon materials because of the resultant short pathways for mass transport and minimized viscous effects. Heteroatom doping will endow carbon materials with additional functionalities by modifying the electron donor/acceptor of carbon materials and increasing the wettability between carbon and an electrolyte. Herein, I demonstrate the synthesis of highly N-doped mesoporous carbon spheres (NMCS) through the self-polymerization of dopamine and spontaneous co-assembly with diblock copolymer micelles (PS-*b*-PEO). The use of micelles enabled the precisely control of pore sizes in the spheres and the use of dopamine offered a simple in situ introduction of heteroatoms into carbon materials. This research shows the first time that narrowly dispersed NMCS possess large mesopores (~16 nm) and small particle sizes (~200 nm). Such large pores and small spherical geometry greatly promote mass transportation, leading to high electrocatalytic activity as the metal-free catalyst for oxygen reduction reaction.

(Shown in Chapter 2)

Then I introduce a facile procedure for the synthesis of N-doped hierarchical porous carbons with a three-dimensional interconnected framework (NHPC-3D). The strategy, based on a colloidal crystal templating method, utilized nitrogenous dopamine as the precursor. NHPC-3D is composed of macropores as well as meso- and microporous textures, providing a

high surface area for electrical charge storage and free diffusion pathways for ion and mass transport when being implemented in electrochemical capacitors. **(Shown in Chapter 3)**

Inspired by the interaction between polydopamine and diblock copolymer, and the deposition of polydopamine on solid surfaces, herein I synthesized N-doped hollow carbon spheres with large tunable mesopores (~20 nm) in the shell. Silica spheres were used as hard template for a hollow core, and PS₁₇₃-*b*-PEO₁₇₀ was selected as a soft template for the generation of mesopores in the shell. The unique structural properties enabled the obtained carbon to be promising materials as adsorbents, catalyst supports, electrode materials, drug delivery carriers, and hosts for active substances. **(Shown in Chapter 4)**

(II) Synthesis of Selectively Functionalized Nanoporous Hybrid Carbon based on Self-Templating Method and Using designed MOFs as the Precursor

In recent years, metal–organic frameworks (MOFs) have been demonstrated to be efficient precursors for preparing diverse porous carbon-based materials. In most of the previous works, however, carbon-based materials were derived from a single MOF precursor and therefore possessed limited properties. In this project, core–shell ZIF-8@ZIF-67 crystals were well designed and prepared through a seed-mediated growth method. The core size of ZIF-8 and the shell thickness of ZIF-67 can be tuned simply. After the direct carbonization of ZIF-8@ZIF-67, I obtained selectively functionalized nanoporous hybrid carbon consisting of N-doped carbon (NC) as the core and highly graphitic carbon (GC) as the shell. This is the first example of the integration of NC and GC in one particle at the nanometer level. Hybrid carbon integrate the advantageous properties of the individual NC and GC, exhibiting a distinguished specific capacitance. The study not only bridges diverse carbon materials with infinite metal–organic frameworks but also opens a new avenue for artificially designed nanoarchitectures with target functionalities. **(Shown in Chapter 5)**

Based on the achievement in **Chapter 5**, I explored a novel cage-type highly graphitic porous carbon-Co₃O₄ polyhedron (GPC-Co₃O₄) by executing a two-step annealing of core–shell ZIFs. A hybrid carbon polyhedron composite, consisting of amorphous carbon (AC)

as the core and graphitic carbon-Co (GC-Co) as the shell, was prepared after the carbonization of core-shell ZIF-8@ZIF-67. AC cores were selectively removed, and Co was oxidized into Co_3O_4 by annealing AC@GC-Co in air. GPC- Co_3O_4 was assembled as an O_2 electrode without an additional conductive agent and displayed a low charge overpotential, good rate capability, and long cycle life in a Li- O_2 battery. (**Shown in Chapter 6**)

The different metal ions in the ZIF precursor will play different roles during carbonization. In this study, I merged the advantages of different metal ions into one ZIF crystal (bimetallic ZIF) to achieve porous carbon materials with tailored properties. By fine-tuning the the compositions in the bimetallic ZIF precursors, the physical and chemical properties of my bimetallic-ZIF-derived carbon can be precisely adjusted, including the specific surface area, pore size distribution, degree of graphitization, and nitrogen doping, providing there is an opportunity to explore the optimal carbon materials for the specified applications. (**Shown in Chapter 7**)

8.2. Future Perspective

Carbon is undoubtedly the most widely used material in all technologies due to its abundance and competitively outstanding properties. During the past five years, metal-organic frameworks (MOFs) (or porous coordination polymers, PCPs) have become a rapidly rising star as a convenient self-templated precursor for preparing carbon-based materials, as shown in **Table 8.1**. The MOF-derived materials are promising in a wide variety of applications, such as gas storage, catalysis, and electronic devices. The applications of metal-organic frameworks (MOFs) and derivatives can be extended by encapsulating various functional species within the frameworks. Furthermore, morphological preservation is critical during the thermal transformation of MOFs in order to maintain the porosity, rigidity, and uniform distribution of the metal species. Based on my previous research experience, I will continue focusing on the exploration of multifunctional novel carbon-based nanomaterials by using elaborately designed MOFs as the main precursor for electrochemical applications.

(I) MOFs Functionalized with Nanoparticles via In Situ Encapsulation

Figure 8.1 Metal nanoparticles encapsulated in an MOF. Reproduced with permission [12]. Copyright 2012, Nature Publishing Group.

As proven by previous studies (**Figure 8.1**), the nanostructured objects capped with a surfactant can be encapsulated in MOFs, which would display synergistic behaviors (catalysis, optical and electrically conductivity). After an initial design and synthesis of nanoparticles encapsulated in MOFs, I will fabricate customized carbon-based nanomaterials after a one-step thermal conversion. The above research will broaden the horizons for exploitation of designed hybrid MOFs and inspire a new way to fabricate infinite derivatives.

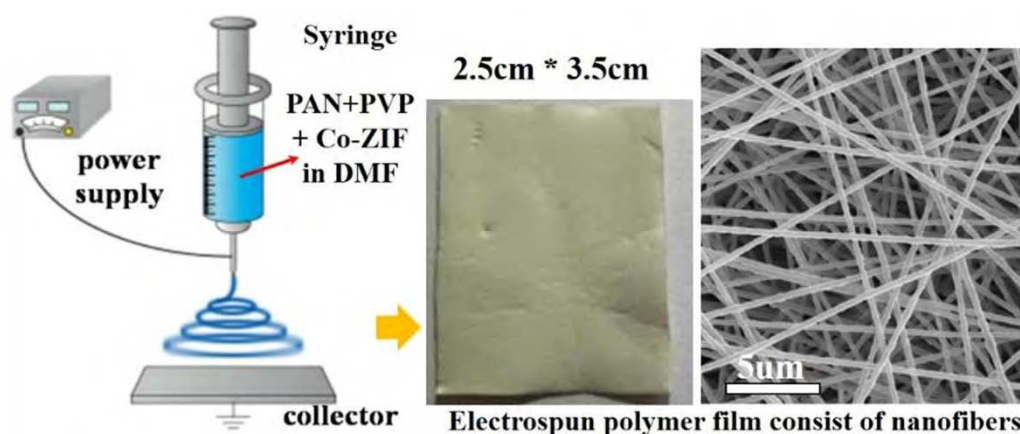
(II) MOFs-Decorated Carbon Nanofiber Network as Flexible Freestanding Electrode Materials

Figure 8.2 Illustration of the electrospinning process.

The state-of-the-art fabrication of electrodes involves the combination of active materials with carbon black and insulated polymer binders. However, the additives will bring out shortcomings including extra cost, contact resistance, and needless weight. The self-supported functional carbon nanofiber network fabricated via electrostatic spinning can be

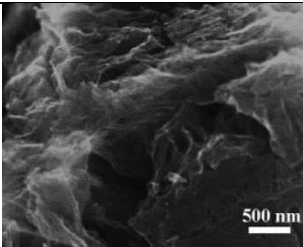
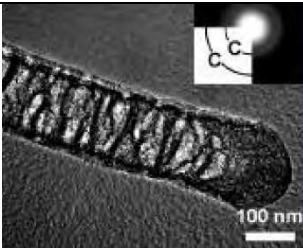
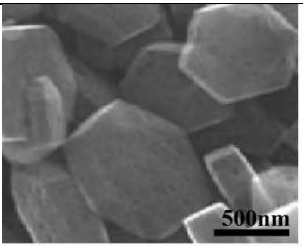
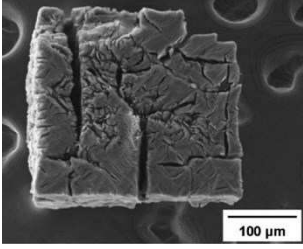
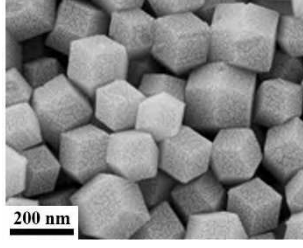
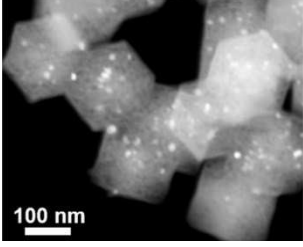
easily scaled up to industrial-scale production and work as electrode materials in lots of fields, such as lithium-ion (lithium-air) batteries, electrochemical capacitors, and alkaline hydrogen evolution reactions.

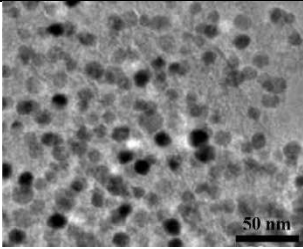
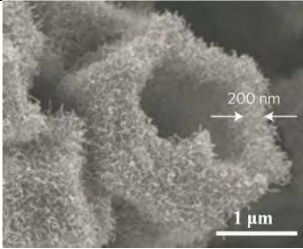
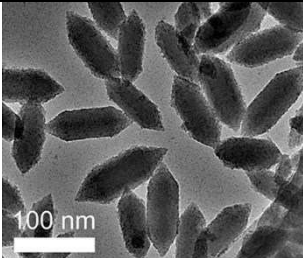
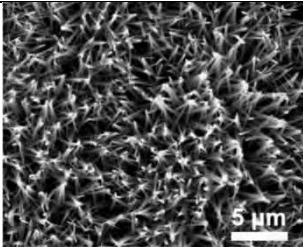
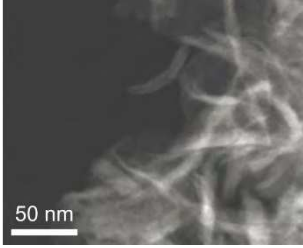
In order to endow the carbon nanofiber network with specific functionalities, the diverse hybrid MOFs and derivatives can be incorporated into carbon fibers and woven into a flexible, cross-linked, and lightweight carbon network. For example, I plan to fabricate a cobalt@graphitic carbon decorated N-doped carbon nanofiber network (Co@GC-NCNF). As schematically shown in **Figure 8.2**, polyacrylonitrile (PAN) and polyvinylpyrrolidone (PVP) are dissolved in N, N-dimethylformamide (DMF) first, and then the freshly prepared Co-ZIFs are added. After ejecting the mixed solution from the stainless steel capillary with a voltage of 12 kV, the electrospun polymer nanofiber can be collected and carbonized to be Co@GC-NCNF in N₂. Such a carbon network has great potential for application not only in solid-state supercapacitor devices but also as a freestanding electrode in lithium-ion batteries: (1) The one dimensional (1D) carbon fibers can make ion transfer easy, (2) Co@GC will be electrochemically coupled due to the electrical conductive carbon fiber, and (3) isolated Co@GC can be prevented from aggregation and deterioration during long-term operation.

(III) Extending the Morphology of MOF from Polyhedron into One or Two Dimensions

Carbon nanomaterials with low dimensions are the focus of research due to their unusual and exceptional electronic properties. Despite rapid progress in the field of MOF-derived carbons, their current morphology is mainly limited to polyhedrons, the typical appearance of parent MOFs. Recently, the fabrication of 1D carbon-based nanowire arrays by constructing a new MOF precursor on copper foil was reported. However, there are not many deep studies focusing on extending the existing MOFs to different morphologies. Breaking the dimensional limitation is the new challenges to further develop MOF-derived carbon-based materials and broaden their application.

Table 8.1 Selected carbon-based materials by adopting MOFs/PCPs as self-templated precursors.

Precursor	Product	Structure	Application	Ref
MOF-5 & furfuryl alcohol	Nanoporous carbon		Electric double-layer capacitor	[1]
Al-PCP	Nanoporous carbon		Sensor	[2]
Fe-PCP	Mesoporous carbon nanodisks		Electric double-layer capacitor	[3]
IRMOF-1	Hierarchically porous carbon		Hydrogen storage	[4]
ZIF-8	N-doped porous carbon		Lithium-ion battery	[5]
Zn/Co bi-MOF	Co-N-C nanopolyhedron		Oxygen reduction reaction	[6]

ZIF-67 & H ₃ BO ₃	Co@N, B-doped carbon		Hydrogen evolution reaction [7]
ZIF-67	Hollow frameworks of N-doped carbon nanotubes		Oxygen reduction and evolution reactions [8]
MIL-88B-NH ₃	Fe-containing N-doped carbon composites		Oxygen reduction reaction [9]
Co-MOF	Co ₃ O ₄ -carbon porous nanowire arrays		Oxygen evolution reaction [10]
MOF-74	Graphene nanoribbons		Electric double-layer capacitor [11]

References

- [1] B. Liu, H. Shioyama, T. Akita, Q. Xu, *J. Am. Chem. Soc.*, 2008, **130**, 5390.
- [2] M. Hu, J. Reboul, S. Furukawa, N. L. Torad, Q. Ji, P. Srinivasu, K. Ariga, S. Kitagawa, Y. Yamauchi, *J. Am. Chem. Soc.*, 2012, **134**, 2864.
- [3] P. P. Su, L. Jiang, J. Zhao, J. W. Yan, C. Li, Q. H. Yang, *Chem. Commun.*, 2012, **48**, 8769.
- [4] S. J. Yang, T. Kim, J. H. Im, Y. S. Kim, K. Lee, H. Jung, C. R. Park, *Chem. Mater.*, 2012, **24**, 464.
- [5] F. Zheng, Y. Yang, Q. Chen, *Nat. Commun.*, 2014, **5**, 5261.
- [6] B. You, N. Jiang, M. Sheng, W. S. Drisdell, J. Yano, Y. Sun, *ACS Catal.*, 2015, **5**, 7068.
- [7] H. Zhang, Z. Ma, J. Duan, H. Liu, G. Liu, T. Wang, K. Chang, M. Li, L. Shi, X. Meng, K. Wu, J. Ye, *ACS Nano*, 2016, **10**, 684.
- [8] B. Y. Xia, Y. Yan, N. Li, H. B. Wu, X. W. Lou, X. Wang, *Nat. Energy*, 2016, **1**, 15006.
- [9] S. Zhao, H. Yin, L. Du, L. He, K. Zhao, L. Chang, G. Yin, H. Zhao, S. Liu, Z. Tang, *ACS Nano*, 2014, **8**, 12660.
- [10] T. Y. Ma, S. Dai, M. Jaroniec, S. Z. Qiao, *J. Am. Chem. Soc.*, 2014, **136**, 13925.
- [11] P. Pachfule, D. Shinde, M. Majumder, Q. Xu, *Nat. Chem.*, 2016, **8**, 718.
- [12] G. Lu, S. Li, Z. Guo, O. K. Farha, B. G. Hauser, X. Qi, Y. Wang, X. Wang, S. Han, X. Liu, J. S. DuChene, H. Zhang, Q. Zhang, X. Chen, J. Ma, S. C. J. Loo, W. D. Wei, Y. Yang, J. T. Hupp, F. Huo, *Nat. Chem.*, 2012, **4**, 310.

List of Publications

I. Original Papers

1. Tailored Design of Functional Nanoporous Carbon Materials toward Fuel Cell Applications
Nano Today, 2014, 9(3), 305-323. (Published on 4 Jul 2014)

Jing Tang, Jian Liu, Nagy L. Torad, Tatsuo Kimura, Yusuke Yamauchi

2. Towards Vaporized Molecular Discrimination: A Quartz Crystal Microbalance (QCM) Sensor System Using Cobalt-Containing Mesoporous Graphitic Carbon.

Chemistry - An Asian Journal, 2014, 9(11), 3238-3244. (Published on 11 Sep 2014)

Jing Tang, Nagy L. Torad, Rahul R. Salunkhe, Jang-Hee Yoon, Md Shahriar Al Hossain, Shi Xue Dou, Jung Ho Kim, Tatsuo Kimura, Yusuke Yamauchi

3. Synthesis of Nitrogen-Doped Mesoporous Carbon Spheres with Extra-Large Pores through Assembly of Diblock Copolymer Micelles

Angewandte Chemie International Edition, 2015, 54(2), 588-593. (Published on 12 Nov 2014)

Jing Tang, Jian Liu, Cuiling Li, Yunqi Li, Moses O. Tade, Sheng Dai, Yusuke Yamauchi

4. Thermal Conversion of Core–Shell Metal–Organic Frameworks: A New Method for Selectively Functionalized Nanoporous Hybrid Carbon

Journal of the American Chemical Society, 2015, 137(4), 1572-1580. (Published on 12 Jan 2015)

Jing Tang, Rahul R. Salunkhe, Jian Liu, Nagy L. Torad, Masataka Imura, Shuhei Furukawa, Yusuke Yamauchi

5. A Facile Preparation of Mesoporous Carbon Composites with Well-Dispersed Pd Nanoparticles and Their Utilization as Supports for Pt Catalysts

Electrochimica Acta, 2015, 183, 112-118. (Published on 29 Apr 2015)

Jing Tang, Tao Wang, Victor Malgras, Jung Ho Kim, Yusuke Yamauchi, Jianping He

6. Three-Dimensional Nitrogen-Doped Hierarchical Porous Carbon as an Electrode for High-Performance Supercapacitors

Chemistry - A European Journal, 2015, 21(48), 17293-17298. (Published on 14 Oct 2015)

Jing Tang, Tao Wang, Rahul R. Salunkhe, Saad M. Alshehrid, Victor Malgras, Yusuke Yamauchi

7. Nitrogen-Doped Hollow Carbon Spheres with Large Mesoporous Shells Engineered from Diblock Copolymer Micelles

Chemical Communications, 2016, 52(3), 505-508. (Published on 21 Oct 2015)

Jing Tang, Jian Liu, Rahul R. Salunkhe, Tao Wang, Yusuke Yamauchi

8. Cage-Type Highly Graphitic Porous Carbon–Co₃O₄ Polyhedron as the Cathode of Lithium–Oxygen Batteries

ACS Applied Materials & Interfaces, 2016, 8(4), 2796-2804. (Published on 20 Jan 2016)

Jing Tang, Shichao Wu, Tao Wang, Hao Gong, Huabin Zhang, Saad M. Alshehri, Tansir Ahamad, Haoshen Zhou, Yusuke Yamauchi

9. Carbon Materials: MOF Morphologies in Control.

Nature Chemistry, 2016, 8(7), 638-639. (Published on 21 June 2016)

Jing Tang, Yusuke Yamauchi

10. Bimetallic Metal–Organic Frameworks for Controlled Catalytic Graphitization of Nanoporous Carbons

Scientific Reports, 2016. (Accepted on 2 Jul 2016)

Jing Tang, Rahul R. Salunkhe, Huabin Zhang, Victor Malgras, Tansir Ahamad, Saad M. Alshehri, Naoya Kobayashi, Satoshi Tominaka, Yusuke Ide, Jung Ho Kim, Yusuke Yamauchi

11. Asymmetric Supercapacitors Using 3D Nanoporous Carbon and Cobalt Oxide Electrodes Synthesized from a Single Metal–Organic Framework

ACS Nano, 2015, 9(6), 6288-6296. (Published on 15 May 2015)

Rahul R. Salunkhe, **Jing Tang**, Yuichiro Kamachi, Teruyuki Nakato, Jung Ho Kim, Yusuke Yamauchi

12. A Synergistic System for Lithium–Oxygen Batteries in Humid Atmosphere Integrating a Composite Cathode and a Hydrophobic Ionic Liquid-Based Electrolyte

Advanced Functional Materials, 2016, 26(19), 3291-3298 (Published on 29 Feb 2016)

Shichao Wu, **Jing Tang**, Fujun Li, Xizheng Liu, Yusuke Yamauchi, Masayoshi Ishida, Haoshen Zhou

13. Ultrahigh Performance Supercapacitors Utilizing Core–Shell Nanoarchitectures from a Metal–Organic Framework-Derived Nanoporous Carbon and a Conducting Polymer

Chemical Science, 2016, DOI: 10.1039/C6SC01429A. (Published on 10 Jun 2016)

Rahul R. Salunkhe, **Jing Tang**, Naoya Kobayashi, Jeonghun Kim, Yusuke Ide, Satoshi Tominaka, Jung Ho Kim, Yusuke Yamauchi

14. High-Loading Nano-SnO₂ Encapsulated in situ in Three-Dimensional Rigid Porous Carbon for Superior Lithium-Ion Batteries

Chemistry - A European Journal, 2016, 22(14), 4915-4923. (Published on 25 Feb 2016)

Hairong Xue, Jianqing Zhao, **Jing Tang**, Hao Gong, Ping He, Haoshen Zhou, Yusuke Yamauchi, Jianping He

15. A High-Performance Supercapacitor Cell based on ZIF-8-Derived Nanoporous Carbon Using an Organic Electrolyte

Chemical Communications, 2016, 52(26), 4764-4767. (Published on 01 Mar 2016)

Rahul R. Salunkhe, Christine Young, **Jing Tang**, Toshiaki Takei, Yusuke Ide, Naoya Kobayashi, Yusuke Yamauchi

16. Co₃O₄-Embedded Porous ZnO Rhombic Dodecahedron Prepared by the Use of Zeolitic Imidazolate Frameworks as Precursors for CO₂ Photoreduction

Nanoscale, 2016, 8(12), 6712-6720. (Published on 22 Feb 2016)

Tao Wang, Li Shi, **Jing Tang**, Victor Malgras, Shunsuke Asahina, Guigao Liu, Huabin Zhang, Xianguang Meng, Kun Chang, Jianping He, Osamu Terasaki, Yusuke Yamauchi, Jinhua Ye

17. Dual Soft-Template System Based on Colloidal Chemistry for the Synthesis of Hollow Mesoporous Silica Nanoparticles

Chemistry - A European Journal, 2015, 21(17), 6375-6380. (Published on 4 Mar 2015)

Yunqi Li, Bishnu Prasad Bastakoti, Masataka Imura, **Jing Tang**, Ali Aldalbahi, Nagy L. Torad, Yusuke Yamauchi

18. Multimetallic Mesoporous Spheres Through Surfactant Directed Synthesis

Advanced Science, 2015, 2(8), 1500112. (Published on 25 Jun 2015)

Bo Jiang, Cuiling Li, Masataka Imura, **Jing Tang**, Yusuke Yamauchi

19. Ordered Hexagonal Mesoporous Aluminosilicates and their Application in Ligand-Free Synthesis of Secondary Amines

ChemCatChem, 2015, 7(5), 747-751. (Published on 5 Feb 2015)

Pavuluri Srinivasu, Dupati Venkanna, Mannepalli Lakshmi Kantam, **Jing Tang**, Suresh K. Bhargava, Ali Aldalbahi, Kevin C.-W. Wu, Yusuke Yamauchi

20. Polymeric Micelle Assembly for the Smart Synthesis of Mesoporous Platinum Nanospheres with Tunable Pore Sizes

Angewandte Chemie International Edition, 2015, 54(38), 11073-11077. (Published on 11 Aug 2015)

Yunqi Li, Bishnu Prasad Bastakoti, Victor Malgras, Cuiling Li, **Jing Tang**, Jung Ho Kim, Yusuke Yamauchi

21. A Highly Energetic N-Rich Metal–Organic Framework as a New High-Energy-Density Material

Chemistry - A European Journal, 2015, 22(3), 1141-1145. (Published on 10 Dec 2015)

Huabin Zhang, Mingjian Zhang, Ping Lin, Victor Malgras, **Jing Tang**, Saad M. Alshehri, Yusuke Yamauchi, Shaowu Du, Jian Zhang

II. Oral & Poster Presentations in Conferences/Symposiums

1. Thermal Conversion of Core–Shell Metal–Organic Frameworks: A New Method for Selectively Functionalized Nanoporous Hybrid Carbon (Oral presentation)

The 6th NIMS (MANA)-Waseda International Symposium (Tokyo, Japan), 29 July, 2015.

Jing Tang, Rahul R. Salunkhe, Yusuke Yamauchi

2. A Facile Preparation of Mesoporous Carbon Composites with Well-Dispersed Pd Nanoparticles and Their Utilization as Supports for Pt Catalysts (Poster presentation)

The 10th International Symposium on Electrochemical Micro & Nanosystem Technologies (Okinawa, Japan), 6 Nov 2014.

Jing Tang, Tao Wang, Yusuke Yamauchi, Jianping He

3. Layer-by-Layer Architectures of Metal–Organic Frameworks (MOFs): Synthesis of Core–Shell ZIF-8@ZIF-67 Particles (Oral presentation)

The 5th NIMS (MANA)-Waseda International Symposium (Tsukuba, Japan), 24 Mar 2014.

Jing Tang, Yusuke Yamauchi

4. Synthesis of Novel Nanoporous Carbons for Application as Electrode Materials (Oral presentation)

Joint Graduate Student Seminar of NIMS (Tsukuba, Japan), 14 Jan 2014

Jing Tang

5. Graphitic Nanoporous Carbons-Co composite: Synthesis and Applications (Oral presentation)

Joint Graduate Student Seminar of NIMS (Tsukuba, Japan), 15 Jan 2013

Jing Tang

Acknowledgements

The past three years' study in Waseda University and National Institute for Materials Science (NIMS) is a wonderful and unforgettable journey in my life, which lays a significant foundation for my whole research career. I deeply appreciate everyone who has supported and helped me when I meet challenges.

First of all, I would like to express my most sincere gratitude to my supervisor, Prof. Yusuke Yamauchi, for his invaluable guidance and continuously support throughout my three years' graduate study. I have learnt a lot of fundamental and significant knowledge of nanofabrication from him and have been deeply influenced by his enthusiasm and persistence in scientific research, which will lead me to become an excellent researcher in the future. I would not be able to complete my doctoral programme and gradually grow to be a real researcher without his help.

Special appreciation to Profs. Dr. Kazuyuki Kuroda, Dr. Yoshiyuki Sugahara, Dr. Toru Asahi, and Dr. Kiyoshi Shimamura, for their careful review and helpful suggestions. Their invaluable comments and academic advices for my dissertation and presentation have made me think more about my research. I have learnt a lot from the comments and will think deeply and carefully in the scientific research. Thanks for the encouragement and instruction from Prof. Yoshio Bando and Prof. Toyohiro Chikyow. I also appreciate the strong support from Prof. Jinhua Ye, Prof. Haoshen Zhou, and Prof. Yusuke Ide, providing me with the advanced characterization facilities.

Since I joined Prof. Yamauchi's group, I have received countless assistance from my colleagues and collaborators including but not limit to Dr. Tao Wang, Dr. Jian Liu, Dr. Xiangfen Jiang, Dr. Nagy L. Torad, Dr. Cuiling Li, Dr. Yunqi Li, Dr. Rahul R. Salunkhe, Dr. Victor Malgras, Mrs. Kimiko Takai, Mr. Yuichiro Kamachi, Dr. Monica Ostrowska, Mrs. Akemi Tatenno, Mrs. Naoko Kaneta, Mr. Mohamed B. Zakaria, Mr. Bo Jiang, Miss. Jie Wang, Miss. Yanna Guo, Mr. Huayu qian, Mr. Haibo Tan, Dr. Norihiro Suzuki, Dr. Bishnu Prasad Bastakoti, Dr. Malay Pramanik, Dr. Yi-Chen Wu, Miss. Yi-Syuan Lu, and Miss. Pei-Hsin

Young. During the past three years, I meet many new friends and will remember their warm kindness and care in both research and life. I wish to appreciate Dr. Xuebin Wang, Dr. Peng Li, Dr. Kun Chang, Dr. Jing Zhao, Dr. Huabin Zhang, Dr. Mu Li, Mr. and Mrs. Lequan Liu, Dr. Xianguang Meng, Miss. Qin Yu, Miss. Hongmei Wang, Miss. Hong Pang, Dr. Hongpan Rong, Dr. Guowei Wang, and Dr. Pan Xiong.

I really appreciate the “Waseda University-NIMS Joint Graduate Program” which provide me the wonderful opportunity to pursue my doctoral degree in Japan, not only provide me with strong financial support on my life but also perfect study and research environment. I would like to thank the operators and secretaries of Waseda University and NIMS for their help in official bussiness. I am truly grateful to the staffs of Technical-Support Team in International Center for Materials Nanoarchitectonics (MANA) for the technological assistance, especially Dr. Makito Nakatsu, Dr. Kiyotaka Iiyama, and Mr. Toshiaki Takei. Thanks the help from Materials Analysis Station and NIMS Nanofabrication Platform, as well as to all the NIMS staffs and MANA members. I really enjoy the study and work in NIMS. I would like to thank Ms. Xiaoyin Wang from Japan International Science and Technology Exchange Center for the help on my living in Tsukuba.

I would like to express my gratitude to my previous supervisor, Prof. Dr. Jianping He, for the valuable academic training and encouragement during the period of pursuing my mater degree in Nanjing University of Areonautics and Astronautics. Thanks the support from Profs. Dr. Xiaogang Zhang and Dr. Haibo Zeng when I was applying the doctoral programme. I also want to thank my previous group members, including but not limit to Dr. Jianqing Zhao, Dr. Yunxia Guo, Mr. Shichao Wu, Mr. Hairong Xue, and Mr. Hao Gong.

Finally, I heartily thank my mother Mrs. Jihong Wu, my father Mr. Yuwen Tang, my fiancé Dr. Tao Wang, and all the families for their infinite love and always support.

July 2016 in Tsukuba

TANG Jing